DOKUZ EYLÜL UNIVERSITY

GRADUATE SCHOOL OF NATURAL AND APPLIED SCIENCES

DISTRIBUTION, MINERALOGY, AND PETROGRAPHY OF VOLCANICLASTIC SUCCESSIONS ON THE BODRUM-MUGLA PENINSULA BELONGING TO KOS-NISYROS-YALI VOLCANIC ACTIVITIES

by

Cennet ULUKAVAK

December, 2023

İZMİR

DISTRIBUTION, MINERALOGY, AND PETROGRAPHY OF VOLCANICLASTIC SUCCESSIONS ON THE BODRUM-MUGLA PENINSULA BELONGING TO KOS-NISYROS-YALI VOLCANIC ACTIVITIES

A Thesis Submitted to the
Graduate School of Natural and Applied Sciences of Dokuz Eylül University
In Partial Fulfillment of the Requirements for Master of Science in
Department of Geological Engineering, Economic Geology Program

by

Cennet ULUKAVAK

December, 2023

İZMİR

M.Sc THESIS EXAMINATION RESULT FORM

We have read the thesis entitled **"DISTRIBUTION, MINERALOGY AND PETROGRAPHY OF VOLCANICLASTIC SUCCESSIONS ON THE BODRUM-MUGLA PENINSULA BELONGING TO KOS-NISYROS-YALI VOLCANIC ACTIVITIES."** completed by **CENNET ULUKAVAK** under supervision of **PROF. DR. CUNEYT AKAL** and we certify that in our opinion it is fully adequate, in scope and in quality, as a thesis for the degree of Master of Science.

Prof.Dr. Cüneyt AKAL

Supervisor

Assoc. Prof. Dr. Ökmen SÜMER

Jury Member

Assoc. Prof. Dr. Fırat ŞENGÜN

Jury Member

Prof. Dr. Okan FISTIKOĞLU

Director

Graduate School of Natural and Applied Sciences

ACKNOWLEDGMENT

First and foremost, I would like to express my gratitude to myself for never giving up, even in the face of numerous challenges during this academic journey. While this thesis was completed at the master's level, I felt a personal growth beyond the confines of this title, and that determination has been my driving force.

I extend my deepest gratitude to my supervisor, Prof. Dr. Cüneyt Akal, whose remarkable breadth of knowledge spans far beyond volcanology and petrology. He has been a true inspiration with his dedication to science and learning; generously shared insights not only in my field but also in many of fields. His ability to both appreciates and humor my obsessions, as well as his skill in reminding me of the bigger picture, are unmatched. Despite my challenges with ADHD, his unwavering support and kindness, even to a little "Böcük" like me, are deeply grateful.

I also want to express my heartfelt thanks to Dr. Erhan Akay, whose shared passion for volcanology and generous sharing of knowledge has significantly enriched my understanding of this captivating field. His insights and discussions have been invaluable in shaping the direction of my research, and I am genuinely appreciative of his contributions to my growth as a budding volcanologist.

I extend my sincere appreciation to Dr. Ökmen Sümer for his invaluable guidance in teaching me effective research methods and continuously enhancing my research skills. His profound intellectual contributions have played a crucial role in deepening my understanding of the philosophical foundations of scientific inquiry.

I would also like to express my deep appreciation to my dear fellow countrywoman, Fatmanur Çakır. We have been each other's endless source of motivation and support throughout our academic journey. Dear Birsin, our motivational conversations and knitting sessions will forever hold a special place in my heart. Your presence has made this challenging academic journey more manageable, and I eagerly anticipate continuing this path together. To my dear volcanologist Ph.D. candidate, Rengin Özsoy, words cannot adequately express my gratitude for the wealth of knowledge and life experiences you have shared with me, both in the realm of volcanology and

beyond. The time spent during the academic week in Rome with Berke, Simge, and you... Era perfetto!

I would like to express my gratitude to Dr. Locy Vanderkluysen and Dr. Emrah Yılmaz, who shared the publications for their valuable contribution to this study. Also, I would like to acknowledge the contributions of all my professors, including Prof. Dr. Talip Güngör, Prof Dr. Namık Aysal, Dr. Fatma Şişman Tukel, Dr. Semih Eski, Dr. İsmail Işıntek, Dr. Gökhan Atıcı, and colleague Ali Duman, Mihrican Karataş who have provided encouragement, and inspiration throughout this academic journey.

Lastly, I owe an immeasurable debt of gratitude to my beloved family, my mom Nezahat Ulukavak, and my dad İlhan Ulukavak and my uncle Mehmet Erdem without whom I wouldn't have succeeded. Their unwavering support, and encouragement, even in the face of the most challenging circumstances, have been the bedrock of my resilience and determination. Their sacrifices and enduring belief in me have made this journey possible, and for that, I am eternally thankful. And I owe a special debt of gratitude to my beloved dogs Köpük and Dobby, as well as my parrot Pasha, for sharing their purest love and accompanying me during countless nights of research. How could I have persevered without you, my little friends? Your presence has brought joy, comfort, and a sense of purpose to my academic endeavors, and for that, I am truly thankful.

Special thanks go to my fiancé, Berkecan Akdemir, whose unwavering support, both financially and emotionally, has been the bedrock of this study. Without your unwavering dedication and support, from field studies to every step of this academic journey, this study would not have been possible. Your presence during nearly every event, your devotion and patience during my most challenging moments, including when I cried, when I was angry, and when I was insufferable, demonstrate that you've been with me every step of the way. I am grateful that we have faced these challenges together. Your unwavering belief in me and your sacrifices have been invaluable, and I am profoundly grateful for your unwavering presence in my life.

Cennet ULUKAVAK

DISTRIBUTION, MINERALOGY, AND PETROGRAPHY OF VOLCANICLASTIC SUCCESSIONS ON THE BODRUM-MUGLA PENINSULA BELONGING TO KOS-NISYROS-YALI VOLCANIC ACTIVITIES

ABSTRACT

~161ka, a massive volcanic eruption occurred in the Hellenic Arc region, known as the Kos Plateau Tuff (KPT) eruption. The Greek Islands and Western Anatolia, including the Bodrum and Datça peninsulas, were significantly impacted by a pyroclastic density current (PDC). The transportation mechanism of PDC moving northward has been a subject of interest, but there is no detailed study on the Bodrum Peninsula yet. This study aims to address this gap by conducting thorough fieldwork and key analyses to explore the physical volcanological attributes of the Bodrum Peninsula. The sequences contain different depositional environments, including beach deposits and marine shell remains, indicating interactions with coastal environments. Variations in sorting, bedding, and the presence of accretionary lapilli suggest the crucial of topographic complexity in shaping the landscape and distribution of volcanic materials. Petrological examination points to a dynamic volcanic history involving rapid cooling, plastic deformation, and interactions with external fluids. Geochemical analyses align seamlessly with previous KPT datasets, affirming the high rhyolitic compositional field and calc-alkaline nature of volcanic rocks resulting from the violent eruption. This master's thesis emphasizes the significance of adopting a multifaceted approach, combining fieldwork with sedimentological, petrological, and geochemical analyses. This integrated methodology aims to establish correlations between specific features of PDCs and their emplacement and transport mechanisms on the Bodrum Peninsula. The findings not only to adopt understand the local volcanic history but also highlight the broader implications for volcanic hazard assessment and mitigation strategies in similar geological settings.

Keywords: Kos Plateau Tuff, pyroclastic density currents, transport mechanism

KOS-NISYROS-YALI VOLKANIK AKTIVITELERINE AIT VOLKANIKLASTIK ISTIFLERIN BODRUM-MUĞLA YARIMADASINDAKI DAĞILIMI, MINERALOJISI VE PETROGRAFISI

ÖZ

~161binyıl önce, Helenik Yayı üzerinde, Kos Plato Tüfü (KPT) patlaması olarak bilinen devasa bir volkanik patlama meydana gelmiştir. Bodrum ve Datça yarımadaları da dahil olmak üzere Yunan Adaları ve Batı Anadolu, patlama sonucu gelişen piroklastik yoğunluk akıntısından (PDC) önemli ölçüde etkilenmiştir. Kuzeye doğru ilerleyen PDC'nin ulaşım mekanizması ilgi konusu olmuştur ancak Bodrum Yarımadasıyla ilişkin henüz detaylı bir çalışma bulunmamaktadır. Bu çalışma, Bodrum Yarımadası'nın fiziksel volkanolojik özelliklerini araştırmak için kapsamlı saha çalışması ve anahtar analizler yaparak bu boşluğu gidermeyi amaçlamıştır. İstifler sahil ortamları ile etkileşimleri gösteren, sahil çökeltileri ve deniz kabuğu kalıntıları dahil olmak üzere farklı çökelme ortamlarını içermektedir. Boylanma, tabakalanma ve yığışım lapillilerin varlığındaki değişkenlikler, topoğrafik karmaşıklığın güncel araziyi şekillendirmede ve volkanik malzemelerin dağılımındaki etkin rolün altını çizmektedir. Petrolojik incelemeler, hızlı soğuma, plastik deformasyon ve dış akışkanlarla etkileşimi içeren dinamik bir volkanik geçmişe işaret etmektedir. Jeokimyasal analizler önceki KPT veri gruplarıyla mükemmel bir şekilde uyum sağlar ve şiddetli patlama sonucu oluşan volkanik kayaların yüksek riyolitik bileşimi ve kalk-alkali doğasını destekler. Bu yüksek lisans tezi, saha çalışmasının sedimantolojik, petrolojik ve jeokimyasal analizlerle birleştiren çok yönlü bir yaklaşımın benimsenmesinin önemini vurgulamaktadır. Bu entegre metodoloji, PDC'lerin spesifik özellikleri ile bunların Bodrum Yarımadası'ndaki yerleşim ve taşınma mekanizmaları arasında korelasyon kurmayı amaçlamaktadır. Bulgular yalnızca yerel volkanik tarihi anlamakla kalmayıp, aynı zamanda benzer jeolojik ortamlarda volkanik tehlike değerlendirmesi ve azaltma stratejileri için daha geniş sonuçları da vurgulamaktadır.

Anahtar Kelimeler: Kos Yaylası Tüfü, piroklastik yoğunluk akıntıları, taşınma mekanizması.

CONTENTS

Page

LIST OF FIGURES

Page

LIST OF TABLE

Page

LIST OF APPENDIXES

Page

LIST OF ABBREVIATION

AFM	: Alkaline (Na-K), Iron (Fe), Magnesium
amp	: Amphibole
B	: Biotite
EMODnet	: The European Marine Observation and Data Network
EPMA	: Electron Probe Micro-Analyzer
Fp	: Frothy Pumice
G	: Glass
hrnb	: Hornblende
KPT	: Kos Plateau Tuff
KNYVC	: Kos Nisyros Yali Volcanic Complex
LA-ICP-MS	: Laser Ablation Inductively Coupled Plasma-Mass Spectrometry
LLD	: Liquid Line of Descent
MREE	: Middle REE Enrichments
NAF	: North Anatolian Fault
olv	: Olivine
p	: Pumice
PDC	: Pyroclastic Density Current
plg	: Plagioclase
ppl	: Plain Polarized Light
prx	: Pyroxene
REE	: Rare Earth Elements
SAVA	: South Aegean Volcanic Arc
SEM	: Scanning Electron Microscope
SIMS:	: Secondary-Ion Mass Spectrometry
TAS	: Total Alkali-Silica
Tsat	: Temputure $_{saturation}$
Tp	: Tube Pumice
Q	: Quartz
XRD	: X-Ray Diffraction Analysis
xpl	: Crossed Polarized Light

CHAPTER ONE

INTRODUCTION

The subduction of the African plate beneath the Eurasian plate along the Hellenic Subduction Zone led to the formation of volcanic arc sequences on the Aegean Microplate, which can be traced geographically and chronologically from north to south. The initial volcanic arc, comprising magmatic assemblages, emerged approximately 30 million years ago in northeast Greece and northwest Turkey. The effects of intense volcanic activity, characterized by Methana, Milos, Santorini, Kolumbo, and Kos-Nisyros-Yali volcanoes, are evident along the South Aegean Volcanic Arc (SAVA), which assumed its present position roughly 5 million years ago. The southward migration of the volcanic arc, originally originating in the northern parts of the Aegean Microplate, was controlled by the backward bending & subduction of the subducting plate beneath the Aegean Microplate since the Early Miocene (Pe-Piper & Piper, 1989). Matsuda et al. (1999) reported that calc-alkaline volcanic activity within the SAVA system is younger than 4 million years. The northern islands of Aegina, Kos (2.6+0.2, 3.1+0.3 million years), and Poros (2-3.6 million years) have experienced this recent volcanic activity. The southern islands of Methana, Nisyros (0.1+0.1, 0.8+0.7 million years), Milos, and Santorini, however, exhibit the youngest ages, with Santorini being dated to 1627-1600 BC by Friedrich et al. (2006). Geochronological investigations have revealed that volcanic activities along the South Aegean Volcanic Arc have given rise to the volcanic islands of Sousaki, Aegina, Poros, Methana, Milos, Christiana, Santorini, Kolumbo, Kos, Nisyros, and Yali from west to east (Pe-Piper & Piper, 1989). The volcanic rock assemblages on these islands generally fall within the calc-alkaline and high-K calc-alkaline series, although basaltic rocks with tholeiitic characteristics are observed on Santorini (Nomikou et al., 2018). The active volcanic system comprises the islands of Kos, Nisyros, and Yali, which are the closest to the mainland of Turkey. The Kos-Nisyros-Yali Volcanic Complex (KNYVC), situated at the westernmost tip of the South Aegean Volcanic Arc, lies approximately 37 km from the shores of the Bodrum Peninsula. Numerous studies have been conducted to elucidate the geology of Miocene-aged magmatic rock units in the Bodrum Peninsula (e.g., Burri et al., 1967; Robert & Cantagrel, 1977; Pişkin,

1980; Robert et al., 1992; Altunkaynak & Yılmaz, 2001; Genç et al., 2001; Işseven et al., 2005; Karacık, 2006; Oyman & Dyar, 2007; Masse et al., 2015; Akal et al., 2021; Çubukçu et al., 2021).

1.1 Study Area

The Bodrum Peninsula occupies a distinct landmass jutting into the Aegean Sea and is situated between approximately 37° and 37°30' north latitude and 27°15' and 28° longitude. It is surrounded by the Gulf of Gökova to the east, the Gulf of Güllük to the north, and the Aegean Sea to the west and south (Figure, 1.1). Located within the larger Mugla Province, the peninsula benefits from its proximity to the town of Bodrum (Figure, 1.2), which serves as a gateway to the area. This area also holds historical and cultural significance, with the ancient city of Halicarnassus and its iconic Mausoleum at Halicarnassus, one of the Seven Wonders of the Ancient World, once located in this area. The region's blend of archaeological sites, traditional villages, and contemporary tourism infrastructure contributes to its cultural richness.

1.2 Scopes and Aims

The pyroclastic deposits, which form the eruption columns of the Kos-Nisyros-Yali volcanic activity can be identified along the Turkish Aegean-Mediterranean coastline, around the Bodrum and Datça peninsulas. In particular, the sequences described in the Datça peninsula have garnered significant attention from researchers in recent years. Although the presence of Kos Plateau Tuff (KPT) in the Bodrum and Datça peninsulas is documented (Ercan et al. 1982; 1984; Ersoy, 1991; Allen et al. 1999; Allen & Cas 1998; Dirik et al. 2003; Gençalioğlu-Kuşçu & Uslular, 2018; Gençalioğlu-Kuşçu et al., 2020), uncertainties have arisen regarding the stratigraphic correlation of the KPT sequences. While limited studies have been conducted in the Datça region, apart from mapping, detailed investigations are lacking in the Bodrum peninsula. It remains unclear which position & stratigraphic level these sequences correspond to within the overall succession.

This study aims to determine the physical volcanological characteristics of the KPT observed in the Bodrum peninsula by measuring these successions & correlating them with the overall stratigraphy.

Another contentious issue raised in previous studies is the incomplete understanding of sea-level changes (e.g., Ulusoy, 2002; Uluğ et al., 2005; Isler, 2012; Şimşek et al., 2017; Özdemirli-Esat et al., 2022; Çelikbaş, 2022; Zobu & Doğan, 2023) and their transportation mechanisms (e.g., Pe-Piper 2005; Dufek & Bergantz, 2007; Pe-Piper, 2020). Based on the literature (Keller, 1969; Allen, 1998;1999;2000;2001), it is believed that the Kos-Kalymnos side was transported overland, while the Datça-Tilos side was transported over the sea. Pe-Piper et al. (2003) described that the KPT eruption originated from an andesitic stratovolcano and was transported by pyroclastic flows along a coastal plain that was exposed on the continent. They noted the existence of deeper sea or lake basins in the Kos basin. The authors also emphasized that the accumulation of KPT material in the basins south of Nisyros and west of Kalymnos might have occurred through submarine pyroclastic flows caused by the collapse of the edge of the East Kos basin due to volcanic activity-induced landslides. While Pasteels et al. (1986) suggested that the sea level during the Upper Pleistocene could have fluctuated between ~150 and +2-3 meters (above mean sea level) studies in the literature (e.g., Machida, 1981; Mahood & Wallmann, 1985) have shown that differences in O^{18} isotope values, used to infer sea level changes, could be attributed to faulting and volcanic states. Isostatic changes resulting from volcanic explosions could have affected these values. Allen (1998; 2001) mentioned that, as described by Cas & Wright (1991), KPT pyroclastic flows can be saltation across water when coarse, dense volcanic lithics move at high velocities and strike the water at a low incidence angle. Allen, 2001 also suggested that the abundance of crystals found in the distal pyroclastic succession from the KPT eruption could be due to the preferential loss of highly vitric ash resulting from the increased gas flow, generated by steam produced from water saltation in the flow.

Numerous researchers have emphasized that approximately 161 ka, the global sea level was around 60-80 meters lower than the present level, both before and during the Kos-Nisyros volcanic activity (Flemming, 1978; Le Pichon & Angelier, 1981; Chappell & Shackleton, 1986; Pasteels et al., 1986; Allen & Cas, 1998). Allen & McPhie (2001) highlighted that the landmass of Kos might have extended northward to the current island of Kalymnos and the Bodrum peninsula, where the sea is relatively shallow (40-60 meters water depth; Allen & Cas, 2001). In their study on the island of Kos's morphology and its impact on the sea, Piper & Pe-Piper (2020) reported a sea level of -78±12 meters.

Figure, 1.1 attempted to illustrate the paleogeography around the Aegean Volcanic arc around 161 ka. and the probable sea level position using data and maps from previous studies. The deposition of distal facies kilometers away from the KPT eruption, indicating the potential transportability of the Kos-Nisyros-Yali volcanic products, remains an open area for further research. On the other hand, some researchers (Dufek & Bergantz, 2007; Bouvet de Maisonneuve et al., 2009; Palladino et al., 2008; Pe-Piper, 2020) findings are evident of water content/relations. Also, some recent studies (Koutruoli et al., 2018; Koutruoli, 2022; Zhang et al., 2023) suggested that another eruption may also occur. The Kos-Nisyros-Yali volcanic complex is regarded as a classic example of a cycling caldera system and unexpected eruptions of the Kos volcano could happen not as part of the classic eruption cycle, suggesting there is much to learn about the nature of the Kos volcanic system (Zhang et al., 2023).

The materials attributed to the KPT within the Kos-Nisyros-Yali volcanic complex have been dispersed in Western Anatolia and the surrounding islands, such as Tilos, Nisyros, Pachia, and Kalymnos. However, no chronological, mineralogical, petrographic, or geochemical studies have been conducted on the Turkish peninsula specifically focusing on the KPT. This study aims to bridge this gap by conducting petrographic and geochemical analyses on the pyroclastic deposit belonging to the KPT in the Bodrum peninsula.

It compares these findings with existing chemical and physical studies to determine their corresponding phases and stratigraphic levels of pyroclastic succession for the first time in such detail. Additionally, this study seeks to understand the presence of water content in relation to the materials.

Figure 1.1 The distribution of magmatic rocks and geological ages observed in the Aegean and surrounding regions. Ages are represented in millions of years (Simplified using references specified within Marchev et al. 2009 and Ersoy et al. 2013 articles)

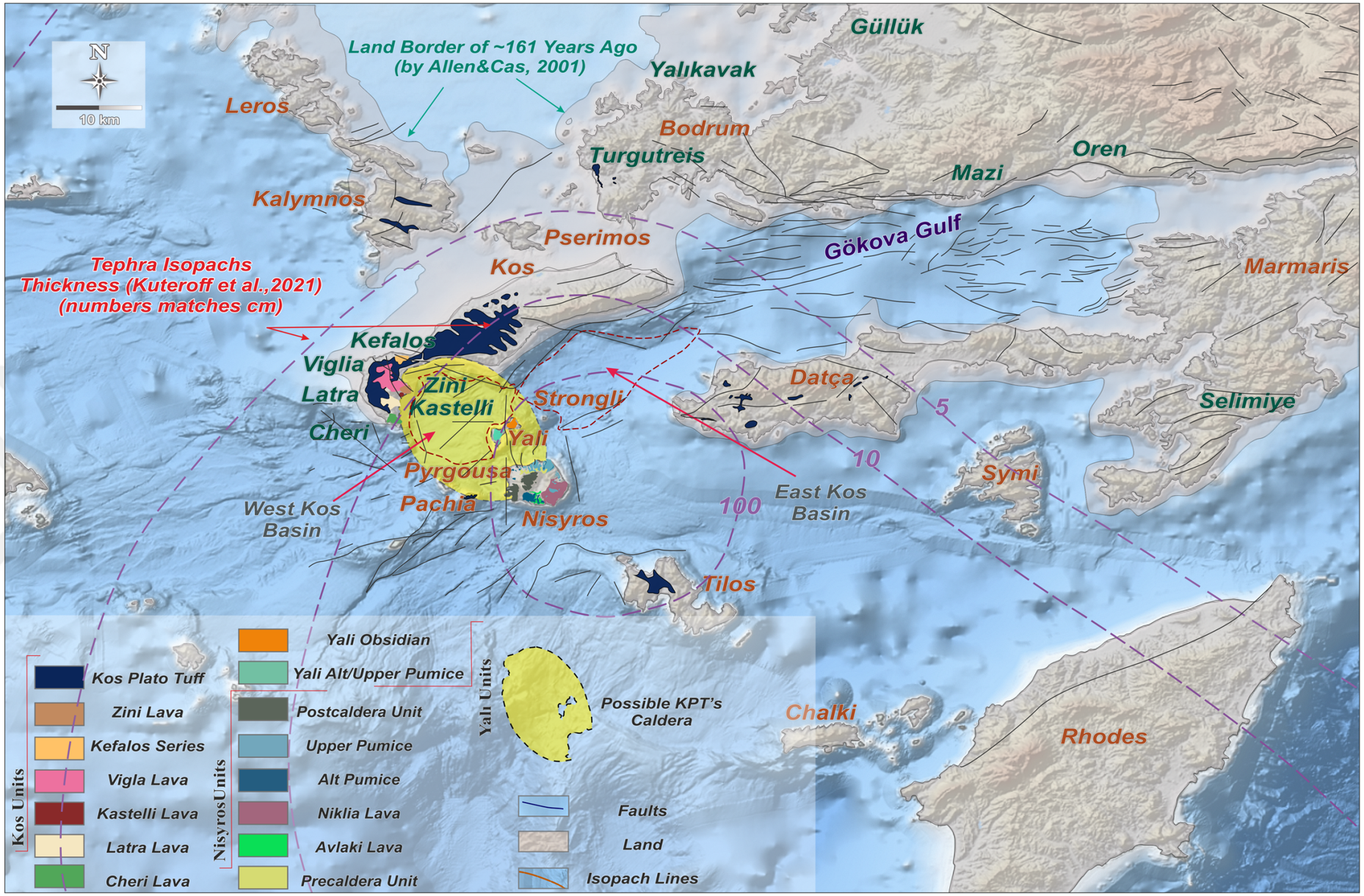

Figure 1.2 Geological Map of the Study Area. A geological map showing the distribution of units specific to the KNYVC compiled for the project proposal and the tectonic faults of the region (dark gray lines). The geological map was constructed using data from relevant geological units as presented in Ulusoy (2002), Pe-Piper & Moulton (2008), Gençalioğlu-Kuşçu et al. (2015), Ganas et al. (2019), Popa et al. (2020), and Bouvet de Maisonneuve et al. (2009), as well as data on tectonic faults from Tur et al. (2015), Nomikou et al. (2021), and Toker (2021). The coastline during the KPT eruption period was adapted using sea-level change data presented by Allen & Cas (2001). The possible caldera boundary for the KPT era was synthesized from Keller (1989), Allen & Cas (1998 and 2001), Bachmann et al. (2007), Piper & Moulton (2008), Zouzias & St. Seymour (2008), Bachmann (2010), and Piper & Pe-Piper (2020), with tephra isopach data overlaid on the map according to Kutterolf et al. (2021). Additionally, bathymetric data used in the map's creation were obtained from open sources available on EMODnet (The European Marine Observation and Data Network, https://portal.emodnet-bathymetry.eu/)

CHAPTER TWO
PREVIOUS STUDIES

The distribution, development, and characteristics of the products belonging to the Kos-Nisyros-Yali Volcanisms of the Bodrum and Datça Peninsulas are presented under two main headings to illustrate their depiction in the literature. The Kos-Nisyros-Yali volcanism has been extensively investigated by numerous researchers over the years. Strabo, in particular, was the first writer to describe the geographical elements of both the islands and the Mugla region. However, observational geological and geographical studies in the Aegean region were conducted by Strickland & Hamilton (1840), Rayet (1876), Plieninger & Sapper (1920), and Phillipson (1915), among others, laying the foundation for further research.

2.1 Kos-Nisyros-Yali

The magmatic processes, eruption characteristics, and distribution patterns of the Kos-Nisyros-Yali volcanism have been the subject of investigation for many years. Researchers have conducted detailed studies, particularly in relation to tephra correlation. Federman & Carey (1980), Vinci (1985), Hardiman (1999), Aksu (2008), Tomlinson et al. (2012), Nomikou et al. (2013), Karnakas et al. (2015), and Satow et al. (2015) are among the researchers who have conducted extensive research in this field. Their studies have focused on core analyses of deep-sea sediments in the Marmara, Aegean, and Mediterranean regions, aiming to observe the dispersal patterns of materials associated with the eruptions of Kos, Nisyros, and Yali. In addition, there are numerous research (e.g. Francalanci et al., 2005; Francalanci et al., 2007; Francalanci & Zelmer, 2019; Greber et al. 2021) magma mingling and mixing processes on the islands besides stratigraphic studies.

The earliest inscribed study on Kos-Nisyros volcanism was conducted by Martelli (1917). In his research, he conducted mineralogical, petrographic, and geochemical analyses and compiled a book on Nisyros, incorporating the work of previous researchers in the region.

The book provides detailed information, showcasing numerous geological and geographical studies dating back to the 1800s. It traces the development of the Kos-Nisyros-Yali volcanism in the literature until the early 1900s. However, due to the age of these publications, which are quite old, they could not be accessed and included in this study. However, some maps and sketches were found in different sources as shown in Figure, 2.1.

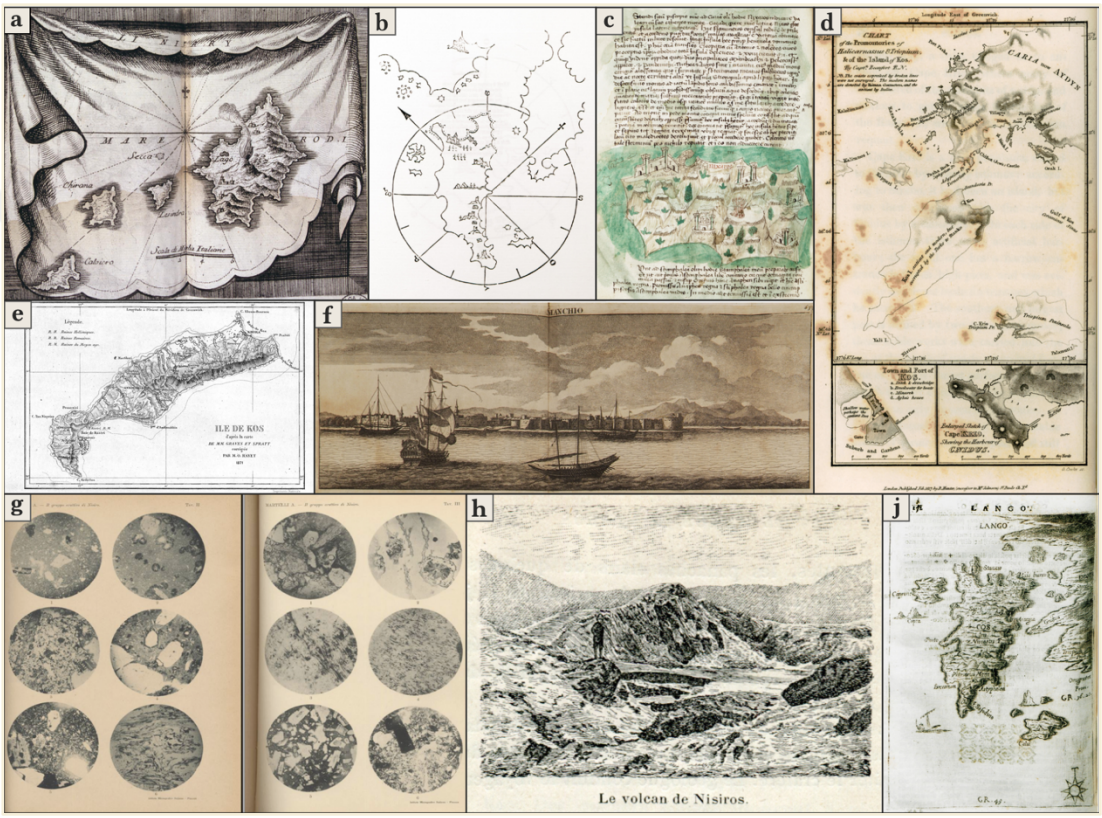

Figure 2.1 Maps and sketches belong to Kos-Nisyros-Yali and Peninsulas places. Sketchs belongs to respectively; a) by Vincenzo Maria Coronelli, 1688 b) by Bartolommeo Dalli Sonetti, 1485 c) by Cristoforo Buendelmonti, 1420 d) Francis Beaufort, 1817 e) by Par. M.O. Rayet, 1871 f) by Cornelis de Bruijn, 1714 g) by Antoine Lavoisier, 1874 h) by Paul Jeancard, 1919 j) by Francesco Piacenza, 1688

Pe-Piper & Piper (1989) conducted a comprehensive study on the small backarc volcanism in the Aegean region, organizing their research into five primary categories: 1. Continental Alkaline Basalts, 2. Incompatible Element Enriched and Nb-depleted sodic basalts, 3. Potassic, 4. Shoshonites, and 5. Calc-Alkaline Andesites. They investigated the distribution and tectonic relationships of these volcanic products, and

they proposed systematic models for magma formation in a mantle layer overlaying the subduction plate at depths ranging from 200 to 400 km.

Varnavas & Cronan (1991) conducted an examination of two hydrothermal fields, where they carried out geochemical studies. Their findings revealed that the hydrothermal waters exhibited higher concentrations of Fe and Mn compared to the average values found in normal seawater. They concluded that the hydrothermal waters off Kos and Yali were particularly enriched in Mn. Additionally, they discussed the observed differences between the Yali-Kos and Santorini hydrothermal systems, attributing them to variations in petrochemical and tectonic characteristics within the Hellenic Volcanic Subduction Zone. Furthermore, they hypothesized the possible formation of submarine metal sulfides in both of the studied hydrothermal fields.

Matsuda et al. (1999) conducted measurements of K-Ar ages on the calc-alkaline lavas within the volcanic arc in order to determine the formation ages of the Aegean volcanic island series. Their findings indicated a southward shift in volcanic activity in accordance with the determined ages. They determined the sliding speed to be 1 cm/year and reported ages of 2.6 ± 0.2 and 3.1 ± 0.3 for Kos, as well as ages of 0.1 ± 0.1 and 0.8 ± 0.7 for Nisyros.

Peltz et al. (1999) aimed to identify chemical signatures of the Minoan Eruption, a volcanic event associated with archaeological findings. To accomplish this, they analyzed pumice samples from different volcanic sources (Milos, Nisyros, Yali, Kos, and Thera) in the Aegean region, focusing on 29 elements. The goal was to establish a comprehensive database and define the pumice and tephra layers. However, it was noted that certain values were missing, which hindered correlation efforts. The study recommended further analytical investigations for a definitive determination.

Pe-Piper et al. (2003) conducted a study with the objective of investigating the neotectonics of the Aegean region between Kos and Tilos islands. They employed high-resolution seismic reflection studies to examine the eruption of the Kos Plateau Tuff and the subsequent development of post-explosion caldera collapse. The tectonic

activities in the region were categorized into three main groups: 1. Basins from the Miocene to Pliocene period, 2. Fault series formed in the Early Pleistocene, and 3. Newly developed fault series around 0.2 Ma. The KPT andesite, which was ejected from the stratocone, was transported by pyroclastic flows along a coastal plain exposed above sea level, despite the presence of deeper sea or lake basins in the Kos basin. Eruption-related landslides occurred along the edges of the Eastern Kos basin, while marine pyroclastic flows were observed south of Nisyros and Kalymnos. As a result, Allen and others argued against the hypothesis that the KPT was transported by crossing the sea, as they believed that there was insufficient evidence to support it.

Bachmann et al. (2010) proposed potential solutions to address these issues. They suggested that reducing the uncertainty in age determination of low Pb zircons could be achieved by minimizing both the analytical gap and the uncertainty in composition. Furthermore, they highlighted the significance of correcting the ^{230}Th-imbalance, which is a significant source of uncertainty that can lead to age discrepancies in high U zircons.

Bachmann et al. (2010) conducted a study on the petrological cycle of silicic magma evolution related to the subsidence of the Kos-Nisyros caldera. Their analysis of rock compositions, mineral chemistry, and zircon Hf isotopes revealed that the three types of siliceous magma followed a consistent differentiation trend. The authors interpreted the conditions of magma formation before and after the caldera collapse as indicative of a slightly drier magmatic column following the decompression event.

Guillong et al. (2014) performed LA-ICP-MS Pb-U dating analyses on zircons from the Kos-Nisyros volcanic center. The study revealed that the eruptions of the Nisyros volcano occurred approximately 140,000 years after the formation of Kos zircons, with ages of 124 ± 35 ka, 111 ± 42 ka, and 70 ± 24 ka, respectively.
The researchers concluded that the ages obtained for the Kos samples were in line with the expected results, while the ages determined for the Nisyros samples were consistent with the predetermined stratigraphy.

Koutroulli (2015) master's thesis focuses on the record of the final stages of explosive volcanic activity in the marine sediments of the Southeast Aegean Sea volcanic arc during the Uppermost Quaternary period. The research aims to investigate and analyze the geological evidence found in these sediments to understand the characteristics and dynamics of the volcanic eruptions that occurred in the region. By studying the composition, ages, and distribution of tephra deposits and other volcanic materials, the thesis seeks to reconstruct the volcanic history of the area and provide insights into the eruptive processes and magmatic evolution. The findings will contribute to a better understanding of the volcanic activity in the Southeast Aegean Sea and its implications for regional geology and hazard assessment.

Koutroulli et al. (2017) investigate the Holocene tephrosratigraphy record of the Kos-Yali-Nisyros Volcanic Centre, aiming to uncover evidence of previously unknown Plinian eruptions. Tephra deposits serve as crucial markers for understanding past volcanic activities, and their identification and characterization contribute to reconstructing the eruptive history of a volcanic system. By analyzing sediment cores and utilizing geochemical and geochronological techniques, this study aims to identify and correlate tephra layers within the Holocene period. The findings reveal the presence of previously unrecognized Plinian eruptions, shedding light on the volcanic activity of the Kos-Yali-Nisyros Volcanic center during this time. This research provides valuable insights into the magnitude, frequency, and characteristics of these eruptions, contributing to a better understanding of the volcanic hazards and dynamics in the region.

Koutrouli et al. (2018) conducted a study with the objective of unraveling the age and characteristics of mid-Holocene volcanism. Their research involved various analyses, including XRD for identifying organic carbon and feldspar content, as well as textural and electron microprobe analyses of volcanic glass fragments and pumice fragments in 20 samples. By examining well-preserved outcrops of tephra layers, they were able to establish accurate age correlations within the Kos-Nisyros-Yali volcanic center, specifically with the Nisyros Lower and Upper Pumice, Yali pumices, and volcanic glasses that are compositionally related to the KPT. They also discovered that

these materials had been reworked from previous sediments and transported by turbidite flows. Traces of Santorini eruptions were observed in the Kalymnos basin. Additionally, the samples collected from the northeastern region of Yali were found to correspond to the ash flow originating from Yali.

Bachman et al. (2019) emphasized the necessity of comprehensive monitoring for the Kos-Nisyros-Yali volcanic region due to recent seismic activity. They highlighted that the volcanic complex remains active and possesses the potential to generate future eruptions.

Kutterolf et al. (2021) investigate the volcanic activity in the region by examining tephra deposits found in marine sediment cores. By employing a multidisciplinary approach that integrates sedimentology, stratigraphy, and geochemical analysis, the authors establish robust correlations between tephra layers, enabling precise dating and identification of volcanic sources. This research sheds light on the eruptive history and volcanic evolution of the Aegean volcanic arc, contributing crucial insights for further investigations on volcanic hazards and long-term volcanic behavior.

Kutterolf et al. (2021) present a comprehensive analysis of tephra ages and volumes, eruption magnitudes, and variations in marine sedimentation rates along the central to eastern Aegean volcanic arc. Utilizing tephrochronology, volumetric analysis, and sediment core examinations, they establish precise age determinations and volumes for tephra deposits, providing insights into the magnitude of past eruptions. Additionally, by assessing sedimentation rate variations, they investigate the relationship between volcanic activity and marine sediment dynamics, contributing to a better understanding of the volcanic system in the region. This study contributes valuable knowledge to the field of explosive volcanism and aids in assessing the hazard potential and long-term behavior of the Aegean volcanic arc.

2.1.1 Kos Island

The internal structure of Kos Plateau Tuff was detailly introduced by Allen & Cas (2001), and it is known that the first geological study of the island was conducted in the 1800s. Several studies have investigated the geothermal potential of the region, including Lagios et al. (1994), La Ruffa et al. (1999), Papoulis et al. (2005), Megalovasilis (2016), and Megalovasilis (2020). Additionally, numerous researchers (e.g. Altherr et al., 1976; Bignot & Guernet, 1976; Bellon & Jarrige, 1979) have examined units belonging to pre-quaternary time conducted on the island, as mentioned in the previous studies' section.

Neumayr (1875) conducted a study on Kos Island where he distinguished various geological units and created a geological map of the island.

Pasteels et al. (1986) conducted K-Ar dating of Kos pumice and obtained an age of 0.24 + 0.02 ma. However, he noted that these ages did not align with the tephra accumulations. Additionally, they mentioned the presence of fumaroles formed on the Kos Plateau, which consists of basic turbulent deposits. These deposits were observed to be 20-30 meters thick and exhibit a collapsed caldera structure.

Dalabakis & Vougioukalakis (1993) identified three units in the Kefalos region in their study: 1) Low-dispersion perlitic pumice, 2) Pyroclastic flow deposits containing well-graded lithic rock fragments, and 3) Thin-bedded, cross-bedded surface deposits. These units were formed as a result of a hydromagmatic eruption, with the Kefalos Tuff dating back to 0.5 million years ago and the nonwelded ignimbrites to 0.14 million years ago. They also noted the presence of a caldera subsidence structure.

Smith et al. (1996) conducted Ar-Ar and K-Ar dating of the Late Quaternary Plinian eruption in their study. The dating study revealed 161.3 + 1.1ka.

Allen & Cas (1997) investigated the physical properties of Lithic Breccia with Co-Ignimbrite, which is associated with the Kos Plateau Tuff. They found that the co-ignimbrites were most commonly observed in the E unit and D unit, and they concluded that the lithic fragments formed in these units were derived from andesite.

Allen (2000) discussed caldera collapse and re-construction. A total of 6 units were distinguished in the area. The (A) unit comprises phreatoplinian debris, while the (B, C) units consist of layered pyroclastic density flow deposits. The dominant volume is occupied by massive and unwelded ignimbrites in the (D, E) units, and the (F) unit consists of layered pyroclastic density flow deposits. They noted that ash debris representing these units could be found on the hill. The study focused on revealing the physical characteristics of all ignimbrites in the region.

Allen & McPhie (2001) conducted research on the physical and chemical properties of chaotic breccias that formed in conjunction with pyroclastic flows. They observed that the chaotic breccias within the KPT units formed simultaneously with highly energetic pyroclastic flows as they interacted with wet and unconsolidated sediment in the lower part of the voluminous and coarsest E unit. The study focused on identifying the stratigraphic location, volume, thickness, composition, and textural features of these breccias.

Allen & Cas (2001) documented the transportation of pyroclastic flows by the sea during the rhyolitic eruption of the Kos Plateau Tuff and provided insights into the extent and physical characteristics of these units. They observed accumulations of the pyroclastic flow deposits up to 60 km away and attributed their ability to be transported over water to their high velocity and turbulent nature. The authors also noted that the deposits in the Datça Peninsula were relatively finer-grained compared to other areas.

Bachmann et al. (2007) presented a model for the formation of the Kos Plateau Tuff using Zr-SIMS, U-Th-Pb dating. According to their findings, the formation process can be summarized as follows:

1. The formation of nearly eutectic rhyolitic magma occurred through closed-system fractionation, involving partial re-melting of younger material, primarily of mafic origin.
2. The magma was emplaced in the upper crust, and a large chimney with a volume exceeding 60 km^3 was formed at a depth of 7-9 km.
3. The deposition of the magma took place over a minimum period of 200,000 years.

Additionally, the authors noted that the magma chamber never reached completed crystallization.

Steinhauser et al. (2007) conducted an investigation on chemical traces from two pumice samples for archaeological applications in the Miletus region. They performed Neutron Activation Analysis on the pumice samples and found chemical traces of Cappadocia and Kos. The presence of chemical traces of Cappadocia in the Miletus region was deemed normal due to trade connections with the Cappadocia region in the past. However, the surprising result was the correlation of chemical traces of pumice from Kos.

Palladino et al. (2008) conducted field and laboratory studies aiming to comprehend the telluric mechanisms underlying the eruption of the Kos Plateau Tuff (KPT). Through the utilization of microscopic and SEM studies, they particularly emphasized the presence of a tube-pumice structure within the D unit. This structure was found to contribute to vesicular elongation and was associated with an increase in shear stress.

Pe-Piper & Moulton (2008) conducted an investigation on the magmatic evolution of Kos during the Pliocene-Pleistocene age range. The observed rocks were found to result from the disintegration and mixing of three main types of magma. Their studies revealed the following: (a) Calc-alkaline high aluminum basalt fragmented into

andesite at the base of the crust; (b) Partially molten meta-basaltic amphibolite underplated at the base of the crust, which decomposed to generate high SiO_2 rhyolite; and (c) A minor component of trachytic magma resulting from partial melting of the enriched subcontinental lithospheric mantle. They emphasized that the younger volcanic rocks on Nisyros exhibit a slightly more trachytic character. Furthermore, their Sr and Nd isotope ratios showed similar values across all rock types, ranging from andesite to high-siliceous rhyolite. Texturally, these rocks exhibited features indicating magma differentiation.

Zouzias & St. Seymour (2008) conducted an investigation on the geochemistry of the Kos Plateau and Tilos D and E Pumices. They revealed that the unit's REE, Th, Pb, U, Zr, and Y values were lower compared to the E unit. Although similarities were observed between Kos-Tilos-Yali, they claimed that there were some differences attributed to Nisyros volcanism, which arose as a result of partial melting.

Bouvet de Maisonneuve et al. (2009) aimed to investigate the eruption dynamics by examining the properties of juvenile fragments of the Kos Plateau Tuff (KPT). They identified four types of pumices in the region and noted that the most common type is tube-pumice with elongated pores. The observed pumices are as follows:

(1) Large, highly porous, semi-circular vesicular pumice: These are found in fine-grained pyroclastic flow units and are characterized by numerous small (<50 μm diameter) vesicles and irregular spaces several millimeters in size.

(2) Pumice found in micro-vesicular fine-grained pyroclastic flow units: This type also exhibits many small (<50 μm diameter) vesicles and irregular spaces several millimeters in size.

(3) Gray or banded pumice: Developed from a more mafic magma, this type of pumice displays highly irregular bubble shapes, suggesting interaction between rhyolite and mafic magma.

Bachmann (2010) investigated the petrological evolution and pre-explosion conditions of the Kos Plateau Tuff (KPT). In his study, he made the following observations and conclusions:

(1) The magma of the KPT evolved from a mafic origin, primarily through partial melting.

(2) The magma chamber was located at a shallow depth of approximately 1.5-2.5 kilometers, and crystallization occurred at temperatures ranging from 670 to 750 degrees Celsius.

(3) Bachmann concluded that the eruption of the KPT occurred as a result of the reheating of rhyolitic magma through interaction with a more mafic fluid.
Furthermore, he suggested that future eruptions of caldera-forming siliceous magma could potentially occur in the region.

Bachmann et al. (2010) conducted a study with the objective of understanding the magma evolution of the Rhyolitic Kos Plateau Tuff. They achieved this by analyzing the concentrations of major, trace, and volatile elements in liquid inclusions present in the samples. Their findings led them to suggest that the absence of a clear correlation between trace elements signifies an evolution that occurred under vapor-saturated conditions in the upper crust.

Degruyter et al. (2010) conducted an investigation on the controls of the Kos Plateau Tuff eruption on magma permeability, specifically focusing on factors such as pores, bubbles, and viscosity. They utilized X-ray computerized microtomography for their analysis.

Zouzias & St. Seymour (2013) conducted a geochemical analysis of the D and E ignimbrites on Kalymnos Island to investigate the Kos Plateau Tuff (KPT). Their study focused on the main element analysis of these ignimbrites. Based on their findings, they concluded that the mineralogy, textural relationships, and mineral chemistry of the Kos Plateau and Kalymnos tuffs exhibit similarities.

Voegelin et al. (2014) conducted a study to investigate the changes in the Mo ratios during magma differentiation in the Kos Plateau Tuff (KPT). They observed that the Mo values exhibit a direct proportionality to the magmatic differentiation process, ranging from basalt to rhyolite.

Piper & Pe-Piper (2020) conducted a study focusing on the chronological and neo-tectonic correlation of the plateau and its surfaces on Kos Island. They further investigated the morphological features, formation, and development of the terraces. The researchers also mentioned the presence of potential metal deposits in the Bros Thermi field and identified two distinct hydrothermal reservoirs in the Kos field.

Zeilinga de Boer et al. (2022) delve into the intriguing question of whether the ancient mythological battle between Poseidon and Polybotes was influenced by a real geological event a late Holocene rock avalanche at Zini, Kos Island. Through a comprehensive analysis of geological and mythological evidence, the authors explore the possibility of a connection between the myth and the geological phenomenon. By examining the landscape and evaluating the cultural context, the study sheds light on the potential interplay between geological events and the development of ancient myths. This investigation provides valuable insights into the intersection of geology and mythology, highlighting the role of natural occurrences in shaping cultural narratives. By bridging the gap between scientific inquiry and folklore, this study offers a captivating exploration of the origins and interpretations of ancient legends.

2.1.2 Nisyros and Yali Island

Due to the close association and similarity of these two volcanic islands, they are often studied together under the same title. Numerous researchers have conducted hydrogeological studies in this region, including Chiodini et al. (1993), Marini et al. (1993), Lagios et al. (2007), Teschner et al. (2007), Kinvig et al. (2010), Spandler et al. (2012), Kanellopoulos & Xirokostas (2016), Bini et al. (2019), and Bini et al. (2020). Additionally, Papanikolaou & Nomikou (2001), Sachpazi et al. (2002), Parcharidis et al. (2004), Lagios et al. (2005), Stiros et al. (2005), Vougiouklas & Fytikas (2005), Zouzias & St. Seymour (2007), Tibaldi et al. (2008), and Nomikou (2011) have focused on uncovering the various aspects of tectonism and the structural controls on these volcanic islands.

Davis (1968) noted that Nisyros Island is situated at the convergence of two fault lines and primarily comprises volcanic rocks, specifically lavas, and tuffs. The initial materials have low SiO_2 content but undergo differentiation, and the lavas exhibit alkaline characteristics. The exact age of the island remains uncertain, but it is believed to have originated from successive eruptions during the middle or late Miocene, persisting until the present geological epochs. The discovery of obsidian tools within pumice layers also suggests that these eruptions may have extended into the Holocene period.

Di Paola (1974) conducted comprehensive geochemical and petrographic investigations on the island of Nisyros, revealing that Nisyros volcanism comprises five distinct phases. These units exhibit a calc-alkaline character, which is typical of orogenic environments, and their composition ranges from basic andesite to rhyolite. Furthermore, the K-Ar dating of the dacitic lava formed during the pre-caldera period yielded an age of 0.2 Ma.

Wyers & Barton (1989) documented that Nisyros experienced volcanic eruptions spanning from 2 BC to 1422 AD. They observed a wide range of compositions, from basaltic andesite to rhyolite, and noted that the lavas prior to the caldera collapse had distinct compositions compared to those after the collapse. The exact age of the caldera collapse remains unknown. Chemical analyses indicated the presence of additional processes. They also identified the occurrence of basaltic andesites (at depths of 12-14 km), rhyodacites, and dacites (at depths of ~27 km) in a relatively shallower magma chamber, under pressures of approximately 8 kb for dacites and rhyodacites, and 3-5 kb for basaltic andesites.

Limburg & Varekamp (1991) conducted a detailed analysis of the stages of Nisyros volcanism by examining the stratigraphic sequences. They observed that the volcanic activity on Nisyros followed a distinct pattern. Initially, there was an explosive phase, followed by a phreatomagmatic phase. This was succeeded by two significant Plinian eruptions approximately 25,000 years ago. Subsequently, caldera-forming eruptions occurred, accompanied by the eruption of the rhyodacitic Nikia Lava. The formation

of the rhyodacitic caldera was followed by a collapse, resulting in stratigraphic complexity and fluctuations, as highlighted by the researchers.

St. Seymour & Vlassopoulos (1992) conducted a study where they analyzed the trace elements in volcanic samples. The results of their chemical analyses showed inconsistent trace element values, suggesting the presence of magma mixture. To support this finding, they also examined the samples using macro and micro petrographic observations, which further confirmed the phenomenon of magma mixing.

Vougioukalakis (1993) proposed a new model for the evolution of volcanic activity based on various data such as chemical composition, mineralogical paragenesis, stratigraphic location, areal distribution, age, and deposition mechanism. According to their findings, the volcanic activity consisted of two distinct explosions. The first explosion was found to have occurred in three stages, while the second explosion was characterized by two different stages.

Francalanci et al. (1995) proposed that the Nisyros volcanism can be divided into three stages of cone formation. They emphasized that any petrological studies aiming to understand the magmatic evolution model should consider the wide range of Sr isotope ratios, evidence of magma mixing, and the broad compositional spectrum of rocks present in the area.

Volentik et al. (2002) conducted stratigraphic studies on the caldera wall and identified that the initial caldera formation was a consequence of the explosive eruption of Lakki. Subsequently, the Melisseri explosive eruption generated a substantial layer of pyroclastic flow. They also suggested the possibility of a second caldera collapse following this eruption, indicating the presence of a distinct trend.

Buettner et al. (2005) conducted a study on the Hf, Nd, Pb, and Sr isotope geochemistry of the Nisyros and Yali volcanoes. They analyzed the trace element results and observed distinct variations between the different volcanic units. Notably,

a compositional gap was identified between the pre-caldera and post-caldera volcanic units, specifically within the SiO_2 range of 61-68%. Furthermore, they found that the eruption of Nikia Lava, the initial lava flow following the caldera collapse, was influenced by the presence of water.

Caliro et al. (2005) conducted a study to provide a comprehensive summary of the structural, geochemical, and seismological investigations conducted on the Nisyros volcano from 1999 to 2001. The structural analysis revealed that the caldera in the Lakki plain was influenced by NE-SW trending veins, as well as secondary N-S faults and fractures. Additionally, the presence of buried faults on the island of Nisyros unveiled various structural and hydrothermal characteristics of the island.

Vanderkluysen et al. (2005) conducted a study with the objective of unraveling the physical and structural evolution of the Nisyros volcano. Their research provided evidence that the caldera collapse and associated faulting undergo periodic recurrence. Furthermore, they elucidated the evolution of Nisyros volcanism through the use of detailed maps and 3D diagrams.

Volentik (2005) conducted a comprehensive study to reconstruct the stratigraphy of the Nisyros volcanic rocks. Their research successfully revealed the volcanological evolution of the area, shedding light on the complex geological processes that have shaped the Nisyros volcano.

Margari et al. (2007) conducted tephra-stratigraphy studies in the Mediterranean region, and their findings indicated that the volcanic products originating from Nisyros and Yali volcanoes extend as far as the island of Lesbos. This suggests a widespread distribution and transportation of volcanic materials in the region.

Zellmer & Turner (2007) conducted extensive geochemical and petrographic investigations, and their findings, along with the analyses performed, provided compelling evidence through thin section and trace element diagrams. These diagrams

clearly demonstrated that the volcanic rocks exhibit trace element values and petrographic properties commonly observed in typical back-arc dacitic lavas.

Aksu et al. (2008) conducted a study with the objective of stratigraphic correlation of tephra units from the Aegean in the Sea of Marmara. They proposed that the Nisyros tephra was continuously deposited beneath the Y5 tephra layer. This stratigraphy had been previously observed in the cores of Lesbos, but it was reported for the first time in Aegean Sea sediments in their study. By employing linear extrapolations using oxygen isotope stratigraphy, they estimated the age of the Nisyros eruption to be approximately 42-44 ka years.

Longchamp et al. (2011) conducted a study to estimate the possible eruption column height, volume, and eruption duration of the Nisyros volcano. They calculated a height of 15 km for the eruption column and an eruption rate of 2x107 kg/s. The estimated erupted volumes were in the range of 2 to 27×108 m^3 for the lower pumice and 1 to 5×108 m^3 for the upper pumice. The researchers also emphasized that an eruption involving both upper and lower pumice could result in significant damage to infrastructure, vegetation, and tourism on Nisyros and neighboring islands.

Sterba et al. (2011) conducted a study to investigate the presence of volcanic materials from the Kyra unit on the island of Tilos. They performed chemical analyses on samples collected during field studies and concluded that there is no evidence of the Nisyros and Minoan eruptions in the analyzed materials. In contrast to previous studies, the researchers defined eight distinct chemical and stratigraphic series based on their findings.

Braschi et al. (2014) conducted a study to assess the dynamics of Sr isotope compositions and various complex open system processes in the volcanic system of Nisyros. They combined textural and compositional data on plagioclase and paste with chemical and petrographic examinations. The findings indicated that open system processes took place during the most recent volcanic activity in Nisyros.

Dietrich & Lagios (2017) published a book that provides a comprehensive analysis of the stratigraphic, structural, geochemical, mineralogical, and petrographic characteristics of the Nisyros volcanism, along with the accompanying Kos-Nisyros-Yali volcanism. The book incorporates extensive literature data as well as findings from field and laboratory studies, presenting a detailed exploration of these volcanic systems.

Popa et al. (2019) conducted a study to investigate the connection between magma chamber processes and eruption styles in the Nisyros-Yali volcanic system. They found that the volcanoes in this system exhibit typical arc magmatism eruption characteristics, which are associated with similar eruption styles and magma processes. The study also suggested that magmatic differentiation and reactivation of magmas can influence the types of eruptions, indicating a temporal cycle. Furthermore, the researchers emphasized the importance of volatile gases in these types of explosive eruptions. They noted that the presence of volatile gases is crucial in predicting future explosions and understanding their temporal patterns. The study proposed that by analyzing these data, a general model can be developed, which can be used in risk calculations for future volcanic eruptions.

Vougioukalakis et al. (2019) conducted a comprehensive literature review focusing on the tectonic and tephra stratigraphic correlations of the Aegean arc and associated volcanic activities spanning a duration of 4.7 million years. The researchers compiled and analyzed the available information from various sources to interpret the tectonic and volcanic evolution of the region.

Popa et al. (2020) reported that the Nisyros-Yali volcanic center exhibits a cyclic pattern of violent eruptions due to its high water and silica content. The researchers identified a series of eight rhyolitic eruptions, including two caldera-forming events, within this volcanic system, indicating a temporal cycle. Through age determinations, they estimated the eruption ages, revealing a range of values. For Nisyros, the eruption ages varied from 118.7 ± 10 thousand to 19.9 ± 1.5 thousand years, while for Yali, the range was between 40 ± 5.2 thousand and 22.7 ± 1.6 thousand years. The eruption in

Yali occurred following the two caldera formation events in Nisyros, which took place approximately 63.1 ± 4.7 thousand and 58.4 ± 2.7 thousand years ago. The intensity and duration of these eruptions were found to be directly related to the length of the intervening rest periods. Based on the current duration of rest periods between eruptions, the researchers suggest that a potential future eruption could be highly intense.

Bouvet de Maisonneuve et al. (2021), in line with previous research, observed that rhyolitic eruptions exhibit cyclic behavior. They identified several indications of increased magma differentiation in recently erupted material, including lower pre-eruption temperatures and higher water content. While certain sections of the magma reservoir (Yali rhyolites) displayed characteristics such as low temperature, high water content, oxidation, and differentiation comparable to pre-Kos Tuff rhyolites, other sections remained less evolved. The researchers also emphasized that, consistent with Bachmann's (2019) suggestions, a large, fully coalesced reservoir has yet to form, and homogenization has not been observed. Furthermore, they predicted rare but potentially significant rhyolitic eruptions in the near geological future, involving the newest products from Nisyros and Yali. They also suggested that ongoing unrest, such as faulting, would likely persist due to increased hydrothermal activity.

Popa et al. (2021) conducted research on volcanoes characterized by explosive eruptions in the magma chamber. They focused on the crystallinity, viscosity, dissolved water content, and water saturation of the melt, which are properties that can undergo significant changes during periods of magma stagnation. These properties can have a profound impact on magma behavior during eruptions and, consequently, on the evolution of chlorine (Cl) in fluid inclusions within the Nisyros-Yali volcanic system. The researchers specifically investigated the separation of chlorine from fluorine (F) in apatite, which is present in various mineral phases. Their main finding indicated a direct relationship between the transitions from CL-F rhyolitic eruptions and the pre-eruption physical state of volatile elements in the magma reservoir.

Furthermore, its geological significance, Nisyros Island has substantial potential as a geosite, a subject that has been highlighted by numerous researchers (Dietrich & Lagios, 2017; Antoniou et al. 2019; Antoniou et al. 2021).

2.2 Bodrum-Datça Peninsulas

The first geological studies conducted in the Bodrum and Datça Peninsulas were carried out by Strickland & Hamilton (1840), Rayet (1879), Phillipson (1915), and Oppenheim (1918). In 1969, Keller investigated the cause of acidic magmas, whether they result from the differentiation of basaltic main magma or anatectic crustal melting. In contrast to the majority of researchers, Keller proposed that acidic magmas are associated with anatectic crustal melting. The study revealed that at a temperature of 680, a pressure of 2kb is present at a depth of 6-8 km.

2.2.1 Bodrum Peninsula

Studies have been conducted in various areas on the peninsula, and in this context, the research will focus on the Kos-Nisyros-Yali volcanism, with more detailed discussions of relevant studies. These include Burri et al. (1967), and Robert & Cantagrel (1977) who conducted petrological studies on the Bodrum volcanics. Additionally, H. Özçiçek & B. Özçiçek (1977) and Pişkin (1980) carried out comprehensive field and laboratory investigations on the mineralization associated with the volcanism in the peninsula.

Ercan et al. (1982) conducted a study with the aim of revealing the geology of the Bodrum peninsula. In this study, it was observed that materials from Kos fall from the air and form agglomerations in the peninsula. Pumice and tuff beds were found on the slopes of Tülüce hill on the N18-c4 sheet, and occasional pumice stones were observed in the alluvial deposits along the coast, near Yarbasan hill and the Turgut Reis sub-district center on the same sheet. It was emphasized that this event likely occurred relatively recently, approximately 100,000 years ago.

Ercan et al. (1984) conducted a study in which petrographic and chemical analyses were performed on all Bodrum volcanics. The Quaternary units were determined to be equivalent to the Kos Monzonite Plutons mentioned in the literature. The analysis results, along with the chemical and petrographic properties, provided further evidence of the presence of Kos materials in the region.

Doutsos & Kokkalas (2001) investigated the tectonics of the South Aegean Region and identified the structural elements of Kos Island and the Bodrum peninsula. Based on the measurements conducted in the area, they highlighted the regional expansion regime of the Upper Miocene age, which occurred in the NWN-SSE direction.

Ulusoy (2002) conducted a comprehensive study on the structural geology of the Bodrum caldera as part of his master's thesis. The research involved detailed geological mapping of the region, with a specific focus on the distribution of the Kos plateau tuffs. The Kos Plateau Tuffs exhibited a fresher appearance compared to other ignimbrite flows found in the Bodrum Peninsula. One distinctive feature of the tuffs is the presence of fibrous pumice, which can reach sizes of 60-70 cm in certain areas. This fibrous pumice serves as a prominent characteristic for identifying the flow. The pumices are observed to contain quartz crystals, typically measuring 5-6 mm in size, occasionally reaching 2.5 cm. Additionally, biotite flakes, measuring 1-2 mm in size, are sporadically dispersed within the glass. The author highlighted that the fibrous structure of the rock imparts a mother-of-pearl shine to clean, fractured surfaces.

Çubukçu et al. (2021) conducted a study that focused on the location of the magmatic arc, including the Kos volcanism, which coincided with Bodrum, an area known for its active volcanism on the peninsula. They proposed the idea that the Bodrum volcanism developed within the influence of the magmatic arc environment. Through geochemical analysis and interpretation, they obtained data that were consistent with previous studies and supported the idea of a mantle source. They highlighted the findings of Altherr & Siebel (2002), who suggested that lambprophic melts contaminated with crustal material through processes such as assimilation, fractional crystallization, or magma mixing do not solely originate from crustal

sources. Regarding the production of monzonitic magmas, the authors emphasized the hypothesis of a hybrid nature, indicating that the potential crustal component involved in the formation of these magmas is still a subject of controversy.

Yücel-Öztürk et al., (2023) present an in-depth examination of the Kadıkalesi monzonite in the Bodrum Peninsula, western Anatolia. Through geochronological and geochemical analyses, the study aims to elucidate the relationship between the Kadıkalesi monzonite and the South Aegean Volcanic Arc. The research findings provide valuable insights into the age and compositional characteristics of the monzonite, shedding light on its origin and geodynamic implications within the broader tectonic framework of the region. The study contributes to a better understanding of the geological history and magmatic processes associated with the South Aegean Volcanic Arc, facilitating further investigations in this geologically significant area.

2.2.2 Datca Peninsula

Ercan (1984) conducted a comprehensive investigation of the volcanic units in the Datça peninsula, focusing on their geochemical and petrographic aspects. According to his findings, the materials associated with Nisyros volcanism were primarily airborne and tended to accumulate in pit basins. Through petrographic analysis, Ercan demonstrated, using diagrams, that the Nisyros volcanism exhibits an alkaline character. Furthermore, he discussed the materials present in the Bodrum peninsula, suggesting that they were transported to the area through marine processes following the Santorini Explosion.

Ersoy (1991) reported in his study that the materials found in Datça are present as volcanic sediments, which have been preserved in sheltered pits throughout the peninsula until the present day. He further mentioned that these sediments have endured external influences such as atmospheric conditions and flooding, largely due to the protective covering of alluvial or fanglomeratic deposits, reaching a maximum thickness of 40 meters in locations such as Cumalı, Nisyros, and Yali. Ersoy also stated

that these sediments were transported from their respective volcanic islands through violent eruptions, sometimes by air and occasionally by water.

Dirik et al. (2003) conducted a study on neotectonism and geomorphology in the Datça region. They noted that a significant portion of the Datça peninsula was initially covered by materials from the Nisyros and Kos volcanoes. However, over time, these materials were likely eroded by river activity, leading to their disappearance. Only the materials that accumulated in pit basins and were subsequently covered by alluvium remained preserved until today. The researchers also mentioned the presence of these materials on fossil soils along the Tavas stream bed between Çeşmeköy and Belenköy. These materials can be observed under the hanging terraces and fanglomerates surrounding Cumalı, Çeşmeköy, and Belenköy, as well as in the valleys to the west of Hızırşah.

Çiftçi (2010) conducted a study on the geology of the Datça region as part of his master's thesis. The study revealed the presence of materials related to the Kos-Nisyros volcanism in the vicinity of Körmen Pier, including pumice and lava fragments. Additionally, tuff formations were observed as layers or thin bands within the middle and upper levels of the Yıldırımlı formation.

Gençalioğlu-Kuşçu (2015) conducted a comprehensive study in the Datça peninsula region to identify the materials associated with the Kos-Nisyros volcanism. The study focused on examining the physical properties, conducting petrographic studies, and performing chemical analyses. The goal was to determine the distribution area of these materials and establish a possible correlation with the Nisyros Kyra subunit successions, which could serve as a potential source. The results of the analyses, as shown in spider diagrams, indicated negative anomalies in elements such as Nb-Ta and Ti, consistent with typical calc-alkaline magma series. The study also revealed negative Eu anomalies in the REE diagrams, suggesting enrichment and plagioclase crystallization in light REEs compared to heavy REEs. Based on field observations, petrographic analysis, and geochemical studies, it was determined that the Nisyros volcanic material is closely related to pre-caldera andesitic tephra units, particularly

the Kyra and Lakki A units. The Datça sequences were found to share similarities with Kyra sub-units NF4, NF5, and NF6. Tephra units were identified in seven regions, including Murdala, Knidos, Yazıköy, Belen, Çeşmeköy, Sındı, and Hızırşah. The study emphasized the need for further research, as correlating Nisyros distally and assessing the associated risks is challenging due to the lack of stratigraphy and geochronology data. Additionally, the large number of unpublished studies on this subject further underscores the importance of additional investigations.

Gençalioğlu & Uslular (2018) provided valuable insights into the distal tephra of Datça. They observed that the tephra consists mainly of secondary ash-lapilli declining, occasionally reworked pumice lapilli fall deposits, which unconformably overlie the Kos ignimbrite. The thickness of the debris deposits was found to reach up to 3.5 meters. In terms of correlation, the researchers associated the distal tephra of Datça with certain proximal units such as LPF, LSB, ZKF, and UPS, as well as distal units including NF2, NF3, NF4a, and NF5 from the Kyra region. However, they acknowledged that the caldera exhibits eruptive characteristics that could potentially give rise to the Lakkí or Melisserí tephra. Nevertheless, due to insufficient geochemical data, the researchers were unable to establish a solid correlation and provide evidence of the deposition of highly overlooked andesitic tephra units in Datça. The study serves as an important contribution to the understanding of the geological characteristics of the region, shedding light on the composition and distribution of the distal tephra deposits in Datça. Further research and additional geochemical data are needed to enhance our knowledge and establish more definitive correlations.

Gençalioğlu-Kuşçu et al. (2020) conducted a comprehensive study, acquiring new geochronological data for the Distal Kyra tephra. Their findings provide compelling evidence that supports its correlation with Nisyros tephra stratigraphy. This newly obtained chronology not only contributes to our understanding of the pre-caldera volcanism of Nisyros but also offers valuable insights into the initiation of the caldera-forming eruption. Moreover, the study emphasizes the significance of incorporating these latest findings into existing risk assessment studies for the Nisyros volcano. By

attributing all new ages distal to the Kyra tephra to the Nisyros tephra stratigraphy, a more comprehensive and up-to-date assessment of volcanic hazards can be achieved. The researchers also note that the tuff cone responsible for the Kyra sequence exhibits evidence of a long-lasting eruption, with an estimated age of approximately 20,000 years. This temporal constraint adds further context to the volcanic activity in the region.

CHAPTER THREE
METHODOLOGY

3.1 Field Observations and Terminologies

Multiple samples were collected from five different locations within the ignimbrite when multiple components were identified, such as pumice and glass shards. Approximately 40 kg of material was collected for bulk rock and facies analysis. Subsequently, sub-samples were extracted to create 30 μm polished sections for spot analyses of glass and phenocrysts. The methods **(**Figure 3.1**)** presented in this thesis are categorized into two main groups which are fieldwork studies and laboratory analysis.

3.2 Fieldwork Studies

The ignimbrite deposits were identified at five locations during the field studies conducted between 2021 and 2022 in Bodrum. These new outcrops were added to the ones identified during previous field campaigns to enhance our understanding of the characteristics of KPT distal deposits. Following the lithofacies descriptions by Branney & Kokelaar (2002) based on the behavior of particulate currents, mechanisms of clast support and segregation, interpreting ignimbrite lithofacies and architectures (Table 3.1).

3.2.1 Sampling Procedure

In most outcrops, multiple deposits from the same eruptions were observed at the same location. These deposits typically consist of block to ash-sized pumices, lithic fragments, and isolated crystals. Dark or light brown paleosols commonly separate deposits however it couldn't find the contacts in some locations. Eruptive sequences comprise several stages of the same eruption, and it studied at various outcrops since the entire sequence may not be visible at a single location. Bulk deposits were also sampled for grain size and geochemical analyses.

Figure 3.1 Figure showing the following methodology

Table 3.1 Lithofacies descriptions for pyroclastic deposits taken from Branney & Kokelaar (2002)

Symbol	Lithofacies
mLT	massive lapilli-tuff (or lapilli-ash)
mLT	massive lapilli-tuff/ash with normal-graded lithics and inverse-graded pumices
mLTf	massive lapilli-tuff with directional grain fabric
sLT	stratified lapilli-tuff/lapilli-ash
dsLT	diffuse-stratified lapilli-tuff/lapilli-ash
bLT	thin-bedded lapilli-tuff/ash (beds centimetres-thick)
sT	stratified tuff/ash
//sT	parallel-stratified tuff/ash
xsT	cross-stratified tuff/ash
//bpL	parallel-bedded pumice lapilli
lenspL	lens of pumice lapilli
lenspC	lens of pumice cobbles
lenslBr	lens of lithic-rich breccia
fpoorT	fines-poor tuff/ash
mLTpip	massive lapilli-tuff/ash, with fines-poor pipes
mlBr	massive lithic breccia
mscAg	massive scoria agglomerate
Recommended abbreviations	
T	tuff/ash
LT	lapilli-tuff/lapilli-ash
L	lapilli
Br	breccia
Ag	agglomerate
Co	cobbles (i.e. rounded blocks)
M	massive
(n)	normal-graded
(ni)	normal-graded lithics
(i)	inverse-graded
(ip)	inverse-graded pumices
(n)-(i)	normal-to-inverse graded
s	stratified (e.g. tractional)
xs	cross-stratified (e.g. tractional)
//s	parallel-stratified (laminated)
//b	parallel-bedded (thin beds)
p	pumice-rich
1	lithic-rich
sc	scoria-rich
0	obsidian-rich
cr	crystal-rich
fpoor	fines-poor
frich	fines-rich
f	directional grain fabric
l	isotropic; no directional grain fabric - may have a compaction fabric.
ace	accretionary lapilli-bearing
ves	vesicular
lens	lens(es)
e	eutaxitic
vap	vapour-phase altered (e.g. sillar)
lava-like	lava-like
v	vitrophyre (welded and glassy)
rheo	rheomorphic (e.g. with elongation lineations and folds)

3.2.2 Measured Stratigraphic Section

At each location, outcrops were initially cleared to capture photographs. Subsequently, a detailed description of each unit was conducted, focusing on the framework, fabric, grain type, and size characteristics. The thickness of each layer within the sequence was measured, as well as the major axes of the five largest lithic fragments found in the deposits. These measurements served as the comparing stratigraphical features within the given previous studies.

3.3 Laboratory Studies

3.3.1 Grain Size Distribution

Particle size analysis is integral to understanding particle behavior during transport and deposition. Comparing the KPT unit's previously mapped results with the studies conducted by Allen & Cas in 1998a, 1998b, and 2001, as well as those by Allen et al. in 1999, and Allen & McPhie in 2001 contributes essential insights into transport and source characteristics. Methods for describing volcanic lithofacies are akin to those used in clastic sedimentology, based on Nemeth & Martin's 2007 work. Also, it was used some classification tables for descriptions such as grain size and sorting classification (Table 3.2 and Table 3.3). The grain size characteristics of the deposit unit are crucial for distinguishing lithofacies, as they directly relate to the physical properties of transporting and depositing currents (Nemeth & Martin, 2007). In this study, eleven samples from five selected locations were dried for 24 hours in an oven before sieving. Crystals, pumices, acceleration lapillus, and lithic fragments were manually separated from the samples. A binocular microscope was employed for the smallest particles. Grain size assessment was conducted in two ways: for particles larger than 1 cm, measurements were taken using a caliper, while the method described by Walker (1971) was followed for other samples. Analyses involved a set of sieves with mesh sizes spaced at one-phi intervals, ranging from -4 to 4 phi (-16 to 0.0625 mm). The material retained in each sieve was weighed to 0.01 g on a laboratory balance, and weight percentages were calculated.

Table 3.2 Grain Size Classification taken from White & Houghton (2006)

Grain Size		Primary Volcaniclastic Deposit		Sedimentary Deposit	
(Phi)	(Mm)	Unconsolidated	Lithified	Unconsolidated	Lithified
>4	<1/16	Extremely fine ash	Extremely fine tuff	Clay	Mudrock, shale
3-4	1/16-1/8	Very fine ash	Very fine tuff	Very fine sand	Very fine sandstone
2-3	1/8-1/4	Fine ash	Fine tuff	Fine sand	Fine sandstone
1-2	1/4-1/2	Medium ash	Medium tuff	Medium sand	Medium sandstone
0-1	1/2-1	Coarse ash	Coarse tuff	Coarse sand	Course sandstone
-1 to 0	1-2	Very coarse ash	Very coarse tuff	Coarse sand	Coarse sandstone
-2 to -1	2-4	Fine lapilli	Fine-lapilli tuff	Granule	Grit, granule congl.
-4 to -2	4-16	Medium lapilli	Medium-lapilli tuff	Pebble	Pebble conglomerate
-6 to -4	16-64	Coarse lapilli	Coarse lapilli-tuff	Cobble	Cobble conglomerate
< -6	>64	Block/bomb	Breccia	Boulder	Boulder congl.

Table 3. 3 Differences in descriptive summaries of sorting taken from Cas & Wright (1998)

Sorting(σ)	Sedimentary Deposits	Pyroclastic Deposits
0-1	Very well sorted to moderately sorted	Very well sorted
1-2	Poorly sorted	Well sorted
2-4	Very poorly sorted	Poorly sorted
>4	Extremely poorly sorted	Very poorly sorted

The weight percentages of sieved data were inserted into the Gradistat program (Blott & Pye, 2001). Gradistat gives an overall grain size distribution and the relevant descriptive statistics used in this study in both geometric and logarithmic scales. The grain size statistics are based on those proposed by Inman (1952) and only the logarithmic statistics were used in this study i.e.:

The median grain size (Mdϕ) is defined from Inman (1952):

$$Md\phi = \phi 50 \tag{3.1}$$

The mean grain size (Mϕ) is defined as Equation 3.2 from Inman (1952):

$$M\Phi = \tfrac{1}{2} \times (\Phi 16 + \Phi 84) \tag{3.2}$$

Sorting ($\sigma\phi$) is the dispersion of grain sizes; defined as Equation 3.3 from Inman (1952):

$$\sigma\phi = \tfrac{1}{2} \times (\Phi\ 84 + \Phi 16) \tag{3.3}$$

Skewness ($\alpha\phi$) is the asymmetry of the distribution, defined as Equation 3.4 from Inman (1952):

$$\alpha\phi = \frac{M\phi - Md\phi}{\sigma\phi} \tag{3.4}$$

Kurtosis, or 'peakedness' ($\beta\phi$), is defined as Equation 3.5, from Inman (1952):

$$\beta\phi = \frac{\frac{1}{2} \times (\phi 95 - \phi 5) - \sigma\phi}{\sigma\phi} \tag{3.5}$$

Where ϕx is defined as the phi value (ϕ) at the x'th percentile of the cumulative mass distribution. These distributions are shown in (Figure 7.2).

3.3.2 Componentry Analysis

Componentry was semi-quantitatively measured by estimating the proportions of each component under a stereomicroscope. This analysis was conducted in different classes to enable precise semiquantitative measurements. To ensure consistency in estimating the abundance of different clast types, sample componentry for the entire dataset was performed in a single session. Each sample underwent analysis twice for cross-comparison. Clast types included pumice clasts, glass shards, lithic fragments (previous stage pyroclastic material, andesite), quartz, feldspar, biotite, amphibole, and pyroxene.

3.3.3 Petrographic and Geochemical Analysis

3.3.3.1 Petrographic Analysis

3.3.3.1.1 Thin Section Preparation

Thin sections were prepared from the 30 μm-thick slices of pyroclastic and volcanic clasts under a petrographic microscope to gain insights into the transportation, fragmentation, expansion, and cooling processes. In total, 65 thin sections prepared from five locations were also prepared using the following method for analysis under the petrographic microscope. To prepare the samples, some pumice clasts with high vesicularity were first impregnated in low-viscosity epoxy for 4 hours and left to cure for another 24 hours. After impregnation, all samples were mounted, and thin sections were prepared using Araldite epoxy on the slide. Finally, a coverslip was placed over the samples to complete the preparation process.

3.3.3.1.2 Image Processing and Textural Data Analysis

Thin sections that present mineralogical and textural properties of samples were taken micro photos under a polarizing microscope at the Geological Engineering Department of Dokuz Eylül University. For detailed analysis, it is used different programs which are ImageJ, Adobe Photoshop, and CorelDraw. In this part, ImageJ is

used for values of pumice vesicularity; Adobe and CorelDraw are used for image processing for all thin sections.

3.3.3.2 Geochemical Analysis

3.3.3.2.1 Major Oxides and Trace Elements Analysis

For comprehensive geochemical characterization, major oxide and trace element analyses were conducted on representative samples using the ICP-MS (Inductively Coupled Plasma-Mass Spectrometry) method at İstanbul Cerahpaşa University.

3.3.3.2.2 ICP-MS Analysis

Samples were first separated and then these samples were glued to the mounts and 3 separate mounts were created. These mounts were embedded with epoxy and then waited for drying. After drying the disks were polished with Metkon Forcipol Polisher at Dokuz Eylül University (İzmir, Turkey). After preparing the mounts, these disks were analyzed using ICP-MS at Istanbul Cerahpaşa University (İstanbul, Turkey). ICP-MS is a highly sensitive and versatile analytical technique that offers rapid and simultaneous quantification of various elements within a single sample. During the analysis, it followed the standard followed by Göçmengil et al. (2022);

Perkin Elmer NexION 2000 ICP-MS combined with the ESI NWR213 laser system has been used to measure the whole rock chemistry of the desired samples. It uses BCR-2, AGV-2, BCR-2G, and AGV-2G USGS glass standards and NIST 614 standard to show how accurate the geochemistry analysis done by LA-ICP-MS measurements. Besides, during analysis, a reagent blank glass that only contained 1 gram of ultra-pure $Li_2B_4O_7$, $LiBO_2$, and LiBr was added to the analysis section to allow correction during data interpretation. The surface of the different samples was cleaned with methanol, 2 wt % HNO_3 trace metal grade nitric acid, and 18 MΩ ultrapure water before the analysis. It was used NIST glasses 610 and 612 for initial instrument calibration and within-session measurements. Helium was used as a carrier gas for

ablated aerosol. LA-ICP-MS measurements were carried out using time-resolved analysis operating in a peak jumping mode. The laser repetition rate and the laser energy density are fixed at 10 Hz and ~7 J/cm^2, respectively. Data were collected by runs that consisted of three standard measurements at the beginning (each on 610 and 612), nine spot measurements three standard measurements at the closing of the measurements with the session. For detailed information about the analysis please check for the internal standard values to Göçmengil et al. (2022).

3.4 Data Interpretation

The data obtained from the ICP-MS analysis were meticulously processed and interpreted to yield concentrations of major oxides (e.g., SiO_2, Al_2O_3, Fe_2O_3, MgO, CaO) and trace elements (e.g., rare earth elements, REE) within the ignimbrite samples. These results contribute significantly to the understanding of the ignimbrite's source and transportation mechanism.

CHAPTER FOUR
STRATIGRAPHY

4.1 Background

The KPT eruption sequence displays distinctive variations in textural and lithofacies characteristics, which provide a framework for inferences regarding the eruption style and overall eruption sequence. These KPT eruption sequences are grouped into 6 main categories from bottom to top Allen et al. (1999): mappable stratigraphic units and subunits including fallout (unit A, subunit Ff), stratified pyroclastic-density-current deposits (units B, C, and subunit Fs), and non-welded ignimbrites (units D and E). The KPT contains four regionally mappable ignimbrite subunits (Dl, Dm, E, Eu), each of which comprises two facies: lithic breccia facies and pumiceous ignimbrite facies. These D and E units have variable descriptions due to the complexity of the pyroclastic deposits northern part of the crater. Unit E consists of lower (El) and upper (Eu) ignimbrites. Ignimbrite El represents the eruption climax when the main phase of caldera collapse was most likely initiated (Allen 2001). It is the coarsest, most voluminous, and widespread ignimbrite Allen & Cas (1998). Allen & Cas explained in their 1998 study the deposition type of the D and E units as the lateral and vertical facies relationships displayed by the coarse lithic breccias of units are inconsistent with en masse deposition from deflated pyroclastic flows, however, they are compatible with deposition by means of progressive aggradation from vertically stratified and laterally variable ***pyroclastic density currents***. According to Allen's 2001 studies described as written below to typical KPT stratigraphic section. Unit A is characterized by its fine-grained nature, varying sorting quality (from well to poorly sorted), and a low proportion of lithic clasts. Its composition suggests deposition resulting from phreatoplinian fallout, particularly downwind to the southeast. Unit B is typically poorly sorted and relatively fine-grained compared to other KPT units. It contains a limited number of lithic clasts and even includes fragments of uncharred wood. The presence of steam-rich currents is indicated by thickly fine ash-coated pyroclasts. Unit C positioned between Units B and D, exhibits intermediate textural and lithological features. Its grain size is akin to that of Unit B,

but it presents thin ash coatings and thermal oxidation, suggesting relatively high emplacement temperatures. Unit D consists of three ignimbrites, each with basal lithic breccia and internally massive, pumiceous ignimbrite facies. It is thicker, more extensive, coarser-grained, and lithic-rich compared to Unit C. The pyroclasts within Unit D range from ash to blocks, with an increase in average grain size in successive ignimbrites. Unit E comprises a lower subunit (El) and an upper subunit (Eu), both characterized by basal lithic breccia and pumiceous ignimbrite facies. The lower part of El may contains extremely coarse material. Unit Ff found in central and western Kos; Unit Ff is generally thin away from the source. It primarily consists of fine ash-coated pumice lapilli, occasionally containing lithic lapilli. On Tilos, it can be distinguished by a sharp or gradational lower boundary with Unit E (Figure, 4.1).

Table 4.1 Basic information of Units and subunits

Units	subunit		Type of Unit
F	Ff	upper, finer-grained, stratified, and massive subunit	Fallout
	Fs	a lower, coarser-grained, low-angle cross stratified	Pyroclastic Density Current
E	Eu	an upper finer-grained ignimbrite subunit	Pyroclastic Density Current
	El	a lower coarser-grained ignimbrite subunit	
	Ebx	the coarsest-grained and thickest co-ignimbrite basal lithic breccia	
D	Dm	a coarser-grained, thicker, and more voluminous subunit	Pyroclastic Density Current
	Di	fines-poor lithic breccia and ignimbrite facies	
	Dl	a finer-grained, thinner, and less voluminous subunit	
C			Stratified Pyroclastic Density Current
B			Stratified Pyroclastic Density Current
A			Fallout

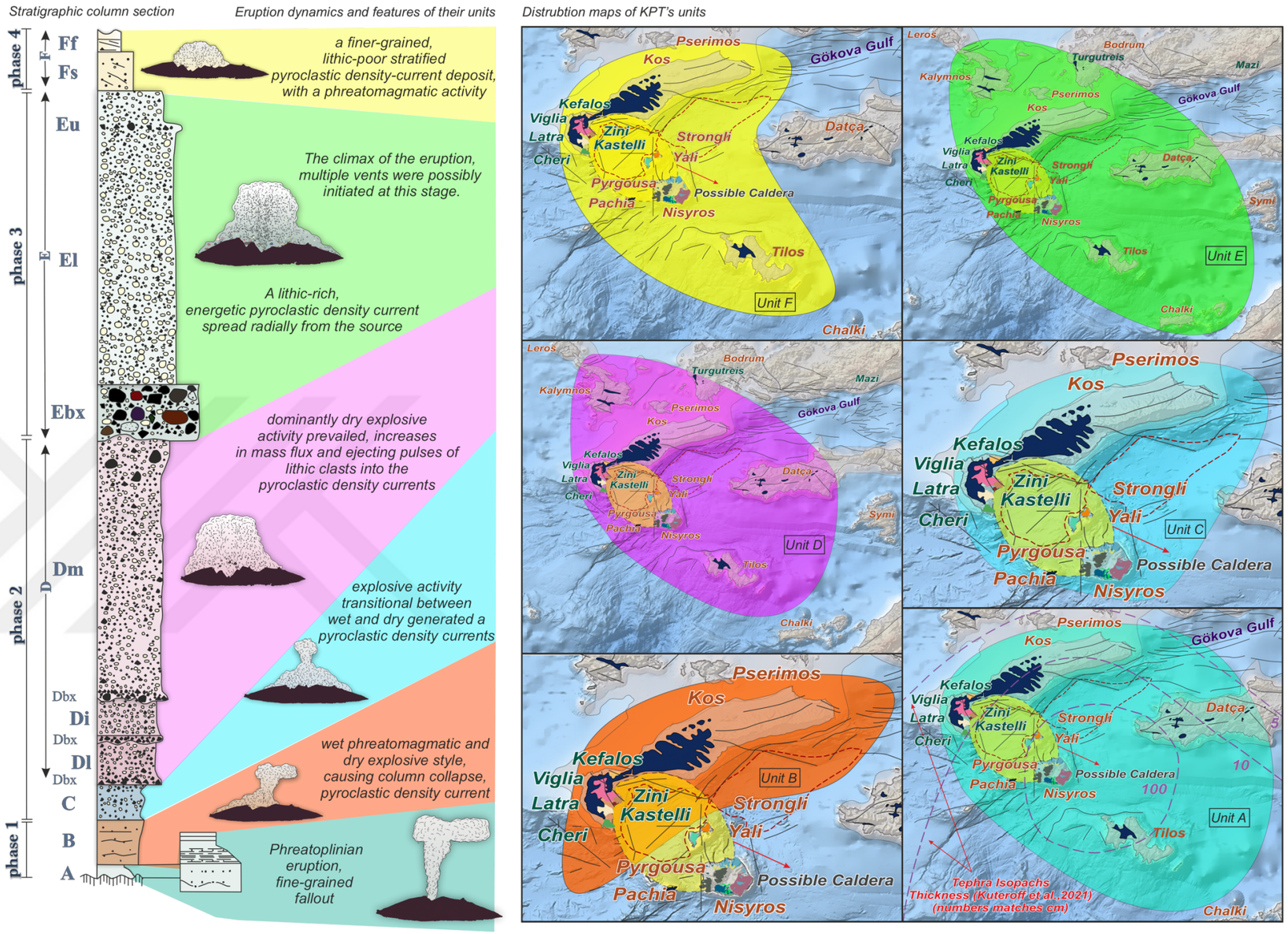

Figure 4.1 This consolidated figure serves as a comprehensive visual reference, offering insights into all unit's distribution, volcanic dynamics, stratigraphical context, and key features within the combined over the map which is given in Figure 1.2. The stratigraphical column section is taken from Allen & Cas, 1998's study.

4.2 Fieldwork Studies and Sedimentological Analysis on Bodrum Peninsula

The distribution of succession which can be traced from the Turgutreis coast to the east was described by Allen & Cas (1998) and its base is 75 m above sea level on paleo-soil. Based on the limited definitions in previous studies (Allen & Cas, 1998; Ercan, 1982; Ulusoy et al., 2004), this sequence is mapped to the Kos Plateau Tuff (KPT) of the Quaternary Kos - Nisyros - Yali volcanic activity. Systematic samplings were carried out from 5 different locations to compare this sequence with the KPT in many ways. To examine vertical and lateral facies variation within the KPT, macroscopic field observations on vertical variations in grain size, based on a visual estimate of maximum grain size, using size ranges outlined in Tables in Chapter 3, and componentry was documented for locations aligning roughly parallel and perpendicular to the deposit axis (Figure, 4.2). The deposit characteristics for locations parallel to the deposit axis are as follows. The sieved samples from 5 locations were carefully inspected to define distinct componentry classes under a binocular microscope. In this case, the characteristics of the defined componentry classes and the rationale behind their definitions are described and illustrated. After these parts, components percent will be present to combine with Allen's 2001 data.

Table 4.2 Information of location and sample names

Location number	Sample Name
Location 1	**88-1, 88-2, 88-3**
Location 2	**90-1,90-2, 90-3**
Location 3	**91-1, TG-1**
Location 4	**92-1, 92-2, IS-1**
Location 5	**KD-1, KD-3**

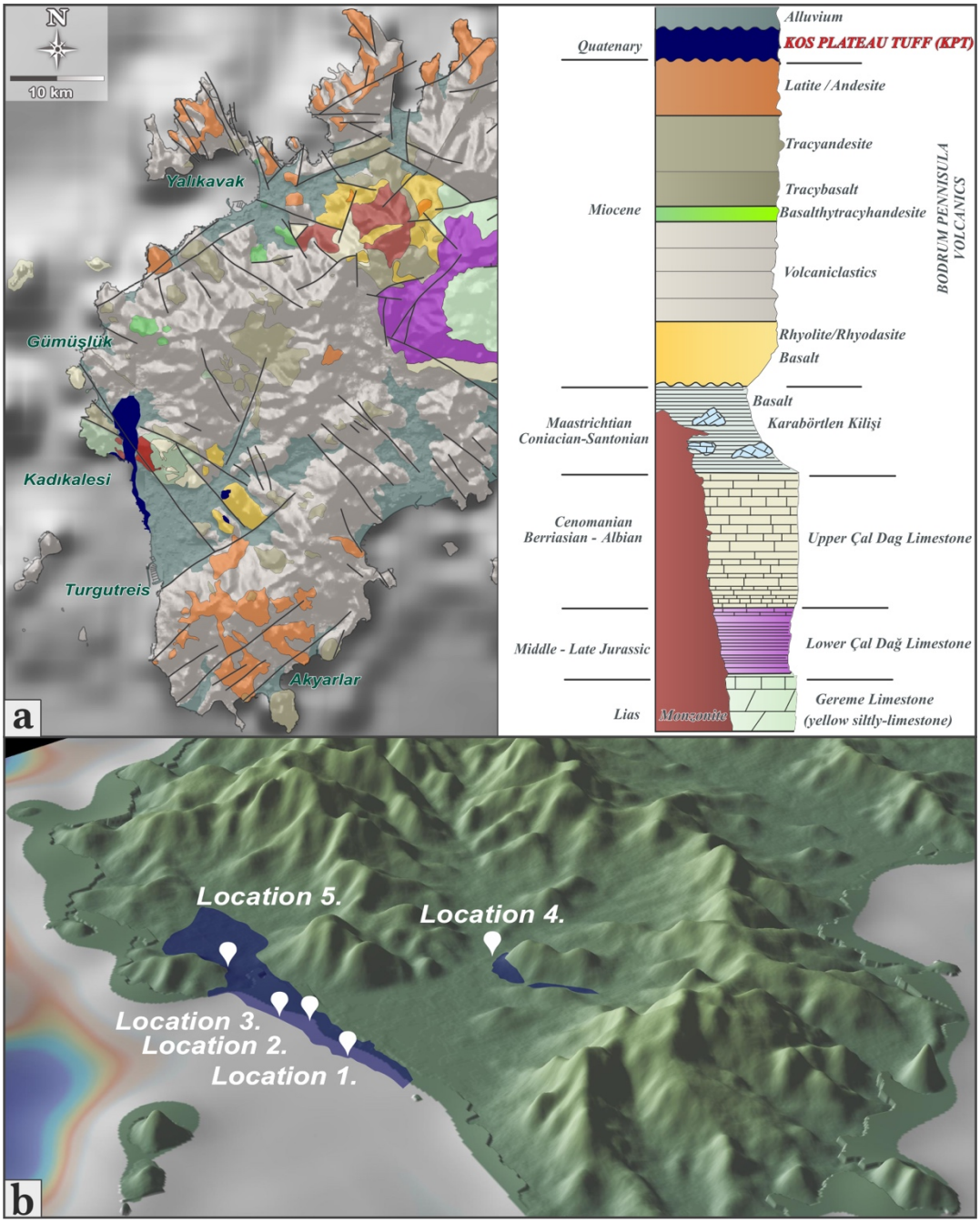

Figure 4.2 Local geological map of the study area. The geological map of the Bodrum Peninsula is based on various sources, including Altunkaynak & Yılmaz (2001), Genç et al. (2001), Kurt & Arslan (2001), İşsever et al. (2005), Karacık (2006), Masse et al. (2015) and Akal, (2023). The determination of the distribution area of the Kos Plateau Tuff (KPT) is credited to Ercan (1982, 1984), Allen (2001), Ulusoy et al. (2004), and Çubukçu et al. (2021), drawing upon the findings of their respective studies

4.2.1 Location 1

Location 1 (**KPT-BOD-88**) on Turgutreis (**N 37,0206539; E 27,2518434**) is the most proximal of the studied locations, at a radial distance of **~42.42 km** from the inferred vent position and where the layer has a thickness of **2.5** m (Figure, 4.3).

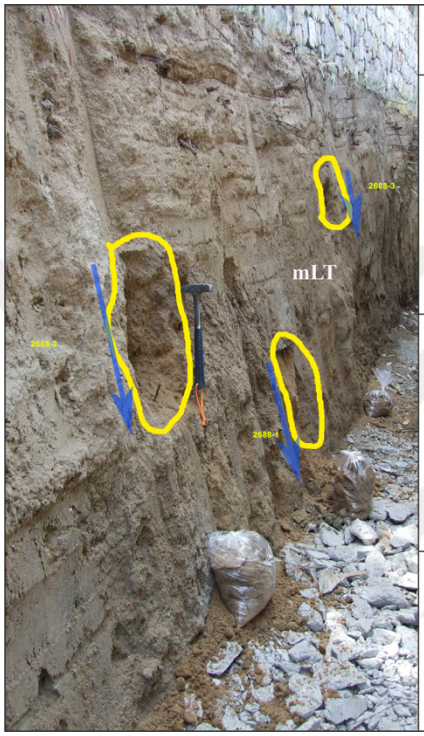

Sample Name	Max Clast Size	Thickness	Color	Field Observation
88-1	MP: 7.2 cm ML: 6 cm MAL: - cm	2.5 m	Gray	Fine ash-rich matrix supported.
88-2	MP:2 cm ML: 11.1 cm MAL: - cm			Lapilli pumice is rich. Lithic-rich fine ash supported section
88-3	MP: 2.5 cm ML: 5.4 cm MAL: 1 cm			Lapilli is found and the range is 0.5 - 1 cm. Lithics are fines grained.

Figure 4.3 The table shows the first observations during the fieldwork study belonging to Location 1 (Personal archive, 2022)

Here, the sequence is predominantly a massive, pumice-lapilli dominated, very poorly sorted, with lithic-rich. The max lithic size of the rounded lithic crystal is **11.1** cm; also, the max pumice is **7.2 cm**, and the matrix is ash-supported. The lower 1/3 of this sequence has an abundance of fine lithics has acceleration lapilli but lacks pumice; The middle part of this sequence which has an abundance of lithics has no acceleration lapilli and lacks pumice; The upper 3/3 of this sequence which has fine ash-rich and lacks pumice to samples 88; Location 1. Described ***Pumice-Lapilli Dominated Massive Ignimbrite Facies with Accretionary Lapilli*** consisting of pumice lapilli, lithic block, lithic lapilli, and accretionary lapilli in an ash matrix and beach deposits have relatively smaller component content.

4.2.2.1 Textural and Lithofacies Characteristics of The KPT Ignimbrites on Location 1

4.2.1.1.1 Granulometry

The results of the Gradistat analysis are presented in the table. While applying the method of Folk & Ward (1957) for classification, it was observed that the first sample (88-1) from the second location (KPT-BOD-88) exhibited ***very poorly sorting*** and ***coarse skewness*** (negative skewness), the D50 value was calculated as -0,829 φ, as shown in Figure 7.2. The second sample (88-2) from the same location exhibited very ***poorly sorting*** and ***coarse skewness*** (negative skewness), the D50 value was calculated as -0,366 φ, as shown in Figure, 7.2.

4.2.2.1.2 Texture

This unit has very poorly sorted and non-welded units **2.5 m thick**. The matrices of this unit are dominated by vitric shards and crystals that have adhered to fine ash.

4.2.2.1.3 Components Percentages

Every size range has a different component percentage and is measured within a detailed pie chart (Figure, 7.2). These units have 54% Pumices; 9% Lithic; 37% Minerals. The pumices are gray-colored and mostly denser than the other pumices. Mineral components have occurred as quartz, plagioclase, biotite, pyroxene, and magnetite minerals. Lithic materials predominantly consist of charcoal, plant remains, and organic remains. Furthermore, in the thin sections, some andesitic lithic fragments were observed.

4.2.2.1.4 Ash Shard Morphology

Pumices are tube-regular-banded pumices, also some of these pumices are filled with fibrous minerals (see Chapter 5). The shapes of ash particles are dominantly blocky, moss-like, drop-like, and platy types and these glasses are covered with fine

ash. To understand the morphology, all samples were cleaned and detailed examination photos were taken under the microscopes (Figure, 4.4).

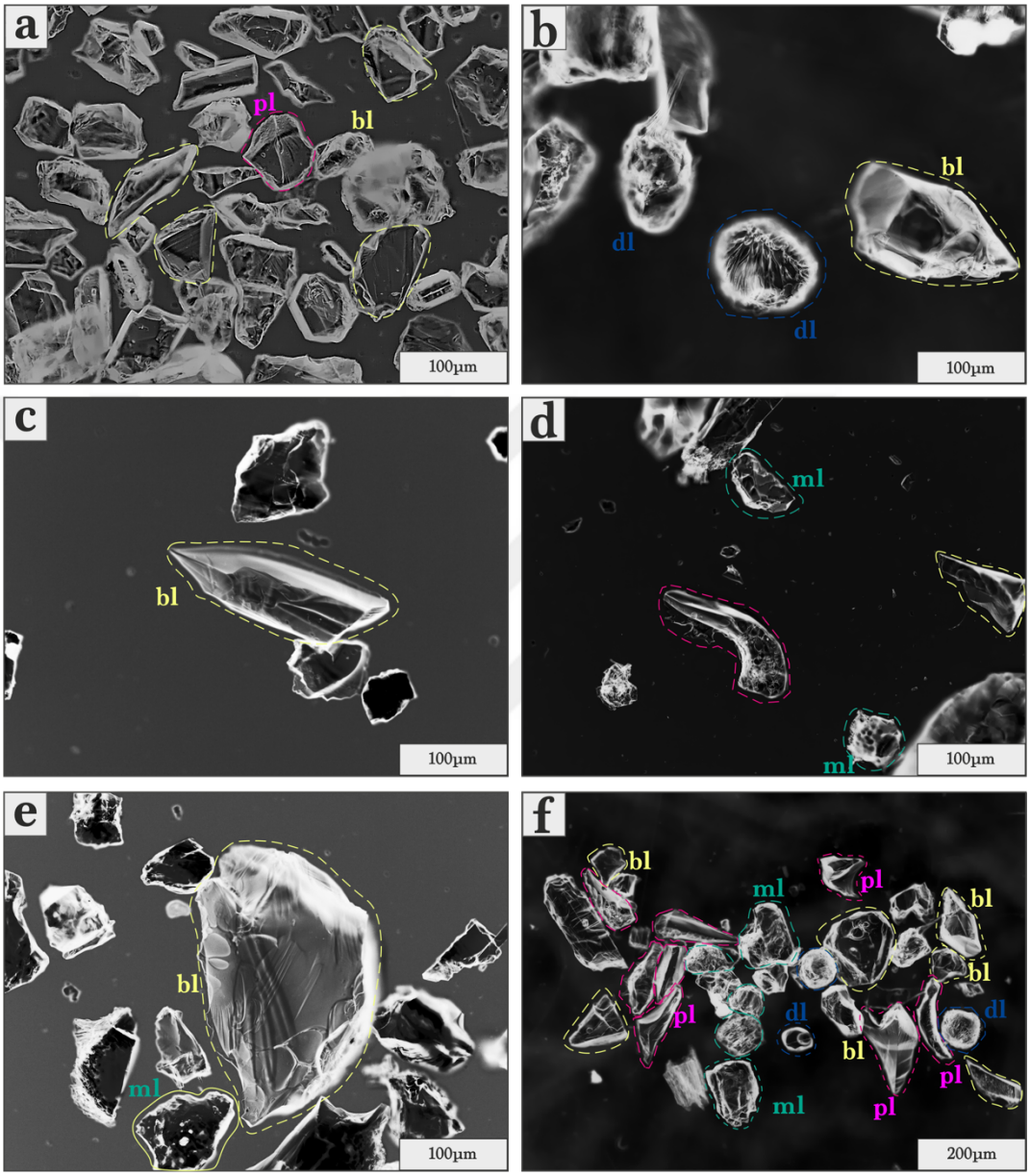

Figure 4.4 Glass morphologies belong to the first location

4.2.2 Location 2

Location 2 (**KPT-BOD-90**) on Turgutreis (**N 37,0216185; E 27,2514779**) is at a radial distance of **~42.62 km** from the inferred vent position and where the layer has a thickness of **3 m.** At this location, the stratigraphic layer exhibits beach deposits

(Figure, 4.5-6-7). Furthermore, horizontal observations reveal the presence of distinct bedding variations.

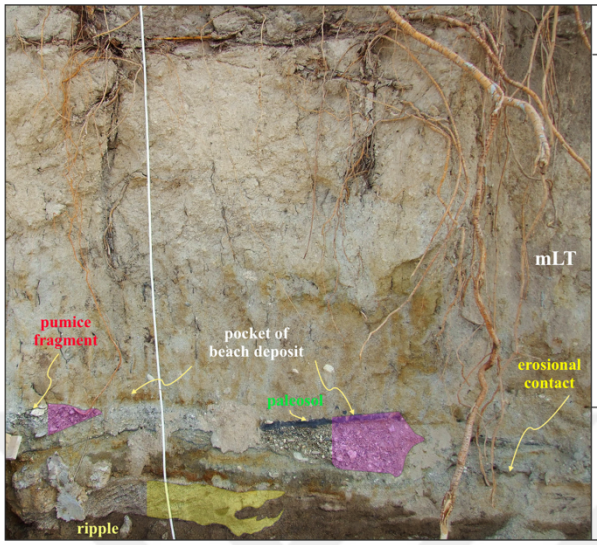

Sample Name	Max Clast Size	Thickness	Color	Field Observation
90	MP: 7 cm ML: 4 cm MAL: 1.1 cm	110 cm	White	Massive ignimbrite layer, sorting is unclear, context is the same with the other samples of second location
B/T deposit	MP: 6 cm ML: - MAL: -	60 cm	Mixed	The pockets of beach depoits, erosional contacts, and presence of paleosols could be relation with tsunamic affects of eruption.

Figure 4.5 The table shows the first observations during the fieldwork study belonging to Location 2. These sections belong to the beach deposition-related unit (Personal archive, 2022)

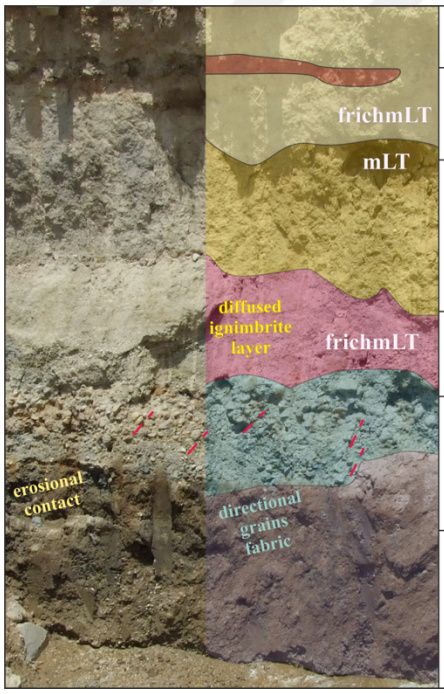

Sample Name	Max Clast Size	Thickness	Color	Field Observation
90F	MP:2 cm	0.5 m	White/ Yellow	Fine ash rich ignimbrite layer.
90D	MP:6.4 cm ML:3.2 cm	0.6 m	White/ Yellow	Massive ignimbrite, containing fine ash to block-size grain
90F	MP:11.4 cm	0.7 m	White/ Yellow	Fine ash rich ignimbrite layer.
90B	MP:12cm	0.6 m	White/ Yellow	Dense pebble clasts rich layer. The grains exhibit a discernible orientation, it could be possibble backwash tsunami deposits
	MP:2cm ML:4cm	0.9 m	White/ Gray	Massive ignimbrite, lapilli pumice rich, containing fine ash to block-size grain

Figure 4.6 The table shows the first observations during the fieldwork study belonging to Location 2. These sections present the different grain size layers of one specific unit (Personal archive, 2022)

Sample Name	Max Clast Size	Thickness	Color	Field Observation
90-1	MP: 7 cm ML: 6 cm MAL: 1.6 cm	2.5 m	White/ Yellow	The pumice clasts in this location are the clearest and whitest clasts found on the peninsula. Massive pyroclastic grain size displays significant variability. Spanning a range between 1 and 12 cm Fine ash-rich matrix supported.
90-3	MP: 7 cm ML: 5 cm MAL: 1.5 cm			Pumice grain size has highly variable grain sizes. Fine ash-rich matrix supported
90-2	MP: 18.3 cm ML: 7.4 cm MAL: 2 cm			Lapilli is found and the range is 0.5 - 1 cm. Lithics are fines grained.

Figure 4.7 The table shows the first observations and the sampling parts belonging to Location 2 during the fieldwork study (Personal archive, 2022)

Here, the sequence is predominantly a massive, pumice-lapilli dominated, very poorly sorted, with lithic content. Max lithic is **7.4 cm** and the lithic fragments are rounded, max pumice is **18.3 cm,** and the matrix is ash supported. Accretionary lapilli have been found at this location too, respectively to samples 90; Location 2. Described ***Unstained Pumice-Lapilli Dominated Massive Ignimbrite Facies with Accretionary Lapilli*** consisting of pumice lapilli, lithic block, lithic lapilli, and accretionary lapilli in an ash matrix and beach deposits have relatively smaller component content.

4.2.2.1 Textural and Lithofacies Characteristics of The KPT Ignimbrites on Location 2

4.2.1.1.1 Granulometry

The results of the Gradistat analysis are presented in the table. While applying the method of Folk & Ward (1957) for classification, it was observed that the first sample (90-1) from the second location (KPT-BOD-90) exhibited ***very poorly sorting*** and very

coarse skewness (negative skewness), the D50 value was calculated as -0.748 φ, as shown in Figure, 7.2. The second sample from the same location (90-3) exhibited ***very poorly sorting*** and ***symmetrical***, the D50 value was calculated as -0.999 φ, as shown in Figure, 106.

4.2.2.1.2 Texture

This unit has very poorly sorted and non-welded units **3 m thick**. The matrices of this unit are dominated by vitric shards and crystals that have adhered to fine ash.

4.2.2.1.3 Components Percentages

Every size range has a different component percentage and is measured within a detailed pie chart (Figure, 7.2). These units have 52% Pumices; 13% Lithic; 35% Minerals. Lithic materials predominantly consist of charcoal, plant remains, and organic remains. The pumices are the cleanest, white pumices than the other pumices on the peninsula, and mostly pumices were non-adhered. Mineral components have occurred as quartz, plagioclase, biotite, pyroxene, and magnetite minerals. Lithic materials predominantly consist of charcoal, plant remains, and organic remains. Furthermore, in the thin sections, some andesitic lithic fragments were observed.

4.2.2.1.4 Ash Shard Morphology

Pumices are tube-regular-banded pumices. The shapes of ash particles are dominantly covered with fine ash, blocky, moss-like, drop-like, and platy types (see Chapter 5). To understand the morphology, all samples were cleaned and detailed examination photos were taken under the microscopes (Figure, 4.8).

4.2.3 Location 3

Location 3 (KPT-BOD-91) on Turgutreis (**N 37,0208968; E 27,2517942**) is at a radial distance of **42.63 km** from the inferred vent position and where the layer has a thickness of **2.5 m**. Here, the sequence is predominantly a massive, pumice-lapilli

dominated, very poorly sorted, with a lithic-rich. The lithics is sharp and the max size is **13 cm**. Max pumice is **18 cm**. The 1/3 and 3/3 of this sequence have intercalated with the fine ash and lapilli-rich material. The middle of this sequence has more lithic-rich and block pumice materials. The ash intercalations are all similar, poorly sorted, massive, fine ash with admixed coarse-to-very coarse lapilli pumice and accretionary lapilli. These ash beds correlate, respectively, to samples 91; Location 3 (Figure 4.9).

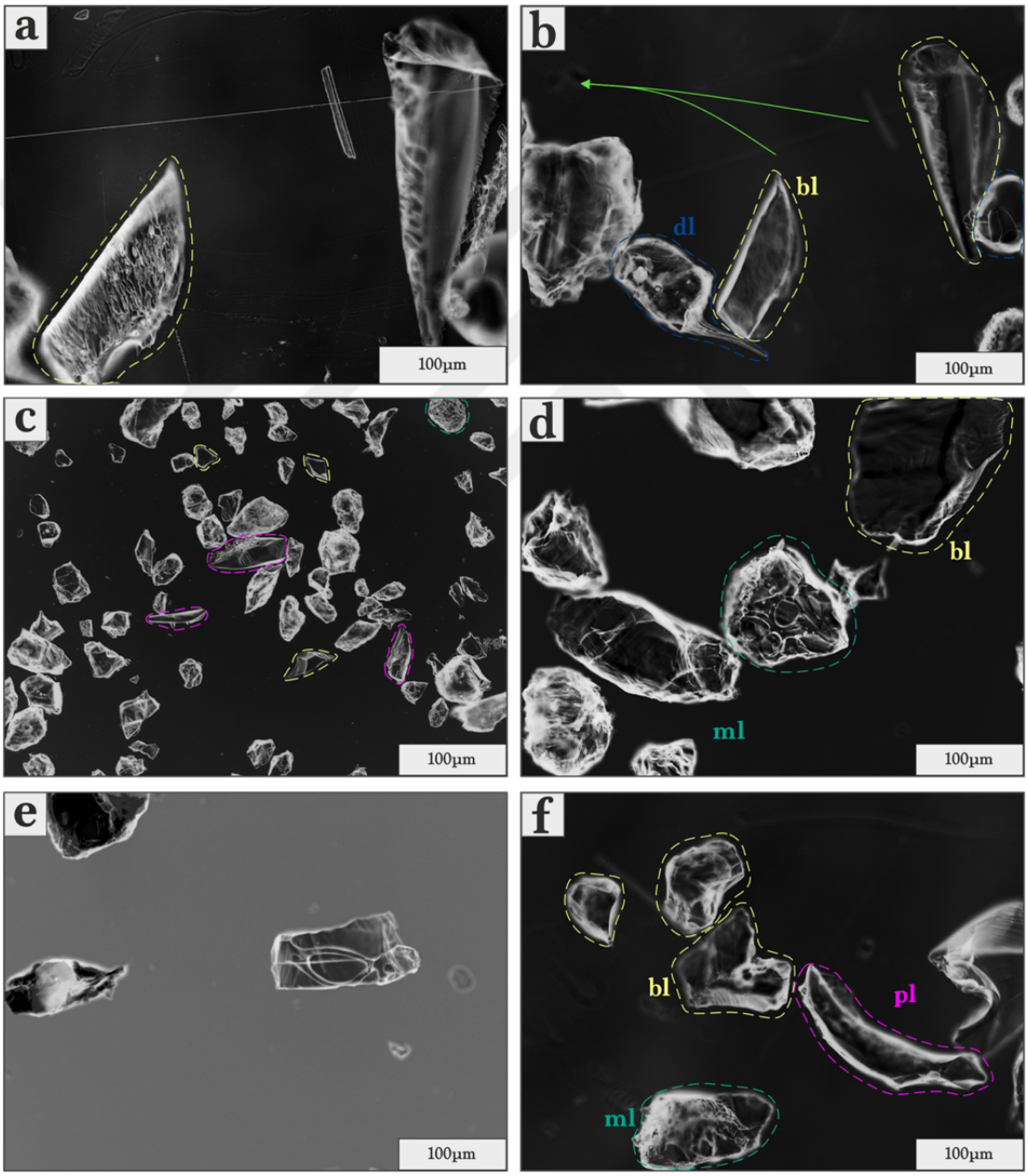

Figure 4.8 Glass morphologies belong to the second location

Sample Name	Max Clast Size	Thickness	Color	Field Observation
91-1	MP: 7.2 cm ML: 6 cm MAL: 1 cm	2.5 m	White/ Yellow	Fine ash-rich matrix supported.

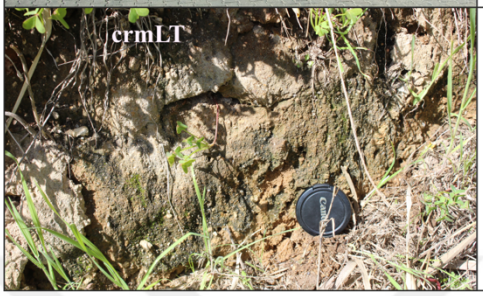

TG-1	MP:2 cm ML: 11.1 cm MAL: - cm	0.8 m	White/ Yellow	Lapilli pumice is rich. Lithic-rich fine ash supported section

Figure 4.9 The table shows the first observations during the fieldwork study belonging to Location 3 (Personal archive, 2022)

Described as ***Pumice-Lapilli Dominated Massive Ignimbrite Facies with Lithic-Rich Middle Layer and Accretionary Lapilli*** consisting of pumice lapilli, lithic block, and lithic lapilli in an ash matrix, and shell fragments were found as broken.

4.2.3.1 Textural and Lithofacies Characteristics of The KPT Ignimbrites on Location 3

4.2.3.1.1 Granulometry

The results of the Gradistat analysis are presented in the table. While applying the method of Folk & Ward (1957) for classification, it was observed that the first sample (91) from the third location (KPT-BOD-91) exhibited ***very poorly sorting*** and ***very fine skewness*** (positive skewness), the D50 value was calculated as -2.981 φ, as shown in Figure, 7.2. The second sample from the same location (TG-1) exhibited ***very poorly sorting*** and ***fine skewed*** (positive), the D50 value was calculated as -2.285 φ, as shown in Figure, 7.2.

4.2.3.1.2 Texture

This unit has very poorly sorted and non-welded units **2 m thick**. The matrices of this unit are dominated by vitric shards and crystals that have adhered to fine ash and lithic-rich deposits.

4.2.3.1.3 Components Percentages

Every size range has a different component percentage and is measured within a detailed pie chart (Figure, 7.2). These units have 58% Pumices; 13% Lithic; and 29% Minerals. Lithic materials predominantly consist of charcoal, plant remains, and organic remains. The pumices mostly were ash adhered. Mineral components have occurred as quartz, plagioclase, biotite, pyroxene, and magnetite minerals. Lithic materials predominantly consist of charcoal, plant remains, and organic remains. Furthermore, in the thin sections, some andesitic lithic fragments were observed.

4.2.3.1.4 Ash Shard Morphology

Pumices are tube-regular-banded pumices also some of these pumices are filled with fibrous minerals. The shapes of particles are dominantly covered with fine ash, blocky, moss-like, drop-like, and platy types. To understand the morphology, all samples were cleaned and detailed examination photos were taken under the microscopes (Figure, 4.10).

4.2.4 Location 4

Location 4 (KPT-BOD-92) on Turgutreis (**N 37,0226558; E 27,2806372**) is at a radial distance of **43.60 km** from the inferred vent position and where the layer has a thickness of **10 m** (Figure, 15-16).

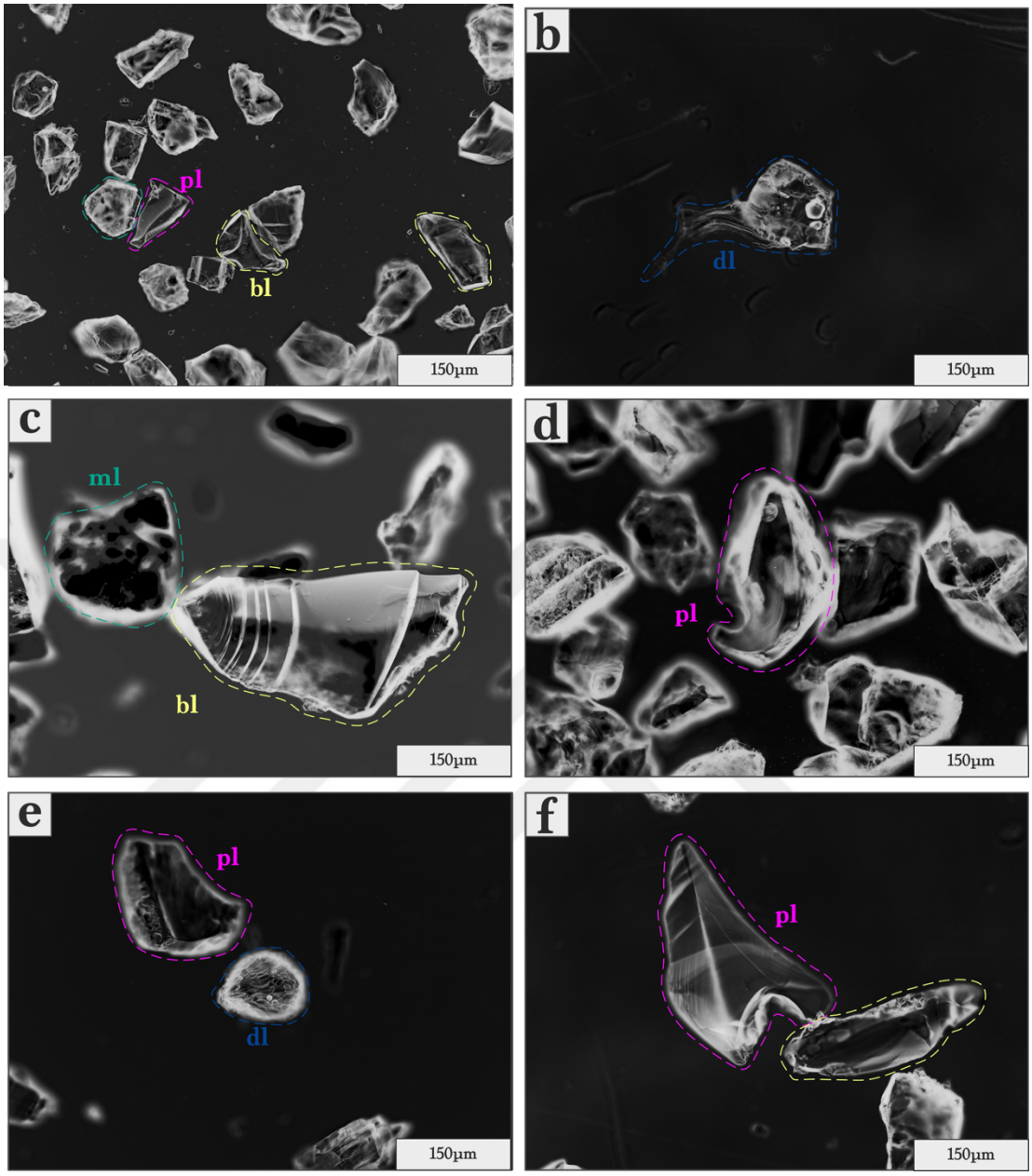

Figure 4.10 Glass morphologies belong to the third location

Here, the sequence is predominantly a massive, pumice-lapilli dominated, very poorly sorted, with a lithic rich. Lithics are rounded, and the max lithic is **17 cm**. Max pumice is **22 cm**. There is a thin ash fall layer thought to be a coignimbritic ash cloud. Additionally, there is an ignimbrite layer with accretionary lapilli, which is rich in lithics and has a basal lithic-rich layer. These ash beds correlate, respectively, to samples 92; Location 4.

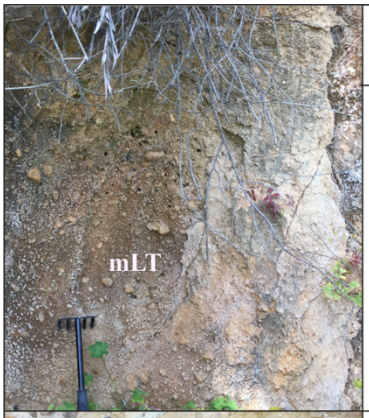

Sample Name	Max Clast Size	Thickness	Color	Field Observation
KD-1	MP: 26.5 cm ML: 7 cm MAL: -	2 m	White/ Yellow	Various size pumice fragments. Angular shape lithic-rich, Marineshell-rich ash matrix.

KD-2	MP: 10 cm ML: 18 cm MAL: -	2.5 m	White/ Yellow	Angular shape lithic-rich, Various clast range size pumices

Figure 4.11 The table shows the first observations and the sampling parts during the fieldwork study belonging to Location 5 (Personal archive, 2022)

Described as ***Pumice-Lapilli Dominated Massive Ignimbrite Facies with Coignimbritic Ash-Cloud Layer and Accretionary Lapilli*** consisting of pumice lapilli, lithic block, lithic lapilli, and accretionary lapilli in an ash matrix and found max lithic fragment which is **17 cm**.

4.2.4.1 Textural and Lithofacies Characteristics of The KPT Ignimbrites on The Location 4

4.2.4.1.1 Granulometry

The results of the Gradistat analysis are presented in the table. While applying the method of Folk & Ward (1957) for classification, it was observed that the first sample (92-1) from the fourth location (KPT-BOD-92) exhibited ***very poorly sorting*** and

symmetrical as depicted. The D50 value was calculated as -0.909 φ. The second sample from the same location (92-2) exhibited ***very poorly sorting*** and ***symmetrical***, the D50 value was calculated as -1.438 φ, as shown in Figure, 7.2. The third sample from the same location (IS-1) exhibited ***very poorly sorting*** and ***very fine skewed*** (positive skewed), the D50 value was calculated as -3.016 φ, as shown in Figure, 7.2.

4.2.4.1.2 Texture

This unit has very poorly sorted and non-welded units **10 m thick**. The matrices of this unit are dominated by vitric shards and crystals that have adhered to fine ash. The lower part is the fine ash-rich layer, and some part of the section has a basal lithic-rich layer.

	Sample Name	Max Clast Size	Thickness	Color	Field Observation
	KD-3	MP: 12 cm ML: 7 cm MAL: -	3.2 m	White	Various size pumice fragments. Angular shape lithic-rich,
	KD-4	MP: 4.7 cm ML: 1.8 cm MAL: -	0.5 m	White	Angular shape lithic-rich, Crystal-rich ash matrix.

Figure 4.12 The table shows the first observations during the fieldwork study belonging to Location 5 (Personal archive, 2022)

4.2.4.1.3 Components Percentages:

Every size range has a different component percentage and is measured within a detailed pie chart (Figure, 7.2). These units have 69% Pumices; 5% Lithic; 26% Minerals. Lithic materials predominantly consist of charcoal, plant remains, and organic remains. Lithic materials predominantly consist of charcoal, plant remains, and organic remains. The pumices mostly were ash adhered. Mineral components have occurred as quartz, plagioclase, biotite, pyroxene, and magnetite minerals. Lithic materials predominantly consist of charcoal, plant remains, and organic remains. Furthermore, in the thin sections, some andesitic lithic fragments were observed.

4.2.4.1.4 Ash Shard Morphology:

Pumices are tube-regular-banded pumices also some of these pumices are filled with fibrous minerals. The shapes of particles are dominantly covered with fine ash, blocky, moss-like, drop-like, and platy types. To understand the morphology, all samples were cleaned and detailed examination photos were taken under the microscopes (Figure, 4.13).

4.2.5 Location 5

Location 5 (KPT-BOD-KD) on Turgutreis (**N 37,041197; E 27,2434684**) is the most distal of the studied locations, at a radial distance of **44.45 km** from the inferred vent position and where the layer has a thickness of **2 m**.

Here, the sequence is predominantly a massive, pumice-lapilli dominated, very poorly sorted. Maximum lithic size is **7 cm**, and lithics are rounded. The maximum pumice size is **26.5 cm**. The unit contains pumice lapilli, pumice blocks, and lithic lapilli in the ash matrix. These ash beds correlate, respectively, to samples KD-1-3, Location 5. Accretionary lapilli are observed at this location. Described as ***Pumice-Lapilli Dominated Massive Ignimbrite Facies with Large Pumice Blocks*** content of pumice lapilli, pumice block, and lithic lapilli in the ash matrix and found maximum pumice which is **26.5 cm** (Figure, 4.14-15).

4.2.5.1 *Textural and Lithofacies Characteristics of The KPT Ignimbrites on Location 5*

4.2.5.1.1 *Granulometry*

The results of the Gradistat analysis are presented in the table. While applying the method of Folk & Ward (1957) for classification, it was observed that the first sample (KD-1) from the fifth location (KPT-BOD-KD) exhibited ***very poorly sorting*** and ***very fine skewness*** (negative skewness). The D50 value was calculated as -5.848 φ. The second sample from the same location (KD-2) exhibited ***very poorly sorting*** and ***very fine skewed*** (positive skewness), the D50 value was calculated as -2.845 φ.

4.2.5.1.2 Texture

This unit has very poorly sorted and non-welded units **2 m thick**. The matrices of this unit are dominated by vitric shards and crystals that have adhered to fine ash. The lower part is a fine ash-rich layer, and some part of the section has a basal lithic-rich layer.

4.2.5.1.3 Components Percentages

Every size range has a different component percentage and is measured within a detailed pie chart (Figure, 7.2). These units have 73% Pumices; 6% Lithic; 21% Minerals. Lithic materials predominantly consist of charcoal, plant remains, and organic remains. Lithic materials predominantly consist of charcoal, plant remains, and organic remains. The pumices mostly were ash adhered. Mineral components have occurred as quartz, plagioclase, biotite, pyroxene, and magnetite minerals. Lithic materials predominantly consist of charcoal, plant remains, and organic remains. Furthermore, in the thin sections, some andesitic lithic fragments were observed.

4.2.5.1.4 Ash Shard Morphology

Pumices are tube-regular-banded pumices also some of these pumices are filled with fibrous minerals. The shapes of particles are dominantly covered with fine ash, blocky, moss-like, drop-like, and platy types. To understand the morphology, all samples were cleaned and detailed examination photos were taken under the microscopes (Figure, 4.16).

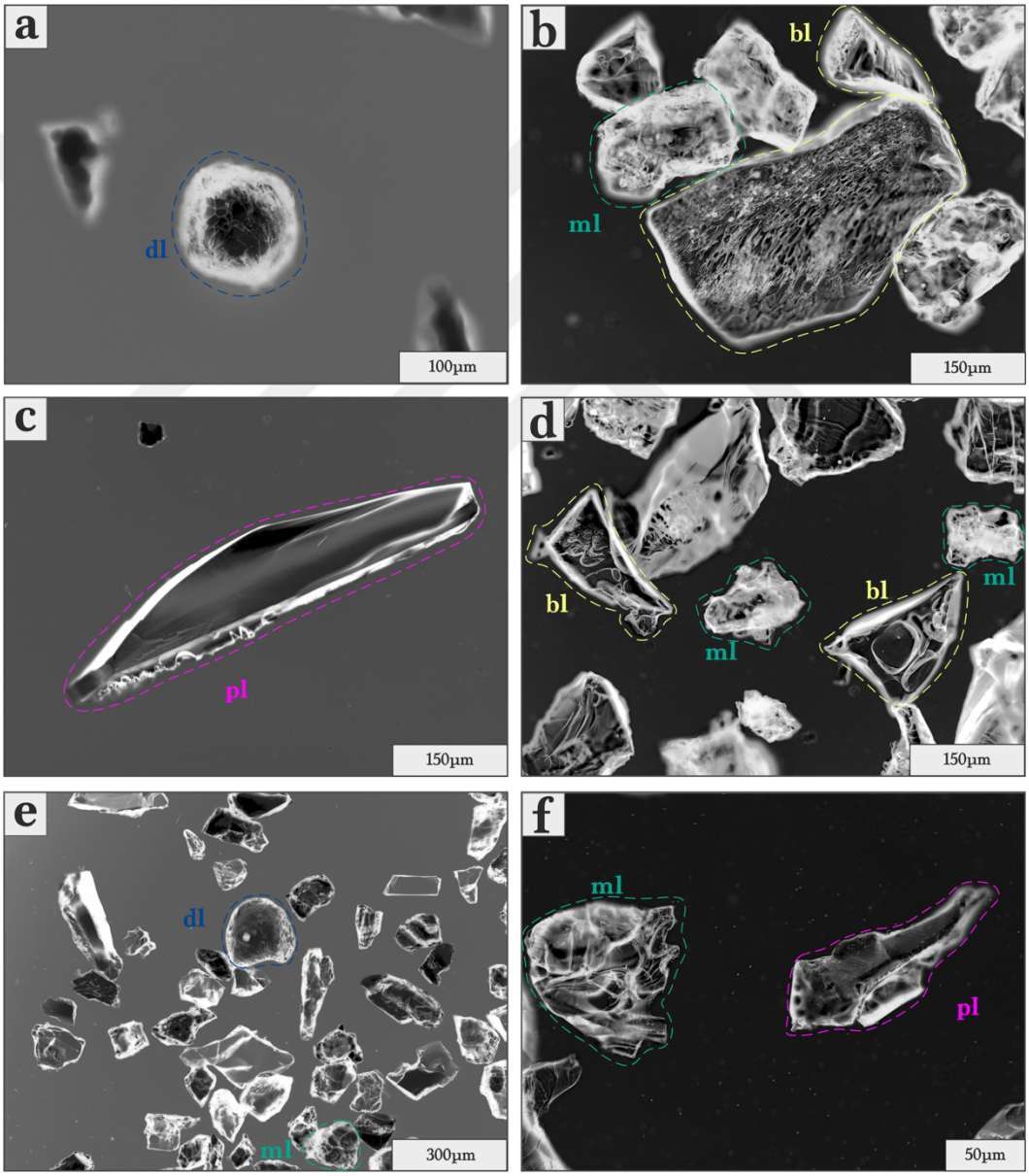

Figure 4.13 Glass morphologies belong to the fourth location

Sample Name	Max Clast Size	Thickness	Color	Field Observation
IS-1	MP: 22 cm ML: 5.5 cm MAL: 0.2 cm	2 m	Yellow / Orange	The lithics are abundant and the shape of the fragments is angular. The layer is massive.
IS-2	MP: 12 cm ML: 10 cm MAL: 0.3 cm	2.5 m		Ignimbrite from a highly unsteady current. Noted grainsize changes range variously from subtle to marked, and from sharp to gradational, with abundant reversals in grading trend. Saltation of lithic fragments Under the masive units; Thin-bedded (bLT) or Diffuse thin-bedded tuff (dbLT)

Figure 4.14 The table shows the first observations and the different layers belonging to Location 4 during the fieldwork study (Personal archive, 2022)

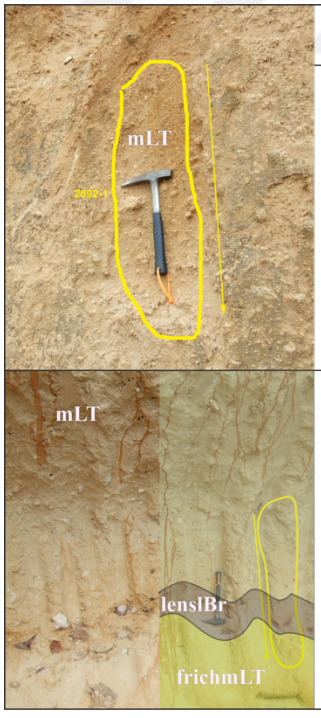

Sample Name	Max Clast Size	Thickness	Color	Field Observation
92-1	MP: 10 cm ML: 5 cm MAL: 0.3 cm	3 m	Yellow / Orange	Pumice grain size has highly variable grain sizes. Lithics are rounded and fine-grained. The color at this unit is distinctively orange.
92-2	MP: 10 cm ML: 17 cm MAL: 0.5 cm	2.5 m		Lapilli exist different size range. There exists a lithic-rich layer at the base. Angular lithic clasts can be observed within lens shape because of concentrated within a diffuse layer Meteorological conditions caused some changes in color.

Figure 4.15 The table shows the first observations and the sampling parts belonging to Location 4 during the fieldwork study (Personal archive, 2022)

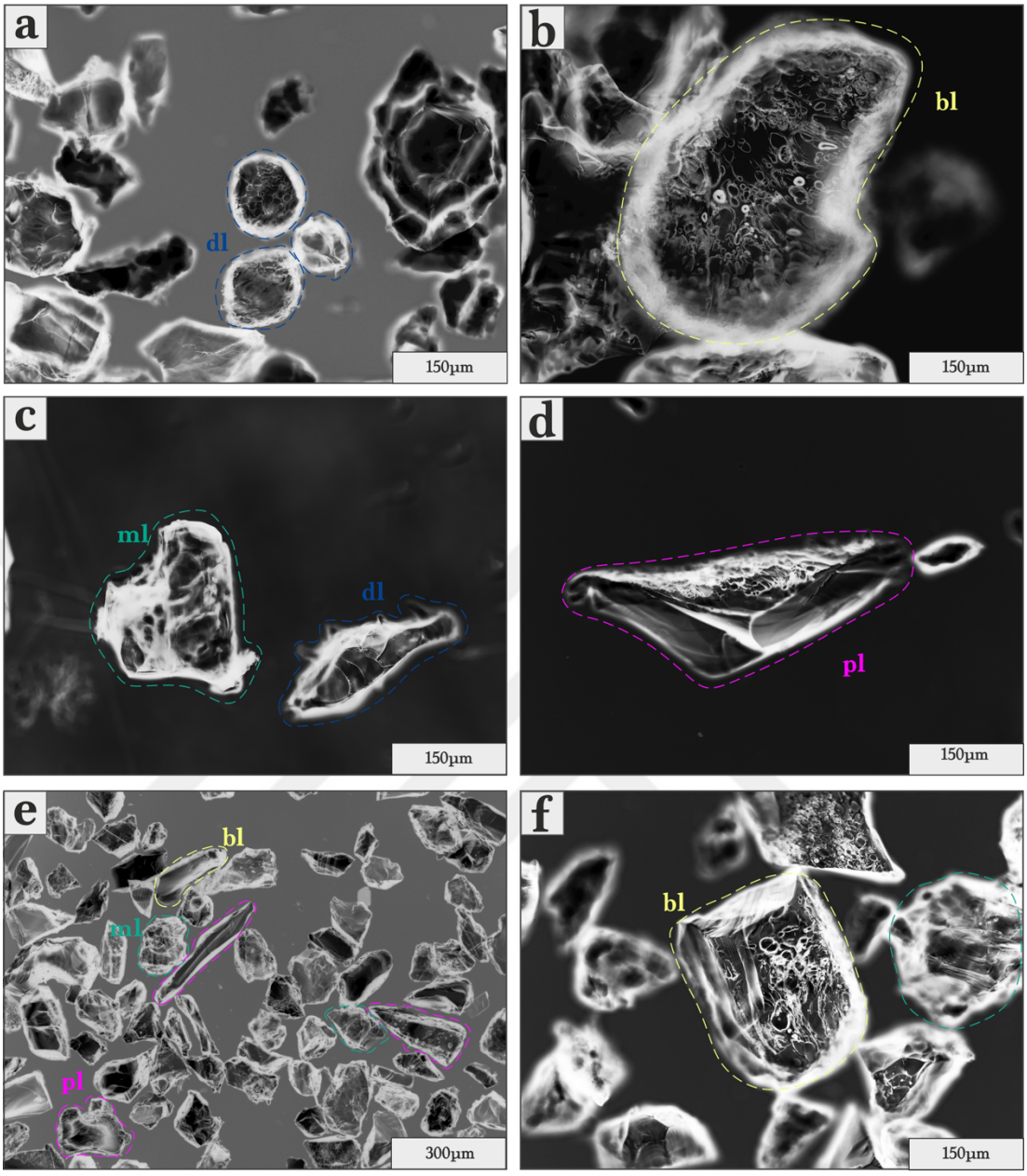

Figure 4.16 Glass morphologies belong to the fourth location

CHAPTER FIVE
MINERALOGY AND PETROGRAPHY

5.1 Introduction

Volcanic phenomena have fascinated geoscientists and researchers for a long time, providing valuable insights into the dynamic processes and geological history of the Earth. Pyroclastic density currents (PDCs) are one such fascinating and powerful volcanic phenomenon that shapes landscapes and leaves a lasting impression on the geological record. In recent years, there has been an increased interest in studying the dynamics and characteristics of PDCs, which has yielded invaluable knowledge about eruption and transportation mechanisms, hazard assessment, and the magmatic processes driving volcanic activity. While the study of PDCs has expanded worldwide, some regions remain relatively unexplored, presenting unique opportunities for detailed investigation. The Bodrum Peninsula, located at the intersection of tectonic boundaries and known for its volcanic history, is an exciting site for studying PDCs. However, the PDC units in this area have yet to be subjected to a comprehensive petrological analysis. This research project aims to bridge this crucial knowledge gap by thoroughly investigating the petrological features of the pyroclastic density current units on the Bodrum Peninsula. By concentrating on this area, the project aims to gain a comprehensive understanding of the mineralogical composition, textural properties, and eruption dynamics associated with the Bodrum Peninsula's PDCs.

The primary focus is on the transportation mechanism of the PDCs, as specific findings have revealed inconsistencies that require further clarification. The insights obtained from this study could improve volcanic hazard assessments and offer a nuanced perspective on the evolution of volcanic systems. The research team conducted a comprehensive investigation of 65 rock samples from the Bodrum Peninsula, primarily focusing on analyzing the pyroclastic density current unit. The examination revealed several components, including pumice fragments, non-welded pyroclastic fragments, acceleration lapilli, lithic fragments, and the ash matrix. Notably, the ash matrix contained various essential minerals, such as feldspar, quartz, volcanic glass, and accessory minerals. This pumice fragments assemblage

encompasses juvenile, lithic, and micro pumices. Juvenile fragments are direct products of the erupting magma, comprising densely compacted or inflated particles of rapidly chilled melt and crystals pre-existing within the magma before eruption, as explained by Fisher & Schmincke (1984) (Figure 5.1). The characterization of juvenile fragments typically hinges on their outward appearances.

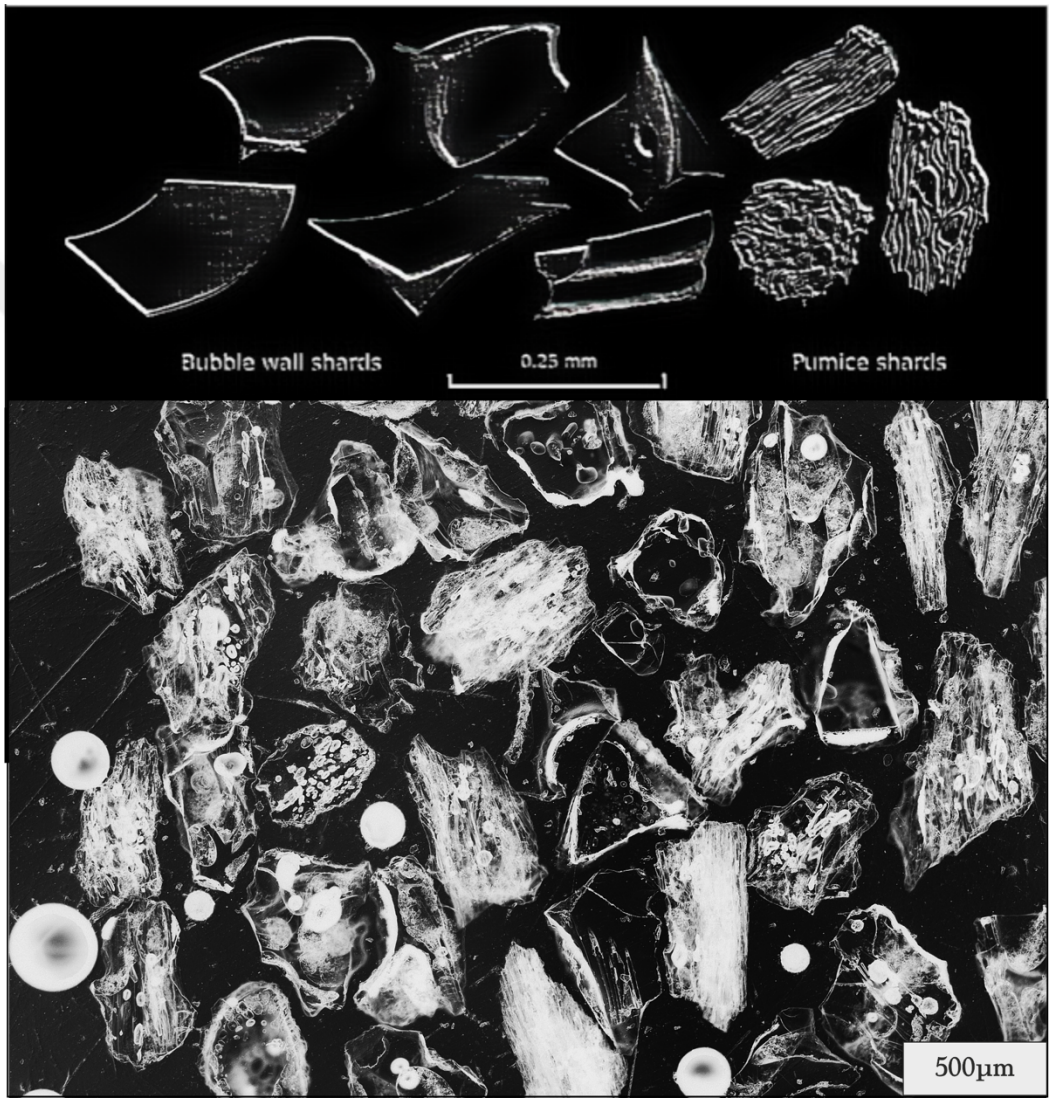

Figure 5.1 The diagram compares the glass classifications identified in the Fisher & Schmincke in 1984's study within the samples collected from the peninsula

The classification of pumice types, as previously mentioned, derives from the investigations of Bouvet de Maisonneuve et al. (2009) and Allen (2001). Instances of abrupt cooling may also manifest as vesicles adopting a collapsed morphology, as

posited by Taddeucci et al. (2004). Many studies have been carried out on the morphology of glass structures since the 70s (Heiken, 1972; Wohletz, 1983; Heiken, 1974;1994; Schumacher & Schmincke, 1991; Wohletz & Heiken, 1992; Gilbert & Lane, 1994). The characterization of glass shard shapes resulting from hydrovolcanic fragmentation was initially outlined by Wohletz in 1983. Wohletz's work categorized five predominant shapes: blocky and equant, vesicular and irregular with smooth surfaces, moss-like and convoluted, spherical or drop-like, and plate-like. These shapes exhibited different prevalence based on pyroclast size; types 1 and 2 dominated in pyroclasts larger than 100 μm, while types 3 and 4 were common in fine ash. For ash below 100 μm, type 5 was characteristic due to pronounced vesiculation during hydrovolcanic fragmentation. Experimental investigations into melt/water interactions revealed underlying mechanisms including vapor-film generation, expansion, and collapse. Additionally, fragments of congealed melt resulted from several mechanisms, such as stress-wave cavitation, detonation waves, and fluid instability mixing. These mechanisms collectively facilitated rapid heat transfer, elucidating the observed pyroclast shapes.

Stress-wave cavitation was particularly associated with high pressure and temperature gradients at the melt/water interface. Type 1 pyroclasts were formed through concurrent brittle fracture and quenching, whereas type 2 exhibited smooth surfaces due to turbulent water mixing post-fracture. Fluid instabilities induced turbulent meltwater mixing, contributing to the generation of fine ash, particularly during high-energy explosions. Enhanced melt surface area achieved through fine fragmentation subsequently led to efficient heat exchange with water, influencing pyroclast shapes based on factors such as maximum surface area (Type 3) and surface tension effects (Type 4). Finally, type 5 pyroclasts originated from nearly simultaneous vesicle bursting and melt/water fragmentation (Wohletz, 1983; Schumacher & Schmincke, 1991; Gilbert & Lane, 1994). Figure 5.2 shows a sketch that compares our samples with the five pyroclast types according to Wohletz & Heineken's work in 1985. In the pyroclastic sequence on Bodrum Peninsula, there are all types of clasts, as mentioned before, related to hydrovolcanic fragmentation.

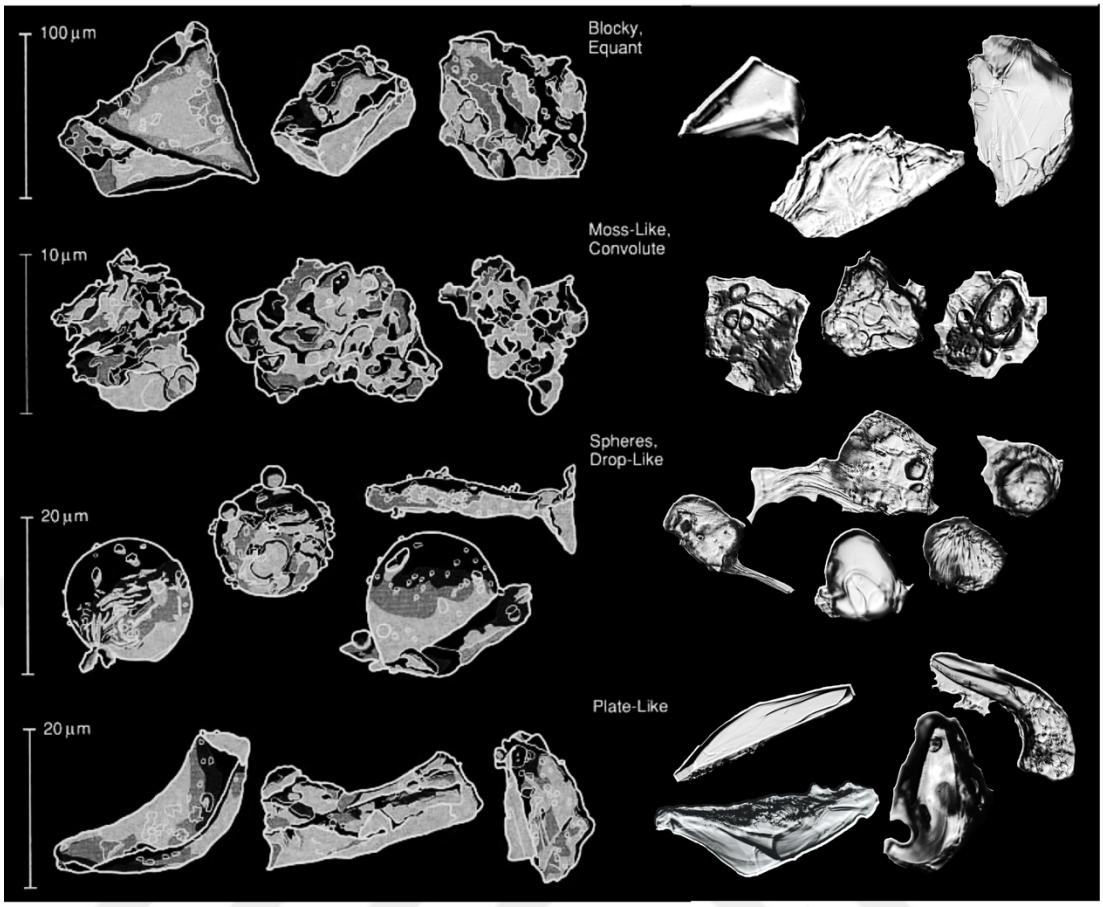

Figure 5.2 The diagram compares the glass classifications identified in the Wohletz 1983 study within the samples collected from the peninsula

In Bouvet de Maisonneuve and colleagues' 2009 study, the characterization of pumice samples involved the identification of four distinct pumice types through methods such as thin section observation, SEM imagery, porosimetry, and permeametry. These pumice types were categorized as tube pumices (~type II in Allen, 2001), frothy pumices (~type III and IV), microvesicular pumices (~type I), and grey-banded pumices (~type V). Their unique petrophysical attributes, including connected porosity, permeability, and the β factor, primarily develop during the ascent within the conduit, as indicated by previous studies (Marti et al. 1999; Polacci et al. 2001). The differentiation between crystal-rich pumice types is attributed to shearing effects, such as simple or pure shear, which influence coalescence dynamics and flow path constraints. This shearing also contributes to the variation in the development of inertial effects during gas flow through the magmatic foam. Consequently, tube

pumices exhibit an earlier establishment of a permeable network compared to frothy pumices. Conversely, the distinctions between crystal-poor and crystal-rich pumices stem from the occurrence of a homogeneous bubble nucleation event in the former but not in the latter (Bouvet de Maisonneuve et al., 2009). A schematic model presented in Figure 5.3 illustrates shallow conduit dynamics, elucidating macro- and microtextures, and is informed by previous research findings (Keller, 1969; Allen & Cas, 1998; Allen, 2001; Bouvet de Maisonneuve et al., 2009; Degruyter, 2010; Gonnerman & Manga, 2013; Cassidy et al., 2018; Jones et al., 2019; Mitchell, et al. 2019; Davies et al., 2021; Knafelc et al., 2022).

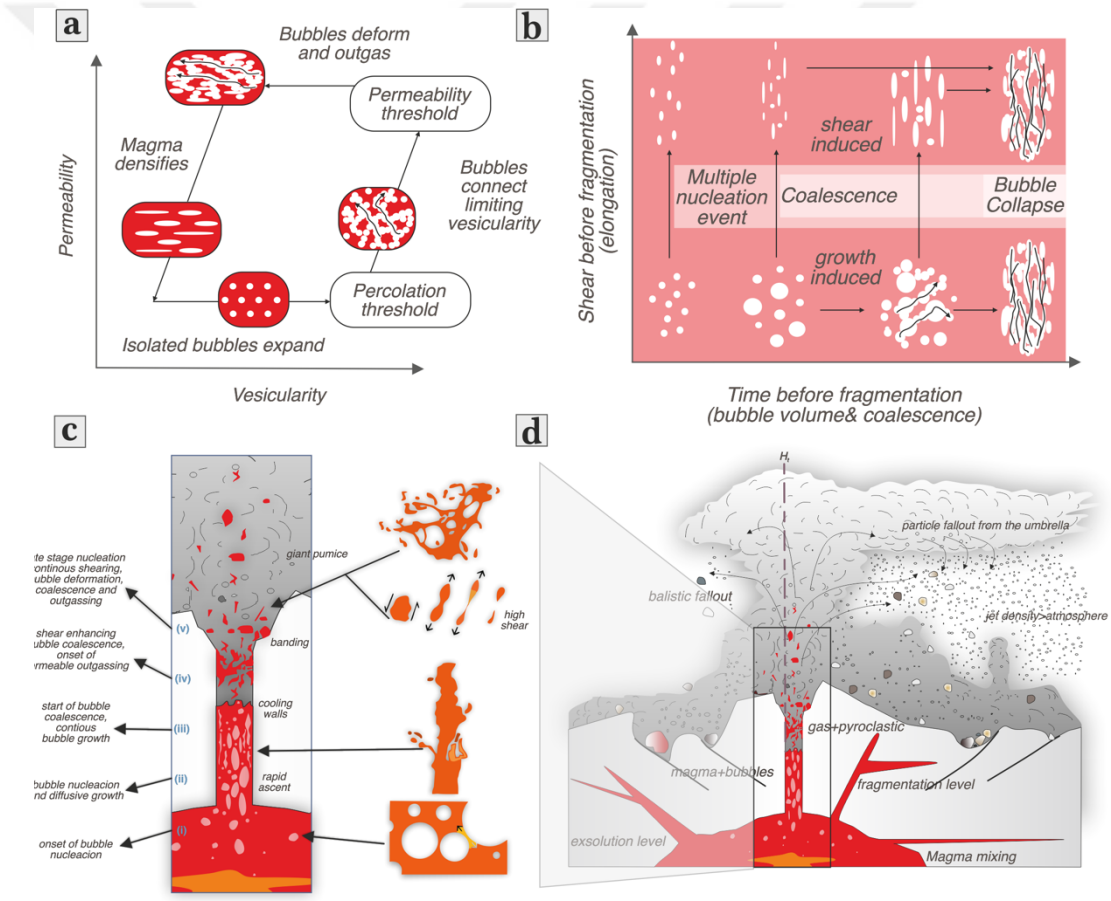

Figure 5.3 Magma dynamics cause the morphology of pumice pores (Gonnerman & Manga, 2013; Cassidy et al., 2018; Jones et al., 2019; Mitchell, et al. 2019; Davies et al., 2021; Knafelc et al., 2022)

The analysis of textural and lithofacies characteristics within the KPT (the specific name of the pyroclastic density current unit) provides compelling evidence for an ongoing eruption that intensified progressively, culminating in an eruption climax marked by the transition from unit A to subunit El. This heightened activity was followed by the initiation of a catastrophic caldera collapse (Allen, 2001).

A subsequent waning phase ensued, indicated by the transition from subunit Eu to unit F, effectively concluding the eruption sequence. The juvenile components within the phreatomagmatic units exhibited a moderate to highly vesicular nature, comprising approximately 45–84% volume of vesicles. Remarkably, the absence of schist and metabasalt clasts sourced from a deep basement suggests that interactions between magma and water primarily transpired at shallow depths within the conduit, primarily above the level of vesiculation (Allen & Cas, 1998). It's noteworthy that, despite these interactions, the eruption maintained a dry explosion nature (Allen, 2001).

Acceleration lapilli played a significant role in understanding the transportation mechanism of particles and the presence of vapor/water. Accretionary lapilli from pyroclastic flow and surge deposits, in contrast, have more densely packed cores (Schumacher & Schmmincke, 1991). The lapillus are spherically shaped, lapilli-sized particles made up of aggregated fine ash (Schumacher & Schmincke, 1991,1995; Gilbert & Lane, 1994) and identified two major types (Figure, 5.4) (Schumacher & Schmincke 1991, 1995); (1) rim-type, that are cored by coarser ash, lapilli, or aggregates of variable-sized clasts (Figure, 5.5) and rimmed by a fine ash layer, and (2) core-type that have no rims, and usually composed of coarser grained ash. Accretionary features such as mud clots or armored mud balls are also common in fine ash deposits from phreatomagmatic eruptions (Nemeth & Martin, 2007).

These findings provide valuable insights into the geological characteristics of the KPT in the Bodrum Peninsula. Furthermore, they shed light on the nature and behavior of pyroclastic density currents in this region, as discussed in Chapter Discussion. Identifying various pumice and lithic fragment types significantly improves our

understanding of volcanic processes and unveils crucial information regarding the area's geological history, which is extensively discussed in this chapter.

The research encompassed thorough investigations across all locations and content types, ensuring a comprehensive and robust analysis in this chapter. Polished grain mounts were produced from grab samples from each of the localities of Bodrum (Methods); their characteristics are described here.

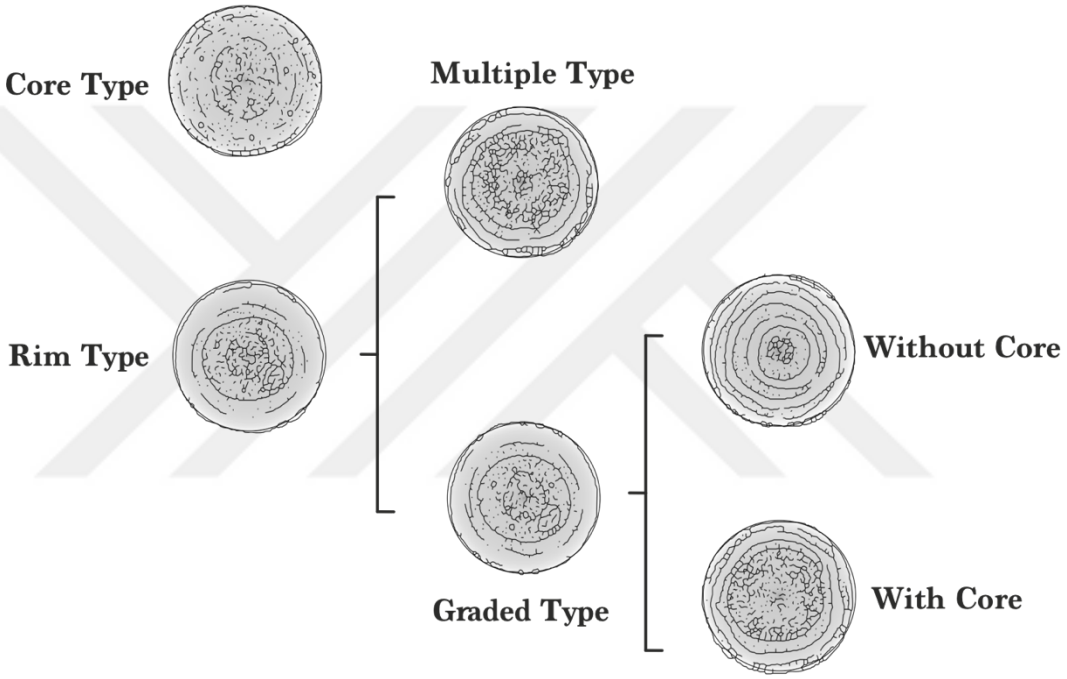

Figure 5.4 Acceleration lapillus types. (Schumacher & Schimincke in 1991)

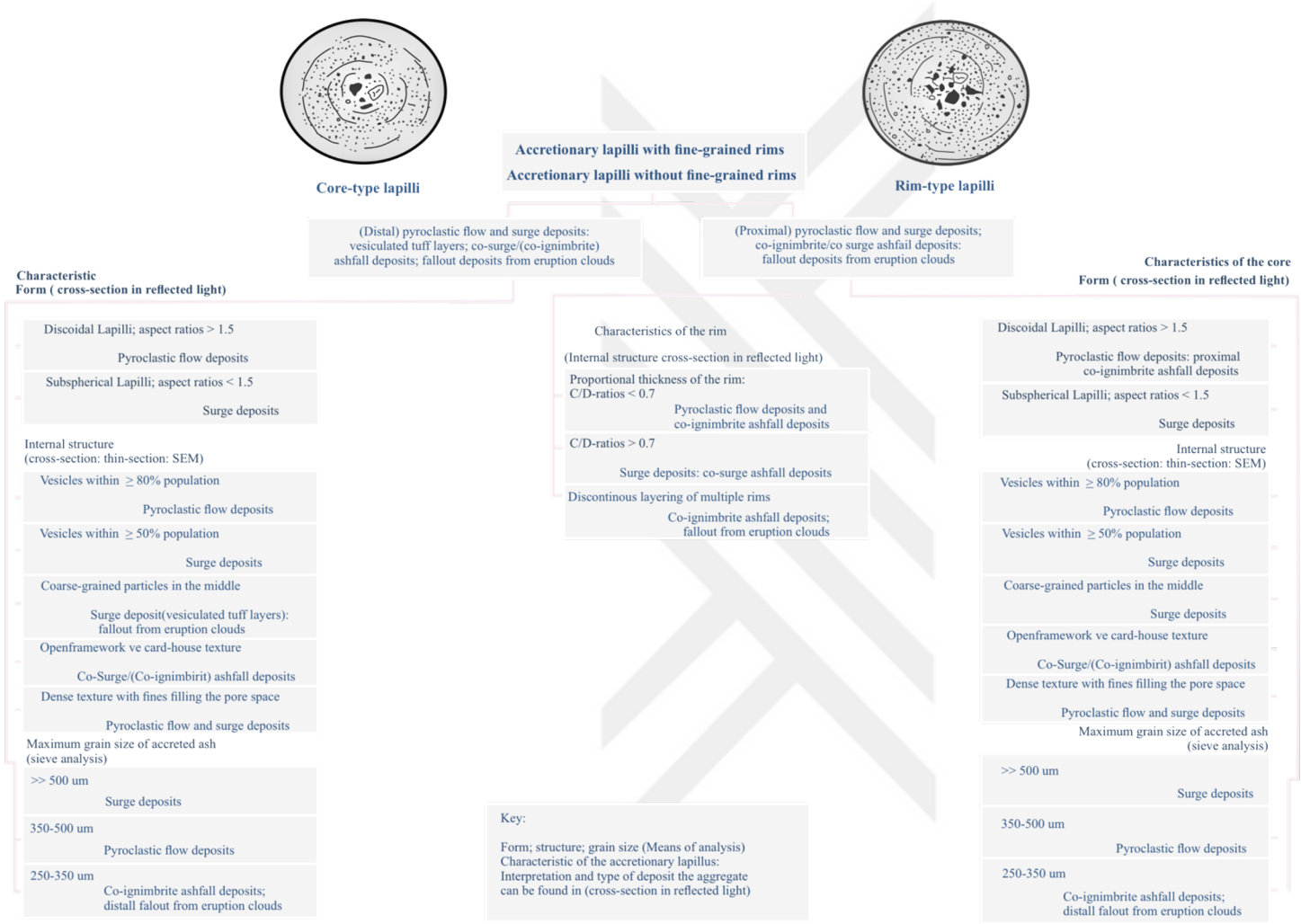

Figure 5.5 Morphological and petrographic features of acceleration lapillus types. (Conducted by Schumacher & Schimincke in 1991)

5.2 Petrographic Analysis

5.2.1 Petrographic Analysis of Location 1

The collected field samples undergo a meticulous cleaning and sorting process, employing a combination of manual techniques and specialized tools within the laboratory environment. These samples reveal a diverse assortment of solid pyroclastic components, including pumice, lithic fragments, fine particulate material, and mineral constituents. These components are embedded within a consolidated ash matrix. The pyroclastic materials are characterized by their non-welded nature, predominantly defined by a glassy matrix and a crystal content ranging from 5% to 10%. Additionally, some particles have adhered to the fine ash (Figure, 5.6). The vesicularity of these materials varies from 25% to 40%, often giving the matrix a fibrous or fluid-like appearance.

Figure 5.6 There are particles of pyroclastic material present that have not undergone welding belong to the sample from the first location (Personal archive, 2022)

The paragenesis of these materials mainly consists of glass shards, pumice fragments, and diverse minerals. Biotite, quartz, plagioclase, feldspar, and some accessory minerals (such as zircon, rutile and apatite) are discernible among these minerals. The examined materials exhibit a diverse mineral composition, encompassing pyroxene, apatite, zircon, and rutile crystals, as well as fluid and gas inclusions within subhedral and euhedral quartz. Euhedral-subhedral biotite crystals reveal the presence of zircon inclusions, while feldspar displays a similar content to quartz. Notably, the samples also contain particles like charcoal, fresh plant remains, and organic materials. At this location, there are specific features that have been altered, with deposits rich in clay (fibrous minerals) and charcoal (Figure 5.7, Figure 5.8, Figure 5.9; Figure 5.10).

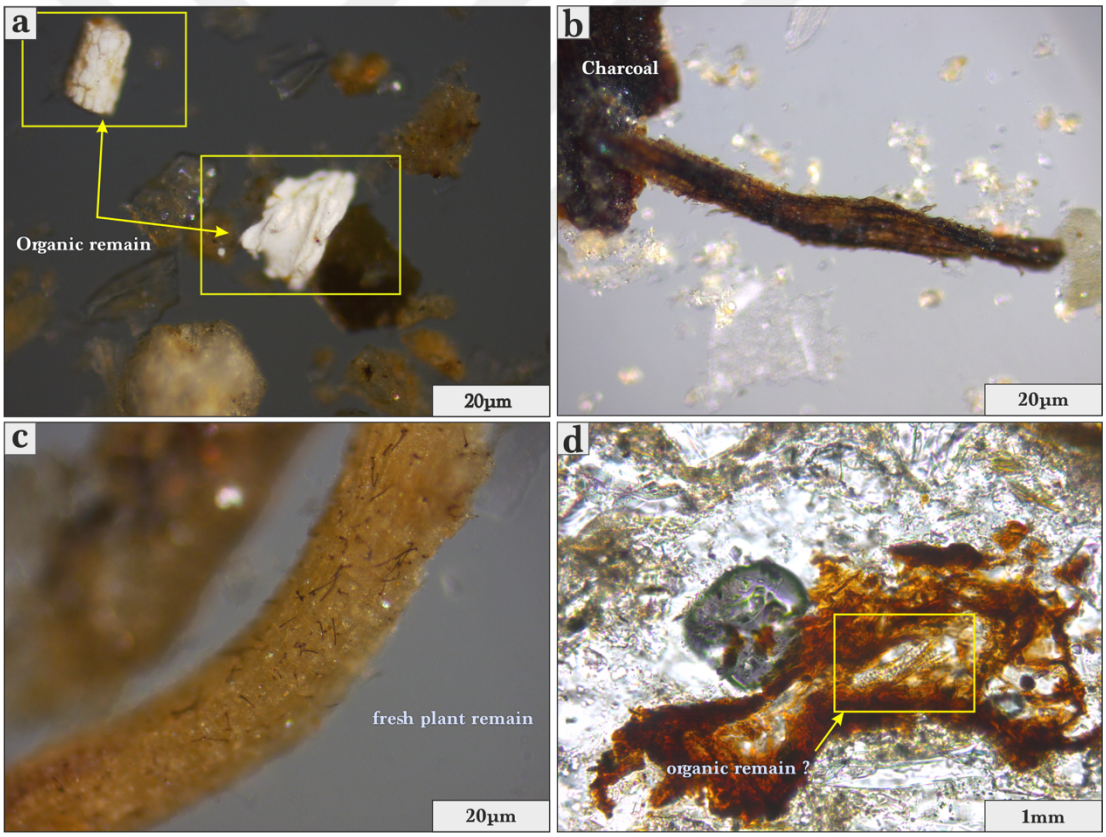

Figure 5.7 The figure displays organic materials remains. a) is organic materials, b) is charcoal, c) is fresh plant remain, and d) is plant remain under the polarizan microscope

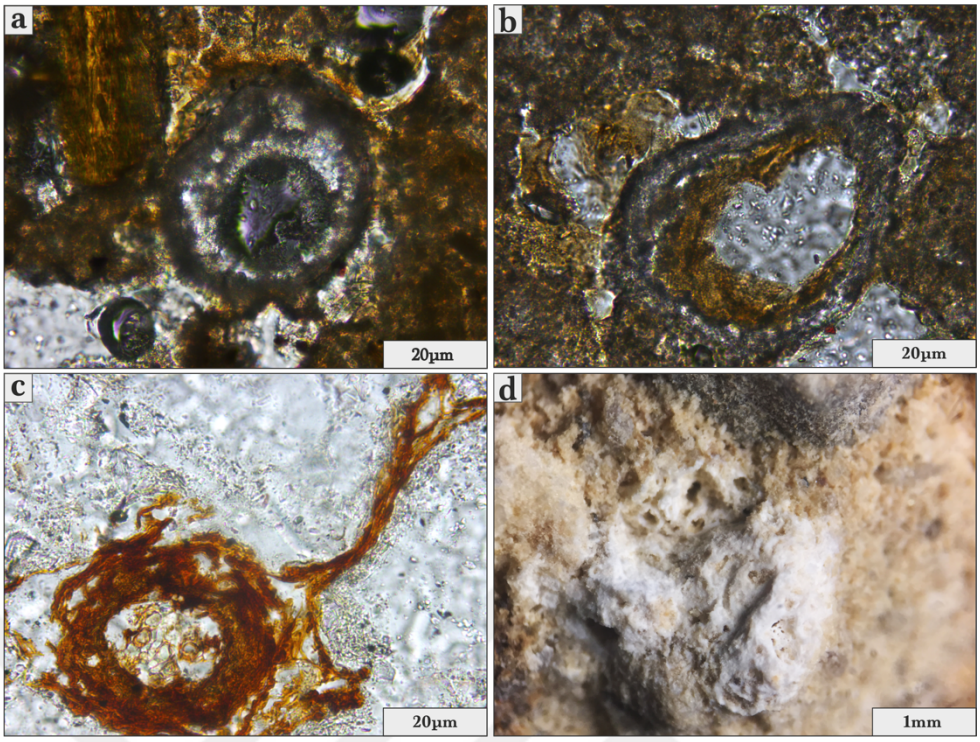

Figure 5.8 The figure shows polygonizations glass circle structure, alteration, and organic remains

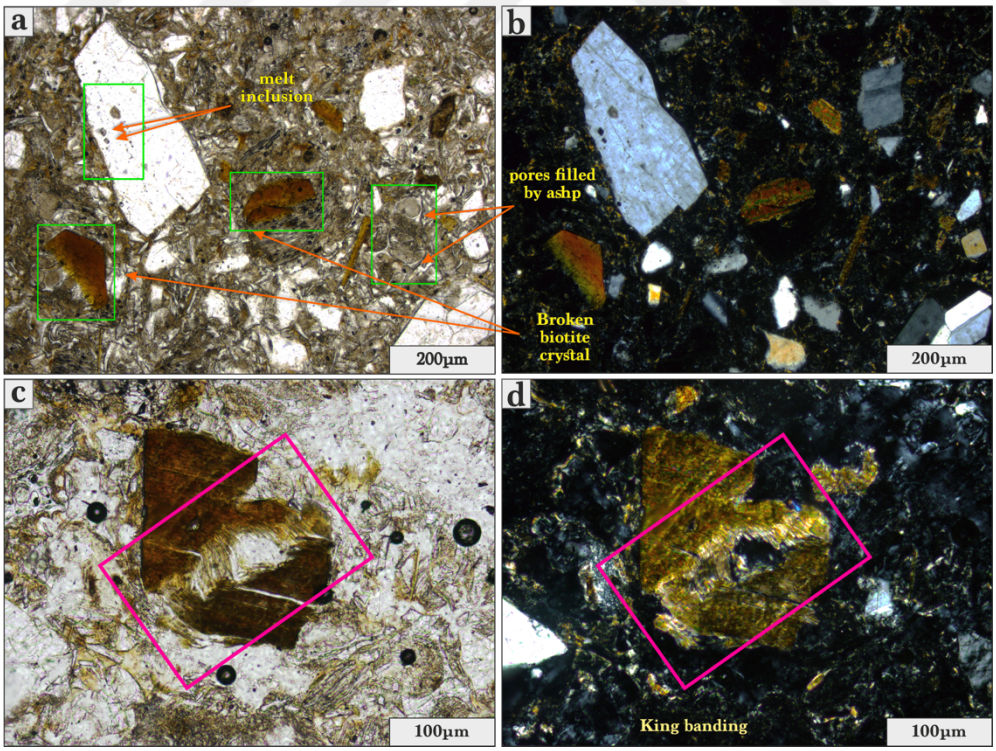

Figure 5.9 The figure shows crystal behavior during magma mixing. The upper images feature plagioclase and fractured biotite clasts, while the lower images highlight biotite clasts within the king banding.

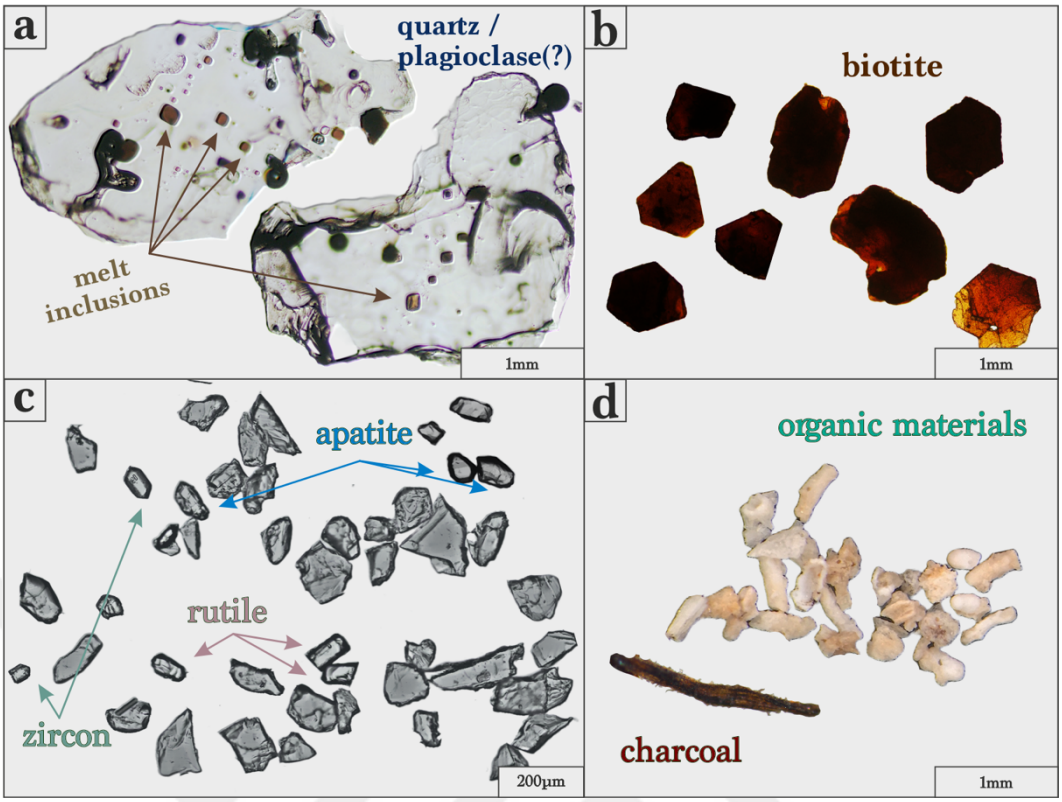

Figure 5.10 The figure displays the internal structure of pyroclastic materials; a) including a photograph of quartz morphology and inclusions, b) a figure of euhedral and anhedral biotite crystals, c) a figure of accessory minerals found in the ash, d) a figure of randomly dispersed organic materials

5.2.1.1 Lithics

Within this location, the morphological features of lithic fragments predominantly display rounded borders, indicating their formation during transportation processes (Figure, 5.11). In the matter of the lithic features examined microscopically four meticulously prepared thin sections were derived from the collected samples. Thin sections corresponding to samples 47 and 48 revealed the coexistence of pyroxene, olivine, plagioclase, and amphibole minerals. Notably, these sections exhibited distinct porphyry textures leading to their classification as trachyandesite. This specific rock specimen predominantly consists of plagioclase and feldspar minerals, observed within thin sections showcasing a zoned texture along the rim (Figure, 5.12; Figure, 5.13).

Figure 5.11 The lithic rock fragments extracted from the first location are depicted in the figure, their physical characteristics including size and morphology (Personal archive, 2022)

The presence of hornblende, biotite, and olivine crystals further complements the mineral composition. Notably, the plagioclase crystals exhibit subhedral to euhedral morphology. The occurrence of sieved and oscillatory-zoned textures, along with the presence of perlitic cracks, is attributed to magma mixing during crystallization.

5.2.1.2 Pumice

In this location, pumices exhibit a diverse array of morphologies, encompassing vesicular and non-vesicular forms, tubular, frothy, and micro pumices. These categories are presented in greater detail through distinct thin-section and macro images provided below (Figure, 5.14).

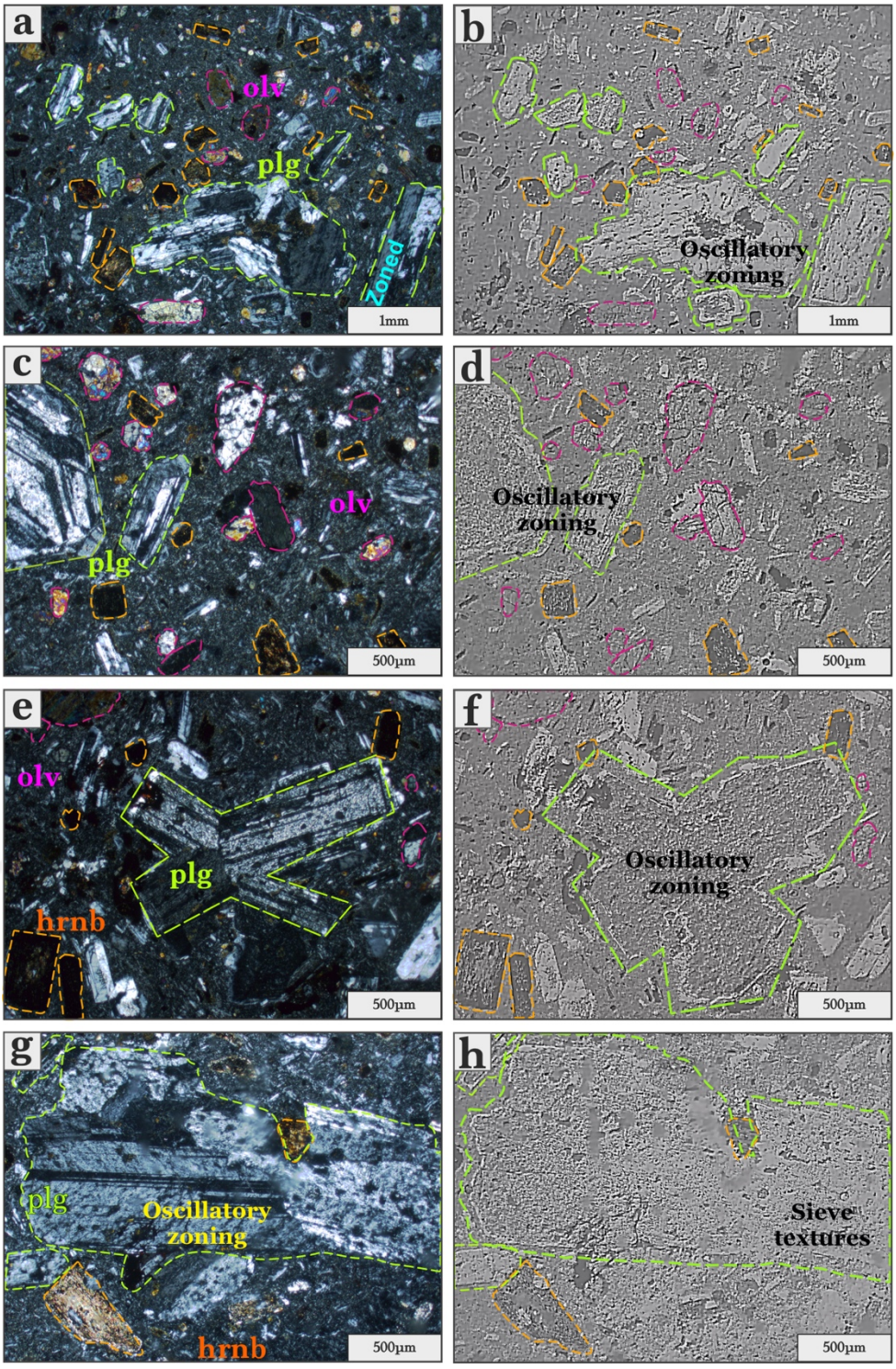

Figure 5.12 Left Images (ppl); Right Images (xpl, edited with a black scatter effect). The figure shows microscopic lithic material views; a and b) Display oscillatory zoning in plagioclase (plg), zoned plagioclase, subhedral olivine, euhedral alternating hornblende; c and d) Show oscillatory zoning, alternating euhedral hornblende, and a microcrystalline matrix; e and f) Depict oscillatory zoning and growing plagioclase, subhedral olivine, and euhedral alternating hornblende; g and h) Exhibit oscillatory zoning and sieve textures in plagioclase crystals, along with subhedral-altered hornblende

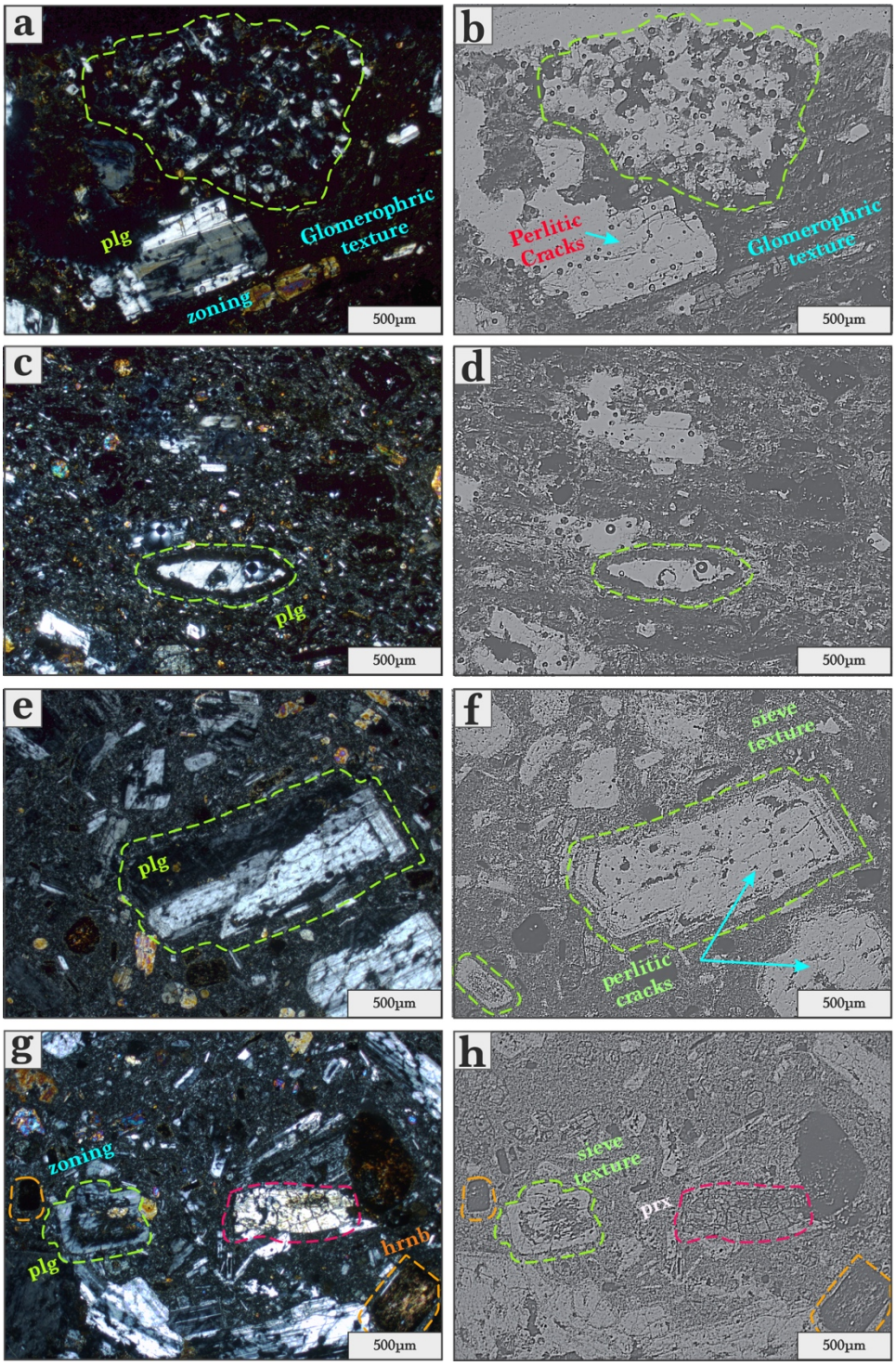

Figure 5.13 Left Images (ppl); Right Images (xpl, edited with a black scatter effect). The figure shows microscopic lithic material views; a and b) Show glomeroporphyritic texture, perlitic cracks on plagioclase (plg), and glassy microcrystalline matrix; c and d) Feature zoned plagioclase (plg) within the microcrystalline matrix; e and f) Show growing zoning, sieve-textured plagioclase (plg), random plagioclase clasts, subhedral olivine, and hornblende in microcline plagioclase matrix; g and h) Exhibit sieve textures in plagioclase (plg) crystals and subhedral-altered hornblende.

Figure 5.14 Macro-scale views of pumice grains with various morphological features extracted from massive pyroclastic materials (Personal archive, 2022)

Several notable observations emerge from the collected samples. Firstly, the presence of ash-filled vesicles is apparent, indicating the entrapment while reworked during the transportation. Furthermore, certain vesicles are intricately filled with mineral deposits, underscoring the complex interplay between magmatic processes and mineral precipitation. Additionally, the occurrence of brittle fractures is noteworthy, signifying instances of brittle deformation during conduit vent dynamics. These fractures provide valuable insights into the dynamic processes shaping the volcanic conduit. Moreover, the presence of stretching structures is evident, particularly in elongated vesicles found within tube pumices. These structures offer compelling evidence of mechanical deformation, shedding light on the complex conditions that the volcanic materials experienced. To illustrate, a distinct pumice specimen exhibits intriguing features. Also, pumice found within the section showcases remarkably thin bubble walls alongside localized accumulations of fine ash. The presence of bubble coalescence becomes evident, as breached bubble walls converge to form larger, irregularly shaped vesicles (Figure, 5.15; Figure, 5.16). When examining micro pumices, the figure shows the formation of all pore types during eruption (Figure, 5.17).

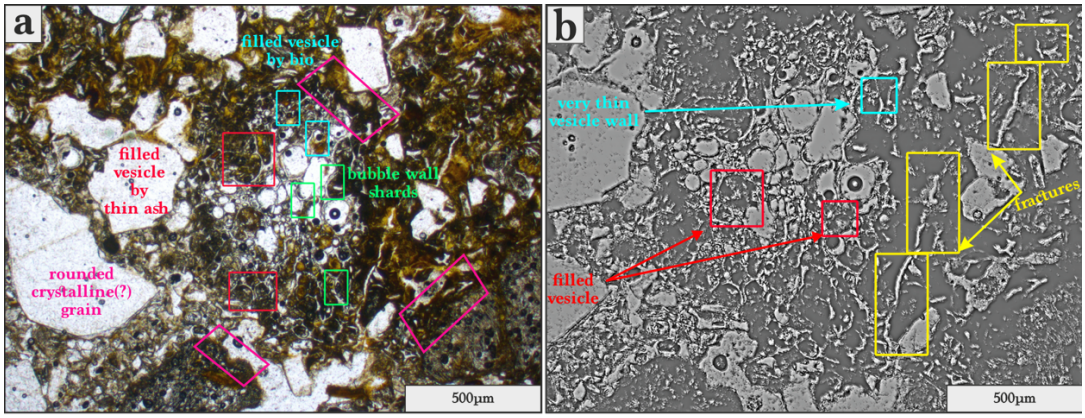

Figure 5.15 This image displays pumice fragments with granular vesicles. The vesicles contain fine ash and biotite crystals, and some of these vesicles have caused dynamic fractures. Additionally, there are rounded crystalline grains present

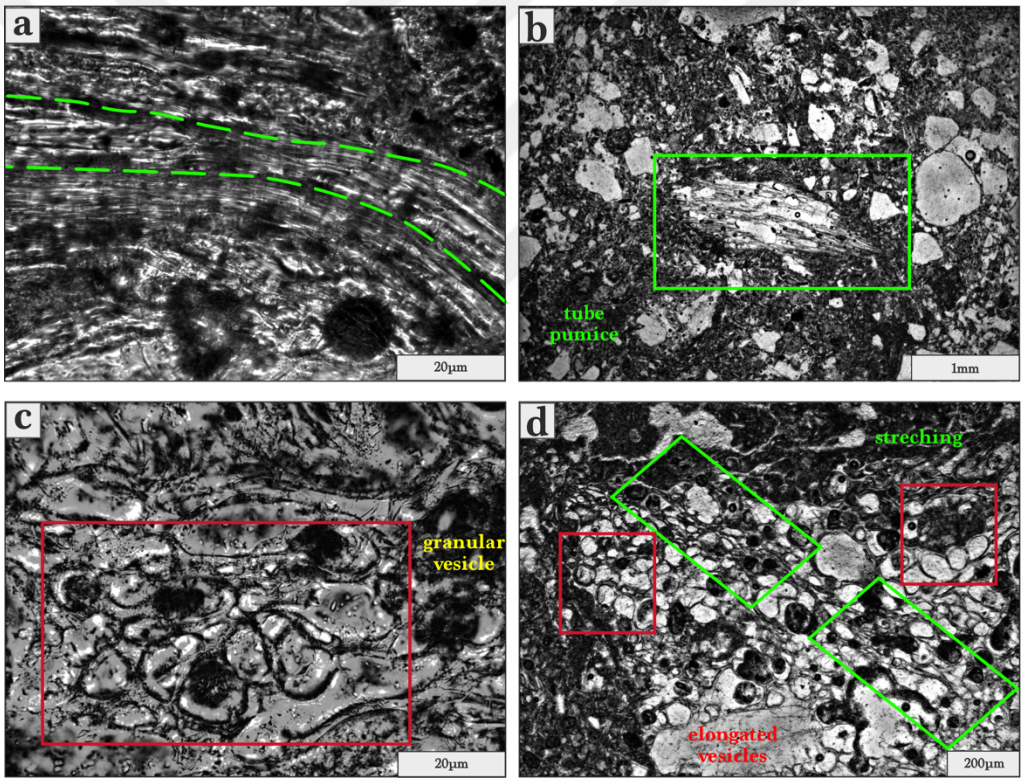

Figure 5.16 Microscopic views of pumice materials. This figure reveals of pumice some parts has elongated vesicles on the contrary the other parts have granular vesicles, and these textures reason is showing the dynamics of the magmatic eruption

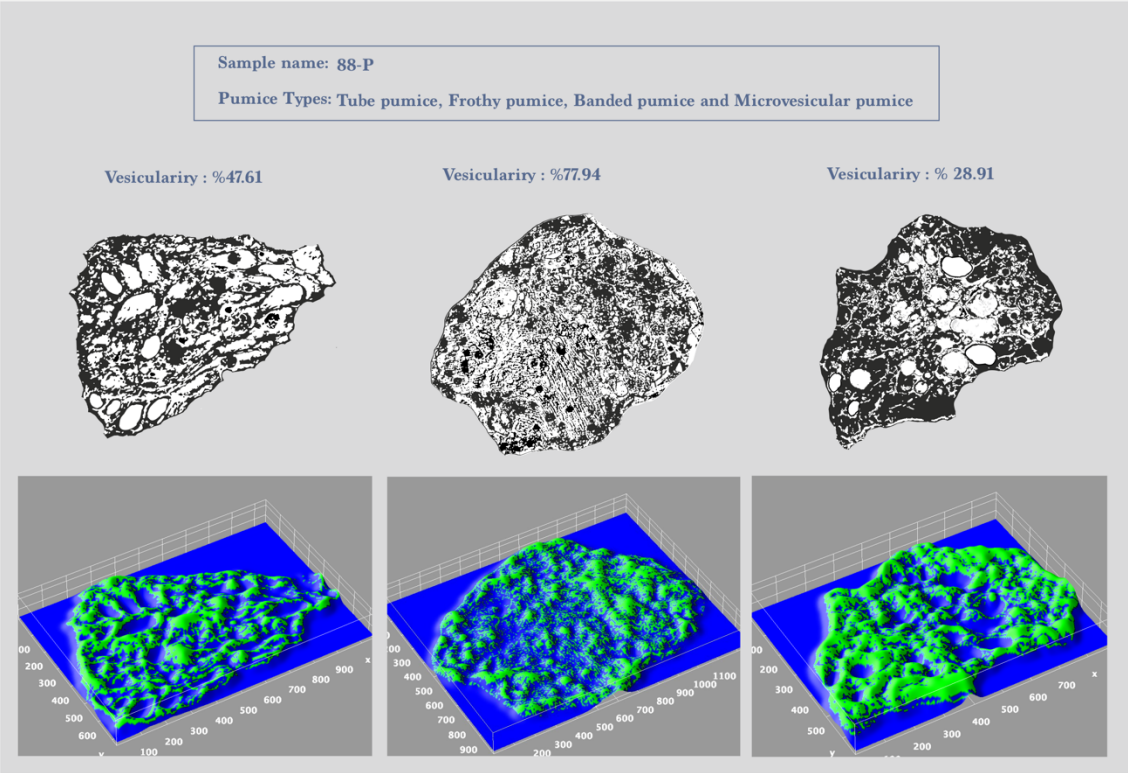

Figure 5.17 Microscopic views of pumice materials

5.2.1.3 Acceleration Lapilli

The accretionary lapilli exhibits distinctive characteristics, notably featuring a substantial and denser outer rim distinguished by an augmented concentration of fine grains in its outer layers. Encasing a central core with a coarser grain structure, the lapilli's transition towards the rim lacks gradual progression. The interior of these lapilli manifests significant deformation, indicative of dynamic processes at play. In the context of this thin section, a composition comprising glass, biotite, plagioclase, magnetite, and accessory crystals has been identified within the lapilli segment (Figure, 5.18). Furthermore, this section revealed a distinct texture known as 'rim type-multiple-without core,' as described in studies conducted by Schumacher & Schimincke in 1991. This distinctive texture suggests the reworking of ash particles, implying an association with water influence in their formation.

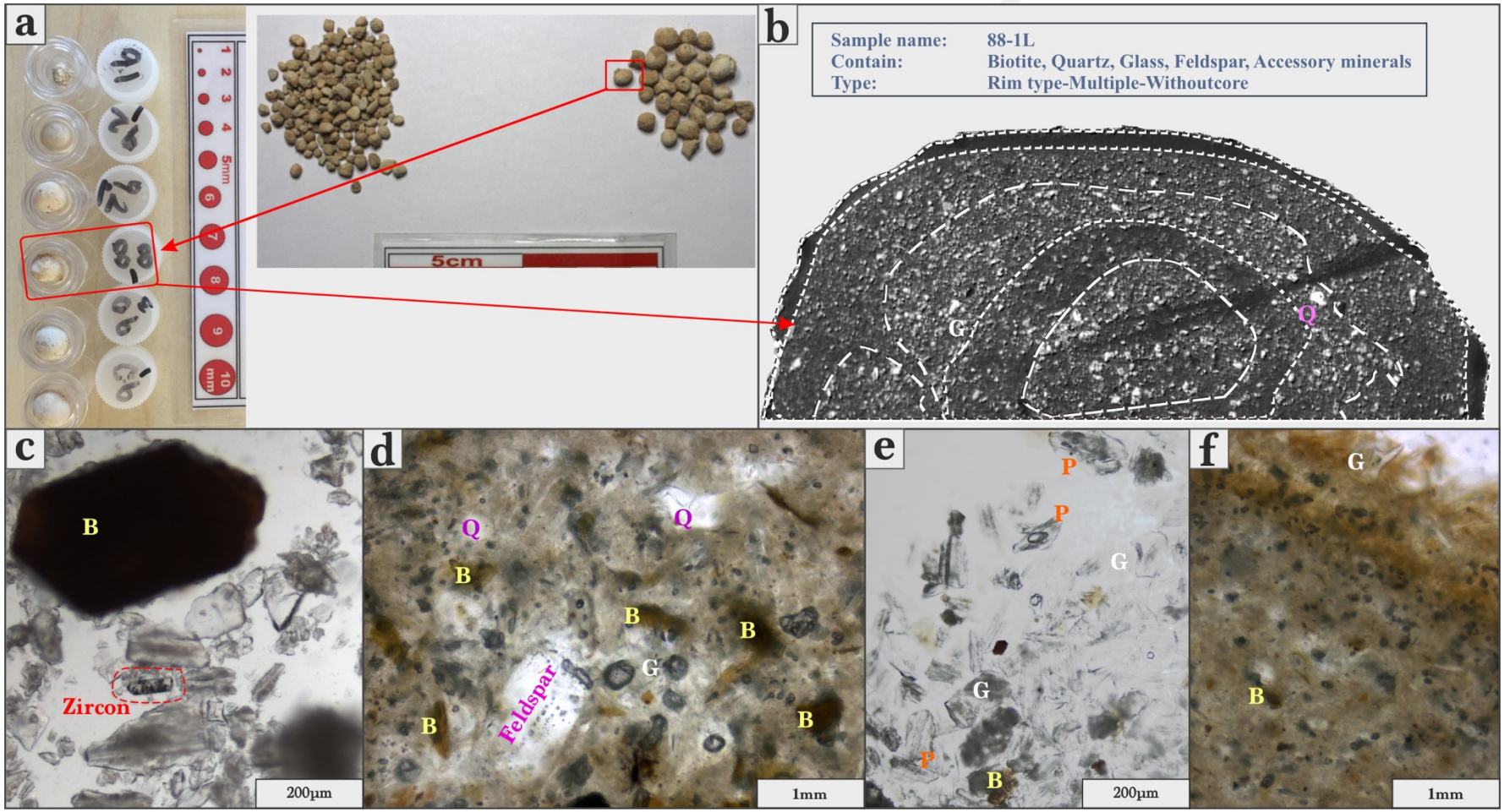

Figure 5.18 The figure includes internal structure on a thin section, mineralogical content under a binocular microscope, and a macro view with a scale for measurement samples from location 1

5.2.2 Petrographic Analysis of Location 2

In the collected field a diverse amalgamation of solid pyroclastic components is evident, inclusive of pumice, lithic fragments, fine particulate material, and mineral constituents, all ensconced within an unconsolidated ash matrix (Figure, 5.19). These pyroclastic materials are characterized by their unwelded nature, predominantly characterized by a glassy gel matrix and a crystal content ranging from 5% to 10%. The vesicularity of these materials exhibits a range spanning from 30% to 50%. The paragenesis of these materials predominantly encompasses glass shards, pumice fragments, and various minerals. Biotite, quartz, plagioclase, and feldspar crystals are discernible among these minerals. The examined materials exhibit a diverse mineral composition, encompassing pyroxene, apatite, zircon, and rutile crystals, as well as fluid and gas inclusions within subhedral and euhedral quartz. Euhedral-subhedral biotite crystals reveal the presence of zircon inclusions, while feldspar displays a similar content to quartz (Figure, 5.20; Figure, 5.21; Figure, 5.22; Figure, 5.23).

Figure 5.19 There are particles of pyroclastic material present that have not undergone welding belong to the sample from the second location (Personal archive, 2022)

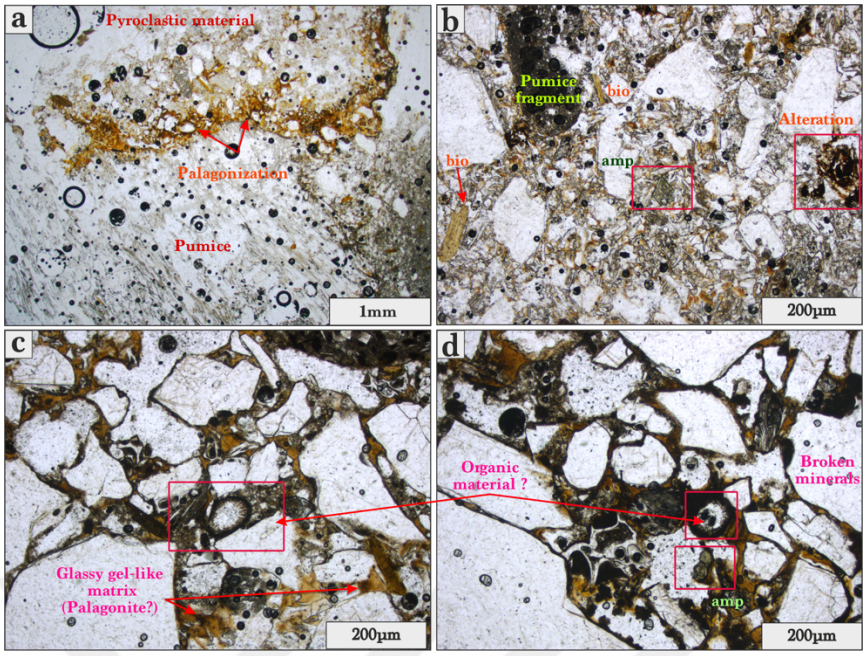

Figure 5.20 a) The yellow crystal-rich zone in this image reveals the presence of regionally crystal-rich zones between ash and pumices, highlighting variations in depositional conditions. b) This image displays euhedral amphibole and biotite crystals, broken pumice fragments, as well as quartz and plagioclase minerals in a silica gel matrix. c) and d) A close-up view of the crystal-rich zone is depicted in this image.

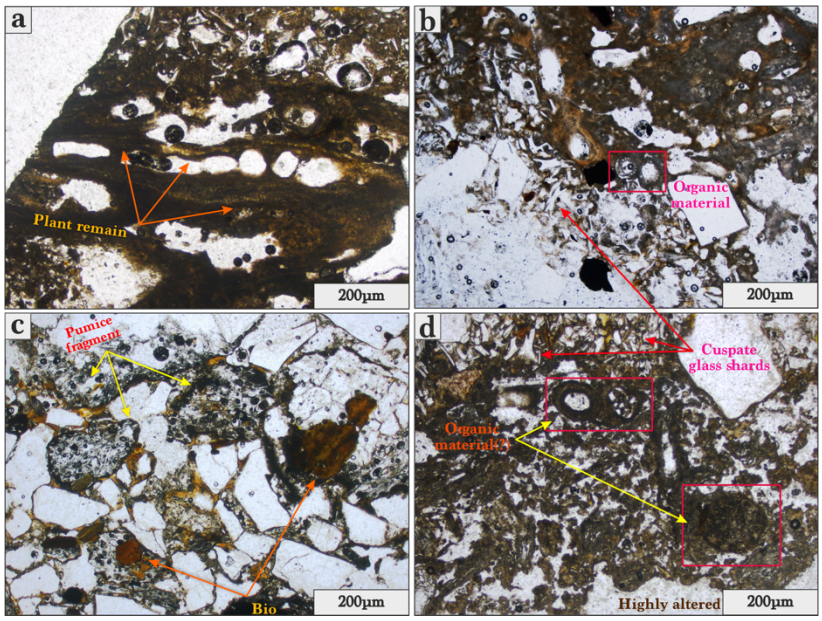

Figure 5.21 a) This image shows the plant remaining in the pyroclastic fragment. b) This image displays a cuspate glass shards zone and silica gel-like matrix. c) Rounded pumice fragments and broken biotite clast within the silica gel-like matrix. d) In this thin section has highly altered fragments which include organic materials.

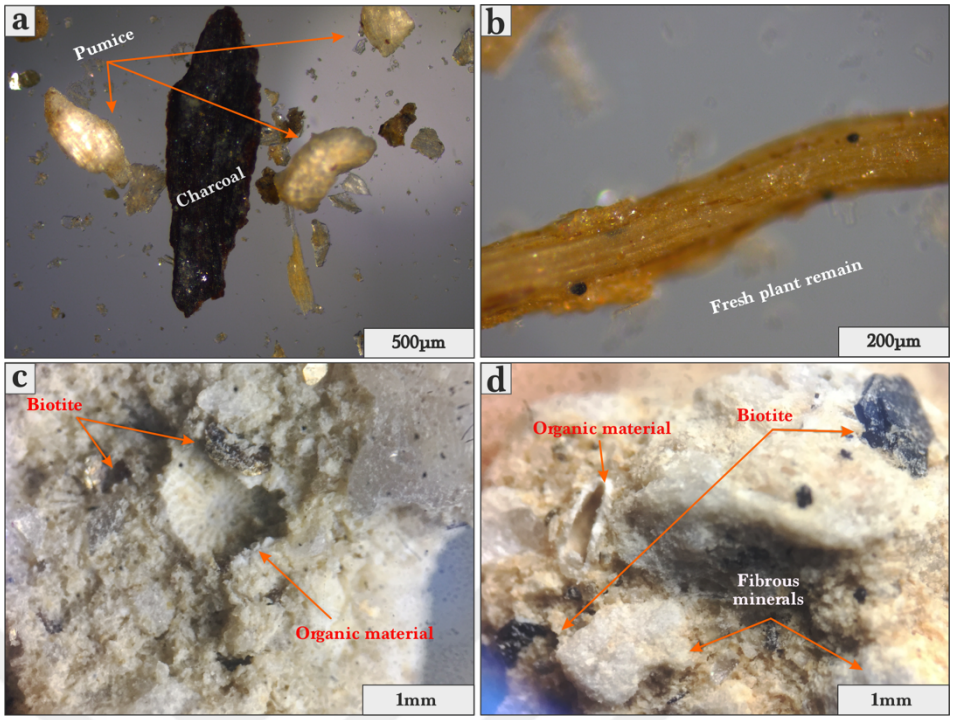

Figure 5.22 The figure displays organic materials remains. a) charcoal, b) fresh plant remains, c) is marine shell, and d) fibrous minerals surrounded shell

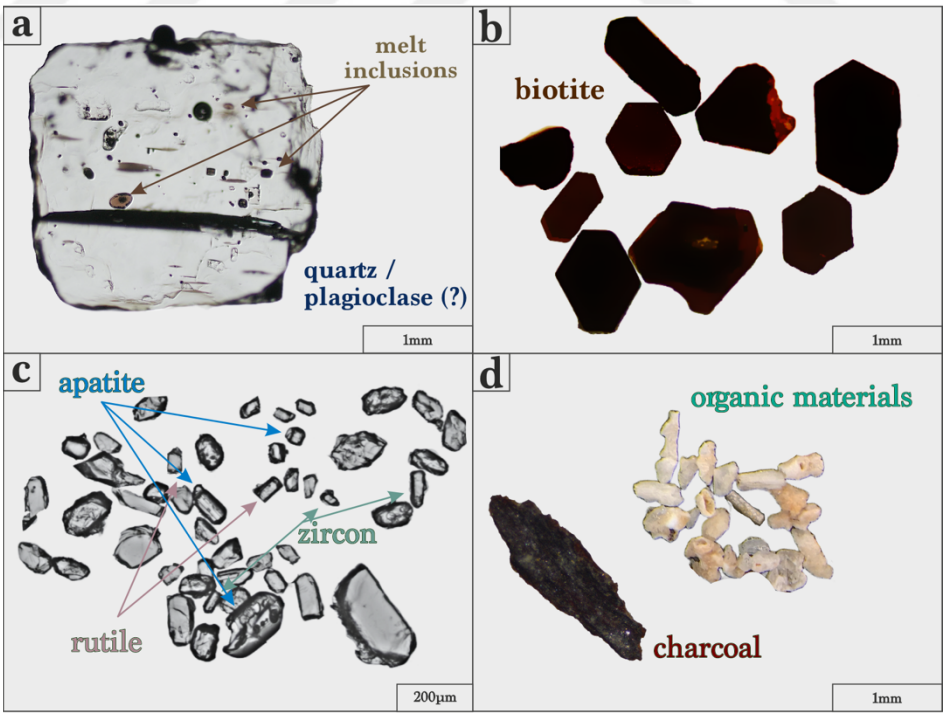

Figure 5.23 The figure displays the internal structure of pyroclastic materials; a) including a photograph of quartz morphology and inclusions, b) a figure of euhedral and anhedral biotite crystals, c) a figure of accessory minerals found in the ash, d) a figure of randomly dispersed organic materials

5.2.2.1 Lithics

The seven rock samples examined under the microscope were meticulously prepared. It was observed that the lithic fragments were sharper when compared to the first location (Figure, 5.24). Thin sections corresponding to samples 44 and 57 revealed the presence of pyroxene, sub-euhedral plagioclase, and feldspar minerals, forming a thin sieve with a zoned texture along the rim, as well as olivine minerals. Attributes such as porphyry texture, glomerophyric texture, and flow banding were also identified, leading to their classification as *trachyandesite*. Likewise, in the thin section corresponding to sample 45, the presence of zoned plagioclase, flow banding, and amphibole minerals was noted. In sample 46, feldspar minerals exhibited a thin sieve with a zoned rim texture alongside discernible olivine minerals, resulting in their classification as *andesite*. Sample 53, characterized by significant hydrothermal alteration, displayed zoned plagioclase and pilotaxitic textures, ultimately classifying it as trachyte. Conversely, in sample 56, the presence of fresher minerals with identical compositions led to its classification as *trachyte*. The mineral composition of sample 54 encompassed sanidine, biotite, and pyroxene, resulting in its classification as *basaltic trachyandesite*. Moreover, within the sieve texture, the matrix revealed dark blobs that compose the sieve appearance, indicative of melt inclusions formed during rapid crystal growth, possibly skeletal. Subsequent slower growth phases resulted in the closure of spaces between skeletal projections, and entrapping liquid (Figure, 5.25; Figure, 5.26).

5.2.2.2 Pumice

The prominent macroscopic distinction observed in the pumices at this site is their exceptionally pristine and white appearance, setting them apart as the cleanest and whitest specimens across the peninsula. Additionally, a noteworthy characteristic is that the lithic pumice here remains without ash coated (Figure, 5.27). The thin sections obtained from this location's notable features include the presence of fractures in juvenile pumice fragments over the phenocrysts as well as elongated and irregular vesicles, signifying their formation during the ascent of magma. Some minerals are

affected by shear stress, and this results there some broken and/or stretched minerals (e.g., plagioclase). Also, in this location, there is present to mostly euhedral feldspar crystals embedded in the matrix (Figure, 5.28; Figure, 5.29; Figure, 5.30; Figure, 5.31).

Figure 5.24 The lithic rock fragments extracted from location 2 are depicted in the figure, and their physical characteristics include size and morphology (Personal archive, 2022)

5.2.2.3 Acceleration Lapilli

The accretionary lapilli is characterized by a substantial, denser outer rim consisting of an increased concentration of fine grains in the outer layers. The lapilli encompass a central core with a coarser grain structure, which exhibits a gradual transition toward the rim (Figure, 5.32). The interior of the lapilli displays pronounced deformation. The composition comprising glass, biotite, plagioclase, and accessory crystals was identified. Furthermore, this section revealed a distinct texture known as 'rim type-multiple-without core,' as described in studies conducted by Schumacher and

Schimincke in 1991. This texture is indicative of reworked ash particles and suggests an association with water influence.

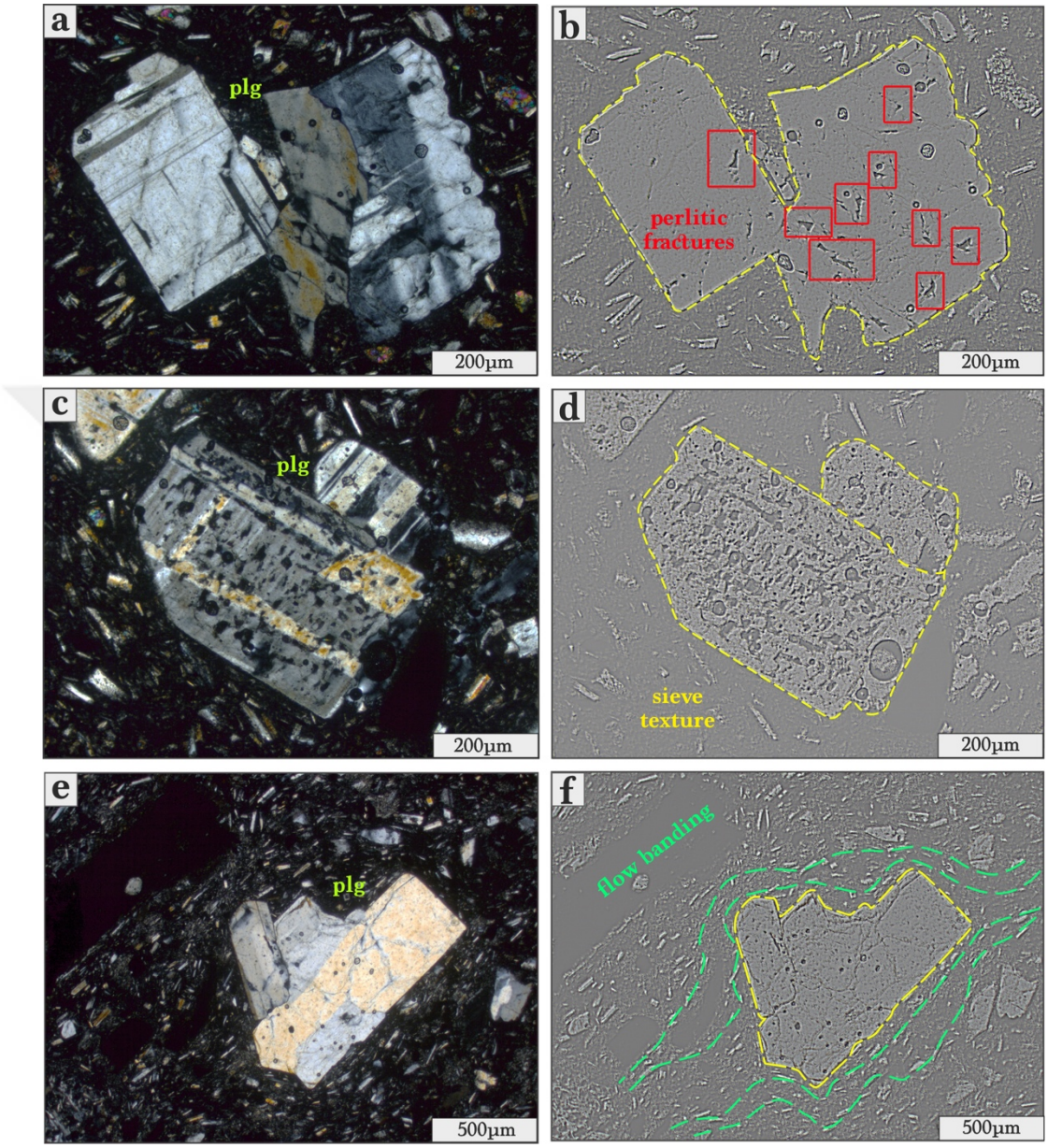

Figure 5.25 Left Images (ppl); Right Images (xpl, edited with a black scatter effect); The figures display microscopic views: a) perlitic fractures, b) sieve texture, c) flow banding

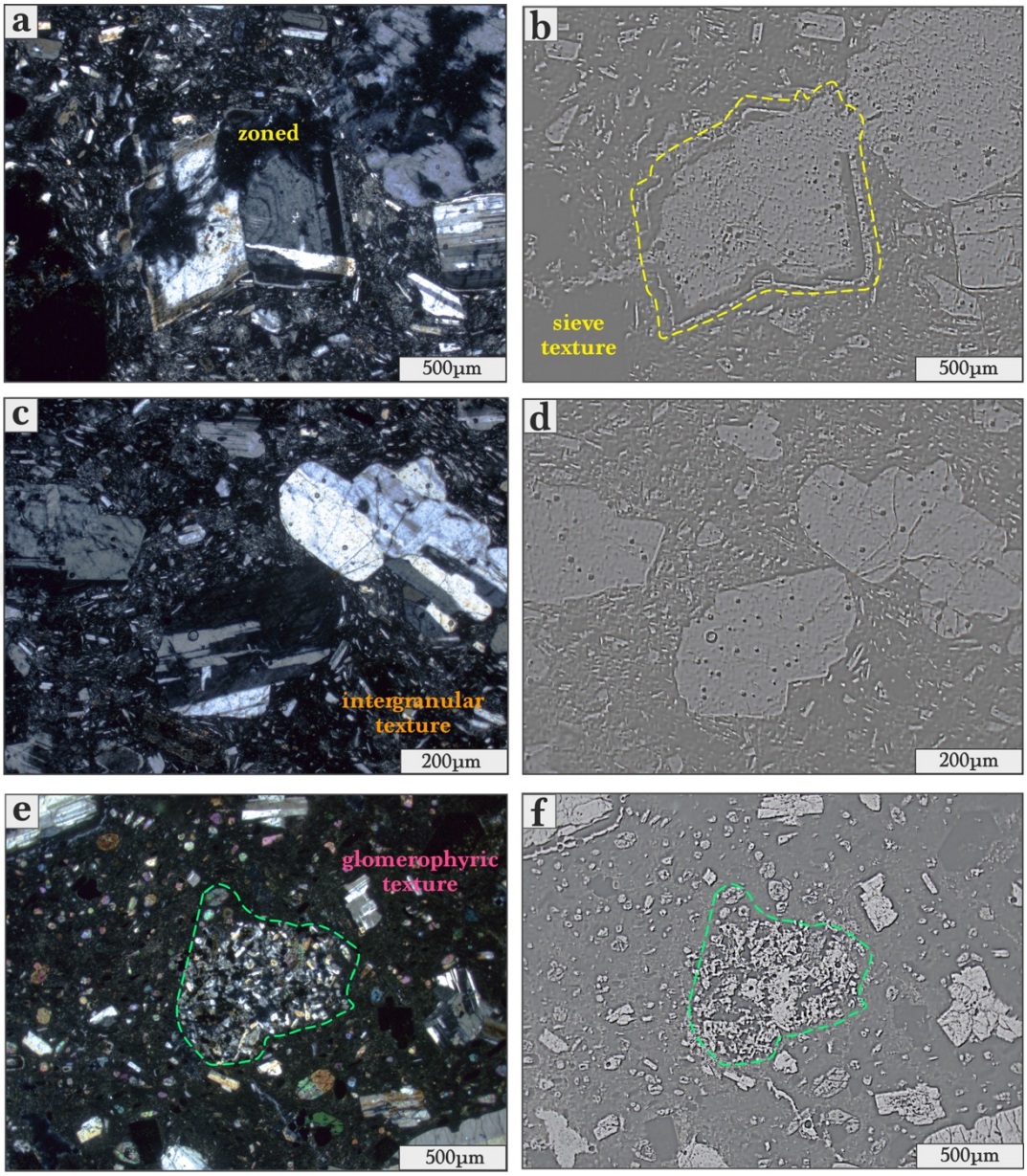

Figure 5.26 Left Images (ppl); Right Images (xpl, edited with a black scatter effect); The figures display microscopic views: a) sieve fractures, b) intergranular texture, c) glomerophyric texture

Figure 5.27 Macro-scale views of pumice grains with various morphological features extracted from massive pyroclastic materials (Personal archive, 2022)

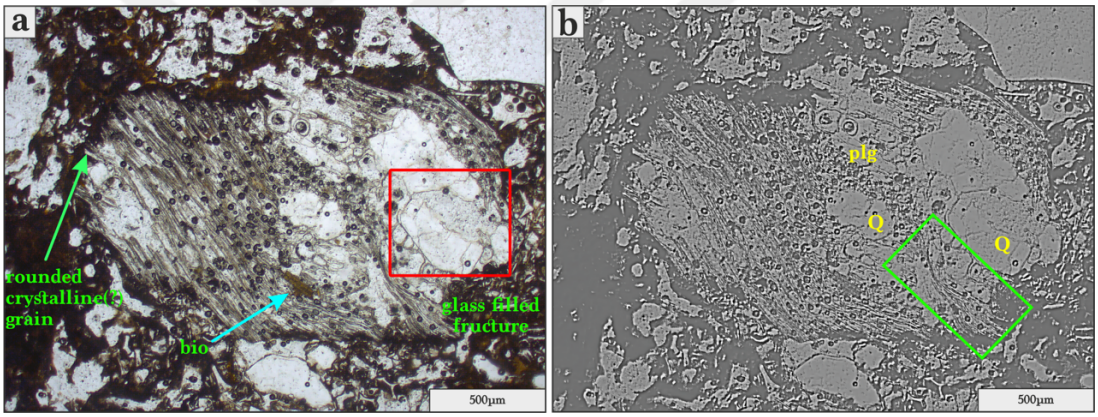

Figure 5.28 Microscopic views of pumice materials. This image showcases biotite-quartz clasts and mineral-filled fractures within a rounded, tubular pumice fragment. Additionally, the image reveals stretched and highly irregular vesicles inside this tubular pumice

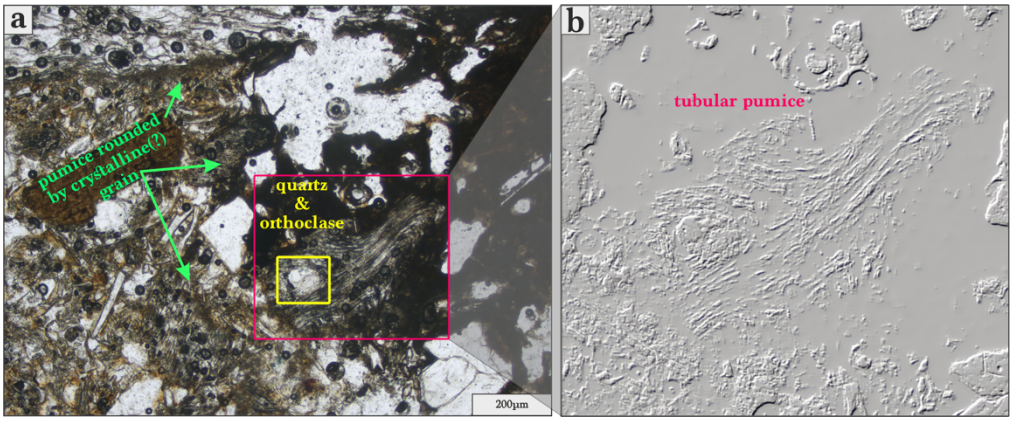

Figure 5.29 Microscopic views of pumice materials. Within this pyroclastic fragment, you can observe a subhedral biotite clast, bubble wall glass shard, plagioclase, and quartz crystals. The image also features a stretched and highly irregular vesicle pumice, highly altered pumices, and rounded pumices

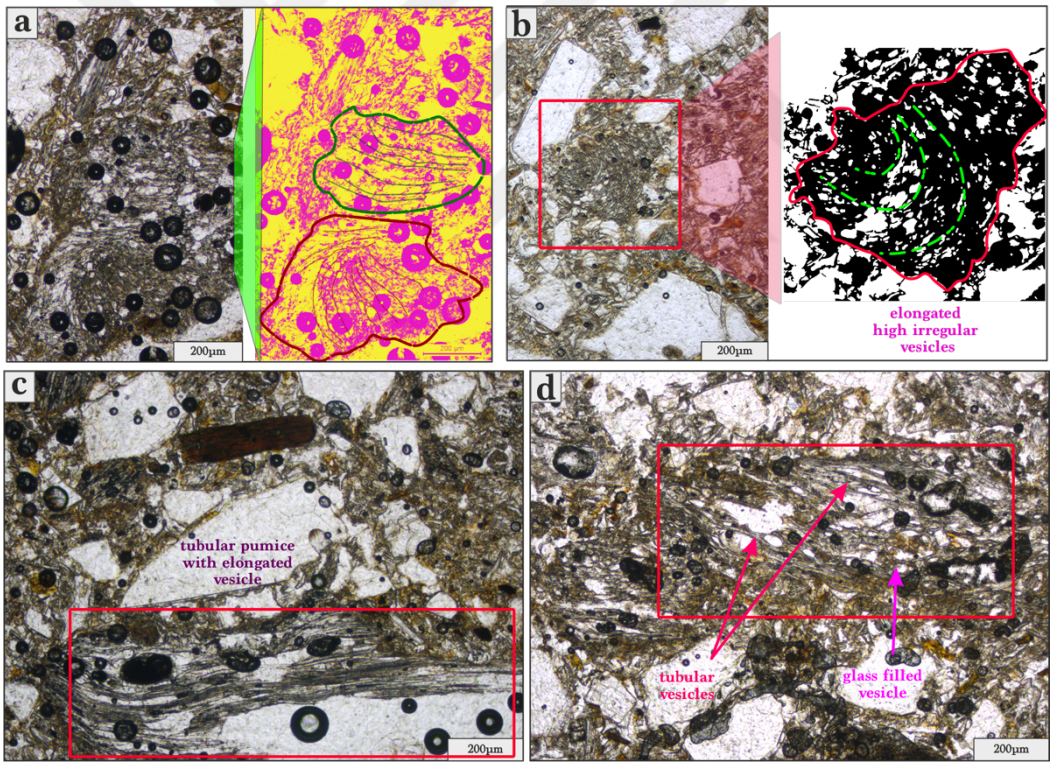

Figure 5.30 Microscopic views of pumice materials. a) Various pumices with distinct elongated vesicles are displayed in this image. b) This image focuses on a pumice fragment with elongated highly irregular vesicles. c) The image presents a tubular pumice with elongated vesicles. d) Within this tubular pumice fragment, there are glass-filled vesicles

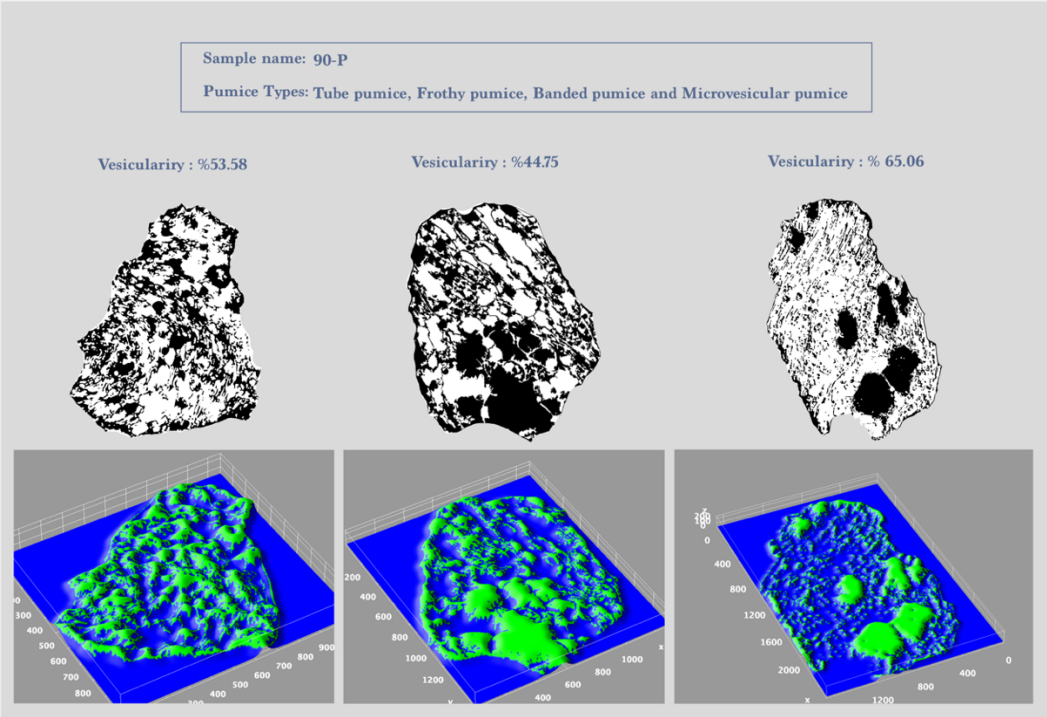

Figure 5.31 Microscopic views of pumice materials

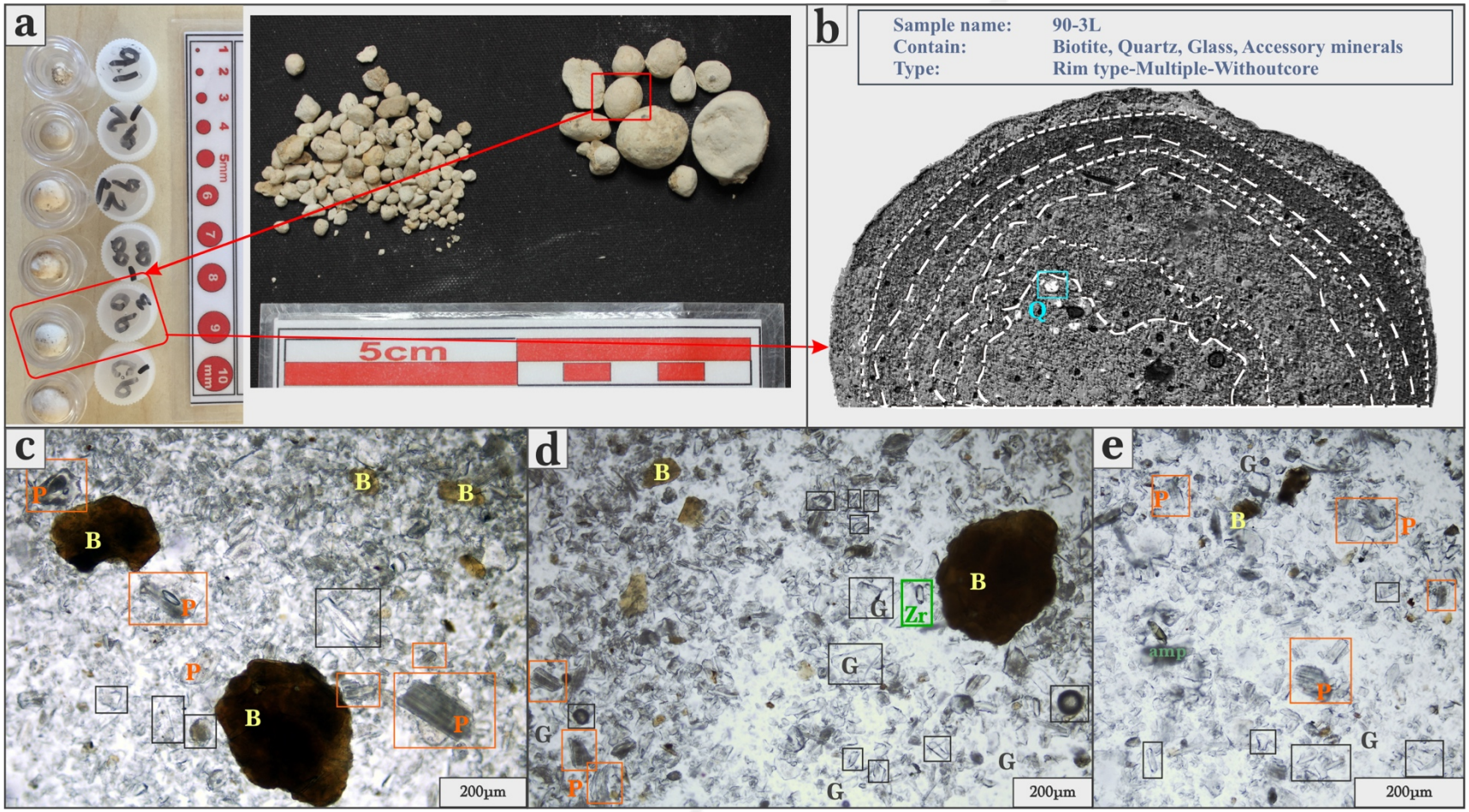

Figure 5.32 The figure includes internal structure on a thin section, mineralogical content under a binocular microscope, and a macro view with a scale for measurement samples from location 2

5.2.3 Petrographic Analysis of Location 3

The acquired field samples resemble the other locations, and these pyroclastic materials are predominantly characterized by an ash-coated glassy gel matrix (Figure, 5.33) and a crystal content ranging from 5% to 10%. The vesicularity of these materials exhibits a range spanning from 30% to 50%. The paragenesis of these materials resembles the other location encompassing glass shards, pumice fragments, biotite, quartz, plagioclase, and feldspar crystals. Likewise, examined materials exhibit a diverse mineral composition, encompassing pyroxene, apatite, zircon, and rutile crystals, as well as fluid and gas inclusions within subhedral and euhedral quartz; euhedral-subhedral biotite crystals reveal the presence of zircon inclusions, while feldspar displays a similar content to quartz (Figure, 5.34; Figure, 5.35; Figure, 5.36; Figure, 5.37).

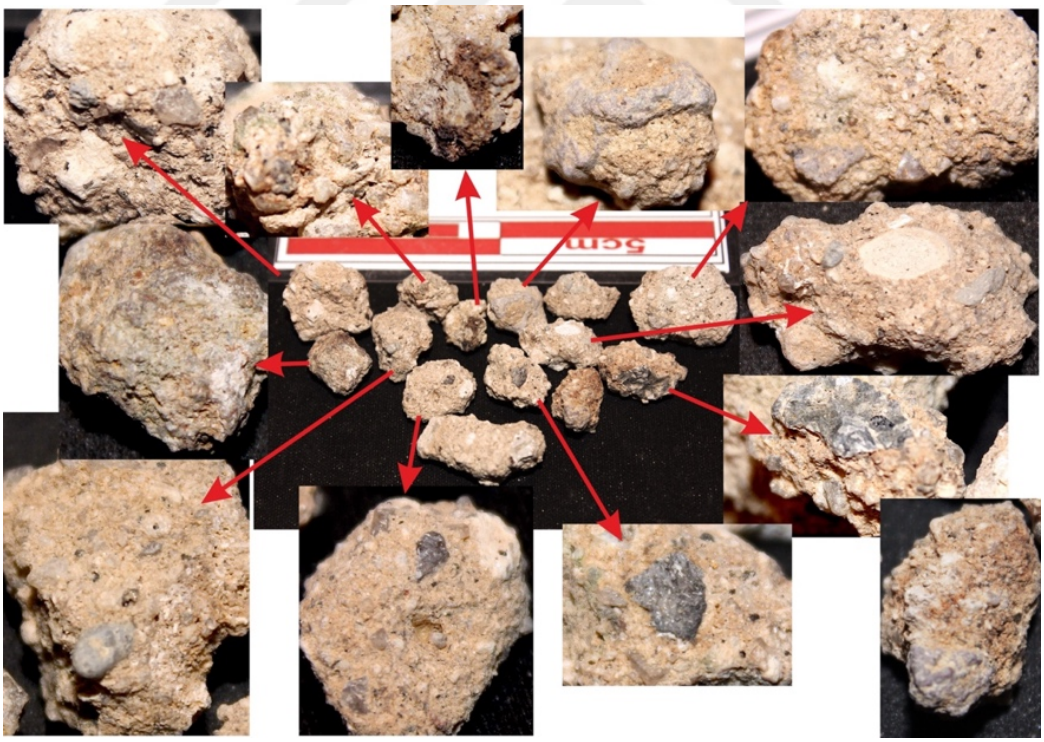

Figure 5.33 There are particles of pyroclastic material present that have not undergone welding belong to the sample from the third location (Personal archive, 2022)

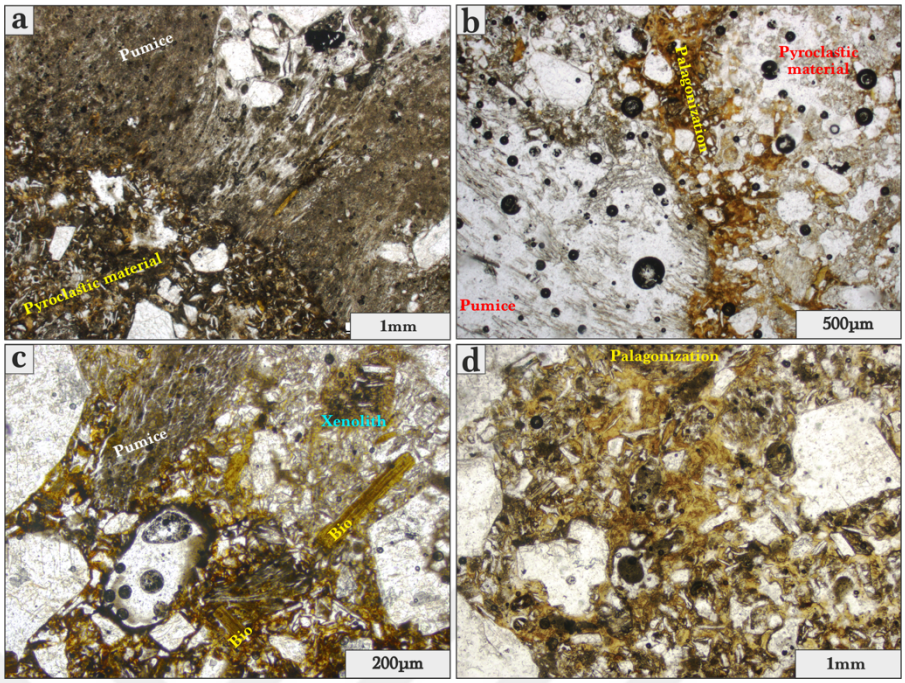

Figure 5.34 The figure expertly illustrates the effects of water on ignimbrite deposits, showcasing how infiltrating fluids interact with rock or sediment, leading to various diagenetic changes

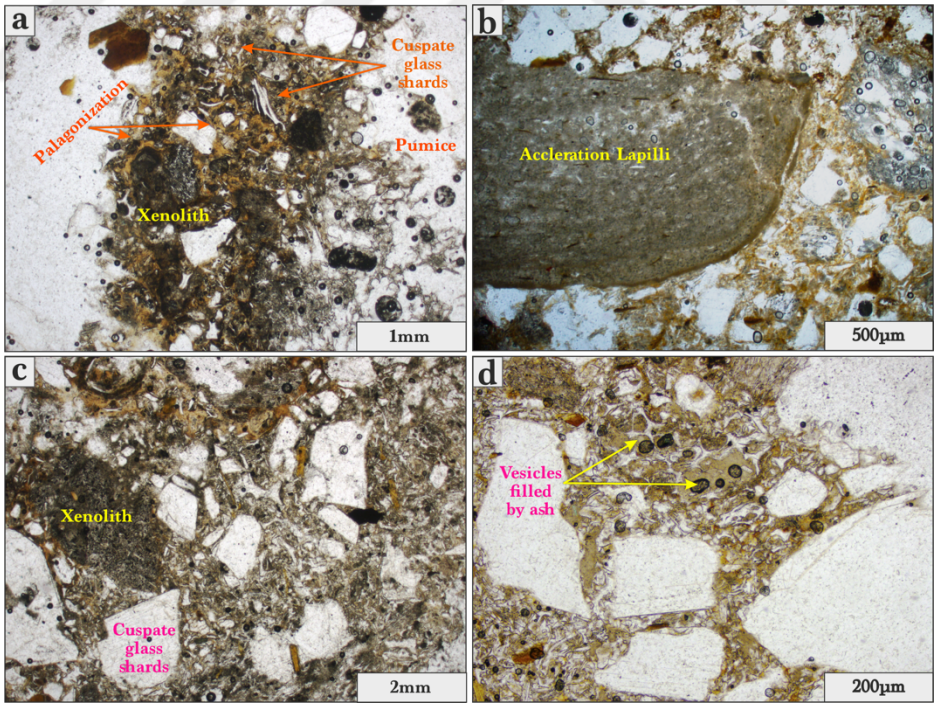

Figure 5.35 a) Thin section of pyroclastic material showing palagonitization zone. b) Alteration effects on acceleration lapilli fragments in pyroclastic material. c) The focus is on the various components within pyroclastic material. d) Vesicle-filled pyroclastic material with a glassy matrix

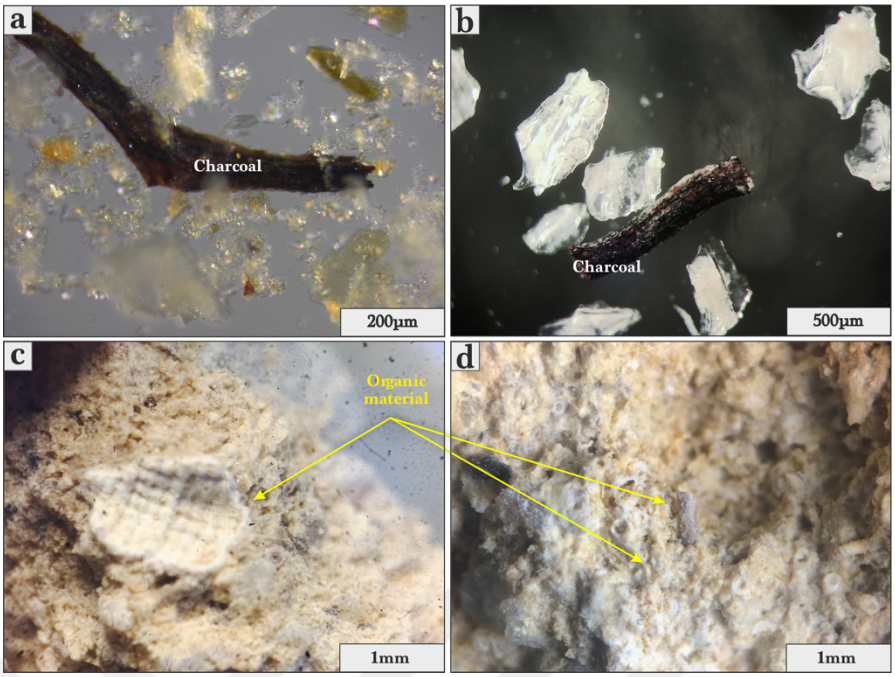

Figure 5.36 a) Detailed charcoal fragment analysis under binocular microscope b) Presents an in-depth analysis of a charcoal fragment under a binocular microscope. c) Macroscopic view of marine shell fragment d) Worm like organic material surrendered by clay minerals

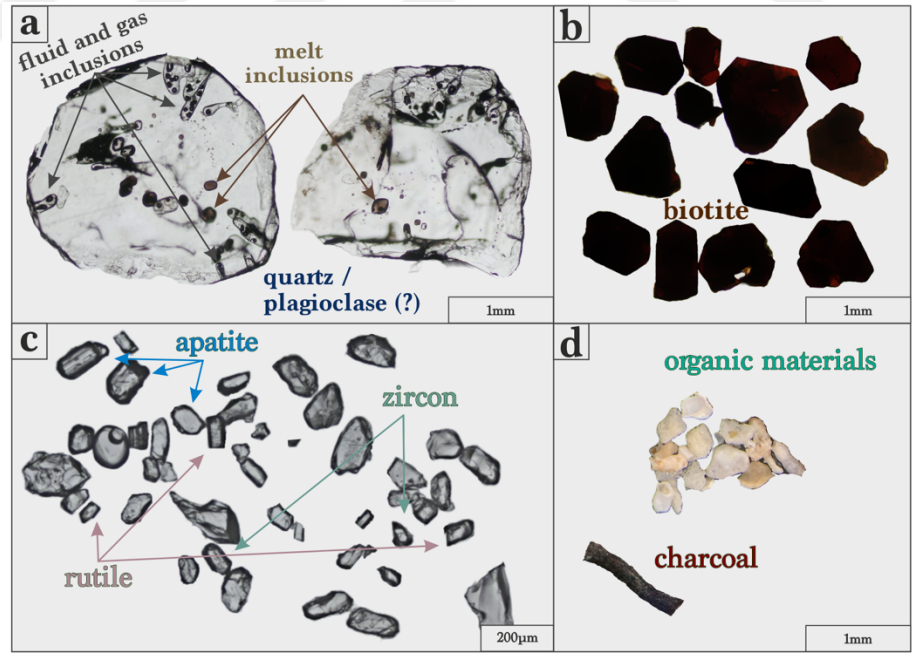

Figure 5.37 The figure displays the internal structure of pyroclastic materials; a) including a photograph of quartz morphology and inclusions, b) a figure of euhedral and anhedral biotite crystals, c) a figure of accessory minerals found in the ash, d) a figure of randomly dispersed organic materials

5.2.3.1 Lithic

A total of nine thin sections were meticulously prepared from the collected samples. It can be observed in lithic rocks at a macroscopic level that the grains are primarily sharp and possess altered properties (Figure, 5.38). Among these, thin sections corresponding to samples 4, 5, and 6 showcased pyroxene, subhedral and euhedral plagioclase, and feldspar minerals exhibiting a zoned texture along the rim. Olivine minerals were also observed in these sections. Notably, distinctive features like porphyry texture and flow banding were discerned, contributing to their classification as *Trachyandesite*. For samples 1, 3, and 9, the prevailing presence of plagioclase and the characteristic pilotaxitic textures led to their categorization as *Trachyte*. In samples 2 and 7, a mineral assemblage including sanidine, biotite, and pyroxene led to the classification of these samples as *Basaltic Trachyandesite*. Additionally, within the sieve texture, microclines in the matrix revealed the presence of dark blobs, which contribute to the appearance of the sieve. These dark blobs are, in fact, melt inclusions formed during rapid, likely skeletal crystal growth. As growth continued slower, the spaces between the skeletal projections closed off, consequently entrapping liquid (Figure 5.39 and Figure 5.40).

Figure 5.38 The lithic rock fragments extracted from location 3 are depicted in the figure, their physical characteristics include size and morphology (Personal archive, 2022)

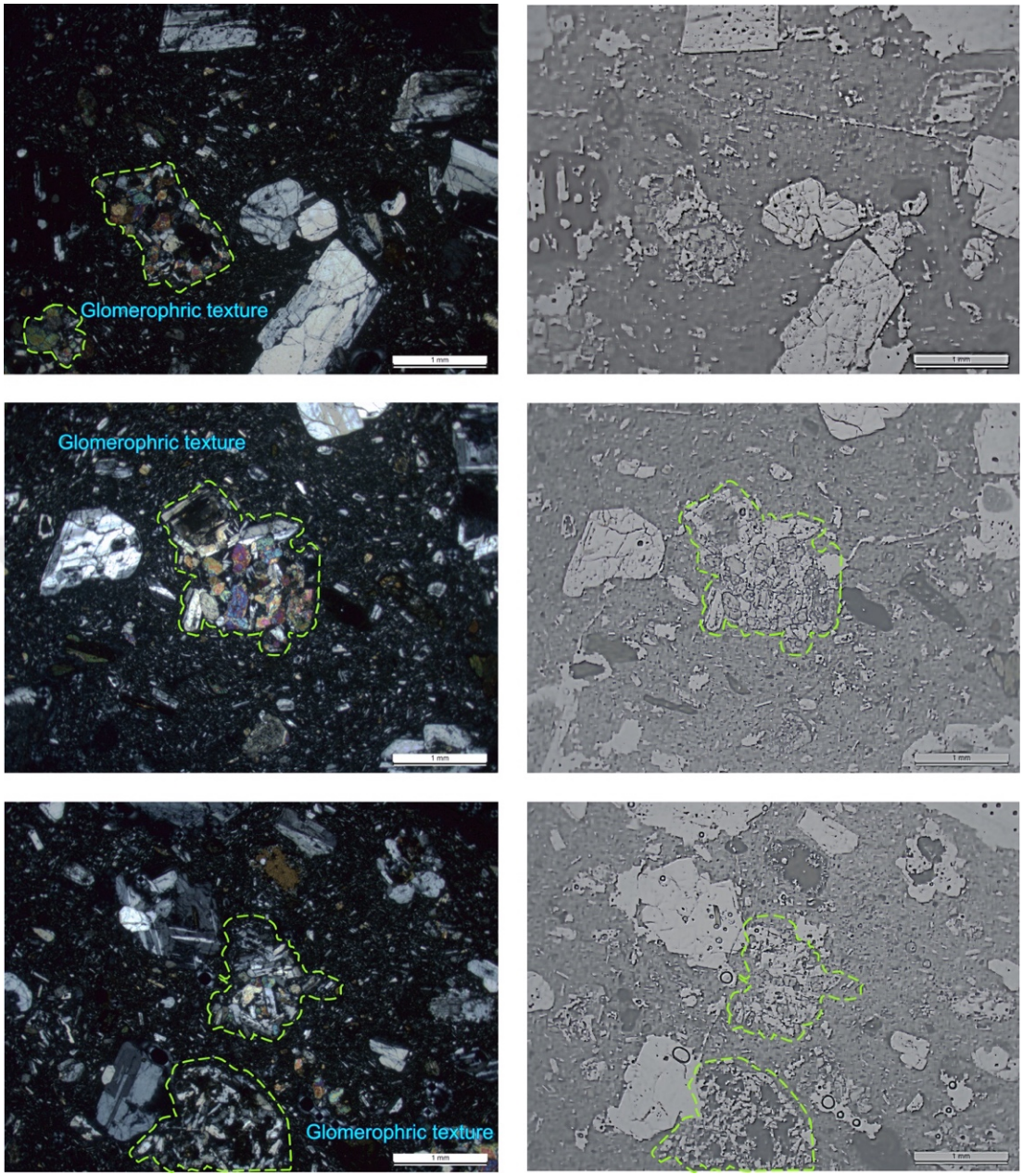

Figure 5.39 Left Images (ppl); Right Images (xpl, edited with a black scatter effect); the images showing different glomerophyric texture in lithic materials at location 3

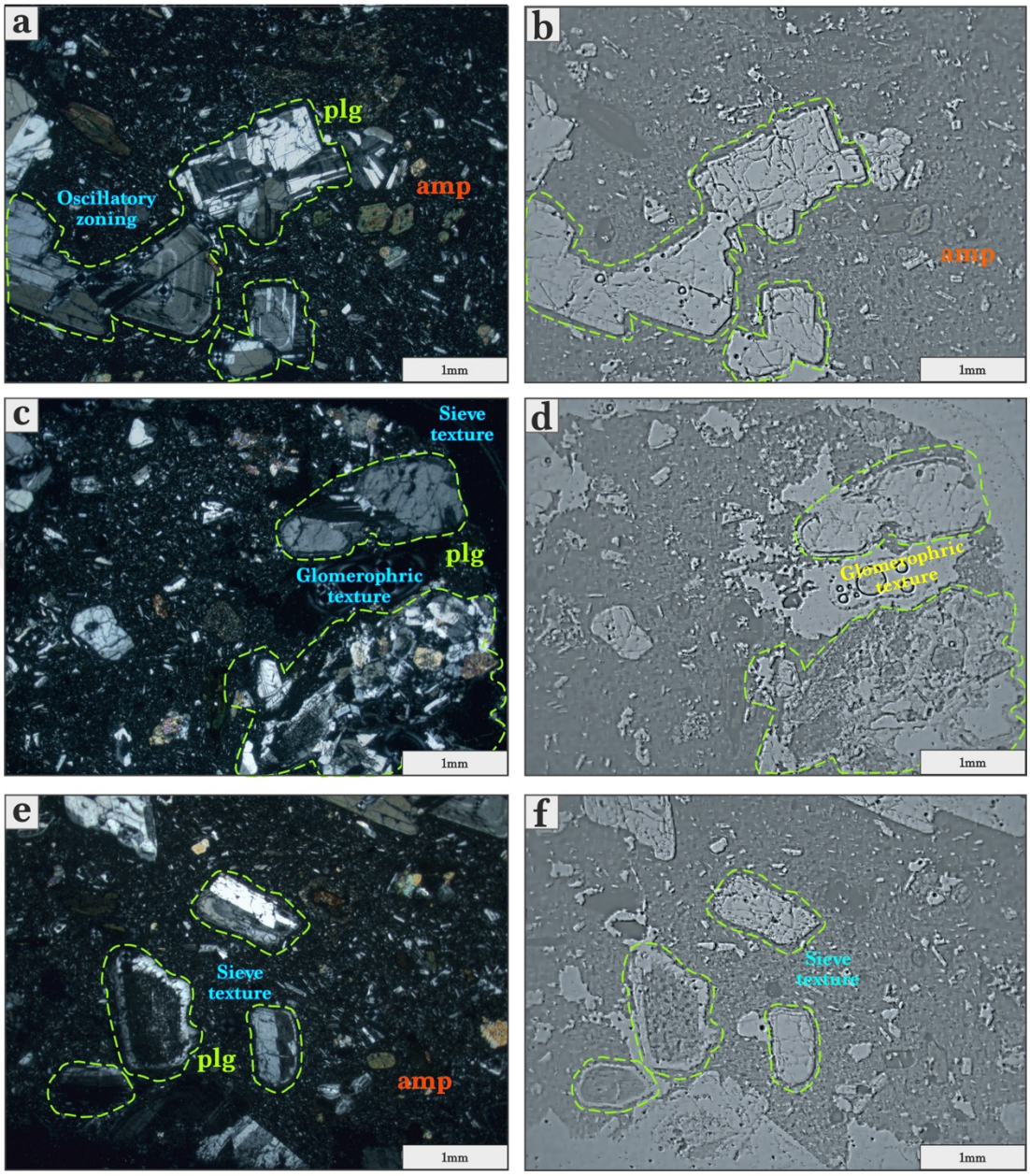

Figure 5.40 Left Images (ppl); Right Images (xpl, edited with a black scatter effect); The figure shows microscopic lithic material views; a and b) showing oscillatory textures; c and d) showing glomerophyric texture; e and f) showing sieve texture

5.2.3.2 Pumice

The pumices at this site appear pristine and white, similar to the second location (Figure, 5.41). Additionally, the characteristic is that the lithic pumice here remains unsurrending by ash deposits too, and there is the crystals-rich matrix. The notable features of this location's thin sections include elongated minerals, irregular vesicles, and micro pumice fragments randomly distributed, indicating their formation during magma ascent. In the examined thin sections, a significant amount of pumice has pores covered with ash, likely influenced by water/vapor presence (Figure, 5.42 and Figure 5.43).

Figure 5.41 Macro-scale views of pumice grains with various morphological features extracted from massive pyroclastic materials (Personal archive, 2022)

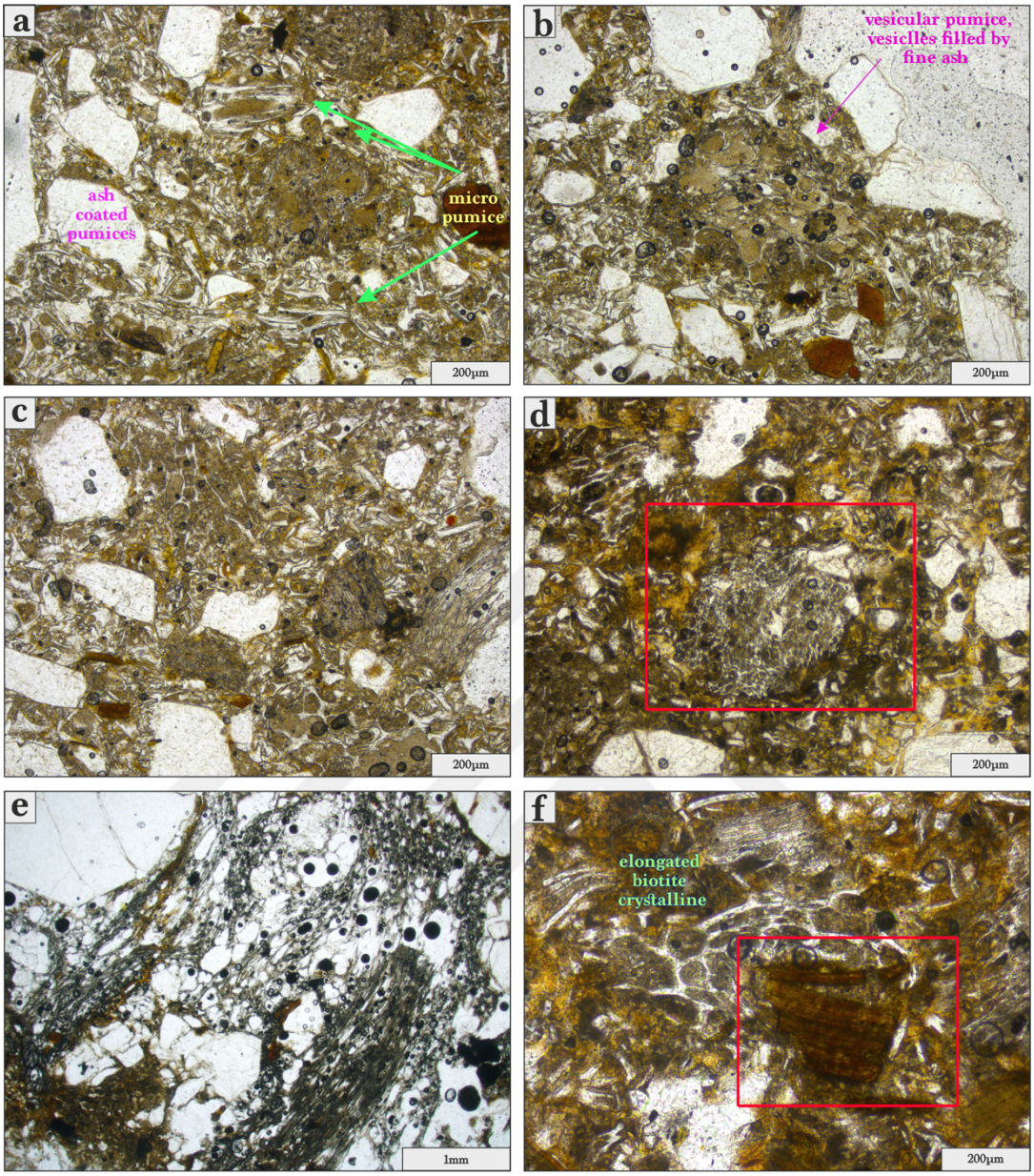

Figure 5.42 Microscopic views of pumice materials. a) Various micro pumices with filled by ash aggerated and ash-coated bubble wall shards are displayed in this image. b) This image focuses on an ash-coated pumice and broken clasts like jigsaw textures found in fine ash matrix. c) The image presents ash-coated pumices and glass. d) Border of the tubular pumice fragment coated by silica gel-like glass. e) While examining the pumice texture in detail, observed both granular and tube vesicles. This observation suggests that these features formed during the explosive activity within the volcanic vent, indicating dynamic processes at play. f) The image provides a close-up view of elongated biotite crystals within the rock matrix. The elongation of these biotite crystals is a notable feature, suggesting that they have undergone deformation and alignment, likely as a result of dynamic geological processes such as tectonic forces or magmatic flow.

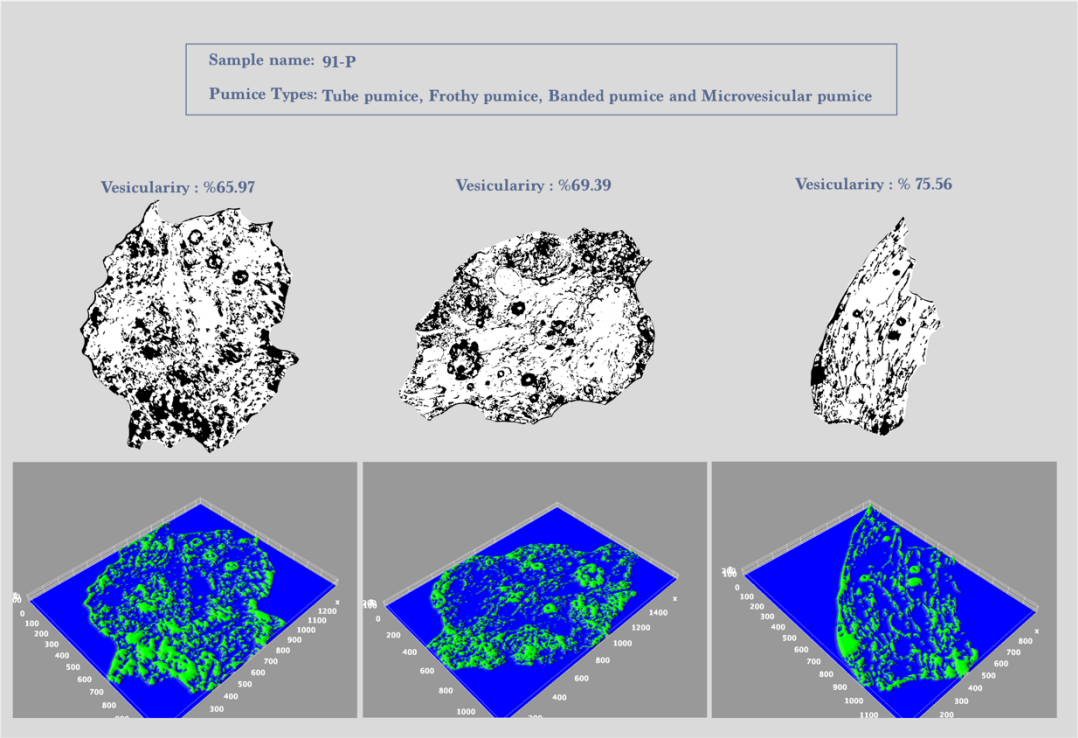

Figure 5.43 Microscopic views of pumice materials

5.2.3.2 Acceleration Lapilli

The lapilli specimens found at this location have an irregular, aggregate-like texture, which may be a result of high energy altering their original characteristics. Pronounced deformation is also present in the interior of the lapilli. The sample's composition includes glass, biotite, plagioclase, magnetite, and amphibole crystals. Furthermore, these sections revealed a distinct texture known as "rim type-multiple-without core," as described in studies conducted by Schumacher & Schimincke in 1991, indicative of reworked ash particles and suggesting an association with water influence (Figure, 5.44).

5.2.4 Petrographic Analysis of Location 4

The acquired field samples undergo a meticulous regimen of cleaning and sorting, encompassing both manual techniques and utilizing specialized tools like brushes within the laboratory setting. Within these samples, a diverse amalgamation of solid

pyroclastic components is evident, inclusive of pumice, lithic fragments, fine particulate material, and mineral constituents, all ensconced within an unconsolidated ash matrix (Figure, 5.45). These pyroclastic materials are characterized by their unwelded nature, predominantly characterized by a glassy matrix and a crystal content ranging from 5% to 10%.

The vesicularity of these materials exhibits a range spanning from 35% to 50%, often imparting a fibrous or fluidal appearance to the matrix. The paragenesis of these materials predominantly encompasses glass shards, pumice fragments, and various minerals (Figure 5.46 and Figure 5.47). Biotite, quartz, plagioclase, and feldspar crystals are discernible among these minerals (Figure 5.48). The examined materials exhibit a diverse mineral composition, encompassing pyroxene, apatite, zircon, and rutile crystals, as well as fluid and gas inclusions within subhedral and euhedral quartz. Euhedral-subhedral biotite crystals reveal the presence of zircon inclusions, while feldspar displays a similar content to quartz (Figure, 5.49).

5.2.4.1 Lithic

One can observe in lithic rocks at a macroscopic level that the grains are primarily rounded and possess fresh properties (Figure, 5.50). Three meticulously prepared thin sections were generated from the collected samples. Thin sections corresponding to samples 4, 5, and 6 exhibited a mineral composition featuring pyroxene, subhedral and euhedral plagioclase, and feldspar minerals, presenting a distinct zoned texture along the rim. Furthermore, olivine minerals were identified within these sections. Notably, these sections displayed prominent features such as porphyry texture and flow banding, resulting in their classification as *Trachyandesite*. In the case of sample 54, the presence of sanidine, biotite, and pyroxene minerals facilitated its classification as basaltic *Trachyandesite*. Within the context of the sieve texture, the microcline within the matrix revealed dark inclusions contributing to the sieve-like appearance. These dark inclusions, specifically melt inclusions, originated during rapid, potentially skeletal crystal growth. As growth progressed slower, the spaces between skeletal projections eventually closed, entrapping liquid (Figure, 5.51).

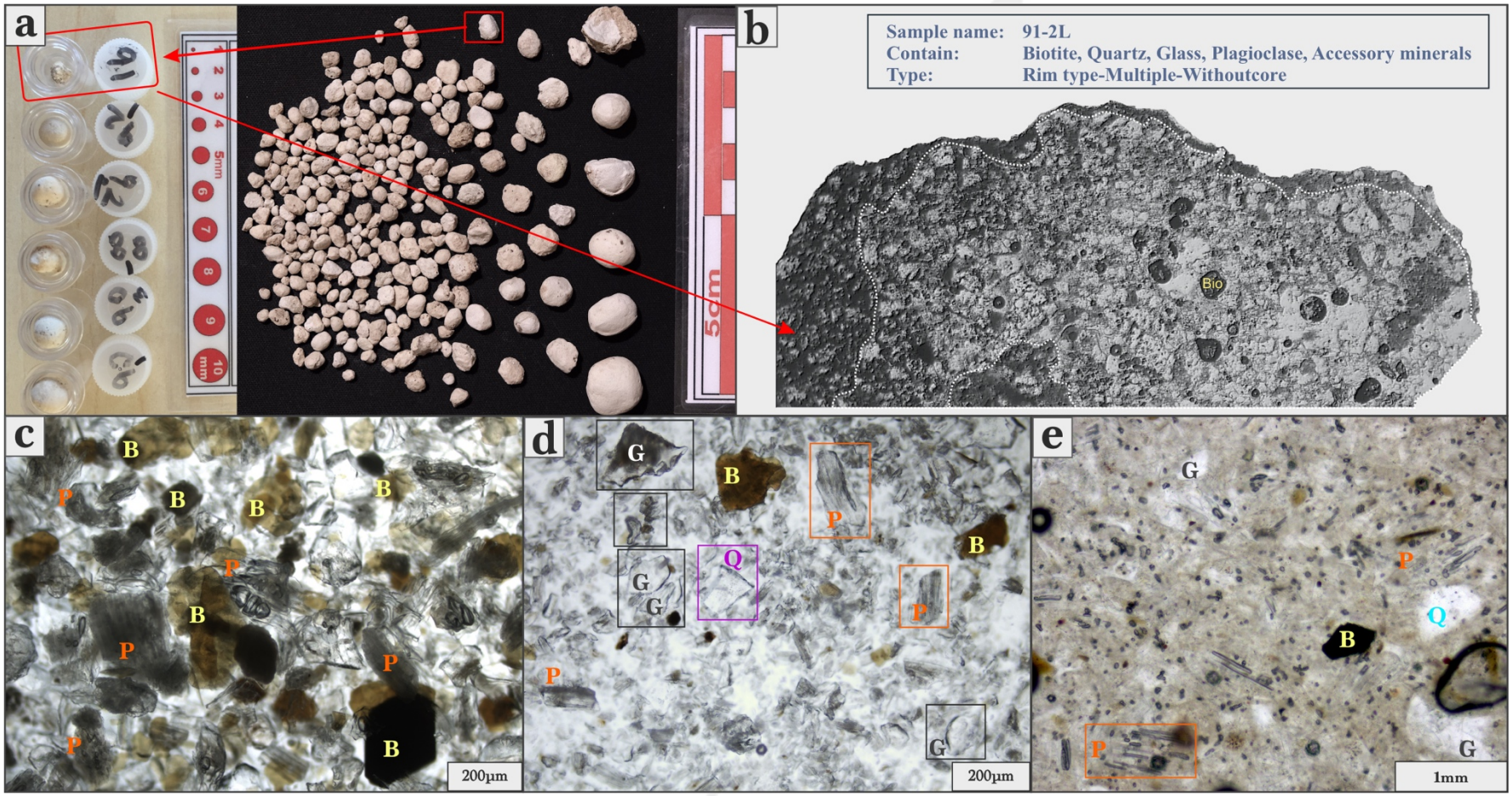

Figure 5.44 The figure includes internal structure on a thin section, mineralogical content under a binocular microscope, and a macro view with a scale for measurement samples from location 3.

Figure 5.45 There are particles of pyroclastic material present that have not undergone welding belong to the sample from the fifth location (Personal archive, 2022)

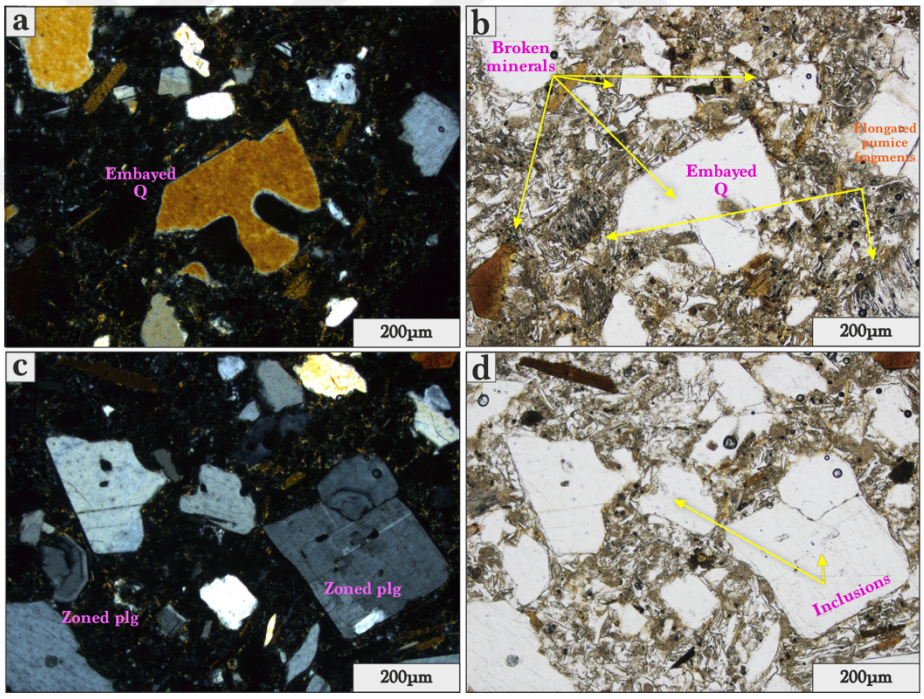

Figure 5.46 Microscopic views of pumice materials. a) This figure shows the embayed quartz crystals and broken crystals presence in a glassy matrix. Also, there is some pumice fragment with elongated vesicles. b) This figure shows the presence of the broken and zoned plagioclase within the melt inclusion inside a matrix full of bubble-type glass shards.

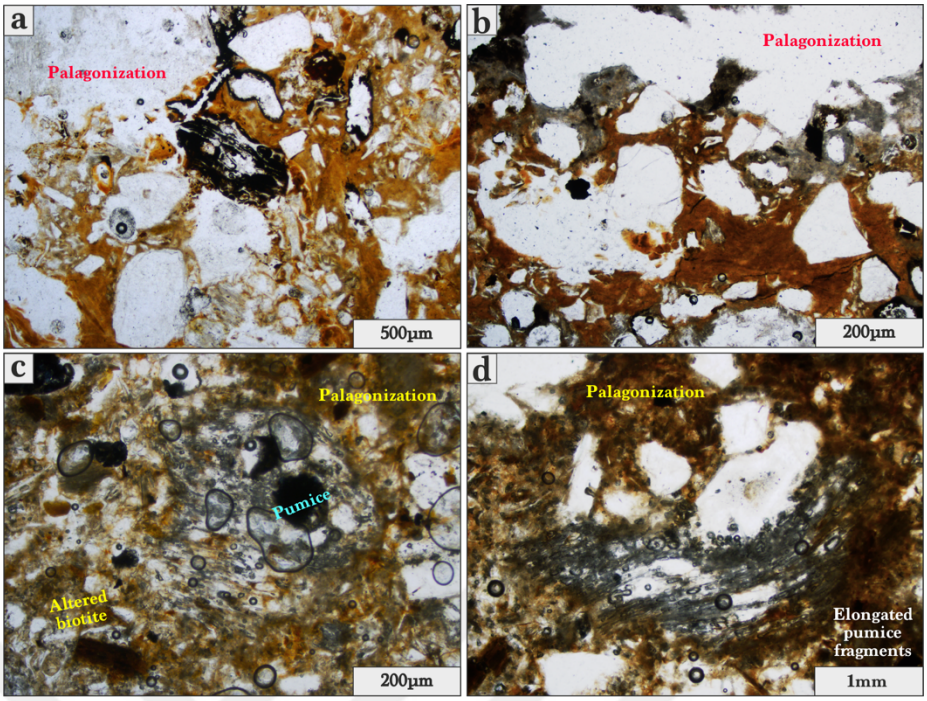

Figure 5.47 In this figure, all four images depict pyroclastic materials extensively affected by palagonization. These materials include fragmented pumice, altered biotite, and broken minerals. Notably, the matrix exhibits a highly decayed, silica gel-like texture

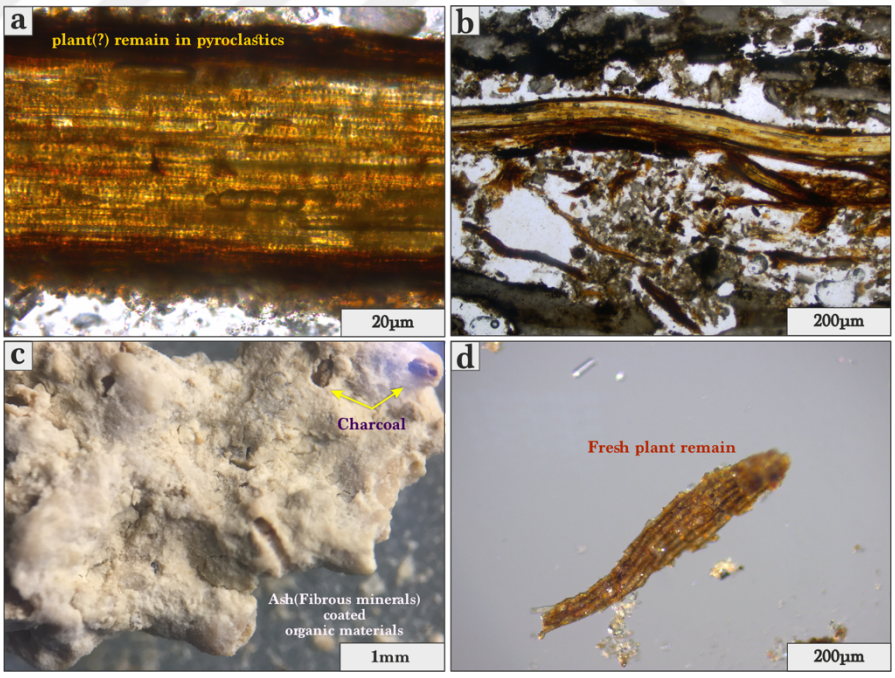

Figure 5.48 a) Detailed charcoal fragment analysis under binocular microscope b) Presents an in-depth analysis of a charcoal fragment under a binocular microscope. c) Macroscopic view of marine shell fragment d) Charcoal fragment under binocular microscope

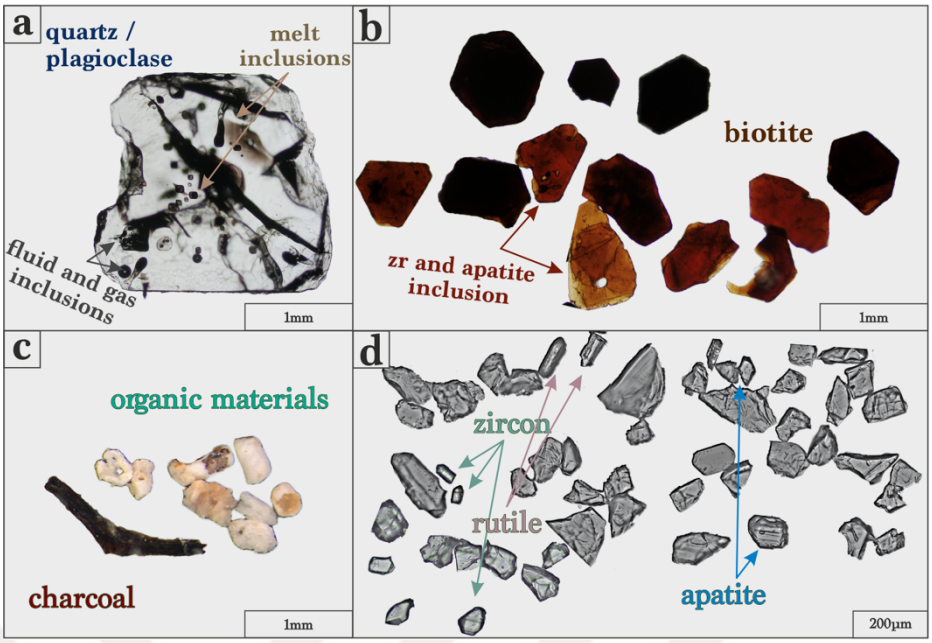

Figure 5.49 The figure displays the internal structure of pyroclastic materials; a) including a photograph of quartz morphology and inclusions, b) a figure of euhedral and anhedral biotite crystals, c) a figure of accessory minerals found in the ash, d) a figure of randomly dispersed organic materials

Figure 5.50 The lithic rock fragments extracted from location 4 are depicted in the figure, their physical characteristics include size and morphology (Personal archive, 2022)

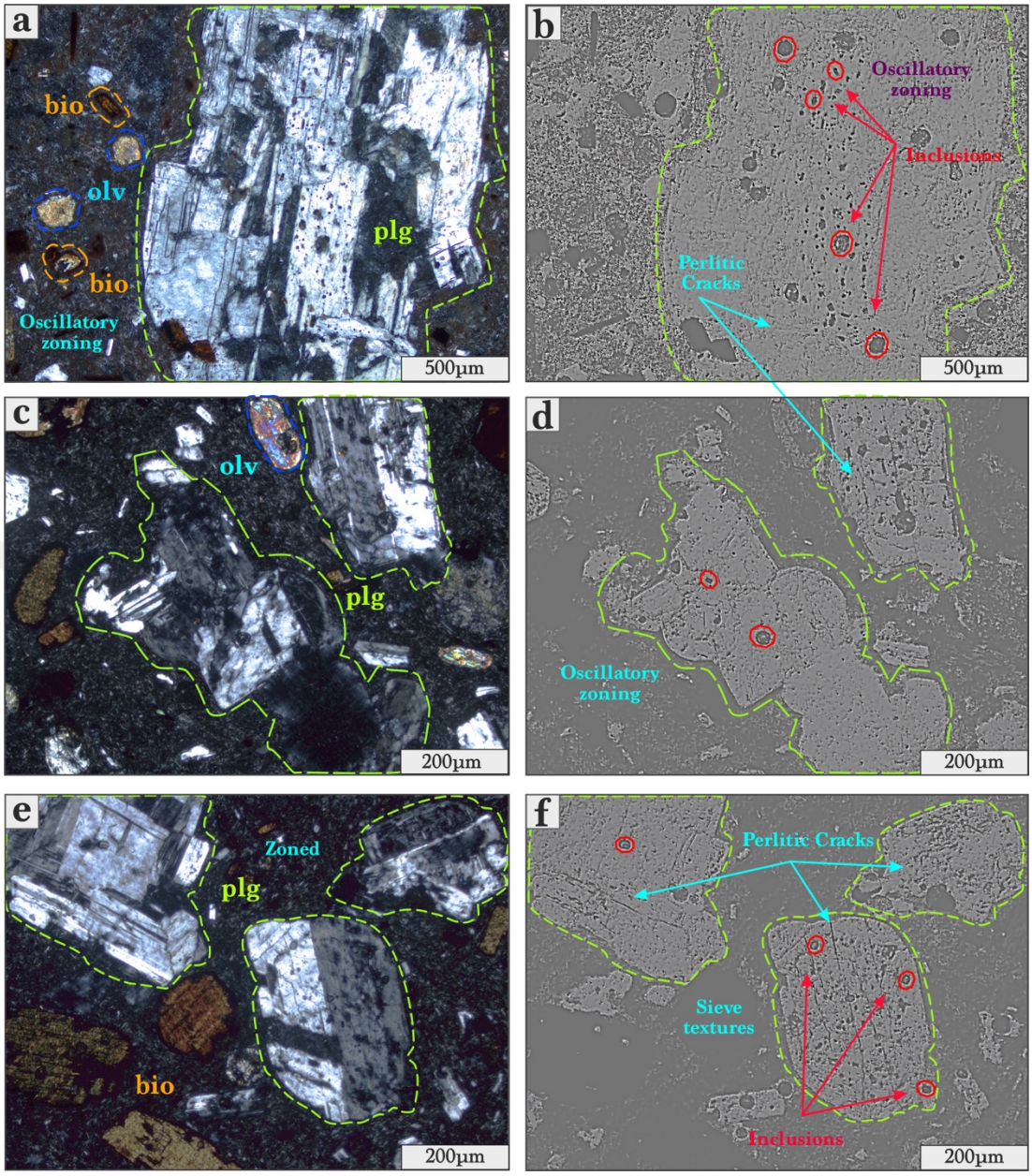

Figure 5.51 Microscopic views of lithic materials belong to the third location. Left Images (ppl); Right Images (xpl, edited with a black scatter effect); a and b) images that reveal within plagioclase crystals – the presence of oscillatory zoning and perlitic cracks; c and d) image that showcase perlitic cracks on plagioclase crystals with a distinctive oscillatory zone and subhedral olivine crystals glassy microcline matrix; e and f) The image displays plagioclase within sieve textures

5.2.4.2 Pumice

The prominent macroscopic distinction observed in the pumices set them apart as the most altered and yellowish specimens across the peninsula. Additionally, lithic pumice here is covered by ash (Figure, 5.52). Likewise, the thin sections obtained from this location notable features include the presence of fractures over the phenocrysts as well as elongated and irregular vesicles, signifying their formation during the ascent of magma. Some minerals are affected by shear stress and resulting there some broken and/or stretched minerals. Also, in this location, there is present to mostly euhedral feldspar crystals embedded in the matrix. Nearly all pumice edges are surrounded with ash coated, which is possibly affected by water/vapor presence, too (Figure, 5.53).

Figure 5.52 Macro-scale views of pumice grains with various morphological features extracted from massive pyroclastic materials (Personal archive, 2022)

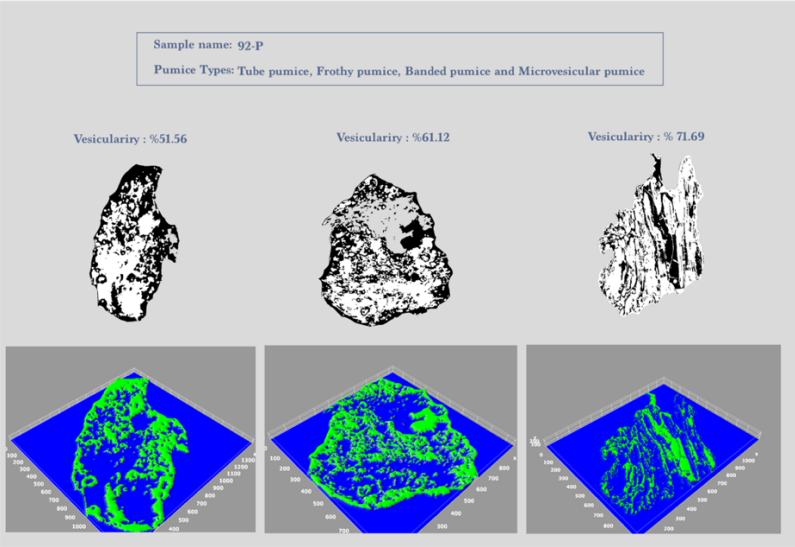

Figure 5.53 Microscopic views of pumice materials

5.2.4.3 Acceleration Lapilli

In the context of the specific sample, the lapilli section reveals a composition that includes glass, biotite, plagioclase, and magnetite crystals. Additionally, these segments display a unique texture referred to as the "rim type-multiple-without core," as described in studies conducted by Schumacher & Schimincke in 1991. This texture signifies the reworking of ash particles, suggesting a potential connection with the influence of water during their formation. The accretionary lapilli showcases distinct characteristics. Notably, they feature a notable and denser outer boundary characterized by an increased concentration of fine particles in its external layers. The lapilli are enclosed with a thinner grain structure, which is a gradual transition toward the outer boundary (Figure 5.54).

5.2.5 Petrographic Analysis of Location 5

The acquired field samples resemble the other locations, and these pyroclastic materials are characterized by their unwelded nature, predominantly characterized by an ash-coated (Figure, 5.55) matrix and a crystal content ranging from 5% to 10%. The vesicularity of these materials exhibits a range spanning from 35% to 55%, often imparting a fibrous or fluidal appearance to the matrix.

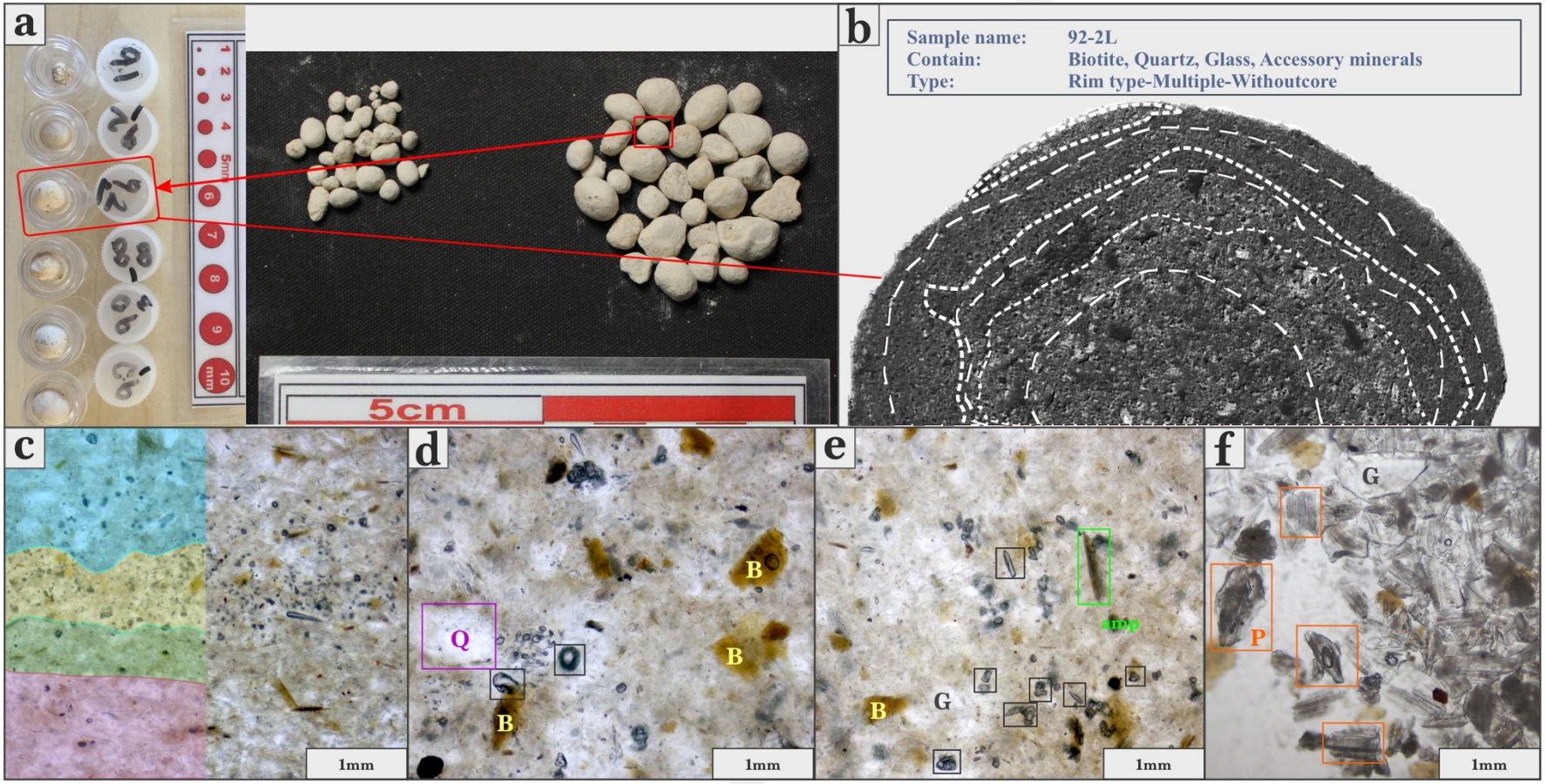

Figure 5.54 The figure includes internal structure on a thin section, mineralogical content under a binocular microscope, and a macro view with a scale for measurement samples from location

Figure 5.55 There are particles of pyroclastic material present that have not undergone welding belong to the sample from the fifth location. (Personal archive, 2022)

The paragenesis of these materials predominantly encompasses glass shards, pumice fragments, and various minerals. Biotite, quartz, plagioclase, and feldspar crystals are discernible among these minerals and resemble the other locations (Figure 5.56). The examined materials exhibit a diverse mineral composition, encompassing pyroxene, apatite, zircon, and rutile crystals, as well as fluid and gas inclusions within subhedral and euhedral quartz. Euhedral-subhedral biotite crystals reveal the presence of zircon inclusions, while feldspar displays a similar content to quartz. However, the context of the organic materials shows diversity, such as the presence of Bivalvia, Foraminifera, and Turritella (Figure, 5.57, Figure 5.58 and Figure 5.59).

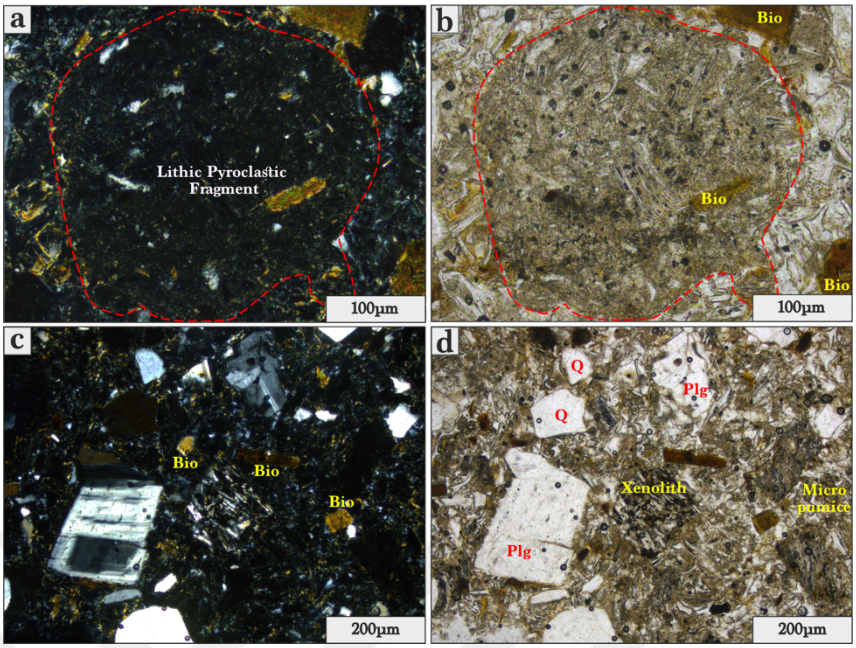

Figure 5.56 a) The internal structure of the lithic pyroclastic fragment reveals the presence of biotite, micropumices, and glass shards. b). It exhibits a heterogeneous texture with xenoliths, lithic pumice, and biotite crystals dispersed within a matrix of plagioclase and glassy material.

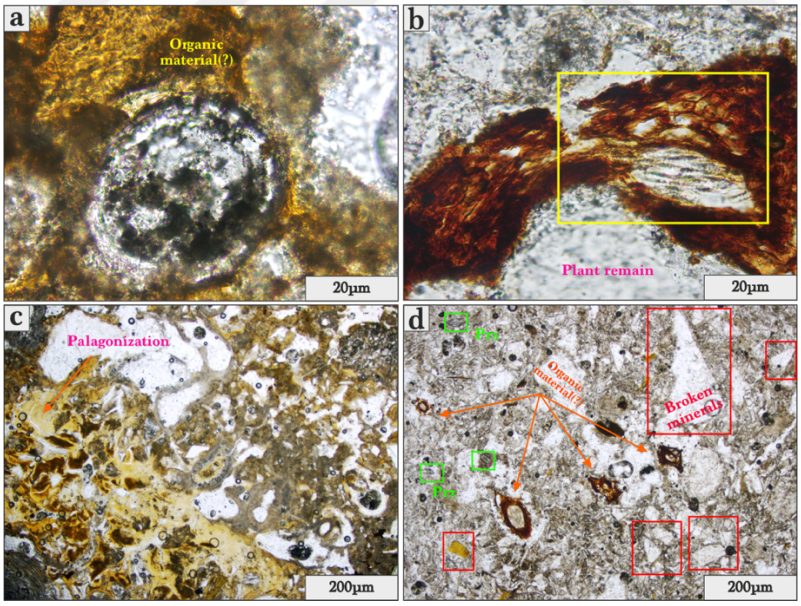

Figure 5.57 Microscopic views of pyroclastic materials. a) This image showcases palagonite formations characterized by distinctive rims surrounding vesicles. b) In this image, the remarkable preservation of plant remains c) The image reveals extensive palagonization and the presence of siderolemane content within the volcanic materials. d) This image displays a diverse assemblage of materials, including broken minerals, glass shards, and altered rounded minerals or potentially preserved plant remains.

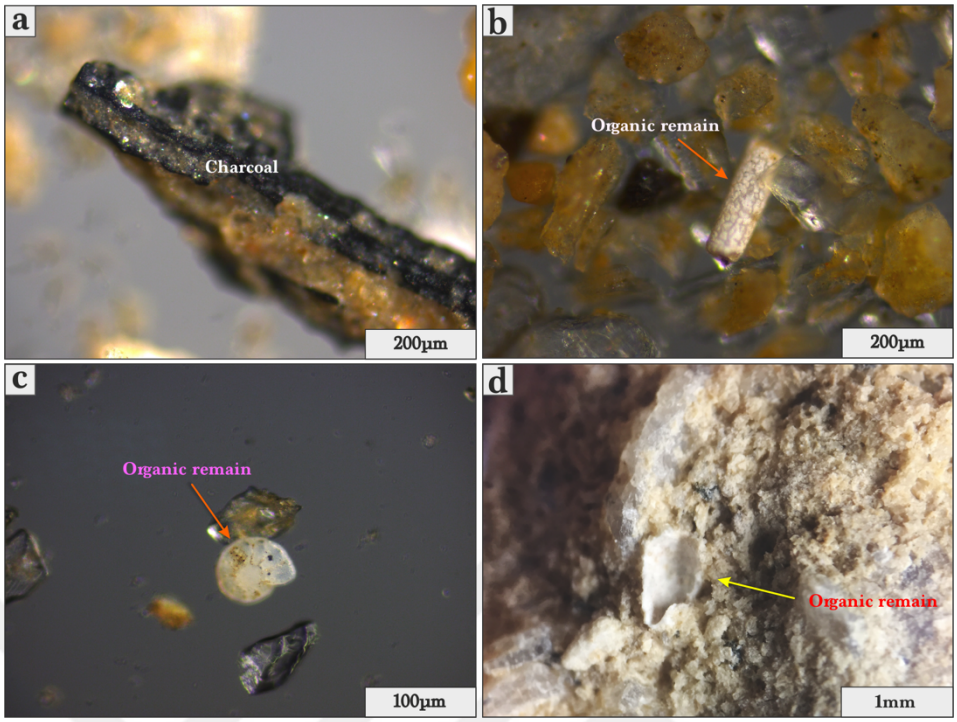

Figure 5.58 a) Detailed charcoal fragment b) and c) Microscopic view of marine shell fragment d) Macroscopic view of marine shell fragment

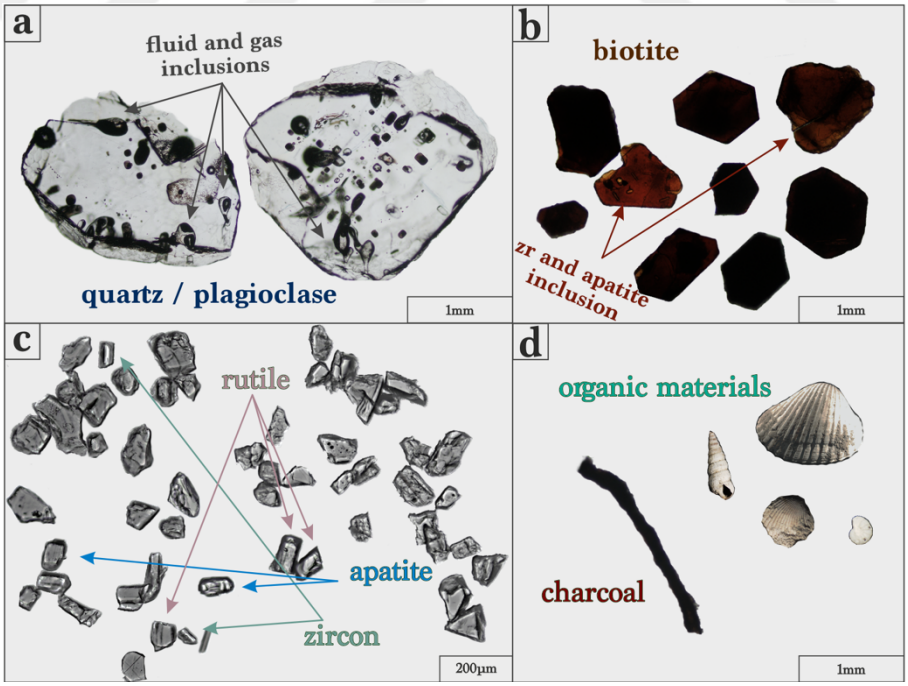

Figure 5.59 The figure displays the internal structure of pyroclastic materials; a) including a photograph of quartz morphology and inclusions, b) a figure of euhedral and anhedral biotite crystals, c) a figure of accessory minerals found in the ash, d) a figure of randomly dispersed organic materials

5.2.5.1 Lithic

One can observe in lithic rocks at a macroscopic level that the grains are primarily rounded and possess fresh properties (Figure, 5.60). A set of three thin sections was meticulously prepared from the collected samples. Among these, the thin sections corresponding to samples 59 and 60 exhibited a mineral composition including pyroxene, subhedral and euhedral plagioclase, and feldspar minerals, with a distinct zoned texture along the rim. Additionally, olivine minerals were identified in these sections. Noteworthy features such as porphyry texture and flow banding were also observed, resulting in their classification as *Trachyandesite*. In the case of sample 58, a mineral assemblage comprising sanidine, plagioclase, biotite, and pyroxene facilitated its classification as *Lamprophyre*. Within the context of the sieve texture, the microcline within the matrix revealed dark inclusions that contribute to the sieve-like appearance. These dark inclusions, identified as melt inclusions, were formed during rapid, potentially skeletal crystal growth. Subsequent slower growth resulted in the closure of spaces between skeletal projections, effectively trapping liquid (Figure, 5.61).

Figure 5.60 The lithic rock fragments extracted from location 5 are depicted in the figure, their physical characteristics including size and morphology (Personal archive, 2022)

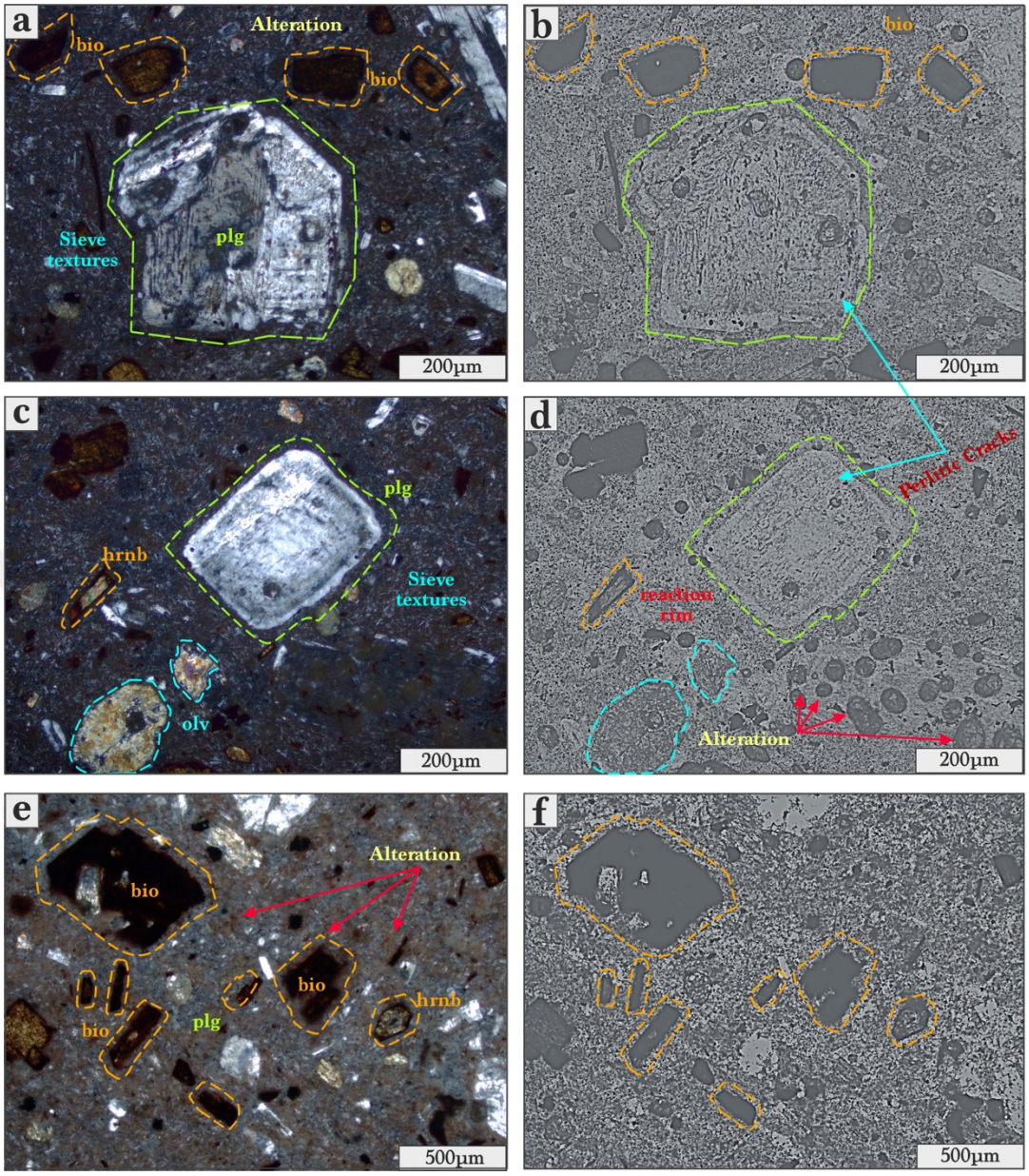

Figure 5.61 Microscopic views of lithic materials belong to the third location. Left Images (ppl); Right Images (xpl, edited with a black scatter effect); a and b) images that reveal within plagioclase crystals – the presence of sieve textures and altered hornblende crystals in microcline crystals matrix, c and d) image that showcases perlitic cracks on plagioclase crystals and subhedral olivine crystals on a glassy microcline matrix e and f) the image displays altereted hornblende on the matrix

5.2.5.2 Pumice

The prominent macroscopic distinction observed in the pumices at this site is their exceptionally pristine and white appearance, setting them apart as the biggest fragments on the peninsula (Figure, 5.62). Additionally, a noteworthy characteristic is that the lithic pumice here remains unsurrending by ash deposits. The thin sections obtained from this location's notable features include the presence of fractures over the phenocrysts as well as elongated and irregular vesicles, signifying their formation during the ascent of magma. Some minerals are affected by shear stress and resulting there some broken and/or stretched minerals. Also, in this location, there is present to mostly euhedral feldspar crystals embedded in the matrix. Nearly all pumice edges are surrounded with ash coated, which is meaning possibly affected by water/vapor presence (Figure, 5.63).

Figure 5.62 Macro-scale views of pumice grains with various morphological features extracted from massive pyroclastic materials (Personal archive, 2022)

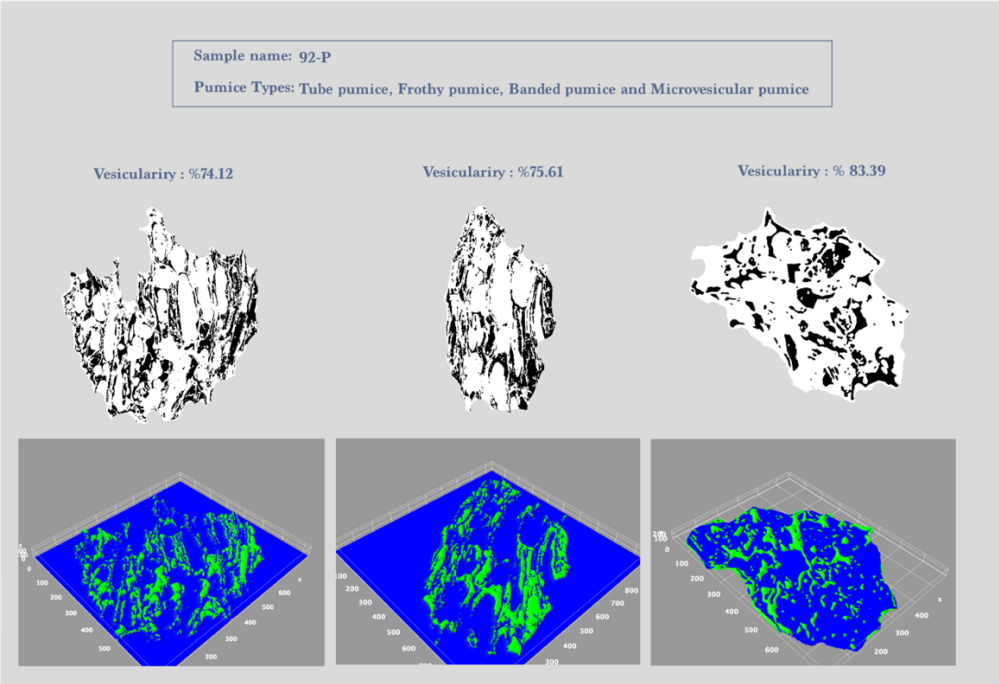

Figure 5.63 Different microscopic images of pumices

CHAPTER SIX
GEOCHEMISTRY

6.1 Introduction

This chapter delves into the results of geochemical analysis applied to volcanic samples collected from various locations across the Bodrum Peninsula. By comparing these results with values of KPT obtained in previous studies, we can identify materials within the peninsula that share a kinship with the KPT. This helps us gain valuable insights into the movement of post-explosive processes, contributing to a better understanding of the region's geological evolution. To ensure thorough analysis, the samples from the Bodrum Peninsula were divided into three distinct groups, as illustrated in Figure, 6.1. EPMA was used to analyze glass shards and pumices from each group of samples. The average major oxide composition and trace elements (%wt) for each sample group are also provided for a more comprehensive understanding. To further assist with comprehension, Table 6.1 features sample names and descriptions. When analyzing the geochemical data obtained from the KPT and applying it to the Total Alkaline Silica classification places them within the rhyolite compositional field, indicative of their evolved silicic nature (Figure, 6.2). Notably, the AFM values indicate a calc-alkaline nature, suggesting a subduction-related origin for the studied rocks (Figure, 6.3). Furthermore, the high K_2O-SiO_2 ratios observed in these samples align with the characteristics of high rhyolite compositions (Figure, 6.4).

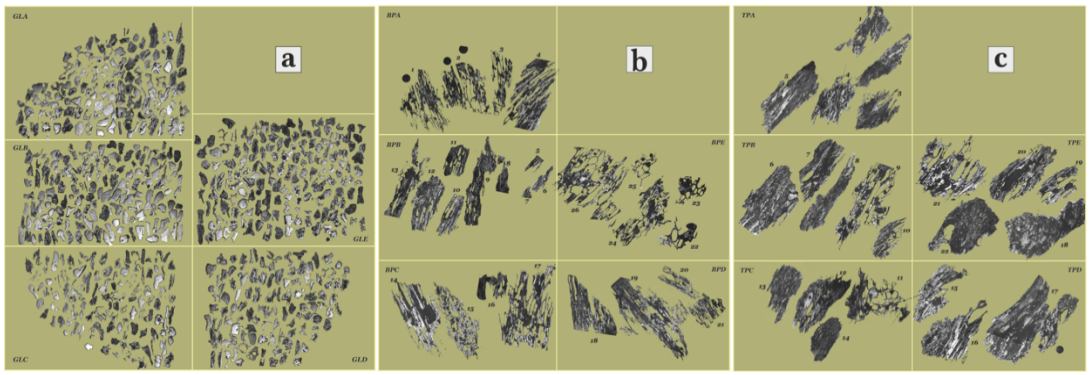

Figure 6.1 Views of 3 separately prepared discs under the microscope.

Table 6.1 Name belongs to each sample for all locations.

Location number	Sample Name
Location 1	lithic pumice - bolder pumice (BPA), juvenile pumice - tiny pumice (TPA), fine graded ash - glass shards (GLA)
Location 2	lithic pumice - bolder pumice (BPB), juvenile pumice - tiny pumice (TPB), fine graded ash - glass shards (GLB)
Location 3	lithic pumice - bolder pumice (BPC), juvenile pumice - tiny pumice (TPC), fine graded ash - glass shards (GLC)
Location 4	lithic pumice - bolder pumice (BPD), juvenile pumice - tiny pumice (TPD), fine graded ash - glass shards (GLD)
Location 5	lithic pumice - bolder pumice (BPE), juvenile pumice - tiny pumice (TPE), fine graded ash - glass shards (GLE)

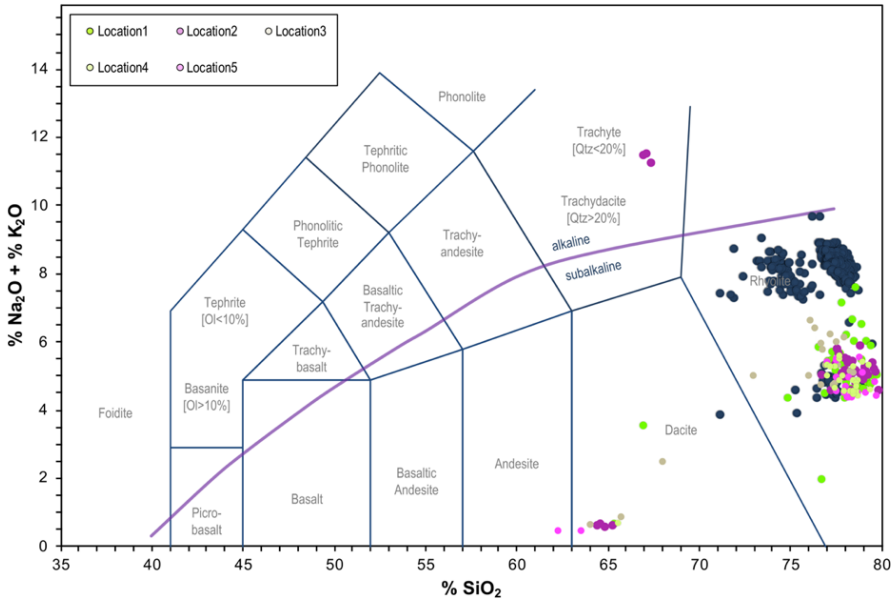

Figure 6.2 The TAS diagram indicates the classification of volcanic rocks. Rhyolite composition falls within the rhyolite field, showcasing the silica-rich nature of these rocks

Marine ash beds of the Kos Plateau Tuff have also been reported by Keller (1969), Keller et al. (1978), Federman & Carey (1980), Vinci (1985), Hardiman (1999), Peltz et al. (1999), Huber et al. (2003), Margari et al. (2007), Páper & Pe-Páper (2008), Zouáas & St. Seymour (2008), Bachmann (2010), Zouáas et al. (2013), Satow et al. (2015), Koutralá et al. (2018), Pe-Páper (2020), Wulf et al. (2020), Kutterolf (2021) án the Aegean Sea but also in the Black Sea by Wegwerth et al. (2019) also in the eastern Mediterranean Sea by Zhang et al. (2023).

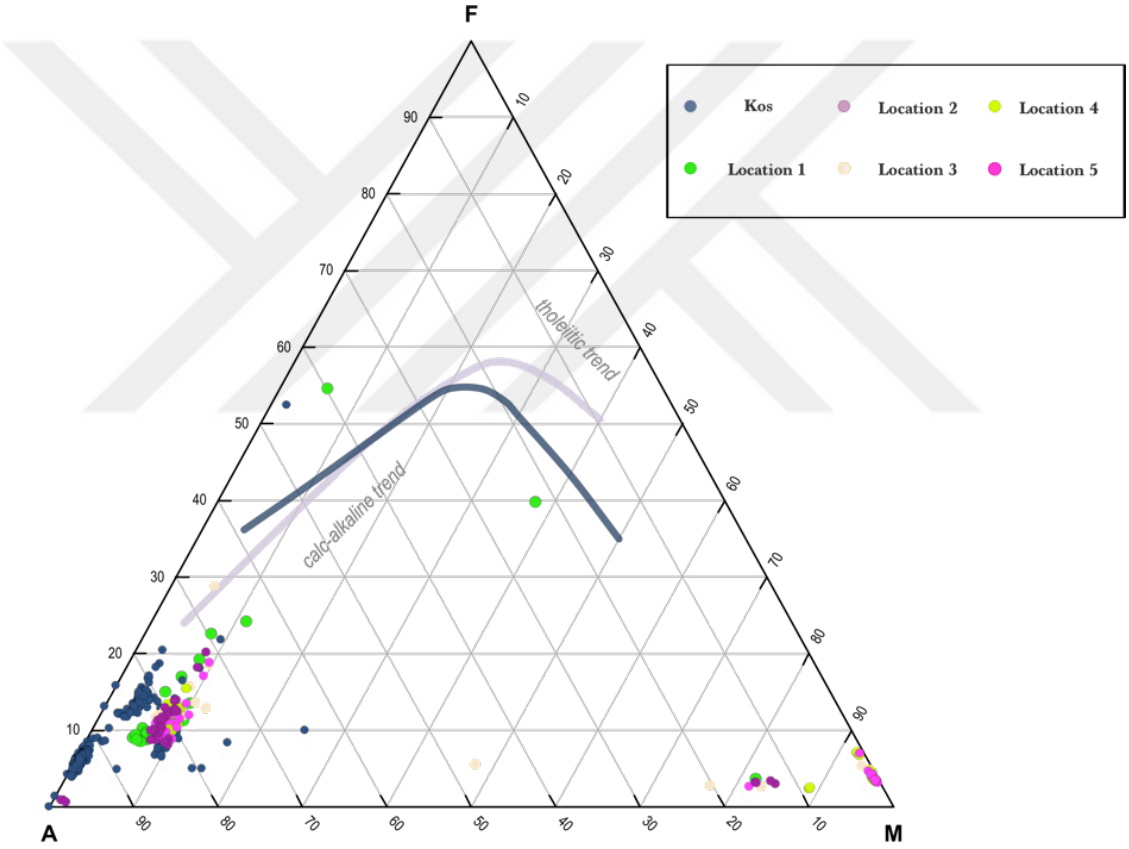

Figure 6.3 AFM diagram highlighting volcanic rock classification. Rhyolite composition is situated under the calc-alkaline field, illustrating the association of rhyolitic rocks with calc-alkaline magmatism

The geochemical investigation, as implemented in Bachman's 2010 studies, utilized diagrams and geochemical parameters to gain deeper insights into petrogenesis. A comparative analysis was conducted, focusing on the values of Bodrum and Kos-Nisyros-Yali. According to Bachmann's 2010 studies, major and trace elements exhibit low variability, with only Ba and Sr displaying significant (and positively correlated) variations, suggestive of feldspar fractionation. REE elements, generally low in abundance, display a bowl-shaped pattern with depletion in MREE and small Eu negative anomalies. While using the diagrams which are the SiO_2/Zr diagram, SiO_2/MgO_2 diagram, SiO_2/Sr diagram, Nb/Y diagram the Rb/Ba diagram. Lastly, Ba-Ce/Th-Yb diagram, the glass compositions match well with the Kos Plateau Tuff (KPT) in agreement with the measurements in previous studies of all other values (Figures, 6.5 and Figure, 6.6).

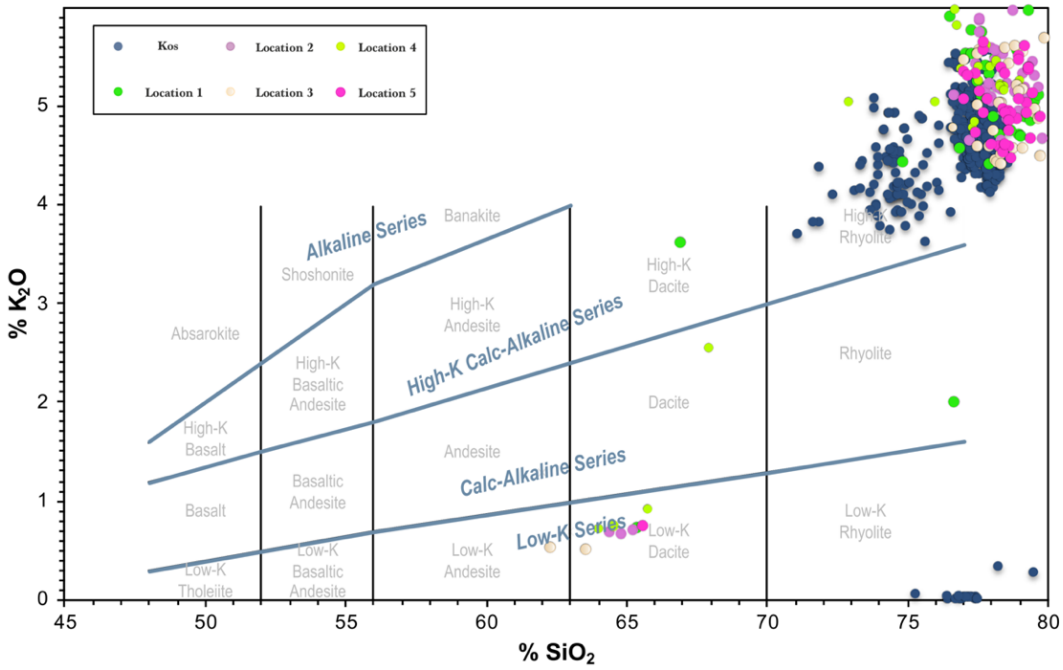

Figure 6.4 K_2O-SiO_2 diagram displaying the relationship between potassium oxide (K_2O) and silica (SiO_2) content in volcanic rocks. The high K_2O-SiO_2 values correspond to a high rhyolite composition, emphasizing the silicic nature of these rocks

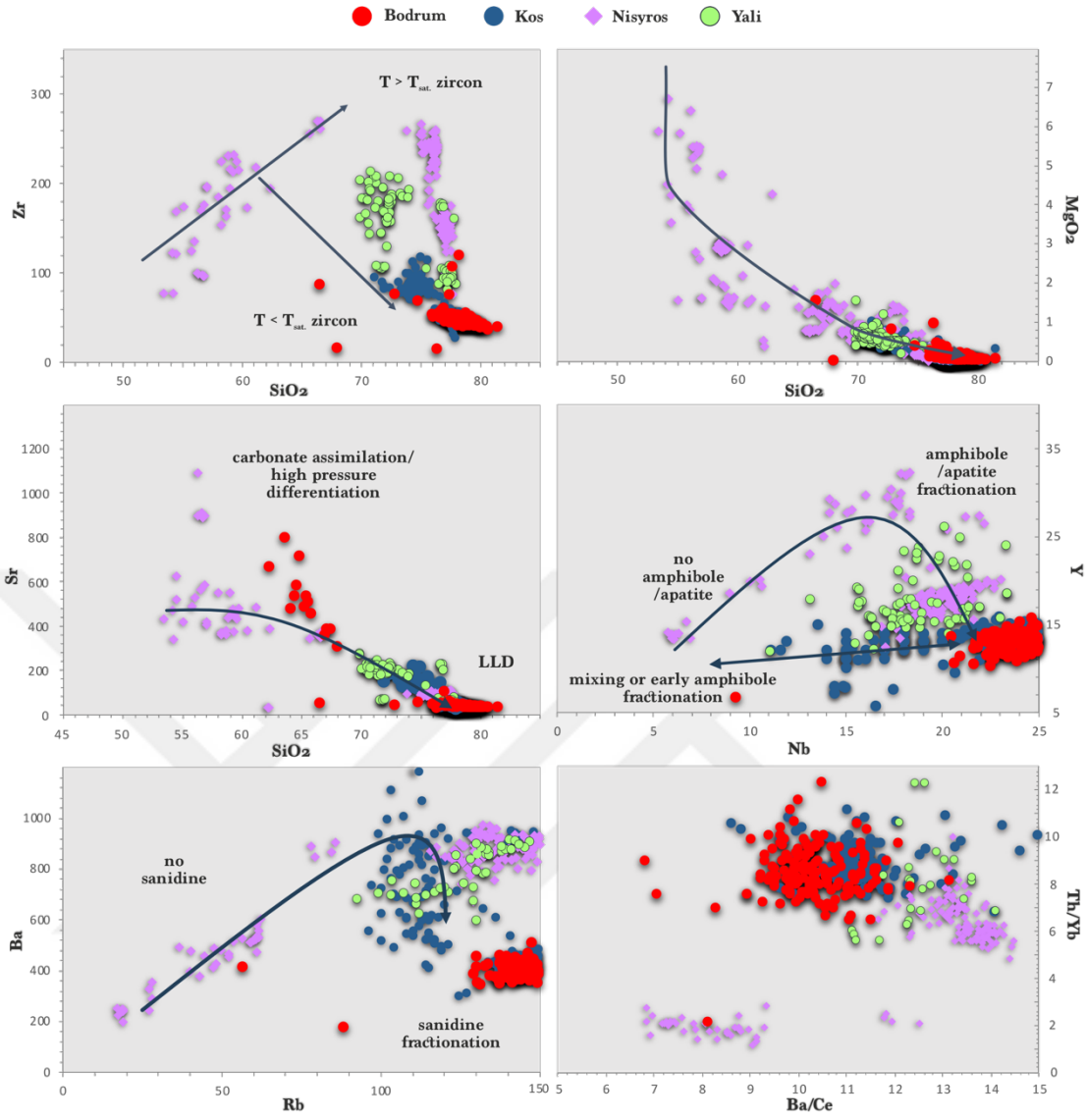

Figure 6.5 Major and trace element compositions of pumice and glass values from the Kos–Nisyros–Yali volcanic field and KPT units on the Bodrum Peninsula. The probable liquid line of descent (LLD) is indicated with an arrowed line; arrowed lines also indicate differentiation trends at temperatures above and below that of zircon saturation (Tsat. zircon); "sat." = saturation. Mafic magmas affected by carbonate assimilation are circled

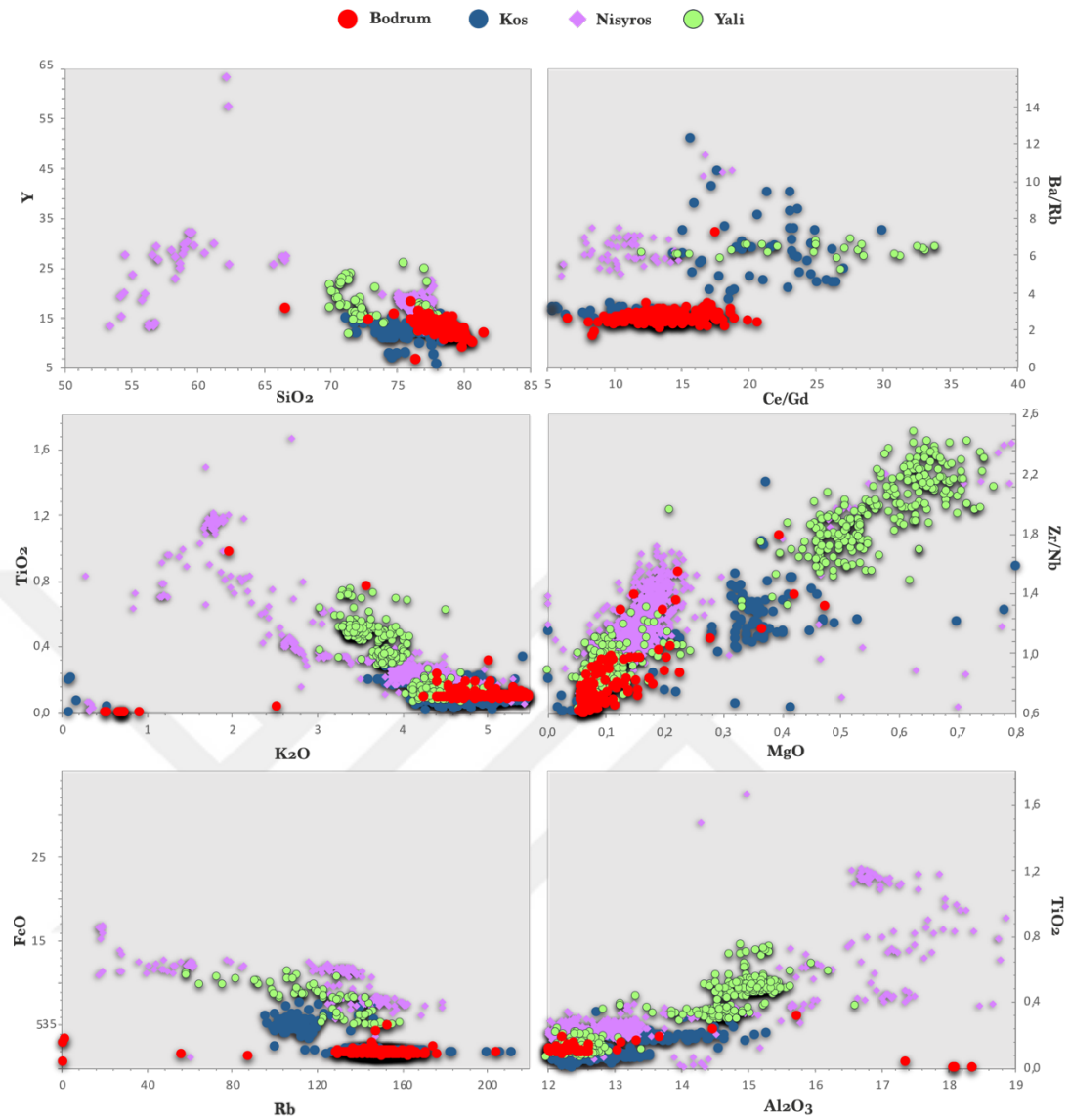

Figure 6.6 Major and trace element compositions of pumice and glass values from the Kos–Nisyros–Yali volcanic field and KPT units on the Bodrum Peninsula

6.2 Geochemical Analysis

6.2.1 Location 1.

It was analyzed 3 different mounts in major elements and trace elements which are lithic pumice - bolder pumice (BPA), juvenile pumice - tiny pumice (TPA), and fine graded ash - glass shards (GLA). This geochemical study conducted a comprehensive analysis of major elements on volcanic samples collected from the Bodrum peninsula.

- SiO_2 content: BPA (**77.00% - 79.47%**), TPA (**77.70% - 80.04%**), GLA (**65.28% - 79.29%**)
- Al_2O_3 concentrations: BPA (**10.99% - 20.64%**), TPA (**9.29% - 10.66%**), GLA (**10.90% - 12.48%**)
- Total Fe_2O_3 content: BPA (**0.58% - 0.75%**), TPA (**0.57% - 0.91%**), GLA (**0.20% - 5.43%**)
- CaO range: BPA (**0.50% - 0.67%**), TPA (**0.41% - 0.52%**), GLA (**0.39% - 4.12%**)
- Na_2O and K_2O variations: BPA (**2.78% - 3.95%, 4.49% - 6.01%**), TPA (2.63% - 4.21%, 4.25% - 5.59%), GLA (**0.79% - 8.84%, 0.74% - 5.05%**)
- TiO_2 range: BPA (**0.10% - 0.12%**), TPA (**0.10% - 0.12%**), GLA (**0.01% - 0.33%**).

The volcanic samples were classified as **rhyolite** based on their alkali and silica content using the **Total Alkali-Silica (TAS)** diagram for geochemical characterization (Figure, 6.7 and Figure 6.8). Furthermore, the trace elements values of the 1. locations samples taken from the Bodrum peninsula PDC units match perfectly with KPT's previous values. Elements like Ba showed concentrations between **176.67** ppm and **828.52** ppm from glass shards; **367.27** ppm and **411.94** from the juvenile pumice; **356.07** ppm and **397.71** ppm from the lithic pumice potentially reflecting the influence of different source rocks and magmatic differentiation. The behavior of other trace elements, such as Sr, Rb, and Y, showed trends relative to SiO_2 content, suggesting possible fractionation processes during magma evolution (Figure 6.9).

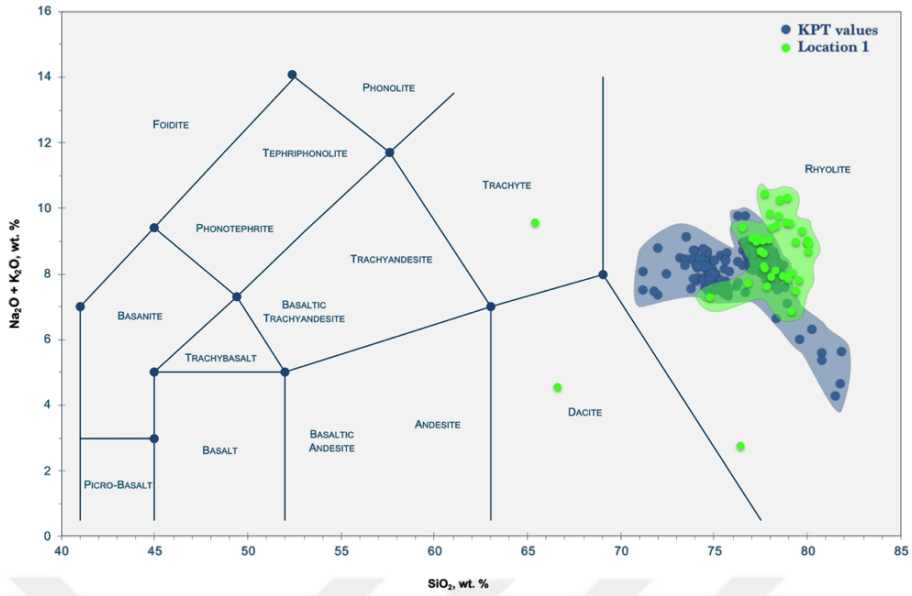

Figure 6.7 This diagram presents a Total Alkali-Silica (TAS) which represents the geochemical composition of the first location's ignimbrite samples. The samples belong to the Rhyolite area categorizing and classifying volcanic rocks based on their alkali ($K_2O + Na_2O$) and silica (SiO_2) content

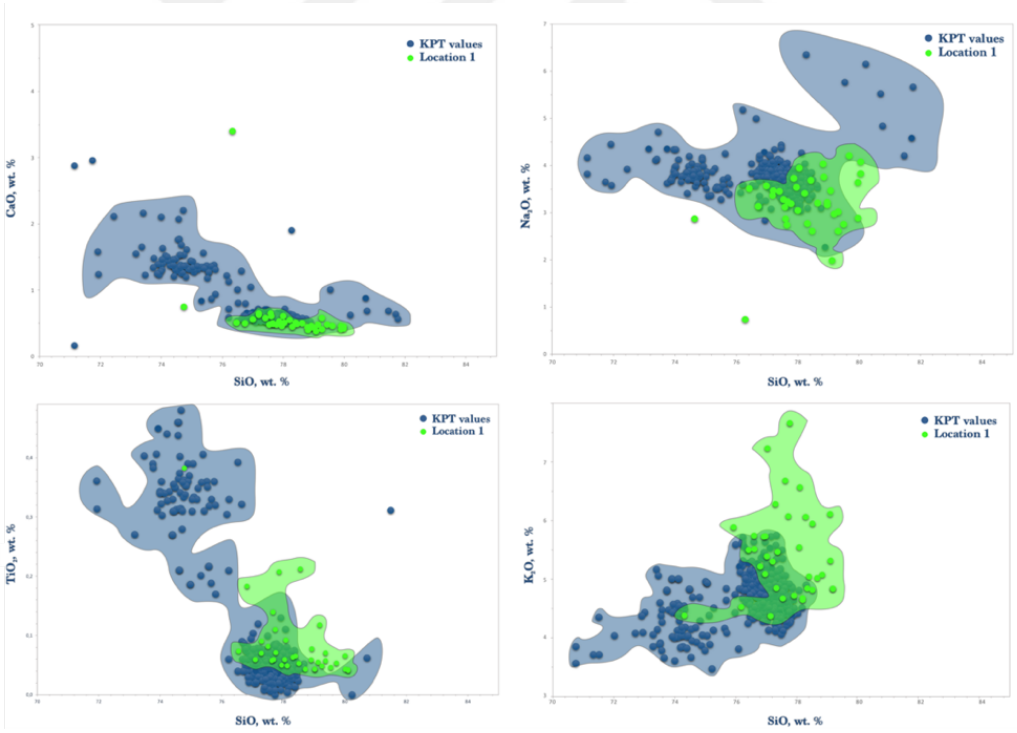

Figure 6.8 This figure presents a series of geochemical diagrams showcasing key elemental ratios, including SiO_2/CaO, SiO_2/Na_2O, SiO_2/TiO_2, and SiO_2/K_2O. These diagrams offer valuable insights into the compositional variations and petrological characteristics of the studied volcanic materials

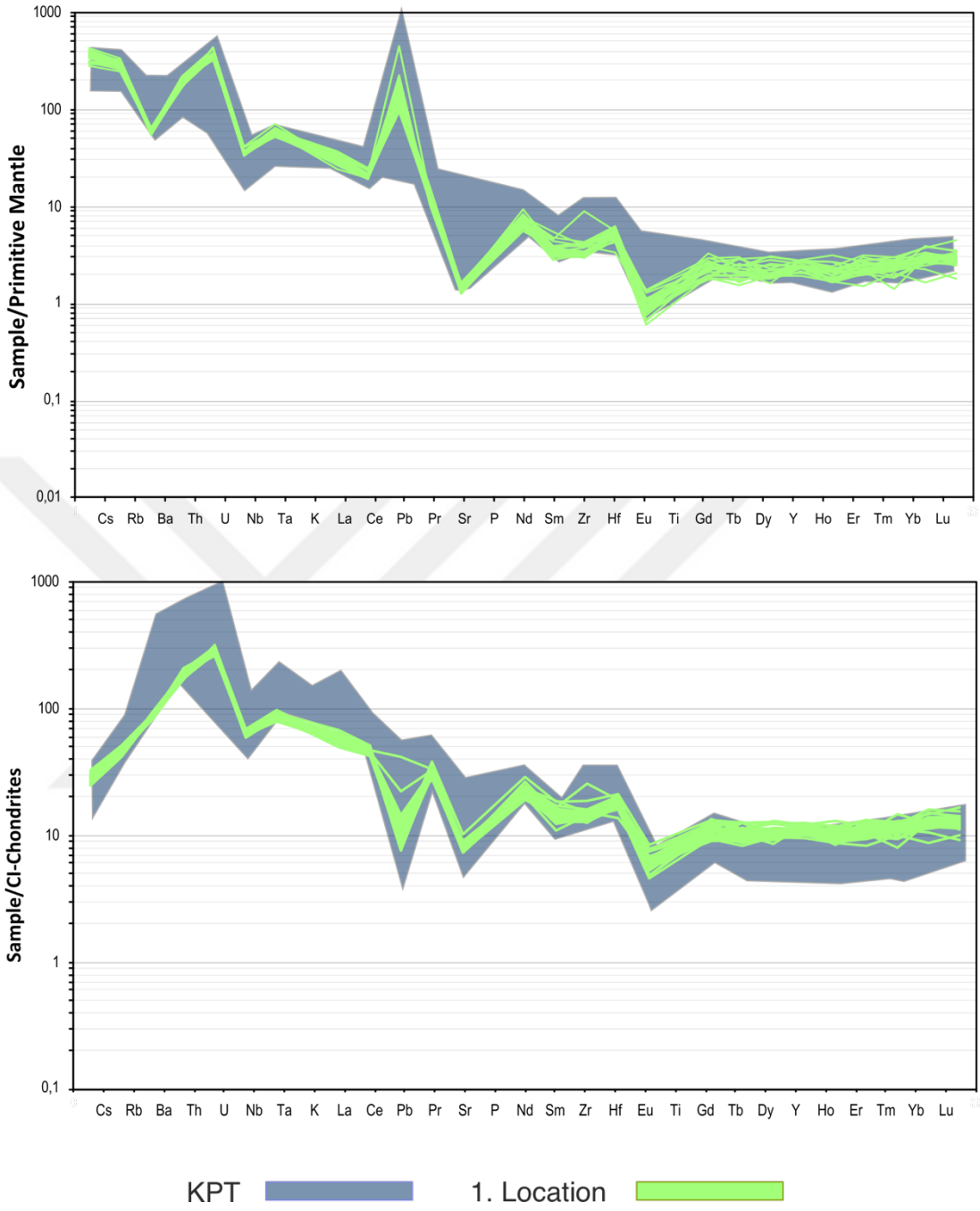

Figure 6.9 By analyzing the glass shards and pumices that were normalized to 'primitive mantle', the previous studies' values of KPT and the rare earth and trace element profiles (blue area) were compared with the rare earth and trace element profiles of the first location of PDC units on the Bodrum Peninsula (green area)

6.2.2 Location 2.

It was analyzed 3 different mounts in major elements and trace elements which are lithic pumice - bolder pumice (BPB), juvenile pumice - tiny pumice (TPB), and fine graded ash - glass shards (GLB). This geochemical study conducted a comprehensive analysis of major elements on volcanic samples collected from the Bodrum peninsula.

- SiO_2 content: BPB (**76.60**% - **79.95**%), TPB (**77.39**% - **79.74**%), GLB (**64.33**% - **78.52**%)
- Al_2O_3 concentrations: BPB (**10.46-12.62**), TPB (**9.95-12.01**), GLB (**11.62-22.14** %)
- Total Fe_2O_3 content: BPB (**0.56** % **- 1.35**%), TPB (**0.49** %**- 0.71**%), GLB (**0.09**%**- 1.39%**)
- CaO range: BPB (**0.44**% - **0.71**%), TPB (**0.46** % - **0.63**%), GLB (**0.10**% **4.45%**)
- Na_2O and K_2O variations: BPB (**2.78** % to **3.95**%**, 5.04**% to **5.89**%), TPB (**2.63** % to **4.21**%**, 4.86**% to **7.64**%), GLB (**0.79** % to **8.84, 0.72**% to **5.41**%)
- TiO_2 range: BPB (**0.10% - 0.12%**), TPB (**0.09% - 0.12%**), GLB (**0.01% - 0.98%**).

The volcanic samples were classified as **rhyolite** based on their alkali and silica content using the **Total Alkali-Silica (TAS)** diagram for geochemical characterization (Figure, 6.10 and Figure 6.11). Also, the trace elements values of the 2. locations samples taken from the Bodrum peninsula PDC units match perfectly with KPT's previous value, too. Elements like Ba showed concentrations between **401.2** ppm and **12932.4** ppm from glass shards; **343.4** ppm and **430.5** from the juvenile pumice; **362.7** ppm and **412.5** ppm from the lithic pumice potentially reflecting the influence of different source rocks and magmatic differentiation. The behavior of other trace elements, such as Sr, Rb, and Y, showed trends relative to SiO_2 content, suggesting possible fractionation processes during magma evolution (Figure, 6.12).

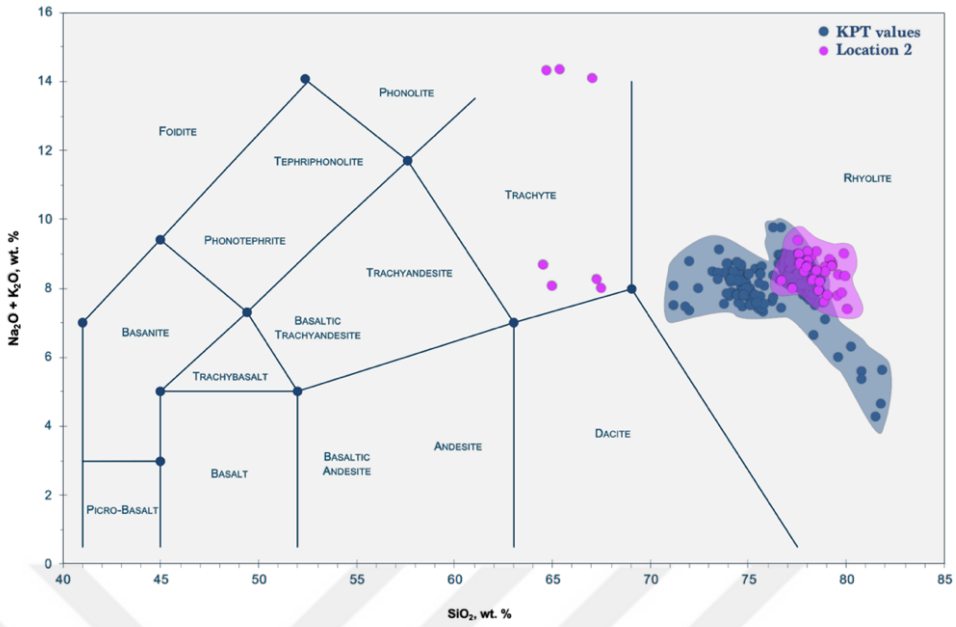

Figure 6.10 This diagram presents a Total Alkali-Silica (TAS) which represents the geochemical composition of the second location's ignimbrite samples. The samples belong to the Rhyolite area categorizing and classifying volcanic rocks based on their alkali ($K_2O + Na_2O$) and silica (SiO_2) content

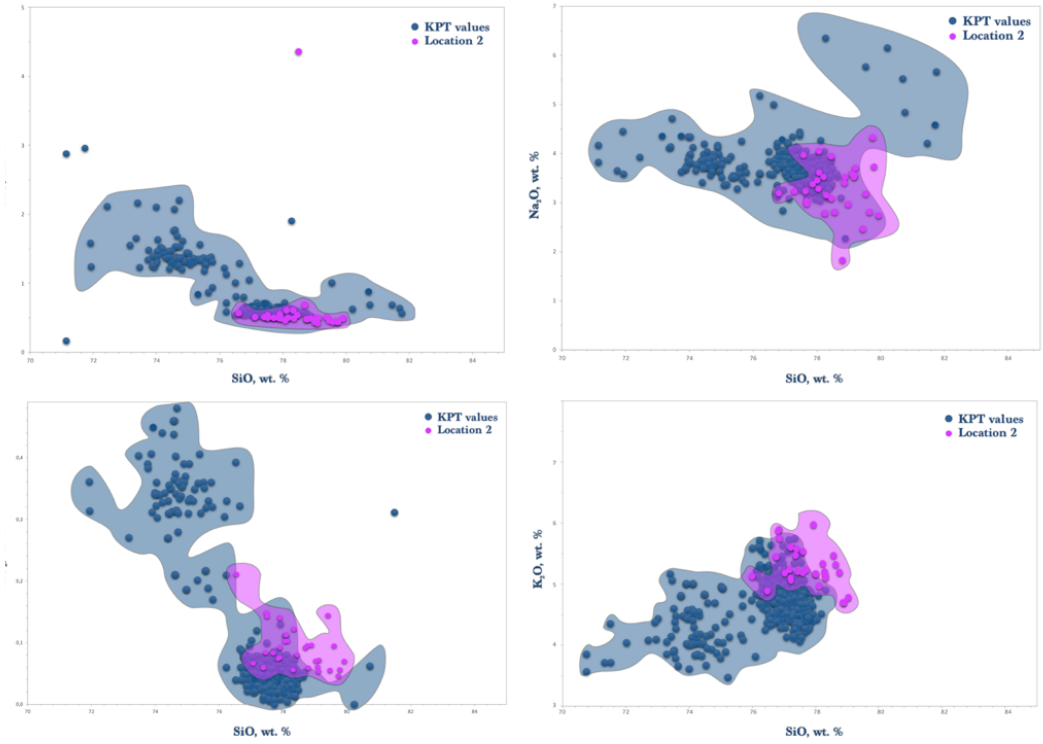

Figure 6.11 This figure presents a series of geochemical diagrams showcasing key elemental ratios, including SiO_2/CaO, SiO_2/Na_2O, $SiO2/TiO_2$, and SiO_2/K_2O. These diagrams offer valuable insights into the compositional variations and petrological characteristics of the studied volcanic materials

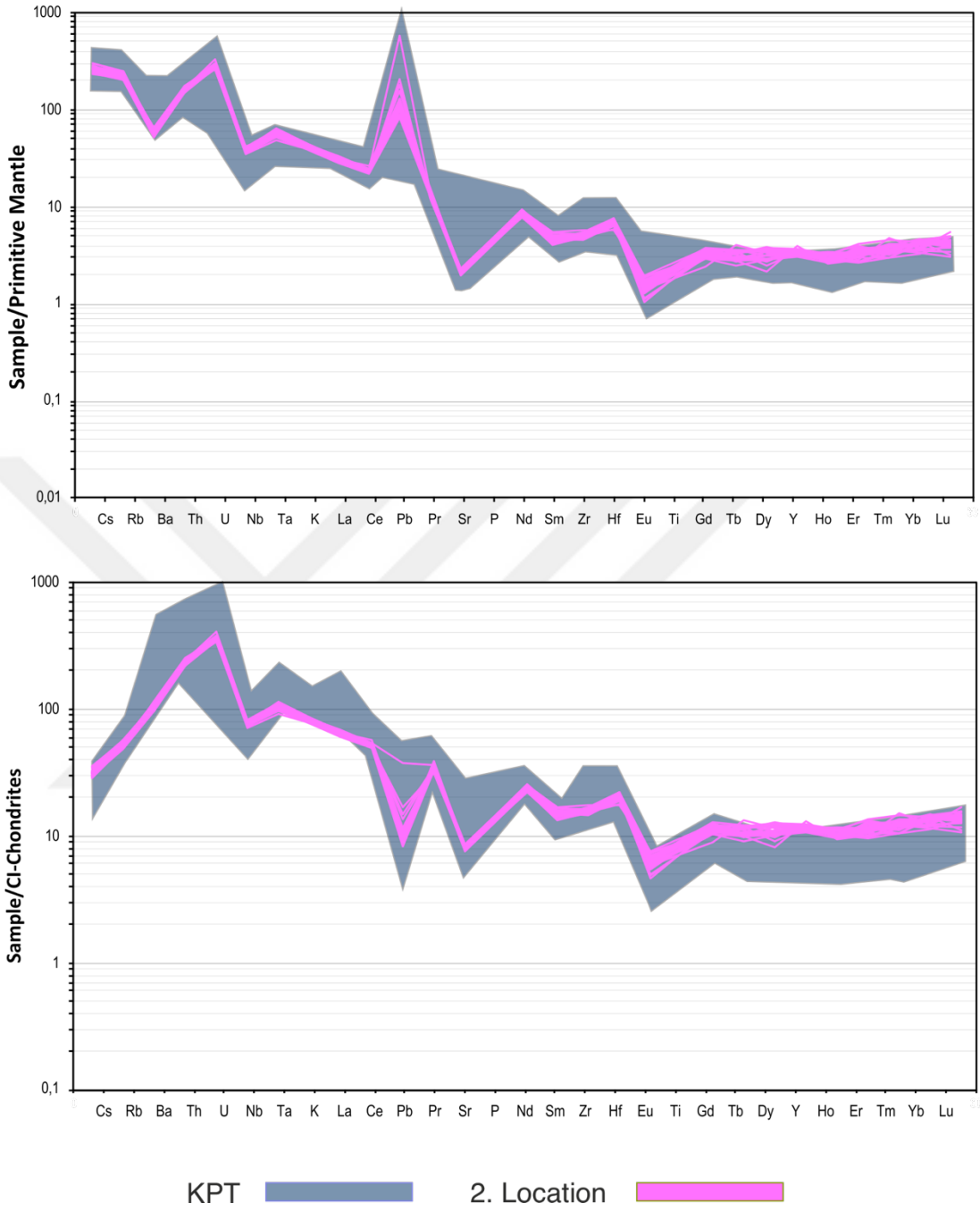

Figure 6.12 By analyzing the glass shards and pumices that were normalized to 'primitive mantle', the previous studies' values of KPT and the rare earth and trace element profiles (blue area) were compared with the rare earth and trace element profiles of the second location of PDC units on the Bodrum Peninsula (green area)

6.2.3 Location 3.

We analyzed 3 different mounts in major elements and trace elements which are lithic pumice - bolder pumice (BPC), juvenile pumice - tiny pumice (TPC), and fine graded ash - glass shards (GLC). This geochemical study conducted a comprehensive analysis of major elements on volcanic samples collected from the Bodrum peninsula.

- SiO_2 content: BPC (**77.54**% - **81.43**%), TPC (**76.00**% - **80.57**%), GLC (**64.01**% - **78.52**%)
- Al_2O_3 concentrations: BPC (**10.30 - 11.99**), TPC (**9.61-12.18**), GLC (**12.64 -22.14** %)
- Total Fe_2O_3 content: BPC (**0.61** % **- 0.85**%), TPC (**0.62** %**- 1.04**%), GLC (**0.13**%**- 2.40%**)
- CaO range: BPC (**0.46**% - **0.59**%), TPC (**0.42** % - **0.92**%), GLC (**0.40**% **4.06%**)
- Na_2O and K_2O variations: BPC (**1.91**% to **3.51**%**, 4.66**% to **5.61**%), TPC (**2.52** % to **4.28**%**, 4.25** % to **6.63**%), GLC (**2.05** % to **9.05, 0.69**% to **5.37**%)
- TiO_2 range: BPC (**0.09% - 0.11%**), TPC (**0.10% - 0.18%**), GLC (**0.01% - 0.33%**).

The volcanic samples were classified as **rhyolite** based on their alkali and silica content using the **Total Alkali-Silica (TAS)** diagram for geochemical characterization (Figure, 6.13 and Figure 6.14). As the other locations, the trace elements values of the 3. locations samples taken from the Bodrum peninsula PDC units match perfectly with KPT's previous values. Elements like Ba showed concentrations between **341.9** ppm and **408.5** ppm from glass shards; **351.8** ppm and **438.5** from the juvenile pumice; **344.1** ppm and **408.5** ppm from the lithic pumice potentially reflecting the influence of different source rocks and magmatic differentiation. The behavior of other trace elements, such as Sr, Rb, and Y, showed trends relative to SiO_2 content, suggesting possible fractionation processes during magma evolution (Figure, 6.15).

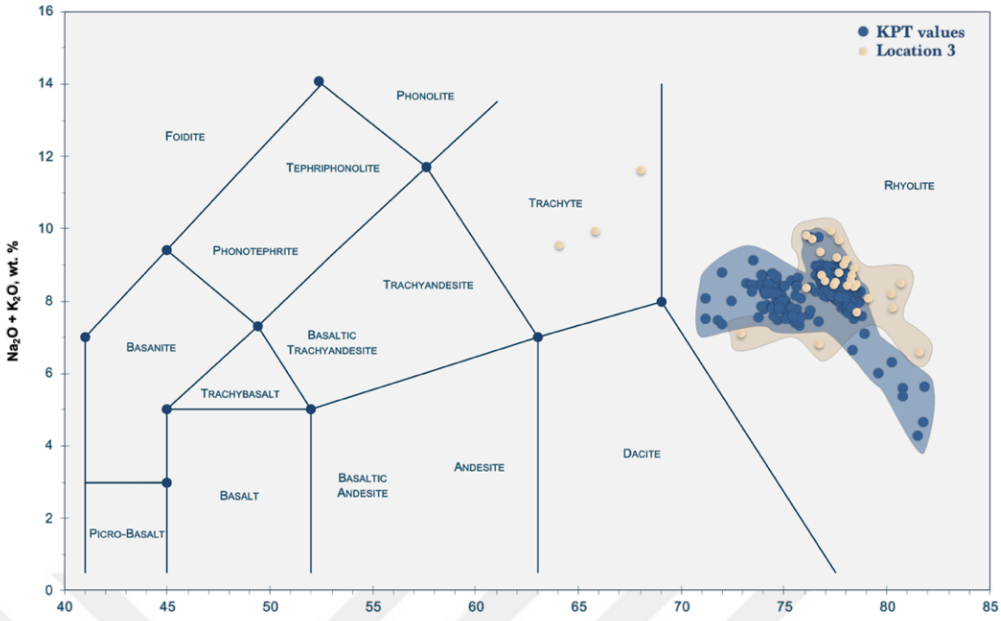

Figure 6.13 This diagram presents a Total Alkali-Silica (TAS) which represents the geochemical composition of the third location's ignimbrite samples. The samples belong to the Rhyolite area categorizing and classifying volcanic rocks based on their alkali ($K_2O + Na_2O$) and silica (SiO_2) content

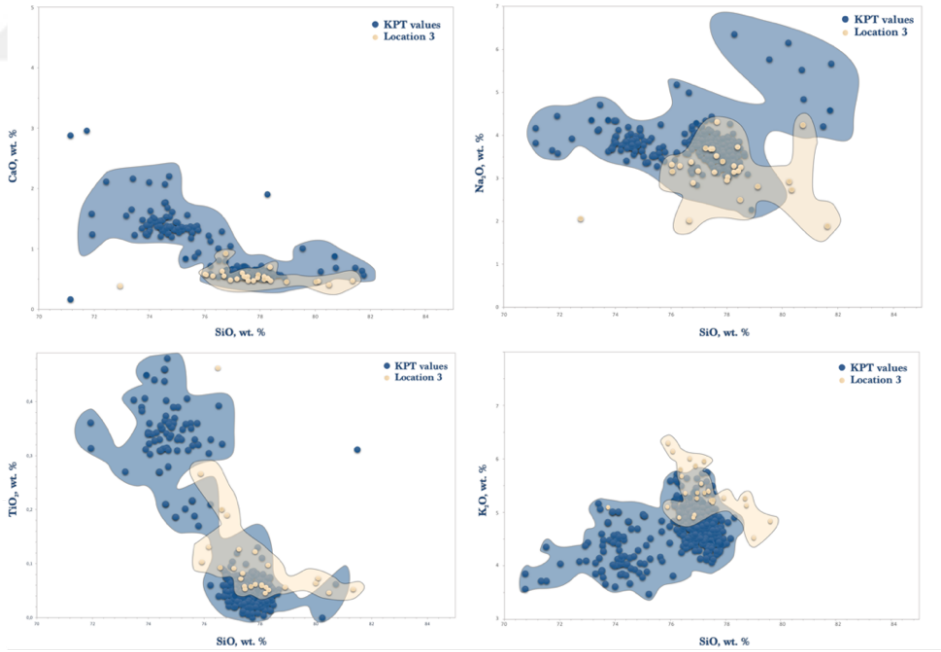

Figure 6.14 This figure presents a series of geochemical diagrams showcasing key elemental ratios, including SiO_2/CaO, SiO_2/Na_2O, SiO_2/TiO_2, and SiO_2/K_2O. These diagrams offer valuable insights into the compositional variations and petrological characteristics of the studied volcanic materials

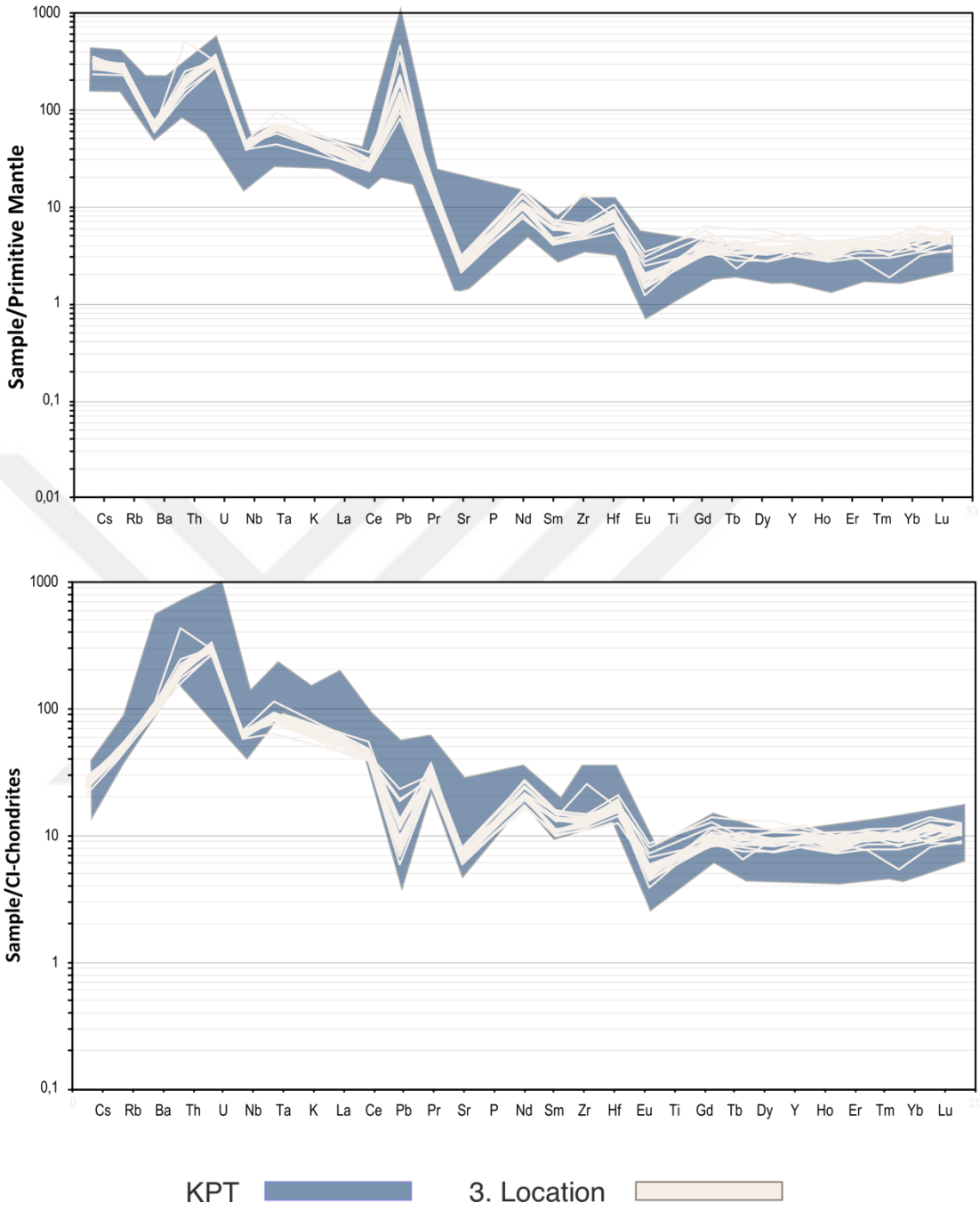

Figure 6.15 By analyzing the glass shards and pumices that were normalized to 'primitive mantle', the previous studies' values of KPT and the rare earth and trace element profiles (blue area) were compared with the rare earth and trace element profiles of the third location of PDC units on the Bodrum Peninsula (creamy area).

6.2.4 Location 4.

It was analyzed 3 different mounts in major elements and trace elements which are lithic pumice - bolder pumice (BPD), juvenile pumice - tiny pumice (TPD), and fine graded ash - glass shards (GLD). This geochemical study conducted a comprehensive analysis of major elements on volcanic samples collected from the Bodrum peninsula.

- SiO_2 content: BPD (**78.16**% - **80.59**%), TPD (**76.95**% - **79.69**%), GLD (**62.22**% - **78.93**%)
- Al_2O_3 concentrations: BPD (**9.56 -11.92**), TPD (**10.33 -12.47**), GLD (**11.64 -23.32**%)
- Total Fe_2O_3 content: BPD (**0.52** % **- 0.72**%), TPD (**0.67** %**- 0.98**%), GLD (**0.16**%**- 0.82 %**)
- CaO range: BPD (**0.38**% - **0.54**%), TPD (**0.46** % - **0.69**%), GLD (**0.50**% **5.38%**)
- Na_2O and K_2O variations: BPD (**2.61** % to **3.33** %**, 4.49**% to **6.01**%), TPD (**2.62** % to **4.11**%**, 4.49**% to **5.59**%), GLD (**2.79** % to **8.25, 0.51**% to **5.14**%)
- TiO_2 range: BPD (**0.09% - 0.11%**), TPD (**0.10 % - 0.17%**), GLD (**0.01% - 0.14%**).

The volcanic samples were classified as **rhyolite** based on their alkali and silica content using the **Total Alkali-Silica (TAS)** diagram for geochemical characterization (Figure, 6.16 and Figure 6.17). As the same patterns of the trace elements values of the 4. locations samples taken from the Bodrum peninsula PDC units match perfectly with KPT's previous values. Elements like Ba showed concentrations between **420.9** ppm and **655.3** ppm from glass shards; **354.5** ppm and **467.9** from the juvenile pumice; **370.2** ppm and **425.3** ppm from the lithic pumice potentially reflecting the influence of different source rocks and magmatic differentiation. The behavior of other trace elements, such as Sr, Rb, and Y, showed trends relative to SiO_2 content, suggesting possible fractionation processes during magma evolution (Figure, 6.18).

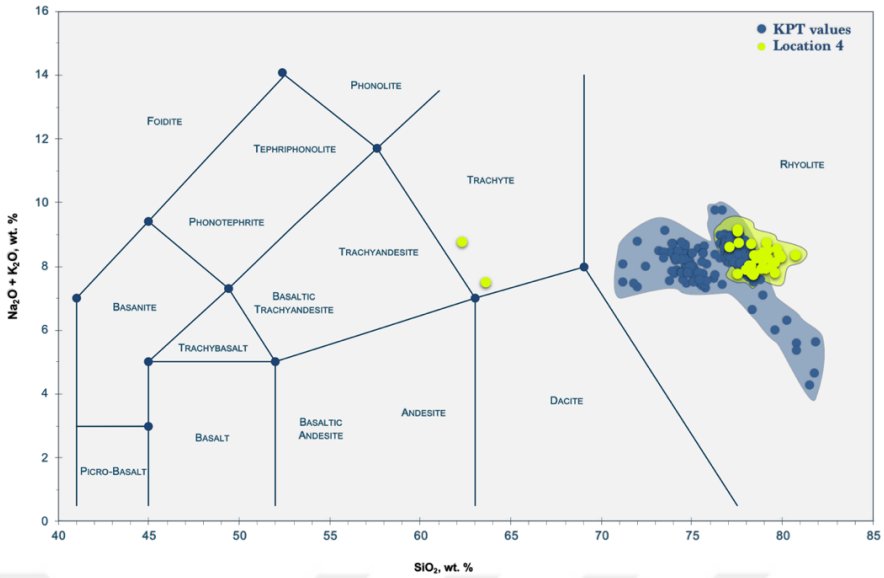

Figure 6.16 This diagram presents a Total Alkali-Silica (TAS) which represents the geochemical composition of the fourth location's ignimbrite samples. The samples belong to the Rhyolite area categorizing and classifying volcanic rocks based on their alkali ($K_2O + Na_2O$) and silica (SiO_2) content

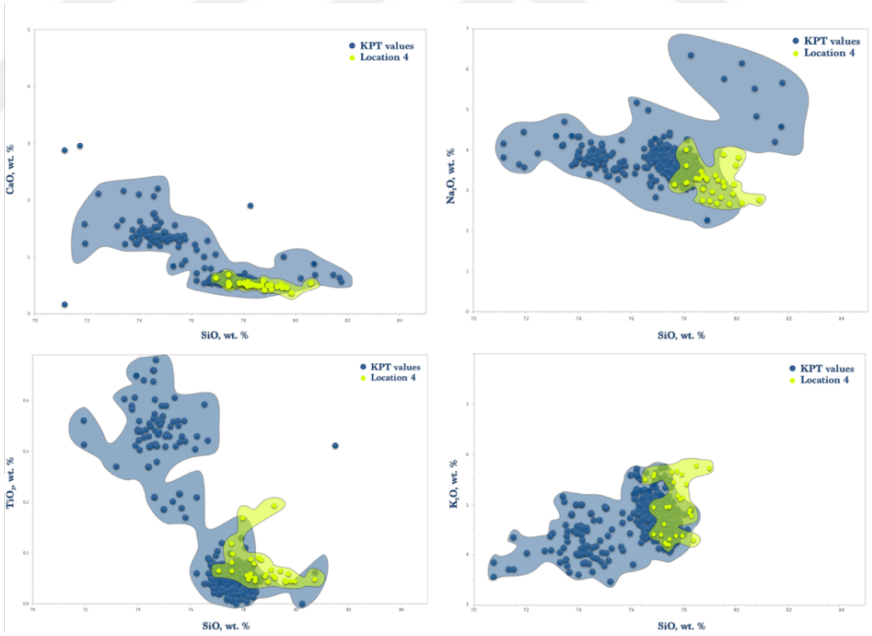

Figure 6.17 This figure presents a series of geochemical diagrams showcasing key elemental ratios, including SiO_2/CaO, SiO_2/Na_2O, SiO_2/TiO_2, and SiO_2/K_2O. These diagrams offer valuable insights into the compositional variations and petrological characteristics of the studied volcanic materials

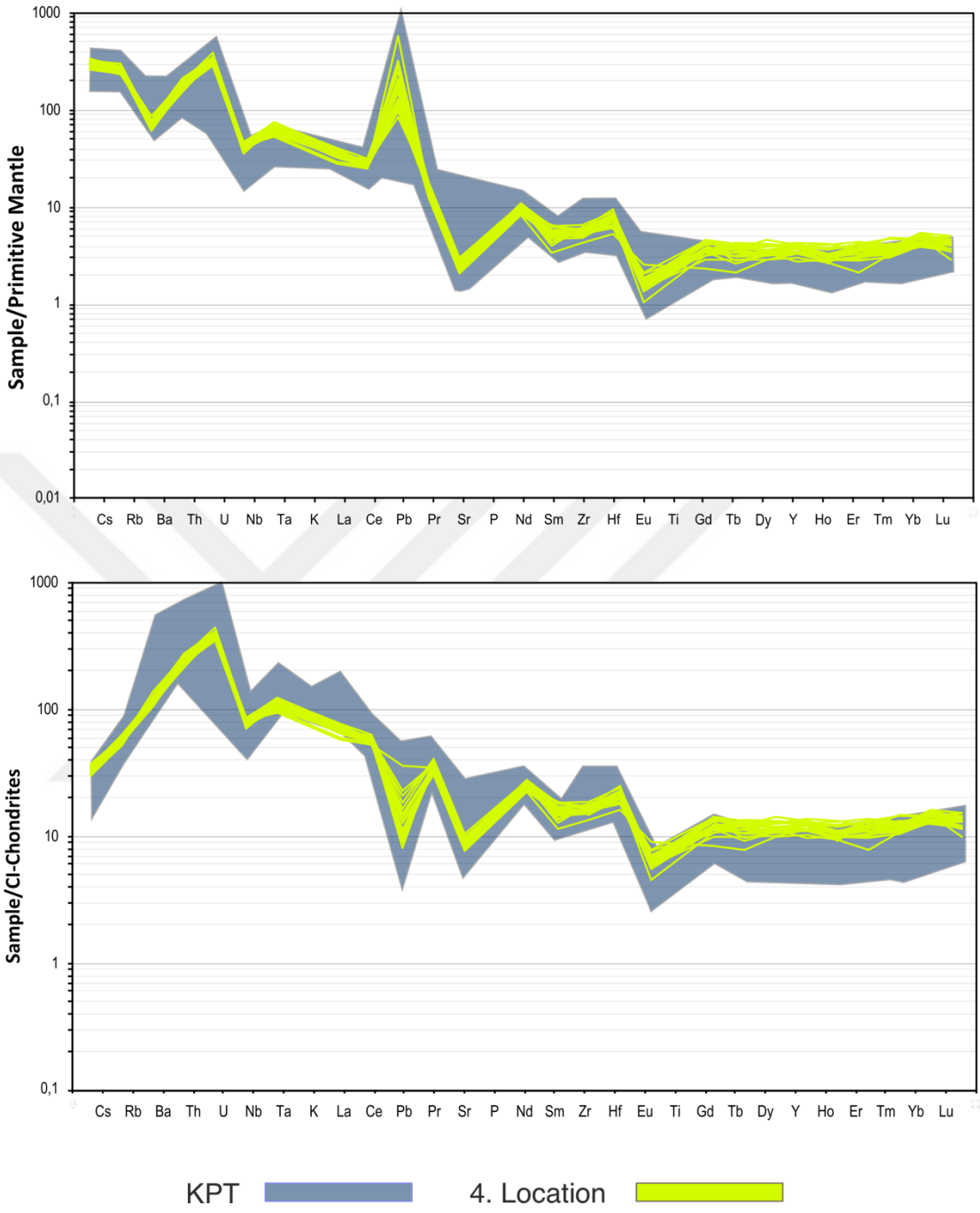

Figure 6.18 By analyzing the glass shards and pumices that were normalized to 'primitive mantle', the previous studies' values of KPT and the rare earth and trace element profiles (blue area) were compared with the rare earth and trace element profiles of the fourth location of PDC units on the Bodrum Peninsula (yellow area)

6.2.5 Location 5.

It was analyzed 3 different mounts in major elements and trace elements which are lithic pumice - bolder pumice (BPE), juvenile pumice - tiny pumice (TPE), and fine graded ash - glass shards (GLE). This geochemical study conducted a comprehensive analysis of major elements on volcanic samples collected from the Bodrum peninsula.

- SiO_2 content: BPE (**77.50**% - **79.68**%), TPE (**76.60**% - **80.28**%), GLE (**65.52**% - **78.67**%).
- Al_2O_3 concentrations: BPE (**10.79 -11.88**), TPE (**9.50 -12.22**), GLE (**11.7-20.74** %).
- Total Fe_2O_3 content: BPE (**0.48** % **- 1.02**%), TPE (**0,59** %**- 0,83**%), GLE (**0,13**%**- 1.39%**).
- CaO range: BPE (**0.50**% - **0.74**%), TPE (**0.44** % - **0.67**%), GLE (**0.51**%-**3.82%**).
- Na_2O and K_2O variations: BPE (**2.77** % - **3.75**%**, 4.86**% to **5.60**%), TPE (**2.76** % -**3.92**%**, 4.65** % to **5.65**%), GLE (**2.85**% to **8.90, 0.74**% to **5.05**%).
- TiO_2 range: BPE (**0.10% - 0.11%**), TPE (**0.10 % - 0.15%**), GLE (**0.01% - 0.19%**).

The volcanic samples were classified as **rhyolite** based on their alkali and silica content using the **Total Alkali-Silica (TAS)** diagram for geochemical characterization. (Figure, 6.19 and Figure 6.20). As the same patterns of the trace elements values of the 5. locations samples taken from the Bodrum peninsula PDC units match perfectly with KPT's previous values. Elements like Ba showed concentrations between **412.1** ppm and **612.9** ppm from glass shards; **375.6** ppm and **4080.3** from the juvenile pumice; **364.1** ppm and **440.9** ppm from the lithic pumice potentially reflecting the influence of different source rocks and magmatic differentiation. The behavior of other trace elements, such as Sr, Rb, and Y, showed trends relative to SiO_2 content, suggesting possible fractionation processes during magma evolution (Figure, 6.21).

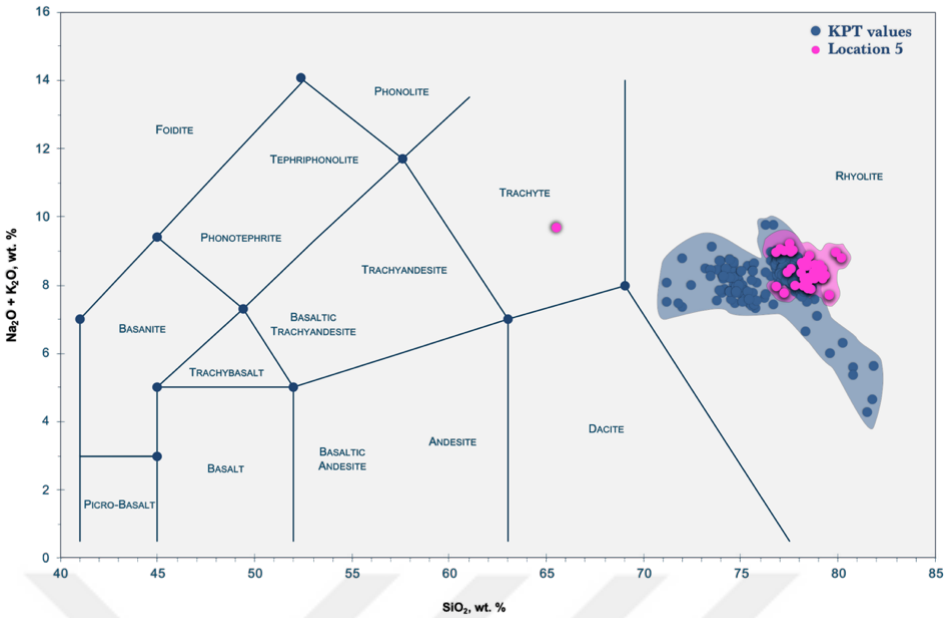

Figure 6.19 This diagram presents a Total Alkali-Silica (TAS) which represents the geochemical composition of the fifth location's ignimbrite samples. The samples belong to the Rhyolite area categorizing and classifying volcanic rocks based on their alkali ($K_2O + Na_2O$) and silica (SiO_2) content

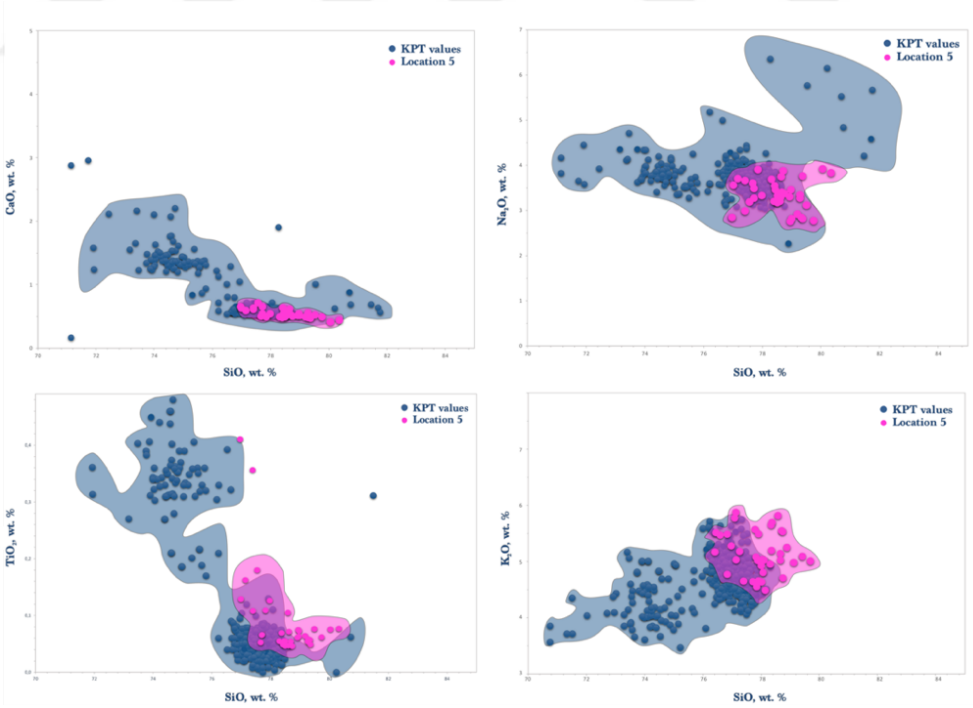

Figure 6.20 This figure presents a series of geochemical diagrams showcasing key elemental ratios, including SiO_2/CaO, SiO_2/Na_2O, SiO_2/TiO_2, and SiO_2/K_2O. These diagrams offer valuable insights into the compositional variations and petrological characteristics of the studied volcanic materials

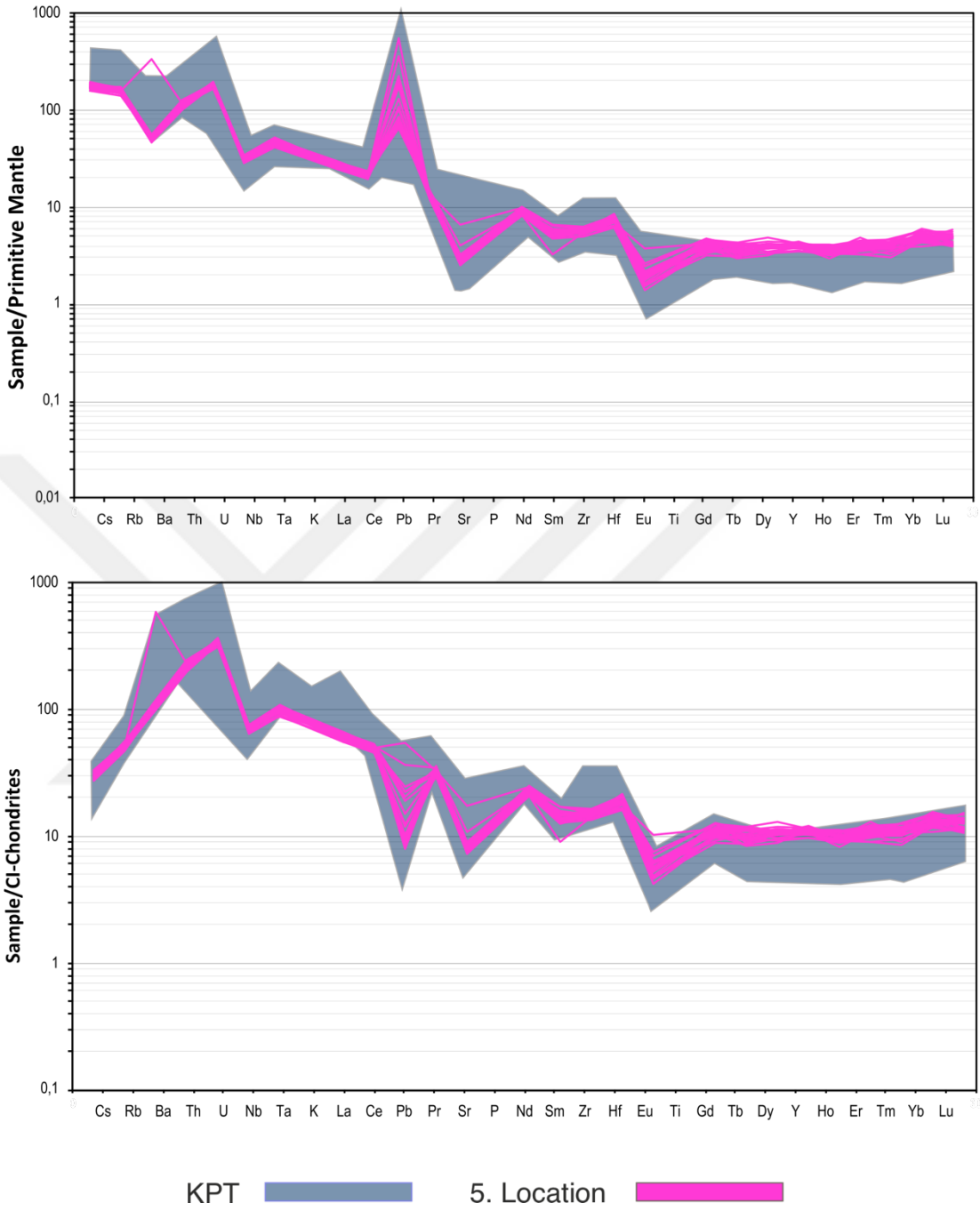

Figure 6.21 By analyzing the glass shards and pumices that were normalized to 'primitive mantle', the previous studies' values of KPT and the rare earth and trace element profiles (blue area) were compared with the rare earth and trace element profiles of the fifth location of PDC units on the Bodrum Peninsula (pink area)

6.3 Results

In the field of geochemistry, understanding the composition of volcanic rocks is pivotal to unraveling the volcanological process and sources of the volcano. One significant aspect of this study involves the assessment of the first-time analysis of KPT ignimbrite on the Bodrum Peninsula. The geochemical investigation, employed a range of diagrams and geochemical parameters to gain deeper insights into the kinships and volcanic processes of the Bodrum ignimbrite and KPT.

The AFM values indicate a calc-alkaline nature, suggesting a subduction-related origin for the studied rocks. Additionally, the TAS classification places them within the rhyolite compositional field, indicative of their evolved silicic nature. The high K_2O-SiO_2 ratios observed in these samples align with the characteristics of high rhyolite compositions. Notably, the SiO_2/Zr ratio, in conjunction with Bodrum and KPT values, delineates distinct areas within the $T < T_{sat}$ zircon field, shedding light on the temperature conditions and zircon saturation states during magma crystallization. Additionally, the SiO_2/MgO ratio reveals overlapping areas that align with specific geochemical trends, exemplified by an arrow indicating shared characteristics. The SiO_2/Sr diagram highlights the complexity of petrogenesis, as some Bodrum samples exhibit features indicative of high-pressure differentiation and carbonate assimilation, whereas KPT values are confined to the LLD (Low La/Yb) areas. Furthermore, the Ba/Rb diagram provides valuable insights into sanidine fractionation processes. Among these diagrams, the SiO_2-Y diagram is employed to unravel the relationships between silica content and yttrium, shedding light on the evolution of these volcanic rocks in terms of silicic character and yttrium enrichment. Meanwhile, the Ce/Gd-Ba/Rb diagram offers valuable insights into the role of cerium and gadolinium in relation to barium and rubidium, further elucidating the geochemical processes that have shaped the Bodrum and KPT formations. The TiO_2-K_2O diagram provides a window into the titania and potassium oxide interplay, aiding in our understanding of the magmatic processes at play. In parallel, the MgO-FeO diagram is employed to scrutinize the variations in magnesium oxide and ferrous oxide content, offering clues about magma evolution. The Rb-Zr/Nb diagram allows us to discern the geochemical

signatures of rubidium, zirconium, and niobium, unraveling their significance in the context of these volcanic formations. The Y/Nb diagram unravels mixing patterns or early amphibole fractionation within these volcanic formations, contributing to a comprehensive understanding of their geochemical evolution. Finally, the Al_2O_3-TiO_2 diagram serves as a valuable tool to explore the alumina-titania relationship, enriching our comprehension of the petrogenetic processes that have shaped these rocks. Each of these diagrams shows the perfect match of the Bodrum ignimbrite and KPT. Also, tells us about geochemistry and petrology, allowing us to piece together more.

CHAPTER SEVEN
DISCUSSION

7.1 Comparing with Previous Study

In this chapter, we discuss and interpret the findings of this study, with a focus on comparing them to previous research conducted by Allen & Cas in 1998a, 1998b, and 2001, as well as those by Allen et al. in 1999, and Allen & McPhie in 2001 and their exploring sedimentological and physical volcanological interpretations. The comparison aims to shed light on the emplacement and transportation mechanisms of PDC during the KPT eruption on the Bodrum Peninsula.

Location 1: Predominantly a massive, pumice-lapilli-dominated, very poorly sorted ignimbrite. Lithic-rich, with sharp lithic fragments up to 11.1 cm. Pumice size up to 7.2 cm. The matrix is ash-supported. Presence of fine lithics in the lower part and fine ash-rich in the upper part. Described as "Pumice-Lapilli Dominated Massive Ignimbrite Facies with Accretionary Lapilli."

Location 2: Similar to Location 1, it's predominantly a massive, pumice-lapilli dominated, very poorly sorted ignimbrite. Lithic content with rounded lithic fragments up to 7.4 cm. Pumice size up to 18.3 cm. Presence of accretionary lapilli. Described as "Fresh Pumice-Lapilli Dominated Massive Ignimbrite Facies with Accretionary Lapilli."

Location 3: Predominantly a massive, pumice-lapilli-dominated, very poorly sorted ignimbrite. Lithic-rich with sharp lithic fragments up to 13 cm. Pumice size up to 18 cm. Intercalations of fine ash and lapilli-rich material. Described as "Pumice-Lapilli Dominated Massive Ignimbrite Facies with Lithic-Rich Middle Layer and Accretionary Lapilli."

Location 4: Predominantly a massive, pumice-lapilli-dominated, very poorly sorted ignimbrite. Lithic-rich with rounded lithic fragments up to 17 cm. Pumice size

up to 22 cm. Presence of coignimbrite ash-cloud layer. Described as "Pumice-Lapilli Dominated Massive Ignimbrite Facies with Coignimbritic Ash-Cloud Layer and Accretionary Lapilli."

Location 5: Predominantly a massive, pumice-lapilli-dominated, very poorly sorted ignimbrite. Maximum pumice size of 26.5 cm. Presence of large pumice blocks. No observed accretionary lapilli. Described as "Pumice-Lapilli Dominated Massive Ignimbrite Facies with Large Pumice Blocks."

During the fieldwork studies, multiple flow units were observed. To identify which units matched within, grain size distribution diagrams were used. As a result:

- Grain Size Distribution Correlation: Grain size distribution analysis not only correlates with previous findings but also reveals variations within particular layers, suggesting complex flow dynamics during the KPT eruption. Comparing sorting/MD values between values on the Bodrum Peninsula, the data aligns with the given diagram in previous publications (Figure, 7.1). Especially matched with ***D and E units***.
- Pie Diagram for Max Clast Size: Pie diagrams displaying max clast size values exhibit intriguing patterns, especially in ***units C, D, and E,*** which align with Allen's observations (Figure, 7.2). These diagrams provide a basis for understanding the dynamics of PDCs and their interaction with the environment and considering the event that collapses.
- Unit contents: The presence of abundant shell fragments, including bivalvia and turritella, suggests a marine influence in this location (Figure, 7.3). Notably, Locations 4 and 5 are situated at a higher elevation than the present sea level, emphasizing the significance of past sea level variation.

7.2 Tectonic Settling

- Numerous researchers have mentioned that approximately 161 ka, the global sea level was around 60-80 meters lower than the present level, both before and during the Kos-Nisyros volcanic activity (Flemming, 1978; Le Pichon &

Angelier, 1981; Chappell & Shackleton, 1986; Pasteels et al., 1986; Allen & Cas, 1998; Allen & McPhie, 2001; Allen & Cas, 2001; Piper & Pe-Piper, 2020). Ulusoy's 2002 doctoral thesis discussed sea-level changes in the Bodrum peninsula. His primary research aimed to uncover the tectonic evolution of the Bodrum caldera and revealed findings that confirmed the relationship between the KPT units and the sea. Murray-Wallache (2007) and Doğan and Özer (2011) have discussed the impact of glacier changes on sea level changes. According to Lambeck et al. (2001), the sea level dropped to -125 m during the last ice age and started to rise with the melting of glaciers after the last glacial maximum. Many studies have noted that the rate of rise in sea level increased until about 6000 years ago and then decreased (Kayan, 2012). According to Zobu's (2023) findings, the northern shores of Gökova Gulf and the southwestern coast of Bodrum demonstrated a tectonic uplift rate of 1.2 mm/year. These researches suggests that the aforementioned regions are subject to consistent increase and decrease in elevation. It is conceivable that such an occurrence could take place during phases of elevated sea levels.

7.3 Sedimentological complexes

- Topographic Influence and Caldera Collapse: The topographic barrier in the study area has implications for deposit distribution and loss, particularly in the north (Figure 7.3). This influence likely contributed to the variation in deposit density observed. Furthermore, the caldera collapse played a pivotal role in shaping the geological features, resulting in the formation of a sea around the crater and the preservation of marine shell fragments.
- Phoenix Plumes and Oscillatory Behavior: The presence of phoenix plumes and oscillatory behavior within the sedimentary record aligns with theoretical analogs and previous studies. These phenomena are influenced by factors such as recirculation, wind, and interactions with obstacles, offering insights into the complexities of the KPT eruption (Figure 7.3). The intra lithic-rich ignimbritic section is particularly interesting, as it contains the largest lithic clast on the peninsula. As affected areas indicate, this lithic-rich zone may

provide evidence of co-ignimbrite ash clouds and hot pyroclastic material. Location 4 stands out due to the presence of a thin ash fall layer and paleosol. These features indicate variations in depositional processes during the eruption's different phases. Additionally, the stratigraphy here may indicate the interaction between PDCs and coastal environments (Fágure, 7.4). These observations contribute to our understanding of the eruption's dynamics.

- Marine Shells and Beach Deposits (Location 2): Location 2 on Turgutreis displays compelling evidence of a marine influence characterized by the presence of beach deposits and marine shell fragments (Table 7.1; Fágure 7.4). Also, án thás locatáon, there ás a possáble backwashed pebble layer whách occurred effect of the tsunamá These findings suggest a close connection to a marine environment and, it could be occurred tsunami event triggered from the caldera collapse during the KPT eruption.

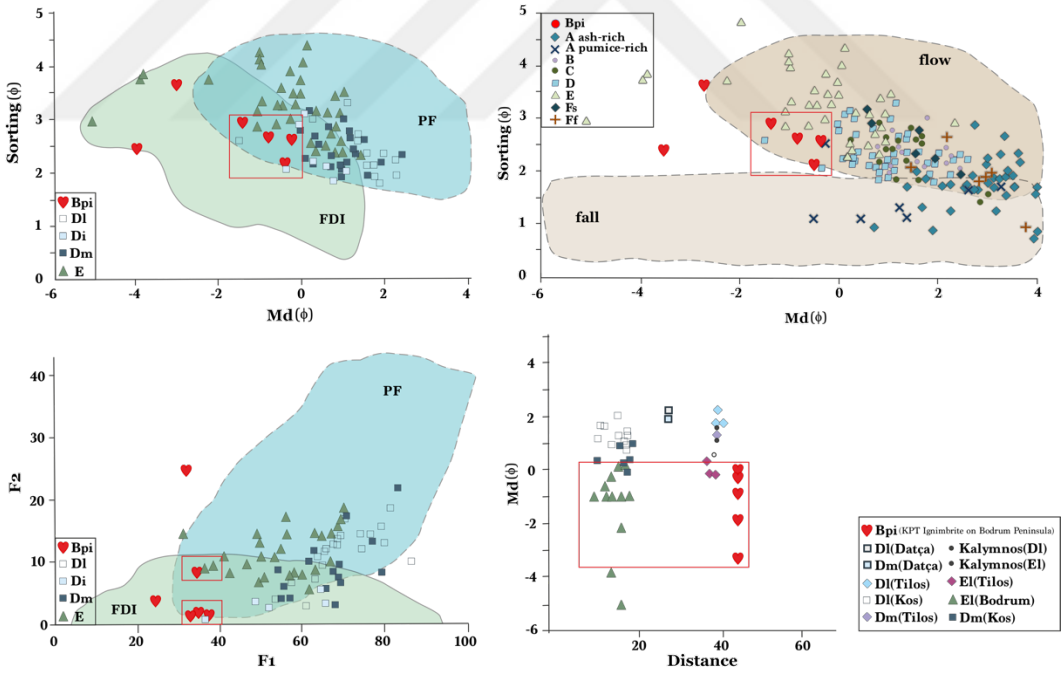

Figure 7.1 Comparing to grain-size data for the KPT units (Allen, 1999) showing fields for pyroclastic fall and flow deposits of Walker (1971)

Table 7.1 A comparative analysis table that highlights the sedimentological and physical volcanological interpretations, is the findings on this study with the prior research conducted by Allen.

	Mentioned in the Previous Study (Allen 2001)	Findings
Unit	El	**Mixed El and Eu or Dm and El (?)**
Thickness	5m	**Max 10m, observed as outcrops in at least 7 locations**
Vitric ash morphology	No specific information but for the El unit; clean cuspate shards and tube pumice	**In one location clean cuspate shards, in the other locations adhere shards, also have bubble-wall fragments; tube, and frothy pumice with ash covered.**
Eruption types and physical parametres	Magmatic-volatile-driven eruption "dry"; Clean tube pumices.	**Adhered glass shards, cross-cut vesicle (bubble wall shards) boundaries rich.**
Transportation Mechanism	Overland	**There should be water relation**

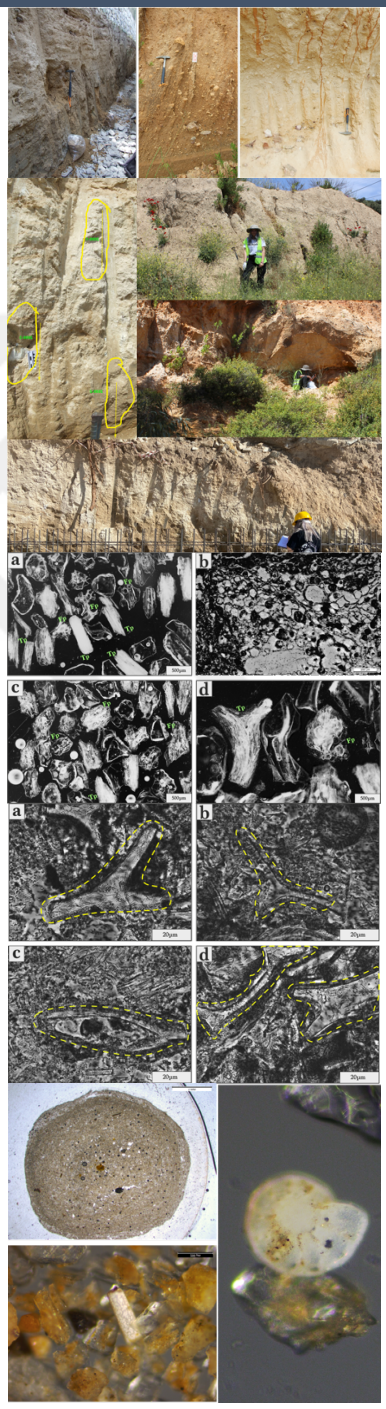

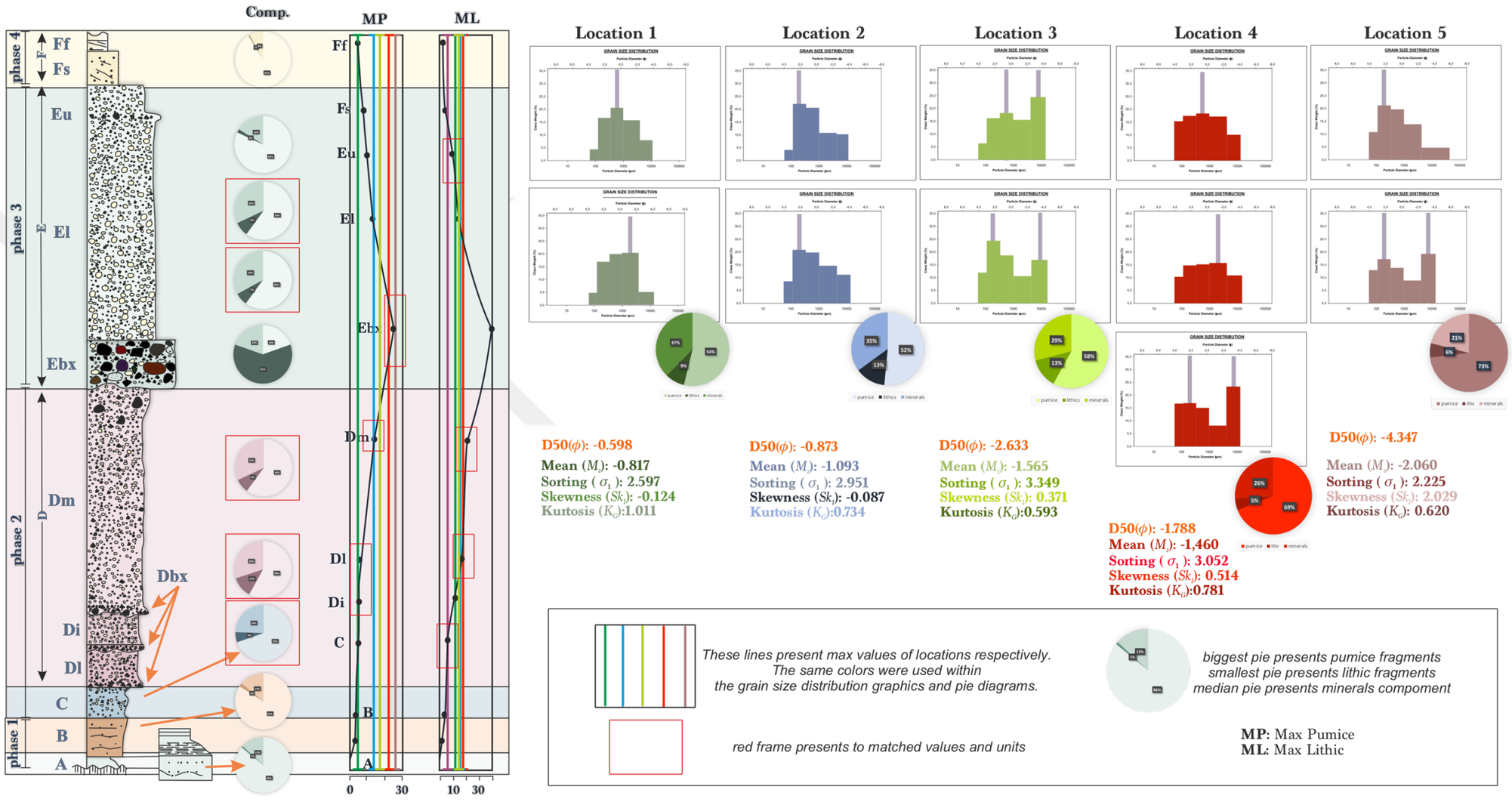

Figure 7.2 Stratigraphy, textural characteristics, and components of the KPT. Grain size and componentry data are averages of all measured exposures on Kos. It has been compared with Allen's 2001 studies' values

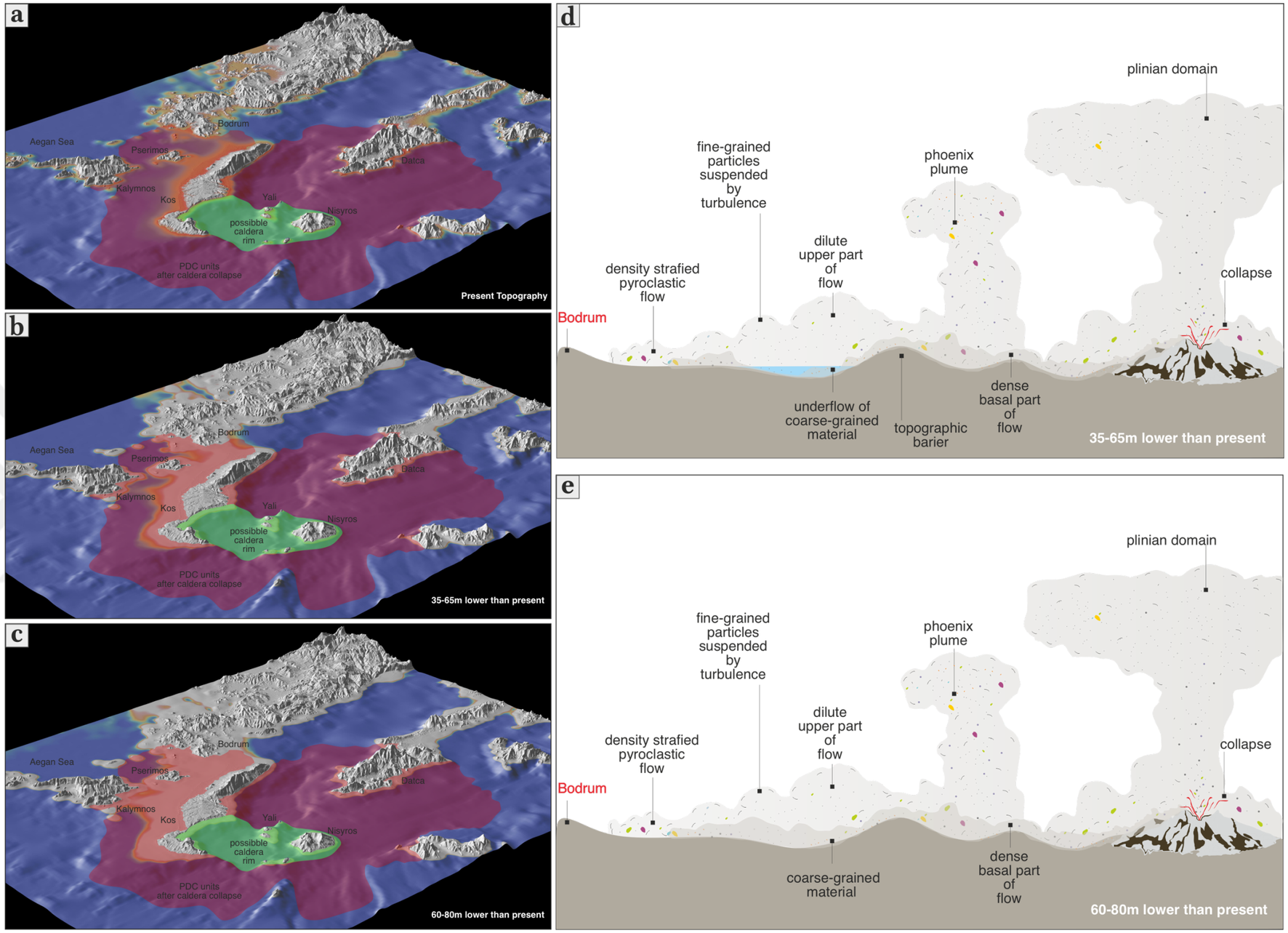

Figure 7.3 Five distinct figures were produced to depict the paleogeography of the area. These include a map(a) showcasing the current topography and the region encompassed by the PDC unit being examined, a secondary map (b) featuring a topography that is roughly 35-65 meters below sea level, a third map (c) depicting a topography lowered by approximately 60-80 meters above sea level, and two additional figures showcasing the approximate topography in the space between the caldera and the Bodrum peninsula when the sea level drops approximately 35-65 meters (d) and 60-80 meters (e), respectively

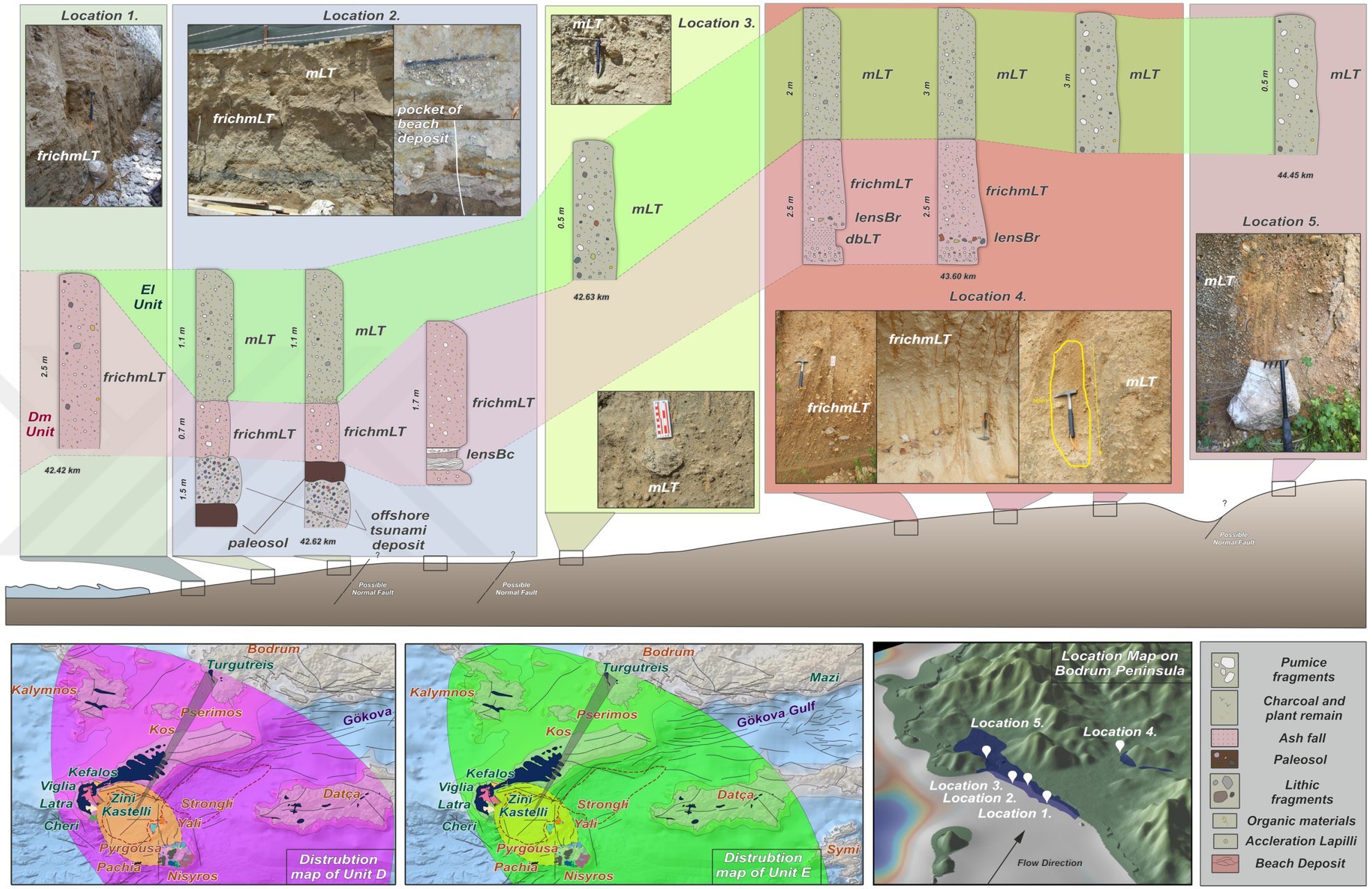

Figure 7.4 Representative stratigraphic sections, distribution of maps, and fieldwork images of KPT on Bodrum Peninsula

CHAPTER EIGHT
RESULTS

This thesis aimed to understand the emplacement and transportation mechanism of pyroclastic density currents by unraveling the internal architecture of an ignimbrite which comprised multiple flow units.

- Were low-density ignimbrites to the north transported by land by catastrophic caldera collapse?
- How do dilute pyroclastic density currents behave result of topographic barrier and caldera collapse?

A combination of detailed fieldwork and closed-spaced sampling for sedimentological geochemical and petrological analysis revealed that multiple, dilute, pyroclastic density currents have complex flow paths and are strongly affected by topography resulting in Phoenix cloud. This master thesis documents the first detailed study of the deposit on the Bodrum Peninsula of the internal architecture of an ignimbrite which comprises multiple flow units. The main conclusions from each chapter are summarized.

8.1 The sedimentological findings of KPT on Bodrum Peninsula

The detailed examination of the volcanic deposits at five distinct locations has yielded valuable insights into the sedimentology and depositional processes of these ignimbrites within a dilute pyroclastic flow regime. Several key conclusions can be drawn from these findings:

The first and most important finding is the transportation mechanism, which has been revealed to be over the sea. This is evidenced by the presence of shell marines, ash aggregate, accretionary lapillus, beach deposits, and backwash pebble layers caused by volcanic tsunamis. This discovery is crucial for future hazard assessments of volcanic activity.

The second conclusion is related to the sorting, mod/median, max lithic and pumice values, content percentages, as well as stratigraphic positions. These findings not only match the El unit but also reveal a match with Unit D.

Finally, it was observed that topographic barriers affected the findings, and a phenomenon known as the Phoneix cloud occurred.

8.2 Further work as sedimentological studies

While this study has shed light on various aspects of dilute pyroclastic flow deposits, several avenues for further research and exploration emerge:

- Stratigraphic and Chronological Investigations: Develop detailed stratigraphic profiles and consider radiometric dating techniques to establish precise eruption chronologies and eruption frequencies, aiding in hazard assessment.
- Paleoenvironmental Reconstruction: Investigate the paleoenvironmental implications of beach deposits and the presence of marine fragments within the ignimbrite. This could involve paleontological and environmental reconstructions. Also, it could give invaluable information about the sea-level change.
- Volcanic Hazard Assessment: Utilize the knowledge gained from this research to contribute to volcanic hazard assessment and mitigation strategies for areas at risk of dilute pyroclastic flow events.

In conclusion, this study represents a significant step toward understanding the sedimentology and dynamics of dilute pyroclastic flows within a complex volcanic setting. The findings presented here open the door to further exploration and research, offering opportunities to enhance our comprehension of volcanic processes and hazards in the studied region and beyond.

8.3 The petrological findings of KPT on Bodrum Peninsula

The petrological analysis conducted on pyroclastic materials from various locations within the dilute pyroclastic flow regime has provided valuable insights into the mineralogical composition, textures, and features of these materials. These conclusions shed light on the volcanic processes and the complex history of deposition and post-depositional alterations. Key petrological conclusions include:

- Diverse Assemblages and Textures: The materials exhibit diverse mineral assemblages and textures, including the presence of silica gel-like matrices, king banding in biotite, amphibole crystals, and ash aggregates. These features reflect a dynamic volcanic history involving rapid cooling, plastic deformation, and interactions with external fluids.
- Melt Inclusions as Time Capsules: The identification of pyroxene and olivine melt inclusions within quartz and feldspar crystals offers valuable insights into the magmatic processes and eruption dynamics.
  These inclusions serve as time capsules, preserving the compositional and physical characteristics of the magma at the moment of crystal growth, providing information on fractional crystallization, magma mixing, and assimilation.
- Post-Depositional Alterations: The presence of altered pumice and minerals, broken feldspar-quartz minerals, and organic materials suggests post-depositional alterations and dynamic processes affecting the pyroclastic materials after deposition. Understanding these alterations can provide clues about hydrothermal interactions and deformation history.
- Crystal-Rich Zones and Their Significance: The existence of regionally crystal-rich zones between layers of ash and pumices highlights variations in depositional conditions. These zones may signify differences in crystallization rates, magma mixing, or source materials, offering insights into the volcanic system's evolution.

8.4 Further work as petrological studies

The petrological analysis presented in this study opens avenues for further research and exploration into volcanic processes and their implications for physical volcanology:

- Experimental Petrology: Conduct experimental petrology studies to simulate the formation of specific textures and features observed in pyroclastic materials under controlled laboratory conditions. This can provide insights into the processes involved.
- Numerical Modeling: Implement numerical modeling to simulate the formation and alteration of pyroclastic materials in response to various volcanic processes. This can help validate petrological observations and deduce eruption dynamics.
- Hydrothermal Alteration Studies: Investigate the hydrothermal alteration of volcanic materials and its role in post-depositional changes. This can help decipher the interaction between volcanic deposits and external fluids.

8.5 The geochemical findings of KPT on Bodrum Peninsula

The geochemical investigation of the Bodrum and KPT volcanic formations has provided critical insights into their petrogenesis and magmatic processes. Several key geochemical conclusions can be drawn from this comprehensive analysis:

- Calc-Alkaline Nature: The AFM (Alkali-Fe-Mg) classification indicates a calc-alkaline nature for the volcanic rocks, suggesting a subduction-related origin. This finding aligns with the understanding of the geological history of these formations, highlighting their connection to tectonic plate interactions.
- Rhyolitic Compositional Field: The TAS (Total Alkali-Silica) diagram places the volcanic rocks within the rhyolite compositional field, indicating their evolved silicic nature. This composition is consistent with the high-silica content observed in the samples.

- High Rhyolite Compositions: The high K_2O-SiO_2 ratios in these samples are characteristic of high rhyolite compositions, further confirming the silicic nature of the volcanic rocks. This consistent geochemical signature across different locations underscores their shared geological history.

8.6 Further work as geochemical studies

Building upon these geochemical conclusions, further research avenues and investigations can be pursued to enhance our understanding of the geological history and magmatic processes associated with the Bodrum and KPT volcanic formations:

- Isotope Geochemistry: Incorporate isotope geochemistry, such as radiometric dating (e.g., U-Pb, K-Ar), to establish precise eruption ages and constraints on magma sources. Isotopic analyses can also provide insights into mantle-crust interactions.
- Magma Evolution Models: Develop magma evolution models to simulate the formation of specific geochemical trends and compositions observed in the volcanic rocks. Numerical modeling can help validate geochemical interpretations.
- Fluid-Magma Interactions: Investigate the role of fluids (e.g., hydrothermal fluids, magmatic volatiles) in shaping geochemical signatures and alteration processes within volcanic formations.
- Field Studies: Conduct additional field studies to collect more samples from different locations within the volcanic formations to assess variations in geochemical signatures and their spatial distribution.

In conclusion, the geochemical analysis of the Bodrum and KPT volcanic formations has provided valuable information about their petrogenesis and magmatic history. Continued research and interdisciplinary collaborations will further advance our understanding of these geological features and their significance in unraveling the Earth's geological history.

REFERENCE

Akal, C., Ersoy, E.Y., Yücel-Oztürk, Y., Prelevic, P., van den Bogaard, P., Mertz-Kraus, R., 2021. Geochronology and Geochemistry of the Bodrum Magmatic Complex (Mugla- Turkey). In: *73rd Geological Congress of Turkey with International Participation (online)*. The Proceedings and Abstracts Book, pp. 633–634.

Aksu, A. E., Jenner, G., Hiscott, R. N., & İşler, E. B. (2008). Occurrence, stratigraphy and geochemistry of Late Quaternary tephra layers in the Aegean Sea and the Marmara Sea. *Marine Geology*, *252*(3-4), 174-192.

Allen, S. R., & Cas, R. A. (1998). Lateral variations within coarse co-ignimbrite lithic breccias of the Kos Plateau Tuff, Greece. *Bulletin of Volcanology*, *59*(5), 356-377.

Allen, S. R., Stadlbauer, E., & Keller, J. (1999). Stratigraphy of the Kos Plateau Tuff: Product of a major Quaternary explosive rhyolitic eruption in the eastern Aegean, Greece. *International Journal of Earth Sciences*, *88*(1), 132-156.

Allen, S. R. (2001). Reconstruction of a major caldera-forming eruption from pyroclastic deposit characteristics: Kos Plateau Tuff, eastern Aegean Sea. *Journal of Volcanology and Geothermal Research*, *105*(1-2), 141-162.

Allen, S. R., & Cas, R. A. (2001). Transport of pyroclastic flows across the sea during the explosive, rhyolitic eruption of the Kos Plateau Tuff, Greece. *Bulletin of Volcanology*, *62*(6), 441-456.

Allen, S. R., & McPhie, J. (2000). Water-settling and resedimentation of submarine rhyolitic pumice at Yali, eastern Aegean, Greece. *Journal of Volcanology and Geothermal Research*, *95*(1-4), 285-307.

Allen, S., & McPhie, J. (2001). Syn-eruptive chaotic breccia on Kos, Greece, associated with an energetic pyroclastic flow. *Bulletin of Volcanology*, *63*(6), 421-432.

Altherr, R., Keller, J., & Kott, K. (1976). Der jungtertiäre Monzonit von Kos und sein Kontakthof (Ägäis, Griechenland). *Bulletin de la Societe géologique de France*, *7*(2), 403-412.

Altherr, R., & Siebel, W. (2002). I-type plutonism in a continental back-arc setting: Miocene granitoids and monzonites from the central Aegean Sea, Greece. Contributions to Mineralogy and Petrology, 143(4), 397-415.

Altunkaynak, S., & Yilmaz, Y. (2001). The Turgutreis stratovolcano of the Bodrum, SW Anatolia. In International Earth Sciences Colloquium on the Aegean Region, Dokur Eylül University, Izmir, Turkey (pp. 38-46).

Antoniou, V., Nomikou, P., Panousis, D., & Zafeirakopoulou, E. (2021). Nisyros Volcanic Island: A Geosite through a Tailored GIS Story. *Geosciences*, *11*(3), 132.

Antoniou, V., Nomikou, P., Zafeirakopoulou, E., Bardouli, P., & Ioannou, T. (2019, May). Geo-biodiversity and cultural environment of Nisyros volcano. In *Proceedings of the 5th International Congress of the Geological Society of Greece—Bulletin of the Geological Society of Greece, Athens, Greece* (pp. 22-24).

Bachmann, O., Charlier, B. L. A., & Lowenstern, J. B. (2007). Zircon crystallization and recycling in the magma chamber of the rhyolitic Kos Plateau Tuff (Aegean arc). *Geology*, *35*(1), 73-76.

Bachmann, O. (2010). The petrologic evolution and pre-eruptive conditions of the rhyolitic Kos Plateau Tuff (Aegean arc). *Open Geosciences*, *2*(3), 270-305.

Bachmann, O., Schoene, B., Schnyder, C., & Spikings, R. (2010). The 40Ar/39Ar and U/Pb dating of young rhyolites in the Kos-Nisyros volcanic complex, Eastern Aegean Arc, Greece: Age discordance due to excess 40Ar in biotite. *Geochemistry, Geophysics, Geosystems*, *11*(8).

Bachmann, O., Wallace, P. J., & Bourquin, J. (2010). The melt inclusion record from the rhyolitic Kos Plateau Tuff (Aegean Arc). *Contributions to Mineralogy and Petrology*, *159*(2), 187.

Bachmann, O., Allen, S. R., & Bouvet de Maisonneuve, C. (2019). The Kos–Nisyros–Yali Volcanic Field. *Elements: An International Magazine of Mineralogy, Geochemistry, and Petrology*, *15*(3), 191-196.

Beaufort, F. (1817). Karamania, or a Brief Description on the South Cost of Asia Minor.

Bellon, H., & Jarrige J. (1979). L'actıvıte magmatıque neogene et quaternaıre dans l'ıle de Kos (Grecee): Donnees Radıochronologıques. C.R. Acad. Sci. Paris, 288 (1979), pp. 1359-1362.

Bignot, G., & Guernet, C. (1976). Sur la presence de Borelis curdica (Reichel) dans le Miocène de l'ile de Kos (Grèce). *Géologie méditerranéenne*, *3*(1), 15-25.

Bini, G., Chiodini, G., Cardellini, C., Vougioukalakis, G. E., & Bachmann, O. (2019). Diffuse emission of CO2 and convective heat release at Nisyros caldera (Greece). *Journal of Volcanology and Geothermal Research*, *376*, 44-53.

Bini, G., Chiodini, G., Lucchetti, C., Moschini, P., Caliro, S., Mollo, S., & Bachmann, O. (2020). Deep versus shallow sources of CO 2 and Rn from a multi-parametric approach: the case of the Nisyros caldera (Aegean Arc, Greece). *Scientific reports*, *10*(1), 1-16.

Blott, S. J., & Pye, K. (2001). GRADISTAT: a grain size distribution and statistics package for the analysis of unconsolidated sediments. Earth surface processes and Landforms, 26(11), 1237-1248.

Boundelmonti, C. F. (1420) Liber insularum Arcipelagi: XVI secolo, Paris, Biblioteca nazionale di Francia, Fonds Latin, Lat. 4823.

Bouvet de Maisonneuve, C., Bachmann, O., & Burgisser, A. (2009). Characterization of juvenile pyroclasts from the Kos Plateau Tuff (Aegean Arc): insights into the eruptive dynamics of a large rhyolitic eruption. Bulletin of Volcanology, 71, 643-658.

Bouvet de Maisonneuve, C. B., Forni, F., & Bachmann, O. (2021). Magma reservoir evolution during the build up to and recovery from caldera-forming eruptions–A generalizable model? *Earth-Science Reviews*, 103684.

Branney, M. J., & Kokelaar, B. P. (2002). Pyroclastic density currents and the sedimentation of ignimbrites. Geological Society of London.

Braschi, E., Francalanci, L., Tommasini, S., & Vougioukalakis, G. E. (2014). Unraveling the hidden origin and migration of plagioclase phenocrysts by in situ Sr isotopes: the case of final dome activity at Nisyros volcano, Greece. *Contributions to Mineralogy and Petrology*, *167*(3), 988.

Buettner, A., Kleinhanns, I. C., Rufer, D., Hunziker, J. C., & Villa, I. M. (2005). Magma generation at the easternmost section of the Hellenic arc: Hf, Nd, Pb and Sr isotope geochemistry of Nisyros and Yali volcanoes (Greece). *Lithos*, *83*(1-2), 29-46.

Burri, C., Tartar, Y., & Weibel, M. (1967). Zur Kenntnis der jungen Vulkanite der Halbinsel Bodrum. *Schweiz. Mineral. Petrogr. Mitt*, *47*, 833-854.

Caliro, S., Chiodini, G., Galluzzo, D., Granieri, D., La Rocca, M., Saccorotti, G., & Ventura, G. (2005). Recent activity of Nisyros volcano (Greece) inferred from structural, geochemical and seismological data. *Bulletin of Volcanology*, *67*(4), 358-369.

Cas, R. A., & Wright, J. V. (1991). Subaqueous pyroclastic flows and ignimbrites: an assessment. Bulletin of Volcanology, 53, 357-380.

Cas, R., & Wright, J. (1998). Volcanic successions modern and ancient: A geological approach to processes, products and successions. Springer Science & Business Media.

Cassidy, M., Manga, M., Cashman, K., & Bachmann, O. (2018). Controls on explosive-effusive volcanic eruption styles. Nature communications, 9(1), 2839.

Chappell, J., & Shackleton, N. J. (1986). Oxygen isotopes and sea level. Nature, 324(6093), 137-140.

Chiodini, G., Cioni, R., Leonis, C., Marini, L., & Raco, B. (1993). Fluid geochemistry of Nisyros island, Dodecanese, Greece. *Journal of volcanology and geothermal research*, *56*(1-2), 95-112.

Coronelli, V. M., & Parisotti, V. (1968). Isola di Rodi geografica, storica, antica e moderna. Venice.

Çelikbaş, B. (2022). Preparation Of Pedestrian Evacuation Time Maps For Southern Coasts Of Bodrum Peninsula, Turkey (Master's Thesis, Middle East Technical University).

Çiftçi, T. (2010). Datça (Muğla) ve Yakın Dolayının Jeolojisi (Doctoral dissertation, Yüksek Lisans Tezi, Çukurova Üniversitesi Fen Bilimleri Enstitüsü, Adana, 103).

Çubukçu, H. E., Aydar, E., Ulusoy, İ., & Gourgaud, A. (2021). Shoshonitic volcanism of the Bodrum caldera (SW Turkey): Hybridization of enriched mantle-derived and crustal melts. *Journal of Asian Earth Sciences*, *219*, 104901.

Dalabakis, P., & Vougioukalakis, G. (1993). The Kefalos Tuff Ring (W. Kos): depositional mechanisms, vent position and model of the evolution of the eruptive activity. Bull. Geol. Soc. Greece, 28(2), 259-273.

Dalli Sonetti, B. (1485). The Isolario: Negroponte P/21(55), Venice. Greenwich (London): national Maritime Museum.

Davies, B. V., Brown, R. J., Barclay, J., Scarrow, J. H., & Herd, R. A. (2021). Rapid eruptive transitions from low to high intensity explosions and effusive activity: insights from textural analysis of a small-volume trachytic eruption, Ascension Island, South Atlantic. Bulletin of Volcanology, 83, 1-40.

Davis, E.N., 1968, Zur geologie und petrologie der inseln Nysiros und Yali (Dodekanes): Geol. Rdsch., 57/3. 811-821

Degruyter, W., 2010, Investigating volcanic eruptions of silicic magmas using 3D textural analysis and computational fluid dynamics. doi: 10.13097/archive-ouverte/unige:12052

Degruyter, W., Bachmann, O., & Burgisser, A. (2010). Controls on magma permeability in the volcanic conduit during the climactic phase of the Kos Plateau Tuff eruption (Aegean Arc). *Bulletin of Volcanology*, *72*(1), 63-74.

Di Paola, G. M. (1974). Volcanology and petrology of Nisyros island (Dodecanese, Greece). Bulletin Volcanologique, 38, 944-987.

Dietrich, V. J., & Lagios, E. (Eds.). (2017). Nisyros Volcano: The Kos-Yali-Nisyros Volcanic Field. Springer.

Dirik, K., Türkmenoğlu, A., Tuna, N., & Dirican, M. (2003). Datça Yarımadası'nın neotektoniği, jeomorfolojisi ve bunların eski medeniyetlerin yerleşimi ve gelişimi üzerindeki etkisi. *Orta Doğu Teknik Üniversitesi AFP-00-07-03-13 No'lu Proje*.

Doutsos, T., & Kokkalas, S. (2001). Stress and deformation patterns in the Aegean region. Journal of Structural Geology, 23(2-3), 455-472.

Dufek, J., & Bergantz, G. W. (2007). Dynamics and deposits generated by the Kos Plateau Tuff eruption: Controls of basal particle loss on pyroclastic flow transport. Geochemistry, Geophysics, Geosystems, 8(12).

Ercan, T., Türkecan, A. ve Günay, E., (1982), Bodrum yarımadasının jeolojisi: Maden Tetkik Arama Enst. Derg., 97/98, 21-32.

Ercan, T., Günay, E., Baş, H., & Can, B. (1984). Datça Yarımadasındaki Kuvaterner yaşlı volkanik kayaların stratigrafisi ve yapısı. *MTA Dergisi*, *97*, 45-46.

Ersoy, Ş. (1991). Datça (Muğla) yarımadasının stratigrafisi ve tektoniği. *Türkiye Jeoloji Bülteni C*, *34*, 1-14.

Ersoy, E. Y., & Palmer, M. R. (2013). Eocene-Quaternary magmatic activity in the Aegean: Implications for mantle metasomatism and magma genesis in an evolving orogeny. *Lithos*, *180*, 5-24.

Federman, A. N., & Carey, S. N. (1980). Electron microprobe correlation of tephra layers from eastern Mediterranean abyssal sediments and the island of Santorini. *Quaternary research*, *13*(2), 160-171.

Fiedrich, A. M., Laurent, O., Heinrich, C. A., & Bachmann, O. (2020). Melt and fluid evolution in an upper-crustal magma reservoir, preserved by inclusions in juvenile clasts from the Kos Plateau Tuff, Aegean Arc, Greece. Geochimica et Cosmochimica Acta, 280, 237-262.

Fisher, R. V., & Schmincke, H. U. (1984). Pyroclastic flow deposits. Pyroclastic rocks, 186-230.

Flemming, N. C. (1978). Holocene eustatic changes and coastal tectonics in the northeast Mediterranean: implications for models of crustal consumption. Philosophical Transactions of the Royal Society of London. Series A, Mathematical and Physical Sciences, 289(1362), 405-458.

Francalanci, L., Varekamp, J. C., Vougioukalakis, G., Delant, M. J., Innocenti, F., & Manetti, P. (1995). Crystal retention, fractionation and crustal assimilation in a convecting magma chamber, Nisyros Volcano, Greece. *Bulletin of Volcanology*, *56*(8), 601-620.

Francalanci, L., Varekamp, J. C., Vougioukalakis, G. E., Innocenti, F., & Manetti, P. (2007). 2 Is there a compositional gap at Nisyros volcano? A Comment on: 3 Magma generation at the easternmost section of the Hellenic arc: 4 Hf, Nd, Pb and Sr isotope geochemistry of Nisyros and 5 Yali volcanoes (Greece).

Francalanci, L., Vougioukalakis, G. E., Perini, G., & Manetti, P. (2005). A West-East Traverse along the magmatism of the south Aegean volcanic arc in the light of volcanological, chemical and isotope data. In Developments in Volcanology (Vol. 7, pp. 65-111). Elsevier.

Francalanci, L., & Zellmer, G. F. (2019). Magma genesis at the South Aegean volcanic arc. *Elements: An International Magazine of Mineralogy, Geochemistry, and Petrology*, *15*(3), 165-170.

Friedrich, W. L., Kromer, B., Friedrich, M., Heinemeier, J., Pfeiffer, T., & Talamo, S. (2006). Santorini eruption radiocarbon dated to 1627-1600 BC. Science, 312(5773), 548-548.

Ganas, A., Elias, P., Kapetanidis, V., Valkaniotis, S., Briole, P., Kassaras, I., & Moshou, A. (2019). The July 20, 2017, M6. 6 Kos earthquake: seismic and geodetic evidence for an active north-dipping normal fault at the western end of the Gulf of Gökova (SE Aegean Sea). Pure and Applied Geophysics, 176(10), 4177-4211.

Genç, Ş. C., Karacık, Z., Altunkaynak, Ş., & Yılmaz, Y. (2001). Geology of a magmatic complex in the Bodrum peninsula, SW Turkey. International Earth Science Colloquium on the Aegean Region, İzmir, Turkey, 63-68.

Gençalioglu Kuscu, G., Uslular, G., 2018. Geochemical characterization of mid-distal Nisyros tephra on Datça peninsula (southwestern Anatolia). J. Volcanol. Geotherm. Res. 354, 13–28.

Gençalioğlu-Kuşcu, G., Uslular, G., Danišík, M., Koppers, A., Miggins, D. P., Friedrichs, B., & Schmitt, A. K. (2020). U–Th disequilibrium, (U–Th)/He and 40Ar/39Ar geochronology of distal Nisyros Kyra tephra deposits on Datça peninsula (SW Anatolia). *Quaternary Geochronology*, *55*, 101033.

Gilbert, J. S., & Lane, S. J. (1994). The origin of accretionary lapilli. Bulletin of Volcanology, 56, 398-411.

Gonnermann, H. M., & Manga, M. (2013). Dynamics of magma ascent in the. Modeling volcanic processes: The physics and mathematics of volcanism, 55.

Göçmengil, G., Şişman Tükel, F., Uzun, F., Guıllong, M., Yılmaz, İ., Aysal, N. & Hanilçi, N. (2022). Accurate whole-rock geochemistry analysis by combined ICP-OES and LA-ICP-MS instruments. Bulletin of the Mineral Research and Exploration, 168 (168), 157-165. DOI: 10.19111/bulletinofmre.947703

Guillong, M. V., von Quadt, A., Sakata, S., Peytcheva, I., & Bachmann, O. (2014). LA-ICP-MS Pb–U dating of young zircons from the Kos–Nisyros volcanic centre, SE Aegean arc. *Journal of Analytical Atomic Spectrometry*, *29*(6), 963-970.

Greber, N. D., Pettke, T., Vilela, N., Lanari, P., & Dauphas, N. (2021). Titanium isotopic compositions of bulk rocks and mineral separates from the Kos magmatic suite: Insights into fractional crystallization and magma mixing processes. *Chemical geology*, *578*, 120303.

Hardiman, J. C. (1999). Deep sea tephra from Nisyros island, eastern Aegean Sea, Greece. *Geological Society, London, Special Publications*, *161*(1), 69-88.

Heiken, G. (1972). Morphology and petrography of volcanic ashes. Geological Society of America Bulletin, 83(7), 1961-1988.

Heiken, G. (1974). Atlas of volcanic ash. *Smithsonian Contributions to the Earth Sciences*.

Heiken, G. (1991). Volcanic ash: what it is and how it forms. In Volcanic Ash and Aviation Safety—Proceedings of the First International Symposium on Volcanic Ash and Aviation Safety (Vol. 2047, pp. 39-45).

Huber, H., Bichler, M., & Musilek, A. (2003). Identification of pumice and volcanic ash from archaeological sites in the Eastern Mediterranean region using chemical fingerprinting. *Ägypten und Levante/Egypt and the Levant*, *13*, 83-105.

Inman, D. L. (1952). Measures for describing the size distribution of sediments. Journal of Sedimentary Research, 22(3), 125-145.

Işler, E. B. (2012). Paleoceanographic and paleoclimatic evolution of the Aegean Sea since the last interglacial (~ 130 ka BP) with special emphasis on sapropel formation (Doctoral dissertation, Memorial University of Newfoundland).

Isseven, T., Tüysüz, O., Genç, S. C., Erturaç, K., (2005). Bodrum Yarımadası (GB Anadolu) Miyosen magmatik kayalarının paleomanyetizması ve petrolojik

ozelliklerinin arastırılması. In: The Scientific and Technological Research Council of Turkey (TUBITAK) Project Report (Project Number 102Y139), 112p.

Jeancard, P. (1919). L'Anatolie, Smyrne – Sparte – Bourdour – Hiérapolis – Le Dodécanèse: Paris, Librairie Française.

Jones, T. J., Reynolds, C. D., & Boothroyd, S. C. (2019). Fluid dynamic induced break-up during volcanic eruptions. Nature Communications, 10(1), 3828.

Karacık, Z. (2006). Stratigraphy and volcanology of the Türkbükü volcanics: Products of a stratovolcano in the Bodrum Peninsula, SW Anatolia. Geological Journal, 41(2), 145-162.

Karkanas, P., White, D., Lane, C.S., Cullen, V.L., Stringer, C., Davies, S.W.G., Smith, V.C., Tomlinson, E.L., Ntinou, M., Tsartsidou, G., Kyparissi-Apostolika, N., 2015. Tephra chronostratigraphy and climatic events between the MIS6/5 transition and the beginning of MIS3 in Theopetra Cave, central Greece. Quat. Sci. Rev. 118, 170-181.

Kanellopoulos, C., & Xirokostas, N. (2016). Mudpots At Stefanos Hydrothermal Crater of Nısyros Volcano. An Insıght at The Hydrothermal Processes of An Actıve Volcano. *Bulletin of the Geological Society of Greece*, *50*(4), 1838-1848.

Keller, J. (1969). Origin of rhyolites by anatectic melting of granitic crustal rocks. *Bulletin Volcanologique*, *33*(3), 942-959.

Keller, J. (1980). Prehistoric pumice tephra on Aegean islands. *Thera and the Aegean World*, *2*, 49-56.

Keller, J., Rehren, T., & Stadlbauer, E. (1990). Explosive volcanism in the Hellenic Arc: a summary and review. *Thera and the Aegean world III*, *2*, 13e26.

Keller, J., Ryan, W. B. F., Ninkovich, D., & Altherr, R. (1978). Explosive volcanic activity in the Mediterranean over the past 200,000 yr as recorded in deep-sea sediments. *Geological Society of America Bulletin*, *89*(4), 591-604.

Kinvig, H. S., Winson, A., & Gottsmann, J. (2010). Analysis of volcanic threat from Nisyros Island, Greece, with implications for aviation and population exposure. *Natural Hazards and Earth System Sciences*, *10*(6), 1101-1113.

Knafelc, J., Bryan, S. E., Jones, M. W., Gust, D., Mallmann, G., Cathey, H. E., & Howard, D. L. (2022). Havre 2012 pink pumice is evidence of a short-lived, deep-sea, magnetite nanolite-driven explosive eruption. Communications Earth & Environment, 3(1), 19.

Koutrouli, A., Anastasakis, G., Kontakiotis, G., Ballengee, S., Kuehn, S., Pe-Piper, G., & Piper, D. J. W. (2018). The early to mid-Holocene marine tephrostratigraphic record in the Nisyros-Yali-Kos volcanic center, SE Aegean Sea. *Journal of Volcanology and Geothermal Research*, *366*, 96-111.

Kutterolf, S., Freundt, A., Hansteen, T. H., Dettbarn, R., Hampel, F., Sievers, C., & Friedrichs, B. (2021). The medial offshore record of explosive volcanism along the central to eastern Aegean Volcanic Arc, part 1: Tephrostratigraphic correlations.

Kutterolf, S., Freundt, A., Druitt, T. H., McPhie, J., Nomikou, P., Pank, K., & Allen, S. R. (2021). The medial offshore record of explosive volcanism along the central to eastern Aegean Volcanic Arc: 2. Tephra ages and volumes, eruption magnitudes and marine sedimentation rate variations. Geochemistry, Geophysics, Geosystems, 22(12), e2021GC010011.

Kurt, H., & Arslan, M. (2001). Bodrum (GB Anadolu) volkanik kayaçlarının jeokimyasal ve petrolojik özellikleri: fraksiyonel kristalleşme, magma karışımı ve asimilasyona ilişkin bulgular. *Yerbilimleri*, *22*(23), 15-32.

La Ruffa, G., Panichi, C., Kavouridis, T., Liberopoulou, V., Leontiadis, J., & Caprai, A. (1999). Isotope and chemical assessment of geothermal potential of Kos Island, Greece. *Geothermics*, *28*(2), 205-217.

Lagios, E., Tzanis, A., Delibasis, N., Drakopoulos, J., & Dawes, G. K. J. (1994). Geothermal exploration of Kos Island, Greece: magnetotelluric and microseismicity studies. *Geothermics*, *23*(3), 267-281.

Lagios, E., Sakkas, V., Parcharidis, I., & Dietrich, V. (2005). Ground deformation of Nisyros Volcano (Greece) for the period 1995–2002: Results from DInSAR and DGPS observations. *Bulletin of volcanology*, *68*(2), 201-214.

Lagios, E., Vassilopoulou, S., Sakkas, V., Dietrich, V., Damiata, B. N., & Ganas, A. (2007). Testing satellite and ground thermal imaging of low-temperature fumarolic fields: The dormant Nisyros Volcano (Greece). *ISPRS journal of photogrammetry and remote sensing*, *62*(6), 447-460.

Lavoisier, A. (1774). Opuscules Physiques Et Chymiques: de l'Academie Royale des Science, Paris.

Le Bruyn, C., (1714). Voyage au Levant, c'est-à-dire, dans les principaux endroits de l'Asie Mineure, dans les isles de Chio, Rhodes, et Chypre: Guillaume Cavelier.

Le Pichon, X., & Angelier, J. (1981). The Aegean Sea. Philosophical Transactions of the Royal Society of London. Series A, Mathematical and Physical Sciences, 300(1454), 357-372.

Limburg, E. M., & Varekamp, J. C. (1991). Young pumice deposits on Nisyros, Greece. *Bulletin of Volcanology*, *54*(1), 68-77.

Longchamp, C., Bonadonna, C., Bachmann, O., & Skopelitis, A. (2011). Characterization of tephra deposits with limited exposure: the example of the two largest explosive eruptions at Nisyros volcano (Greece). *Bulletin of Volcanology*, *73*(9), 1337-1352.

Machida, H., (1981). Tephrochronology and Quaternary studies in Japan. In: S. Self and R.S.J. Sparks (Editors), Tephra Studies. Reidel, Dordrecht, pp. 161-191.

Mahood, G. and Wallmann, P., (1985). Correlation of eruptions at an island volcano with glacial sea level drawdown: Pantelleria, Italy. EOS (Trans. Am. Geophys. Union), 66:1141.

Marchev, P., Georgiev, S., Zajacz, Z., Manetti, P., Raicheva, R., von Quadt, A., Tommasini, S., (2009). High-K ankaramitic melt inclusions and lavas in the Upper

Cretaceous Eastern Srednogorie continental arc, Bulgaria: implications for the genesis of arc shoshonites. Lithos 113, 228–245.

Margari, V., Pyle, D. M., Bryant, C., & Gibbard, P. L. (2007). Mediterranean tephra stratigraphy revisited: results from a long terrestrial sequence on Lesvos Island, Greece. *Journal of Volcanology and Geothermal Research*, *163*(1-4), 34-54.

Marini, L., Principe, C., Chiodini, G., Cioni, R., Fytikas, M., & Marinelli, G. (1993). Hydrothermal eruptions of Nisyros (Dodecanese, Greece). Past events and present hazard. *Journal of Volcanology and Geothermal Research*, *56*(1-2), 71-94.

Marti J., Soriano C., Dingwell D.B. (1999). Tube pumices as strain markers of the ductile-brittle transition during magma fragmentation. Nature 402(6762):650–653

Martelli, A. (1917). *Il gruppo eruttivo di Nisiro nel mare Egeo*. R. Accademia dei Lincei.

Masse, J.P., Fenerci-Masse, M., Ozer, S., Güngor, T., Akal, C., 2015. Berriasian rudist faunas and micropalaeontology of stramberk type carbonate exotics from the lycian nappes, Bodrum peninsula, Southwest Turkey. Cretac. Res. 56, 76–92.

Matsuda, J. I., Senoh, K., Maruoka, T., Sato, H., & Mitropoulos, P. (1999). K-Ar ages of the Aegean volcanic rocks and their implication for the arc-trench system. *Geochemical Journal*, *33*(6), 369-377.

Megalovasilis, P. (2016). Assessment onx hydrothermal partıcle chemıstry from a shallow ventıng system offshore Kmmos, Aegean Sea. *Bulletin of the Geological Society of Greece*, *50*(4), 1933-1942.

Megalovasilis, P. (2020). Hydrothermal fluid particle geochemistry of submarine vents in Kos Island, Aegean Sea East Mediterranean. *Geochemistry International*, *58*, 574-597.

Mitchell, S. J., Houghton, B. F., Carey, R. J., Manga, M., Fauria, K. E., Jones, M. R., & Giachetti, T. (2019). Submarine giant pumice: a window into the shallow conduit dynamics of a recent silicic eruption. Bulletin of Volcanology, 81, 1-21.

Narcisi, B., & Vezzoli, L. (1999). Quaternary stratigraphy of distal tephra layers in the Mediterranean—an overview. *Global and Planetary Change*, *21*(1-3), 31-50.

Nemeth, K., & Martin, U. (2007). Practical volcanology. Geological Institute of Hungary.

Neumayr, M. (1875). Die Insel Kos. *Verhandlungen der Geologischen Reichsanstalt*, 170-174.

Nomikou, P., Krassakis, P., Kazana, S., Papanikolaou, D., & Koukouzas, N. (2021). The Volcanic Relief within the Kos-Nisyros-Tilos Tectonic Graben at the Eastern Edge of the Aegean Volcanic Arc, Greece and Geohazard Implications. *Geosciences*, *11*(6), 231.

Nomikou, P., & Papanikolaou, D. (2011). Extension of active fault zones on Nisyros volcano across the Yali-Nisyros Channel based on onshore and offshore data. *Marine Geophysical Research*, *32*(1), 181-192.

Nomikou, P., Papanikolaou, D., Alexandri, M., Sakellariou, D., & Rousakis, G. (2013). Submarine volcanoes along the Aegean volcanic arc. *Tectonophysics*, *597*, 123-146.

Oppenheim, P. (1918). Das Neogen in Kleinasien. - Ztschrft. d. Deutsch, geol. Ges., Bd. 70, Berlin.

Oyman, T., Dyar, M.D., 2007. Chemical substitutions in oxidized tourmaline in granite related mineralized hydrothermal systems, western Turkey. The Canadian Mineralogist 45, 1397-1413.

Özdemirli-Esat, T., Doğanay-Özkan, M., & Esat, K. (2022). Seismotectonics of the Gulf of Gökova, southwest Anatolia, using double-difference seismic tomography, earthquake relocation, and moment tensor solutions: the 20 July 2017 Mw6. 5 Bodrum-Kos Earthquake.

Palladino, D. M., Simei, S., & Kyriakopoulos, K. (2008). On magma fragmentation by conduit shear stress: evidence from the Kos Plateau Tuff, Aegean Volcanic Arc. *Journal of volcanology and geothermal research*, *178*(4), 807-817.

Papanikolaou, D., & Nomikou, P. (2001). Tectonic structure and volcanic centers at the eastern edge of the Aegean volcanic arc around Nisyros island. *Bulletin of the Geological Society of Greece*, *34*(1), 289-296.

Papoulis, D., Tsolis-Katagas, P., Tsikouras, B., & Katagas, C. (2005). An FT-Raman, Raman and FTIR study of hydrothermally altered volcanic rocks from Kos Island (Southeastern Aegean, Greece). In Developments in Volcanology (Vol. 7, pp. 293-304). Elsevier.

Parcharidis, I., Lagios, E., & Sakkas, V. (2004). Differential interferometry as a tool of an early warning system in reducing the volcano risk: The case of Nisyros Volcano. *Bulletin of the Geological Society of Greece*, *36*(2), 913-918.

Pasteels, P., Kolios, N., Boven, A., & Saliba, E. (1986). Applicability of the K/1bAr method to whole-rock samples of acid lava and pumice: Case of the Upper Pleistocene domes and pyroclasts on Kos Island, Aegean Sea, Greece. *Chemical geology*, *57*(1-2), 145-154.

Peltz, C., Schmid, P., & Bichler, M. (1999). INAA of Aegaean pumices for the classification of archaeological findings. *Journal of Radioanalytical and Nuclear Chemistry*, *242*(2), 361-377.

Pe-Piper, G., & Moulton, B. (2008). Magma evolution in the Pliocene–Pleistocene succession of Kos, South Aegean arc (Greece). *Lithos*, *106*(1-2), 110-124.

Pe-piper, G., & Piper, D. J. (1989). Spatial and temporal variation in Late Cenozoic back-arc volcanic rocks, Aegean Sea region. *Tectonophysics*, *169*(1-3), 113-134.

Pe-Piper, G., & Piper, D. J. (2001). Late Cenozoic, post-collisional Aegean igneous rocks: Nd, Pb and Sr isotopic constraints on petrogenetic and tectonic models. *Geological Magazine*, *138*(6), 653-668.

Pe-Piper, G., & Piper, D. J. W. (2002). The igneous rocks of Greece: The anatomy of an orogen: Berlin-Stuttgart. *Beiträge zur Regionalen Geologie der Erde, Gebrüder Borntraeger*.

Pe-Piper, G., Piper, D. J. W., Kotopouli, C. N., & Panagos, A. G. (1994). Neogene volcanoes of Chios, Greece: the relative importance of subduction and back-arc extension. *Geological Society, London, Special Publications*, *81*(1), 213-231.

Pe-Piper, G., Piper, D. J., Koukouvelas, I., Dolansky, L. M., & Kokkalas, S. (2009). Postorogenic shoshonitic rocks and their origin by melting underplated basalts: The Miocene of Limnos, Greece. *Geological Society of America Bulletin*, *121*(1-2), 39-54.

Pe-Piper, G., Piper, D. J., & Perissoratis, C. (2005). Neotectonics and the Kos Plateau Tuff eruption of 161 ka, South Aegean arc. *Journal of Volcanology and Geothermal Research*, *139*(3-4), 315-338.

Philippson, A., 1915, Reisen und Forschungen in westlichen kleinaisen, III. Heft, Gotha, Perthes.

Piacenza, F. (1688) L' Egeo redivivo, o'sia chorographia dell'Arcipelago. Bibliotheca Regia Monacensis.

Piper, D. J., Pe-Piper, G., Anastasakis, G., & Reith, W. (2019). The volcanic history of Pyrgousa—volcanism before the eruption of the Kos Plateau Tuff. *Bulletin of Volcanology*, *81*(5), 1-15.

Piper, D. J., & Pe-Piper, G. (2020). A reworked isolated deposit of the Kos Plateau Tuff and its significance for dating raised marine terraces, Kos, Greece. *Geological Magazine*, *157*(12), 2021-2032.

Pişkin, Ö., 1980. Kadıkalesi-Girelbelen (Bodrum yarımadası) hidrotermal ve kontakt metasomatik Pb, Zn, Cu cevherlewmelerinin mineralojik ve jeolojik incelenmesi. Habilitation Thesis, Ege University, Izmir.

Plieninger, F., & Sapper, K. (1920). *Kos und Nisyros*. Perthes.

Polacci, M., Papale, P., & Rosi, M. (2001). Textural heterogeneities in pumices from the climactic eruption of Mount Pinatubo, 15 June 1991, and implications for magma ascent dynamics. Bulletin of Volcanology, 63, 83-97.

Popa, R. G., Bachmann, O., Ellis, B. S., Degruyter, W., Tollan, P., & Kyriakopoulos, K. (2019). A connection between magma chamber processes and eruptive styles revealed at Nisyros-Yali volcano (Greece). *Journal of Volcanology and Geothermal Research*, *387*, 106666.

Popa, R. G., Guillong, M., Bachmann, O., Szymanowski, D., & Ellis, B. (2020). U-Th zircon dating reveals a correlation between eruptive styles and repose periods at the Nisyros-Yali volcanic area, Greece. *Chemical Geology*, *555*, 119830.

Popa, R. G., Tollan, P., Bachmann, O., Schenker, V., Ellis, B., & Allaz, J. M. (2021). Water exsolution in the magma chamber favors effusive eruptions: Application of Cl-F partitioning behavior at the Nisyros-Yali volcanic area. *Chemical Geology*, *570*, 120170.

Rayet, O. (1876). *Mémoire sur l'île de Kos*. Imprimerie Nationale.

Rehren, T. H. (1988). Geochemie und Petrologie von Nisyros (östliche ägäis) (Doctoral dissertation).

Robert, U., Cantagrel, J.M., (1977). Le volcanisme basaltique dans le Sud-Est de la mer Egee: Donnes geochronologiques et relation avec la tectonique. In Proceedings of VI. Colloquium on the Geology of the Aegean Region 3, 961-967.

Robert, U., Foden, J., & Varne, R. (1992). The Dodecanese Province, SE Aegean: a model for tectonic control on potassic magmatism. *Lithos*, *28*(3-6), 241-260.

Sachpazi, M., Kontoes, C., Voulgaris, N., Laigle, M., Vougioukalakis, G., Sikioti, O., & Lepine, J. C. (2002). Seismological and SAR signature of unrest at Nisyros caldera, Greece. *Journal of Volcanology and Geothermal Research*, *116*(1-2), 19-33.

Satow, C., Tomlinson, E. L., Grant, K. M., Albert, P. G., Smith, V. C., Manning, C. J., & Menzies, M. A. (2015). A new contribution to the Late Quaternary tephrostratigraphy of the Mediterranean: Aegean Sea core LC21. Quaternary Science Reviews, 117, 96-112.

Schumacher, R., & Schmincke, H. U. (1991). Internal structure and occurrence of accretionary lapilli—a case study at Laacher See Volcano. Bulletin of Volcanology, 53, 612-634.

Spandler, C., Martin, L. H., & Pettke, T. (2012). Carbonate assimilation during magma evolution at Nisyros (Greece), South Aegean Arc: Evidence from clinopyroxenite xenoliths. *Lithos*, *146*, 18-33.

St. Seymour, K. & Vlassopoulos, D. (1992). Magma mixing at Nisyros volcano, as inferred from incompatible trace-element systematics. *Journal of Volcanology and Geothermal Research*, *50*(3), 273-299.

Stadlbauer, E., & Hug-Fleck, C. J. (1989). Geologische und vulkanologische Aspekte der Kefalos-Halbinsel von Kos (Dodekanes–SE-Griechenland). *Berichte der Naturforschenden Gesellschaft zu Freiburg im Breisgau*, *77*, 23-47.

Steinhauser, G., Sterba, J. H., & Bichler, M. (2007). "Chemical fingerprints" of pumice from Cappadocia (Turkey) and Kos (Greece) for archaeological applications. *Applied radiation and isotopes*, *65*(5), 488-503.

Sterba, J. H., Steinhauser, G., & Bichler, M. (2011). On the geochemistry of the Kyra eruption sequence of Nisyros volcano on Nisyros and Tilos, Greece. *Applied Radiation and Isotopes*, *69*(11), 1605-1612.

Stiros, S. C., Pirazzoli, P. A., Fontugne, M., Arnold, M., & Vougioukalakis, G. (2005). Late-Holocene coastal uplift in the Nisyros volcano (SE Aegean Sea): evidence for a new phase of slow intrusive activity. In *Developments in Volcanology* (Vol. 7, pp. 217-225). Elsevier.

Smith, P. E., York, D., Chen, Y., & Evensen, N. M. (1996). Single crystal 40Ar-39Ar dating of a Late Quaternary paroxysm on Kos, Greece: Concordance of terrestrial and marine ages. Geophysical Research Letters, 23(21), 3047-3050.

Şimşek, B., Ergin, M., Evren, M., Türkmen, Ö., Palas, S., Pehlivan, H., & Öcal, F. (2017). Datça ve Hisarönü Körfezlerinin Güncel Sedimanlarında Tane Boyu, Toplam Ağır Mineral ve Element Dağılımları ile Bunları Kontrol Eden Faktörler. Maden Tetkik Ve Arama Dergisi, (154), 61-84.

Taddeucci, J., Pompilio, M., & Scarlato, P. (2004). Conduit processes during the July–August 2001 explosive activity of Mt. Etna (Italy): inferences from glass chemistry and crystal size distribution of ash particles. Journal of Volcanology and Geothermal Research, 137(1-3), 33-54.

Teschner, M., Faber, E., Poggenburg, J., Vougioukalakis, G. E., & Hatziyannis, G. (2007). Continuous, direct gas-geochemical monitoring in hydrothermal vents: Installation and long-term operation on Nisyros Island (Greece). *Pure and Applied Geophysics*, *164*(12), 2549-2571.

Thunell, R., Federman, A., Sparks, S., & Williams, D. (1979). The age, origin, and volcanological significance of the Y-5 ash layer in the Mediterranean. *Quaternary Research*, *12*(2), 241-253.

Tibaldi, A., Pasquare, F. A., Papanikolaou, D., & Nomikou, P. (2008). Tectonics of Nisyros Island, Greece, by field and offshore data, and analogue modelling. *Journal of Structural Geology*, *30*(12), 1489-1506.

Toker, M. (2021). Symptomatic discretization of small earthquake clusters reveals seismic coupling to 2017 Bodrum earthquake (Mw 6.6) in the Gulf of Gökova (SW corner of Turkey): Viscous-compliant seismogenesis over back-arc setting. Journal of African Earth Sciences, 177, 104156.

Tomlinson, E., Kinvig, H. S., Smith, V., Blundy, J. D., Gottsmann, J., Müller, W., & Menzies, M. A. (2012). The Upper and Lower Nisyros Pumices: Revisions to the

Mediterranean tephrostratigraphic record based on micron-beam glass geochemistry. *Journal of Volcanology and Geothermal Research*, *243*, 69-80.

Tomlinson, E. L., Smith, V. C., Albert, P. G., Aydar, E., Civetta, L., Cioni, R., & Zanchetta, G. (2015). The major and trace element glass compositions of the productive Mediterranean volcanic sources: tools for correlating distal tephra layers in and around Europe. *Quaternary Science Reviews*, *118*, 48-66.

Tur, H., Yaltırak, C., Elitez, İ., & Sarıkavak, K. T. (2015). Pliocene–Quaternary tectonic evolution of the Gulf of Gökova, southwest Turkey. Tectonophysics, 638, 158-176.

Uluğ, A., Duman, M., Ersoy, Ş., Özel, E., & Avcı, M. (2005). Late Quaternary sea-level change, sedimentation and neotectonics of the Gulf of Gökova: Southeastern Aegean Sea. Marine Geology, 221(1-4), 381-395.

Ulusoy, I., 2002. Bodrum kalderasının yapısal-volkanolojik incelemesi. MSc thesis, Hacettepe Univ. Ankara, Turkey (with English summary).

Ulusoy, I., Cubukcu, E., Aydar, E. R. K. A. N., Labazuy, P., Gourgaud, A., & Vincent, P. M. (2004). Volcanic and deformation history of the Bodrum resurgent caldera system (southwestern Turkey). *Journal of Volcanology and Geothermal Research*, *136*(1-2), 71-96.

Vanderkluysen, L., Volentik, A. C. M., Principe, C., Hunziker, J. C., & Hernandez, J. (2005). *Nisyros' volcanic evolution: the growth of a strato-volcano*.

Varnavas, S. P., & Cronan, D. S. (1991). Hydrothermal metallogenic processes off the islands of Nisiros and Kos in the Hellenic Volcanic Arc. *Marine Geology*, *99*(1-2), 109-133.

Vinci, A. (1985). Distribution and chemical composition of tephra layers from Eastern Mediterranean abyssal sediments. *Marine Geology*, *64*(1-2), 143-155.

Voegelin, A. R., Pettke, T., Greber, N. D., von Niederhäusern, B., & Nägler, T. F. (2014). Magma differentiation fractionates Mo isotope ratios: evidence from the Kos Plateau Tuff (Aegean Arc). *Lithos*, *190*, 440-448.

Volentik, A., Vanderkluysen, L., & Principe, C. (2002). Stratigraphy of the caldera walls of Nisyros volcano, Greece. *Eclogae Geologicae Helvetiae*, *95*(2), 223-236.

Volentik, A. C. (2005). *Stratigraphy of Nisyros volcano (Greece)*.

Vougioukalakis, G. (1993). Volcanic stratigraphy and evolution of Nisyros island. *Bull. Geol. Soc. Greece*, *28*(2), 239-258.

Vougioukalakis, G. E., & Fytikas, M. (2005). Volcanic hazards in the Aegean area, relative risk evaluation, monitoring and present state of the active volcanic centers. In *Developments in Volcanology* (Vol. 7, pp. 161-183). Elsevier.

Vougioukalakis, G. E., Satow, C. G., & Druitt, T. H. (2019). Volcanism of the South Aegean volcanic arc. *Elements: An International Magazine of Mineralogy, Geochemistry, and Petrology*, *15*(3), 159-164.

Yücel-Öztürk, Y., Akal, C., Ersoy, E. Y., Sevim, S., & Mertz-Kraus, R. (2023). Geochronology and geochemistry of the Miocene Kadıkalesi monzonite (Bodrum Peninsula, western Anatolia): Implications for its relation with the South Aegean Volcanic Arc. Geochemistry, 125982.

Walker, G. P. (1971). Grain-size characteristics of pyroclastic deposits. The Journal of Geology, 79(6), 696-714.

Wegwerth, A., Dellwig, O., Wulf, S., Plessen, B., Kleinhanns, I. C., Nowaczyk, N. R., & Arz, H. W. (2019). Major hydrological shifts in the Black Sea "Lake" in response to ice sheet collapses during MIS 6 (130–184 ka BP). Quaternary Science Reviews, 219, 126-144.

White, J. D. L., & Houghton, B. F. (2006). Primary volcaniclastic rocks. Geology, 34(8), 677-680.

Willmann, R. (1983). Neogen und jungtertiäre Entwicklung der Insel Kos (Ägäis, Griechenland). *Geologische Rundschau*, *72*(3), 815-860.

Wohletz, K. H. (1983). Mechanisms of hydrovolcanic pyroclast formation: grain-size, scanning electron microscopy, and experimental studies. Journal of Volcanology and Geothermal Research, 17(1-4), 31-63.

Wohletz, K., & Heiken, G. (1992). *Volcanology and geothermal energy* (Vol. 432). Berkeley: University of California Press.

Wulf, S., Keller, J., Satow, C., Gertisser, R., Kraml, M., Grant, K. M., et al. (2020). Advancing Santorini's tephrostratigraphy: New glass geochemical data and improved marine-terrestrial tephra correlations for the past ~360 kyrs. Earth-Science Reviews, 200, 102964. https://doi.org/10.1016/j.earscirev.2019.102964.

Wyers, G. P., & Barton, M. (1989). Polybaric evolution of calc-alkaline magmas from Nisyros, southeastern Hellenic Arc, Greece. *Journal of Petrology*, *30*(1), 1-37.

Zeilinga de Boer, J. Z., Pe-Piper, G., & Piper, D. J. W. (2022). The Myth of the Battle between Poseidon and Polybotes: Was it Inspired by a Late Holocene Rock Avalanche at Zini, Kos Island. Bulletin Geological Society of Greece, 59, 1-22.

Zellmer, G. F., & Turner, S. P. (2007). Arc dacite genesis pathways: evidence from mafic enclaves and their hosts in Aegean lavas. *Lithos*, *95*(3-4), 346-362.

Zhang, S., Blockley, S., Armitage, S. J., Satow, C., Manning, C., Barzilai, O., & Timms, R. (2023). Distal tephra reveal new MIS 5e Kos eruptions: Implications for the chronology and volcanic evolution histories in the Eastern Mediterranean region. Quaternary Science Reviews, 307, 108054.

Zobu, R. & Doğan, U. (2023). Holocene Relative Sea-Level Changes Along the Southern Coast of Bodrum Peninsula, SW Anatolia. Coğrafi Bilimler Dergisi, 21 (2) , 481-501. DOI: 10.33688/aucbd.1346327.

Zouzias, D., & St. Seymour, K. (2007). Magma intrusion in" Proto-caldera Caldera" systems: example from the Nisyros volcano. *Δελτίον της Ελληνικής Γεωλογικής Εταιρίας*, *40*(1), 512-522.

Zouzias, D., & St Seymour, K. (2008). Consanguineous geochemistry of the Kos Plateau and Tilos D and E pumices, Aegean volcanic arc, Hellas. *Neues Jahrbuch für Mineralogie-Abhandlungen*, 231-241.

Zouzias, D., & St. Seymour, K. (2013). Kos Plateau Tuff (KPT) on Kalymnos Island, Aegean volcanic arc: A geochemical approach. *Journal of Volcanology and Seismology*, *7*(5), 293.

APPENDICES

APPENDIX 1. Major and trace elements results belong to Bodrum samples

Locations		1. Location	1. Location	1. Location	1. Location	1. Location	1. Location	1. Location	1. Location	1. Location	1. Location	1. Location	1. Location	1. Location	1. Location	1. Location	1. Location
Sample Name		TPA-1	TPA-1	TPA-1	TPA-2	TPA-2	TPA-2	TPA-3	TPA-3	TPA-3	TPA-4	TPA-4	TPA-5	TPA-5	TPA-5	BPA-1	BPA-1
SiO_2	*wt%*	77.70	78.33	78.85	77.98	78.83	78.44	79.06	80.04	79.95	80.03	79.65	78.49	79.93	79.30	77.20	77.56
Al_2O_3	*wt%*	10.00	10.60	9.29	10.66	10.09	10.25	9.92	9.87	9.69	9.68	9.63	9.29	9.57	10.28	11.94	11.94
Fe_2O_3 [T]	*wt%*	0.91	0.72	0.71	0.67	0.66	0.66	0.65	0.60	0.60	0.57	0.58	0.87	0.62	0.62	0.66	0.60
MgO	*wt%*	0.08	0.08	0.09	0.07	0.07	0.07	0.07	0.05	0.06	0.06	0.07	0.23	0.08	0.08	0.08	0.07
CaO	*wt%*	0.51	0.47	0.41	0.48	0.45	0.52	0.45	0.46	0.43	0.44	0.48	0.51	0.48	0.42	0.65	0.50
Na_2O	*wt%*	3.25	2.80	3.77	3.56	4.04	3.69	3.48	3.83	3.66	4.07	4.21	2.63	2.91	3.04	3.38	3.29
K2O	*wt%*	7.22	6.68	6.56	6.28	5.56	6.08	6.07	4.86	5.33	4.86	5.10	7.64	6.11	5.96	5.75	5.74
TiO_2	*wt%*	0.11	0.11	0.10	0.11	0.10	0.10	0.10	0.10	0.09	0.09	0.10	0.12	0.10	0.10	0.12	0.11
P_2O_5	*wt%*	0.01	0.04	0.02	0.02	0.01	0.01	0.02	0.01	0.02	0.02	0.01	0.02	0.01	0.01	0.01	0.01
MnO	*wt%*	0.06	0.06	0.05	0.06	0.06	0.06	0.06	0.05	0.05	0.05	0.05	0.06	0.06	0.06	0.06	0.06
SUM	*wt%*	99.86	99.87	99.87	99.87	99.87	99.87	99.87	99.88	99.88	99.88	99.88	99.86	99.87	99.87	99.86	99.87
Ba	*ppm*	411.94	386.18	377.27	396.39	394.95	392.26	379.78	385.88	375.77	378.40	370.65	367.15	375.28	389.15	387.98	380.29
Ni	*ppm*	0.18	1.55	3.89	1.59	1.30	1.82	1.82	1.32	0.72	0.00	0.93	9.35	0.00	3.29	0.00	2.40
Cr	*ppm*	12.00	13.12	12.48	6.75	2.40	7.97	6.37	1.74	3.16	3.00	6.18	16.68	6.17	<0.1	28.87	2.06
Sc	*ppm*	4.87	4.03	3.93	4.03	3.58	3.55	3.57	3.10	3.22	2.81	2.91	3.97	3.25	3.17	2.94	2.58
Co	*ppm*	1.05	0.50	0.24	0.25	0.31	0.40	0.28	0.08	0.30	0.19	0.23	0.95	0.17	0.35	0.47	0.22
Ga	*ppm*	19.40	16.93	17.00	16.09	14.44	13.95	15.73	12.36	13.79	14.40	13.63	17.64	15.17	15.44	16.97	14.89
Nb	*ppm*	27.64	23.93	23.87	24.93	23.55	23.27	23.38	23.11	22.73	23.02	22.97	23.83	23.47	23.09	23.99	23.48
Rb	*ppm*	171.06	160.45	156.82	146.37	144.40	142.38	150.38	128.95	136.54	134.20	138.57	154.31	141.62	149.41	165.04	155.04
Sr	*ppm*	35.70	36.90	36.11	37.21	36.56	37.16	34.89	35.82	33.83	33.62	33.92	36.93	35.12	36.78	38.68	39.46
Th	*ppm*	13.69	13.75	13.31	14.63	14.00	13.74	13.27	13.23	13.20	13.13	12.79	11.98	12.25	13.29	13.91	14.63
U	*ppm*	7.21	7.32	7.21	6.36	5.91	6.13	6.12	5.83	5.80	5.87	5.94	7.41	5.88	6.13	6.29	6.21
V	*ppm*	3.08	2.18	2.40	1.82	1.87	2.16	1.88	1.68	2.07	1.83	2.07	6.78	2.49	2.07	3.05	2.30
Zr	*ppm*	45.11	41.70	41.64	48.51	44.86	45.18	42.84	43.49	41.08	42.33	41.18	39.71	38.87	42.24	50.30	50.47
Y	*ppm*	12.89	12.69	11.46	13.50	13.62	12.79	12.63	11.63	13.04	11.81	11.97	10.77	11.60	12.74	15.26	14.09
Pb	*ppm*	27.44	17.80	20.76	14.35	15.35	16.87	17.42	13.48	14.41	15.83	17.22	25.86	29.57	20.43	24.17	16.74
Zn	*ppm*	22.80	10.73	17.66	8.95	19.64	15.46	16.80	15.58	14.38	10.33	13.04	31.08	51.22	24.05	19.65	9.87
Cs	*ppm*	7.53	7.16	6.49	5.65	5.61	6.16	6.07	5.09	5.48	5.60	5.59	7.05	5.62	5.71	6.43	6.65
Hf	*ppm*	1.48	1.91	1.63	1.94	1.73	1.77	1.84	1.80	1.65	1.65	1.73	1.53	1.71	1.82	1.79	2.06
Ta	*ppm*	2.53	2.04	2.24	2.23	2.23	1.96	2.05	2.04	2.08	2.01	2.06	2.13	2.07	1.93	2.07	2.14
La	*ppm*	19.19	20.03	18.65	20.66	19.47	20.10	19.16	18.76	18.87	18.70	18.75	16.71	18.08	18.54	21.11	21.26
Ce	*ppm*	39.34	38.41	37.39	37.07	36.19	36.59	36.64	36.34	35.50	34.88	34.22	34.93	34.77	35.99	39.17	38.64
Pr	*ppm*	3.13	3.27	3.02	3.50	3.22	3.19	3.17	3.28	3.15	3.19	3.16	2.94	2.98	3.24	3.56	3.44
Nd	*ppm*	10.36	9.36	8.95	10.42	10.10	10.01	9.61	9.44	9.40	9.45	9.58	9.05	8.42	9.59	10.28	10.39
Sm	*ppm*	1.75	1.76	1.59	1.75	1.61	1.89	1.68	1.85	1.67	1.69	1.53	1.54	1.84	1.45	2.18	1.91
Eu	*ppm*	0.13	0.18	0.27	0.20	0.24	0.19	0.18	0.22	0.15	0.14	0.17	0.17	0.22	0.16	0.17	0.19
Gd	*ppm*	1.34	1.82	1.59	1.56	1.47	1.66	1.38	1.35	1.60	1.74	1.21	1.31	1.31	1.73	1.84	1.62
Tb	*ppm*	0.37	0.22	0.29	0.29	0.27	0.26	0.25	0.25	0.27	0.26	0.27	0.20	0.32	0.27	0.27	0.31
Dy	*ppm*	1.76	1.96	1.80	1.92	1.75	1.81	1.63	1.70	1.75	1.61	1.56	1.70	1.75	1.64	1.43	2.39
Ho	*ppm*	0.35	0.38	0.36	0.33	0.35	0.41	0.40	0.40	0.35	0.32	0.35	0.33	0.36	0.34	0.44	0.37
Er	*ppm*	1.18	1.67	1.21	1.40	1.11	1.30	1.15	1.14	1.28	1.14	1.26	0.88	1.23	1.43	1.45	1.41
Tm	*ppm*	0.19	0.22	0.21	0.21	0.23	0.22	0.20	0.19	0.21	0.16	0.20	0.18	0.13	0.22	0.20	0.24
Yb	*ppm*	1.40	1.49	1.73	1.52	1.59	1.78	1.79	1.58	1.56	1.46	1.41	0.97	1.67	1.67	1.60	1.85
Lu	*ppm*	0.24	0.21	0.23	0.27	0.28	0.26	0.23	0.24	0.21	0.26	0.24	0.18	0.25	0.26	0.24	0.25

APPENDIX 1. continues

Locations	1. Location	1. Location	1. Location	1. Location	1. Location	1. Location	1. Location	1. Location	1. Location	1. Location	1. Location	1. Location	1. Location	1. Location	1. Location	1. Location	1. Location
Sample Name	BPA-1	BPA-2	BPA-2	BPA-2	BPA-3	BPA-3	BPA-3	BPA-4	BPA-4	BPA-4	GLA	GLA	GLA	GLA	GLA	GLA	GLA
SiO_2	77.57	77.43	77.00	76.46	77.61	77.87	77.18	79.47	78.05	79.18	65.28	78.24	66.75	77.70	79.10	76.77	79.29
Al_2O_3	12.24	12.15	12.33	12.48	12.07	11.58	12.09	11.25	10.99	11.27	20.64	11.94	19.95	11.83	12.13	13.11	11.49
Fe_2O_3 [T]	0.75	0.71	0.61	0.68	0.64	0.58	0.59	0.60	0.63	0.62	0.20	0.74	5.43	1.28	0.96	1.28	0.74
MgO	0.15	0.09	0.07	0.09	0.07	0.06	0.10	0.06	0.06	0.06	0.01	0.08	1.55	0.12	0.13	0.20	0.07
CaO	0.67	0.59	0.58	0.53	0.63	0.55	0.67	0.50	0.53	0.50	4.12	0.57	0.52	0.52	0.39	0.52	0.59
Na_2O	3.13	3.46	3.57	3.52	2.90	3.74	3.48	2.78	3.95	3.00	8.84	3.43	0.99	2.77	2.02	3.16	2.64
K2O	5.10	5.23	5.51	5.89	5.74	5.31	5.52	5.04	5.48	5.07	0.72	4.70	3.59	5.41	4.87	4.56	4.84
TiO_2	0.12	0.11	0.11	0.11	0.11	0.10	0.11	0.10	0.10	0.11	0.01	0.11	0.78	0.13	0.13	0.16	0.11
P_2O_5	0.02	0.02	0.02	0.02	0.02	0.01	0.03	0.01	0.02	0.02	0.01	0.02	0.03	0.02	0.02	0.02	0.01
MnO	0.06	0.06	0.06	0.07	0.06	0.06	0.07	0.06	0.06	0.06	0.00	0.06	0.08	0.06	0.07	0.06	0.06
SUM	99.82	99.87	99.86	99.85	99.86	99.87	99.83	99.87	99.88	99.87	99.83	99.86	99.66	99.85	99.83	99.84	99.85
Ba	396.02	385.05	395.97	397.71	392.38	375.95	395.18	365.61	356.08	385.08	828.53	411.11	347.24	366.21	413.16	413.16	414.37
Ni	0.00	1.62	0.85	2.21	0.00	0.00	0.00	0.00	1.50	0.00	2.59	0.00	51.61	4.02	41.99	14.74	1.06
Cr	14.43	2.23	0.00	18.86	1.73	1.58	48.03	4.98	3.57	0.41	6.52	11.39	83.05	2.02	26.82	9.34	4.80
Sc	3.17	2.85	2.53	2.58	2.79	3.12	2.93	2.34	2.66	2.86	0.49	2.43	9.44	3.05	3.62	3.39	2.75
Co	0.66	0.34	0.19	0.46	0.23	0.05	0.49	0.24	0.12	0.40	0.09	0.39	8.28	0.35	2.73	1.18	0.33
Ga	18.32	17.17	15.24	15.82	14.78	13.82	17.61	12.85	14.50	13.54	18.00	14.01	29.35	18.45	16.92	14.78	15.58
Nb	24.91	24.82	25.01	27.09	24.94	25.17	25.99	25.59	25.07	26.18	0.00	23.23	42.58	24.41	24.73	24.60	26.19
Rb	147.63	160.85	151.01	164.20	154.27	148.02	161.26	144.14	151.20	147.19	1.11	148.67	204.09	155.57	163.74	146.18	146.21
Sr	39.57	42.32	39.39	42.32	39.13	38.62	40.83	37.04	33.62	34.91	536.69	38.74	50.57	35.32	43.28	40.12	38.91
Th	15.27	15.00	15.51	15.41	15.08	14.38	13.90	13.25	12.61	13.28	14.33	14.46	19.79	13.63	14.18	14.34	14.21
U	6.63	6.33	6.55	7.08	6.36	6.17	6.22	6.14	6.40	6.26	0.01	5.86	6.12	6.20	5.62	5.96	5.73
V	4.21	3.08	2.27	2.86	4.05	2.50	2.97	1.91	2.20	2.63	0.13	2.34	55.54	6.12	6.97	7.94	2.56
Zr	107.03	53.93	52.27	54.78	53.67	50.92	51.49	46.86	40.84	43.59	0.36	48.10	86.06	49.93	50.84	55.11	48.74
Y	13.18	14.91	15.07	15.03	14.79	14.54	15.09	12.93	11.96	13.77	0.13	13.08	16.99	13.46	15.20	13.64	13.29
Pb	55.97	22.27	18.34	16.98	16.58	16.66	136.37	13.05	15.03	17.35	9.06	14.07	22.11	19.19	14.60	14.28	30.33
Zn	20.92	18.17	12.08	11.04	3.96	9.14	15.28	15.40	9.27	12.72	0.87	14.56	67.49	16.74	27.09	21.39	27.74
Cs	6.32	5.96	6.47	6.82	6.56	6.08	6.61	5.36	5.65	5.22	0.00	5.22	10.89	6.19	6.03	5.33	5.51
Hf	1.89	1.57	1.86	1.81	1.95	1.98	1.87	1.62	1.76	1.90	0.02	2.07	2.62	1.57	1.18	2.08	1.84
Ta	2.32	2.17	2.19	2.19	2.29	2.15	2.19	2.03	2.11	2.04	0.00	2.13	2.97	1.91	1.97	1.93	2.18
La	21.45	23.41	24.44	23.65	22.86	21.30	22.24	19.91	18.93	19.95	8.83	20.60	27.65	20.19	22.10	21.15	24.02
Ce	38.70	41.34	44.19	42.82	39.34	39.08	40.20	37.43	38.50	38.82	10.21	38.75	78.77	37.41	41.93	44.36	39.26
Pr	3.66	3.61	4.34	4.33	3.62	3.54	3.70	3.26	3.13	3.31	0.62	3.45	5.52	3.34	3.61	3.65	3.60
Nd	10.85	12.18	13.27	12.00	10.67	10.56	10.40	9.25	9.13	9.89	1.34	10.30	18.00	9.89	11.29	11.45	10.03
Sm	2.25	1.96	1.92	1.81	1.86	1.56	1.58	1.24	1.66	1.57	0.07	1.82	3.94	1.63	2.66	2.34	2.05
Eu	0.23	0.28	0.28	0.18	0.21	0.22	0.21	0.20	0.19	0.17	0.89	0.20	0.55	0.23	0.22	0.21	0.29
Gd	1.87	2.00	1.83	2.21	1.91	1.70	1.76	1.47	1.25	1.87	0.05	1.72	2.49	1.32	1.52	2.03	1.66
Tb	0.26	0.37	0.36	0.30	0.27	0.31	0.28	0.22	0.23	0.24	0.01	0.32	0.59	0.22	0.36	0.31	0.27
Dy	2.20	1.70	2.55	2.60	1.82	2.02	1.75	1.75	1.59	1.76	0.03	2.03	2.53	1.81	1.99	2.12	2.04
Ho	0.41	0.51	0.46	0.51	0.43	0.39	0.36	0.32	0.33	0.34	0.00	0.42	0.61	0.44	0.58	0.41	0.44
Er	1.53	1.35	1.72	1.13	1.55	1.41	1.26	1.35	1.26	1.05	0.00	1.38	1.36	1.30	1.51	1.45	1.54
Tm	0.26	0.23	0.26	0.19	0.24	0.21	0.23	0.17	0.17	0.20	0.00	0.22	0.21	0.19	0.00	0.21	0.20
Yb	1.64	1.67	2.04	2.12	2.08	1.48	1.82	1.71	1.50	1.48	0.03	1.71	1.74	1.50	1.27	1.55	1.41
Lu	0.27	0.23	0.37	0.29	0.29	0.25	0.21	0.29	0.25	0.25	0.01	0.27	0.29	0.22	0.16	0.26	0.23

APPENDIX 1. continues

Locations	1. Location	1. Location	1. Location	1. Location	1. Location	1. Location	1. Location	2. Location	2. Location	2. Location	2. Location	2. Location	2. Location	2. Location	2. Location	2. Location	2. Location
Sample Name	GLA	GLA	GLA	GLA	GLA	GLA	GLA	TPB-6	TPB-6	TPB-7	TPB-7	TPB-7	TPB-8	TPB-8	TPB-9	TPB-9	TPB-10
SiO_2	74.76	76.33	78.95	78.02	78.65	77.85	78.95	79.14	79.04	79.10	78.79	79.49	78.08	79.42	79.74	77.39	78.09
Al_2O_3	14.47	10.90	11.58	12.09	11.77	11.86	11.58	10.53	10.58	10.74	11.09	10.72	11.37	11.05	9.95	11.70	12.01
Fe_2O_3 [T]	1.79	4.00	0.71	0.89	0.74	1.54	0.77	0.66	0.66	0.60	0.60	0.55	0.69	0.71	0.49	0.59	0.57
MgO	0.40	0.97	0.06	0.11	0.06	0.22	0.06	0.08	0.08	0.07	0.07	0.06	0.11	0.15	0.05	0.07	0.12
CaO	0.77	3.44	0.46	0.63	0.51	0.50	0.48	0.51	0.46	0.52	0.50	0.48	0.48	0.52	0.46	0.52	0.63
Na_2O	2.90	0.79	3.23	3.06	3.22	3.22	3.17	3.70	3.57	3.50	3.50	3.13	3.50	2.36	4.37	3.99	2.70
K2O	4.42	1.98	4.71	4.87	4.75	4.41	4.68	5.08	5.31	5.18	5.14	5.30	5.45	5.45	4.66	5.43	5.55
TiO_2	0.24	0.98	0.11	0.11	0.11	0.19	0.10	0.11	0.11	0.10	0.11	0.10	0.13	0.12	0.10	0.11	0.11
P_2O_5	0.02	0.08	0.01	0.01	0.01	0.01	0.01	0.01	0.01	0.02	0.02	0.00	0.02	0.02	0.01	0.00	0.01
MnO	0.06	0.03	0.06	0.06	0.06	0.05	0.06	0.06	0.05	0.06	0.06	0.06	0.05	0.06	0.05	0.07	0.06
SUM	99.81	99.50	99.86	99.85	99.87	99.84	99.86	99.87	99.88	99.87	99.86	99.88	99.87	99.86	99.88	99.87	99.85
Ba	382.43	176.68	425.27	377.51	401.84	360.36	429.30	382.67	376.29	411.47	429.02	401.58	359.77	343.42	345.71	409.76	430.54
Ni	28.52	172.33	0.26	0.57	1.27	12.11	1.00	2.80	0.88	2.16	1.02	<0.1	8.09	4.86	<0.1	<0.1	<0.1
Cr	23.97	870.32	15.26	12.71	8.16	11.46	2.94	4.81	3.27	0.00	5.73	<0.1	18.97	19.63	<0.1	3.27	8.28
Sc	4.74	15.75	2.35	2.72	2.40	3.04	2.21	3.04	3.41	3.13	3.51	2.88	3.61	3.70	2.82	3.19	2.98
Co	2.26	22.86	0.23	0.55	0.04	1.48	0.23	0.33	0.16	0.24	0.50	0.20	0.71	1.06	0.15	0.32	0.24
Ga	17.85	64.53	13.37	14.22	12.96	15.09	12.53	14.14	14.55	14.66	13.15	15.00	15.46	19.50	11.78	15.84	15.08
Nb	26.14	9.25	21.98	24.91	22.89	23.68	23.63	23.25	23.57	24.45	24.82	24.22	25.63	23.62	23.70	27.33	26.46
Rb	146.27	88.11	139.42	149.63	141.64	137.05	140.41	144.97	135.71	138.26	147.87	139.81	146.80	149.24	131.16	142.00	153.06
Sr	54.15	30.15	39.29	45.48	39.14	41.47	36.24	36.72	35.25	38.23	40.07	37.34	35.71	35.41	33.95	38.23	39.82
Th	16.22	14.18	14.27	14.18	14.34	13.92	14.39	13.42	13.79	13.87	14.21	13.69	14.63	13.40	12.50	14.05	14.13
U	6.28	2.30	6.17	5.90	6.21	5.68	5.86	6.03	5.89	5.95	6.39	5.85	6.14	5.74	5.95	7.43	6.18
V	16.06	31.68	1.86	3.03	1.86	10.72	1.40	3.07	3.07	2.64	2.35	1.82	4.52	4.25	2.19	2.88	2.62
Zr	68.65	14.07	46.69	50.49	48.28	52.72	47.81	44.81	45.91	47.41	47.90	46.37	52.57	46.87	46.10	44.89	46.88
Y	15.76	6.72	13.44	13.15	12.38	13.45	13.06	12.69	13.03	12.99	13.45	12.89	13.40	12.69	11.57	12.73	13.91
Pb	16.51	0.74	12.31	13.49	12.81	14.15	13.30	16.06	18.71	16.30	28.69	16.62	20.41	33.83	12.91	20.37	98.03
Zn	32.58	17.94	13.55	9.73	12.81	20.45	11.86	12.84	14.07	18.76	20.56	10.81	21.00	37.62	7.66	13.42	110.97
Cs	6.56	5.90	5.57	6.09	5.59	5.49	5.40	6.10	5.47	5.30	5.88	5.54	5.92	6.14	5.49	6.68	5.96
Hf	2.20	0.00	1.83	1.86	1.90	1.84	1.67	1.63	1.79	1.83	1.86	1.75	2.02	1.89	1.51	1.87	1.82
Ta	2.35	1.43	2.07	2.22	2.05	1.88	2.10	2.14	2.20	2.13	2.16	1.98	2.42	2.09	2.00	2.37	2.01
La	26.33	11.33	20.30	20.87	20.18	19.91	19.60	19.59	19.46	19.83	21.24	19.83	19.92	18.05	18.10	20.06	21.45
Ce	46.02	21.74	38.70	40.95	39.29	37.10	38.52	37.78	36.47	37.95	38.96	36.93	36.83	36.57	35.82	43.40	40.11
Pr	4.60	6.41	3.53	3.55	3.47	3.56	3.38	3.40	3.16	3.36	3.36	3.21	3.38	2.93	3.10	3.35	3.50
Nd	15.01	9.43	10.68	10.54	10.86	10.89	10.01	10.23	9.80	10.41	10.70	9.91	10.22	9.90	9.17	9.81	10.73
Sm	2.58	4.81	1.69	2.00	2.03	1.80	1.81	1.69	1.74	2.02	1.76	1.73	1.72	1.74	1.46	1.83	2.02
Eu	0.32	1.21	0.19	0.19	0.20	0.20	0.20	0.18	0.20	0.19	0.21	0.22	0.17	0.13	0.24	0.22	0.22
Gd	2.18	2.22	1.43	2.06	1.69	1.82	1.57	1.57	1.63	1.72	1.82	1.47	1.73	1.67	1.39	1.74	1.86
Tb	0.37	0.00	0.28	0.31	0.30	0.27	0.30	0.26	0.32	0.26	0.26	0.27	0.31	0.24	0.24	0.31	0.32
Dy	2.40	5.46	1.61	1.78	2.11	1.94	1.81	1.72	2.11	1.66	2.07	1.86	2.25	1.93	1.70	2.04	1.88
Ho	0.50	0.48	0.35	0.46	0.39	0.38	0.48	0.45	0.39	0.38	0.37	0.39	0.41	0.38	0.35	0.43	0.37
Er	1.75	1.51	1.48	1.24	1.40	1.28	1.38	1.32	1.44	1.23	1.30	1.47	1.31	1.19	1.16	1.20	1.27
Tm	0.24	0.00	0.21	0.25	0.26	0.31	0.19	0.18	0.20	0.25	0.21	0.22	0.20	0.22	0.18	0.23	0.24
Yb	2.30	6.70	1.89	1.72	1.65	1.62	1.70	1.63	1.80	1.52	1.80	1.69	1.78	1.32	1.74	1.68	1.66
Lu	0.34	0.36	0.29	0.24	0.23	0.22	0.22	0.25	0.28	0.28	0.30	0.23	0.23	0.18	0.27	0.24	0.26

APPENDIX 1. continues

Locations	2. Location	2. Location	2. Location	2. Location	2. Location	2. Location	2. Location	2. Location	2. Location	2. Location	2. Location	2. Location	2. Location	2. Location	2. Location	2. Location	2. Location
Sample Name	TPB-10	TPB-10	BPB-5	BPB-6	BPB-7	BPB-8	BPB-9	BPB-9	BPB-9	BPB-10	BPB-10	BPB-10	BPB-11	BPB-11	BPB-12	BPB-12	BPB-12
SiO_2	78.33	77.92	77.48	78.81	79.12	78.78	77.89	78.14	79.62	77.53	77.51	78.35	77.92	79.79	77.71	78.46	79.95
Al_2O_3	11.08	11.47	11.63	11.87	10.80	11.13	11.64	11.82	10.88	11.79	11.67	11.34	11.59	10.46	11.89	11.73	10.97
Fe_2O_3 [T]	0.51	0.60	0.88	0.66	0.62	0.67	0.67	0.78	0.73	0.97	0.97	0.79	0.82	0.56	0.95	0.87	0.79
MgO	0.06	0.10	0.09	0.10	0.06	0.10	0.08	0.11	0.10	0.15	0.16	0.13	0.15	0.06	0.09	0.09	0.08
CaO	0.62	0.50	0.54	0.71	0.44	0.50	0.56	0.51	0.46	0.52	0.56	0.51	0.53	0.45	0.52	0.55	0.51
Na_2O	3.95	4.07	3.18	1.68	3.53	3.37	3.24	3.10	2.73	2.97	2.91	3.03	3.60	3.72	3.34	2.74	2.66
K2O	5.16	5.04	5.86	5.96	5.12	5.14	5.59	5.18	5.17	5.74	5.88	5.52	5.07	4.66	5.16	5.21	4.75
TiO_2	0.10	0.11	0.11	0.12	0.10	0.11	0.11	0.11	0.11	0.12	0.12	0.12	0.11	0.10	0.11	0.11	0.10
P_2O_5	0.01	0.01	0.01	0.03	0.00	0.01	0.01	0.01	0.01	0.01	0.02	0.01	0.01	0.01	0.01	0.02	0.01
MnO	0.06	0.05	0.06	0.06	0.06	0.06	0.06	0.06	0.06	0.06	0.06	0.06	0.06	0.06	0.06	0.06	0.06
SUM	99.88	99.87	99.85	100.00	99.87	99.87	99.85	99.85	99.87	99.86	99.85	99.86	99.86	99.88	99.85	99.86	99.87
Ba	374.04	361.00	389.25	404.32	388.04	367.98	404.14	412.53	367.04	362.94	383.65	368.88	383.72	362.72	387.67	394.53	383.22
Ni	1.42	0.58	1.58	12.88	1.65	2.85	0.00	4.80	5.21	0.82	0.00	2.38	10.95	0.00	2.82	2.99	0.07
Cr	1.18	2.70	<0.1	48.37	4.70	6.70	13.32	15.82	13.96	6.66	15.64	13.40	7.61	3.66	5.62	9.54	3.21
Sc	3.09	3.22	3.61	2.99	2.83	2.90	2.93	3.20	2.73	3.12	3.05	2.99	3.32	2.44	2.97	3.32	2.42
Co	0.18	0.40	0.56	1.10	0.18	0.51	0.10	0.69	0.38	0.60	0.78	0.71	0.60	0.16	0.46	0.22	0.33
Ga	14.05	12.31	17.60	17.73	15.40	16.18	16.95	16.58	14.46	17.81	19.97	17.09	15.98	12.03	16.79	15.13	13.78
Nb	23.62	24.23	26.04	27.77	25.88	24.60	24.93	25.36	23.56	23.60	26.24	25.04	24.63	21.63	26.10	26.53	21.83
Rb	143.77	137.41	162.56	163.60	155.69	152.38	162.26	160.68	140.25	154.08	157.94	161.29	150.47	142.59	162.26	148.18	145.21
Sr	38.31	37.16	37.09	38.62	36.91	34.47	37.86	39.05	36.27	38.23	38.24	36.91	40.05	34.46	37.57	39.61	36.59
Th	14.69	14.71	14.40	13.82	12.46	13.34	14.73	14.45	13.19	13.33	14.24	14.00	14.11	12.49	14.25	14.03	13.49
U	6.12	5.80	6.49	6.10	6.71	6.06	6.68	6.65	6.05	6.09	6.57	6.64	6.10	5.67	6.59	6.50	6.12
V	2.31	3.26	4.53	3.81	2.73	3.22	3.47	3.35	3.47	6.20	7.02	5.52	4.80	1.95	3.49	3.58	2.58
Zr	47.44	50.94	47.34	55.24	45.06	42.92	49.62	46.52	44.46	45.09	48.75	44.18	43.75	40.04	44.49	46.79	43.81
Y	13.82	14.14	12.96	15.28	11.94	11.83	12.70	12.99	12.61	13.98	13.20	13.79	13.06	12.30	13.57	12.39	12.33
Pb	21.51	14.02	19.29	16.20	15.14	16.31	18.18	25.18	15.36	18.52	20.30	18.42	24.25	13.19	16.55	21.02	14.01
Zn	16.72	26.97	13.77	12.12	11.92	13.69	12.25	47.59	12.65	12.74	14.85	9.61	36.26	11.57	13.29	35.22	11.38
Cs	5.46	5.86	6.23	6.89	5.94	6.17	6.03	6.11	5.67	6.04	7.01	6.87	5.65	5.46	6.32	6.61	5.34
Hf	1.89	1.66	1.77	1.48	1.79	1.69	1.75	2.01	1.87	1.68	1.82	1.70	1.63	1.52	1.89	1.61	1.76
Ta	2.17	2.29	2.11	1.96	1.93	2.22	2.15	2.41	1.95	2.08	2.36	2.05	2.02	2.10	2.30	2.18	2.07
La	21.04	20.75	20.38	20.35	19.02	19.04	20.30	19.91	18.77	19.92	20.31	20.17	19.74	17.82	20.54	20.34	19.02
Ce	38.22	37.72	38.31	39.43	37.39	37.69	39.27	40.10	36.11	36.97	38.96	39.22	37.61	36.22	38.83	38.89	37.77
Pr	3.48	3.35	3.49	3.38	3.19	3.12	3.44	3.30	3.07	3.24	3.37	3.57	3.39	2.99	3.87	3.35	3.29
Nd	10.29	10.39	10.20	10.29	8.94	9.48	10.58	10.29	8.95	10.30	9.44	10.84	9.60	8.65	10.40	10.41	9.80
Sm	1.96	1.73	1.90	2.03	1.51	1.72	1.74	1.62	1.65	1.82	1.52	1.72	1.63	1.65	1.67	1.59	1.87
Eu	0.19	0.18	0.21	0.26	0.15	0.15	0.18	0.18	0.18	0.23	0.25	0.20	0.15	0.17	0.19	0.19	0.20
Gd	1.62	1.63	1.66	1.81	1.46	1.52	1.45	1.15	1.41	1.72	1.55	1.72	1.81	1.09	1.52	1.72	1.72
Tb	0.31	0.29	0.26	0.24	0.26	0.25	0.29	0.36	0.22	0.28	0.30	0.29	0.26	0.26	0.30	0.30	0.28
Dy	2.11	2.27	1.87	1.28	1.76	1.89	2.35	2.02	1.71	1.62	1.48	2.12	1.79	1.81	2.13	1.63	1.82
Ho	0.41	0.43	0.41	0.34	0.38	0.38	0.36	0.36	0.39	0.35	0.36	0.45	0.39	0.40	0.38	0.38	0.39
Er	1.40	1.32	1.38	1.09	1.03	1.06	1.35	1.47	1.06	1.54	1.43	1.58	1.40	1.27	1.30	1.44	1.33
Tm	0.21	0.21	0.22	0.29	0.18	0.20	0.19	0.21	0.22	0.20	0.24	0.23	0.20	0.19	0.25	0.21	0.23
Yb	1.79	1.76	1.64	1.47	1.30	1.46	1.79	1.65	1.43	1.62	1.87	1.72	1.47	1.31	1.64	1.41	1.58
Lu	0.28	0.24	0.25	0.34	0.24	0.23	0.31	0.28	0.23	0.26	0.24	0.25	0.22	0.20	0.27	0.26	0.26

APPENDIX1. continues

Locations	2. Location	2. Location	2. Location	2. Location	2. Location	2. Location	2. Location	2. Location	2. Location	2. Location	2. Location	2. Location	2. Location	3. Location	3. Location	3. Location	3. Location
Sample Name	BPB-13	BPB-13	BPB-13	GLB	GLB	GLB	GLB	GLB	GLB	GLB	GLB	GLB	GLB	TPC-11	TPC-11	TPC-12	TPC-12
SiO_2	77.87	78.92	76.60	78.27	78.52	65.19	66.44	77.13	64.33	66.07	64.73	66.27	64.52	76.71	80.57	78.27	77.54
Al_2O_3	11.72	11.39	12.62	12.05	11.62	21.81	17.84	12.31	22.62	18.13	22.21	17.85	22.47	11.93	9.61	11.25	11.19
Fe_2O_3 [T]	0.84	0.92	1.35	0.76	0.80	0.17	0.12	1.39	0.19	0.11	0.17	0.09	0.18	1.04	0.62	0.69	0.74
MgO	0.08	0.10	0.22	0.06	0.07	0.00	0.00	0.15	0.00	0.00	0.00	0.00	0.00	0.21	0.06	0.06	0.06
CaO	0.52	0.50	0.59	0.52	0.53	3.98	0.12	0.55	4.41	0.10	4.45	0.18	4.14	0.94	0.42	0.53	0.48
Na_2O	3.42	2.90	3.15	3.38	3.18	7.99	2.81	3.46	7.61	2.82	7.55	2.82	7.80	2.90	4.20	3.72	4.28
K2O	5.21	4.94	5.10	4.65	4.86	0.71	11.18	4.64	0.68	11.41	0.66	11.44	0.73	5.80	4.25	5.18	5.38
TiO_2	0.12	0.11	0.14	0.11	0.20	0.01	0.01	0.14	0.01	0.01	0.01	0.01	0.01	0.18	0.10	0.10	0.11
P_2O_5	0.01	0.01	0.02	0.01	0.02	0.01	0.01	0.01	0.00	0.01	0.00	0.01	0.00	0.05	0.01	0.01	0.01
MnO	0.06	0.06	0.06	0.06	0.06	0.00	0.00	0.06	0.00	0.00	0.00	0.00	0.00	0.06	0.05	0.06	0.06
SUM	99.86	99.86	99.85	99.86	99.86	99.87	98.53	99.85	99.86	98.65	99.79	98.67	99.85	99.83	99.89	99.87	99.86
Ba	387.18	379.09	373.78	445.26	401.22	554.82	12932.45	434.14	620.16	11850.46	1075.31	11638.91	563.80	406.84	351.83	392.86	405.68
Ni	1.16	2.05	12.50	0.65	1.26	0.95	3.26	5.04	2.57	1.51	0.95	0.63	4.64	14.03	<0.1	0.78	0.00
Cr	8.63	5.65	2.90	2.36	2.98	6.42	1.29	3.46	3.12	5.13	1.16	6.13	13.56	10.36	<0.1	0.80	13.77
Sc	2.85	2.71	3.50	2.33	2.26	0.40	0.59	2.79	0.05	0.28	0.79	0.43	0.74	6.91	2.50	3.16	2.61
Co	0.20	0.57	1.22	0.20	0.24	0.00	0.00	1.02	0.02	0.04	0.00	0.00	0.16	1.88	0.18	0.17	0.16
Ga	14.44	14.95	17.93	11.70	15.12	17.63	11.34	12.38	21.62	11.79	19.18	11.98	22.02	16.45	12.31	14.01	13.01
Nb	24.15	24.21	24.96	24.37	22.55	0.00	0.00	26.29	0.03	0.04	0.00	0.01	0.15	27.76	22.49	24.56	25.68
Rb	155.51	142.55	155.88	137.90	143.00	1.06	106.93	148.28	1.02	104.96	0.94	108.97	0.92	156.27	130.15	144.82	146.55
Sr	38.95	37.33	38.74	38.98	37.92	488.79	384.08	41.82	535.81	360.45	715.68	386.91	582.87	48.77	32.03	38.89	37.46
Th	14.43	13.65	14.80	15.08	14.30	0.00	0.00	14.98	0.00	0.00	0.00	0.00	0.00	19.16	12.00	14.36	14.24
U	6.29	5.96	6.34	6.05	5.92	0.00	0.00	5.93	0.00	0.24	0.00	0.00	0.00	6.43	5.36	6.11	6.43
V	2.80	3.73	8.17	1.48	1.85	0.22	0.05	5.67	0.11	0.08	0.20	0.01	0.05	5.22	1.54	1.93	1.72
Zr	45.36	45.88	49.96	49.91	49.15	0.00	0.00	51.93	0.00	0.00	0.22	0.00	0.11	58.03	40.54	49.67	46.76
Y	12.88	12.41	12.35	13.63	12.10	0.13	0.22	13.95	0.12	0.16	0.26	0.21	0.12	15.17	10.29	13.08	12.39
Pb	16.80	15.72	17.10	13.04	16.92	9.00	18.89	12.81	9.40	17.78	8.87	17.32	8.03	32.66	13.26	17.54	20.69
Zn	10.55	19.19	18.52	9.77	18.96	0.34	0.95	13.92	1.15	1.70	0.90	0.90	1.01	46.14	12.84	9.25	14.74
Cs	6.35	5.36	6.38	5.61	5.72	0.00	0.10	6.08	0.04	0.10	0.04	0.10	0.01	7.24	4.66	5.77	6.41
Hf	2.08	1.64	1.88	2.02	1.94	0.00	0.06	1.97	0.01	0.00	0.01	0.02	0.00	2.48	1.47	1.76	1.91
Ta	2.30	2.08	2.27	2.10	1.82	0.00	0.06	2.12	0.01	0.08	0.00	0.14	0.02	3.18	2.12	2.34	2.29
La	19.88	19.72	20.36	21.18	20.26	8.07	1.57	22.50	9.79	1.28	10.22	1.53	9.20	25.71	17.23	20.61	20.56
Ce	38.80	37.43	37.67	38.90	37.80	9.30	0.87	40.21	10.16	0.76	11.45	0.93	10.13	45.15	36.19	39.45	39.58
Pr	3.36	3.35	3.18	3.60	3.40	0.56	0.04	3.76	0.63	0.10	0.71	0.04	0.65	4.46	2.95	3.35	3.30
Nd	10.96	9.81	10.17	11.08	10.08	1.34	0.00	10.69	1.65	0.11	1.76	0.09	1.60	15.14	8.54	10.62	10.42
Sm	1.66	1.80	1.98	1.85	1.60	0.14	0.02	2.04	0.16	0.05	0.11	0.00	0.06	2.39	1.30	1.89	2.02
Eu	0.21	0.17	0.22	0.25	0.17	0.93	0.81	0.28	0.95	0.65	1.11	0.81	1.12	0.42	0.20	0.17	0.24
Gd	2.00	1.48	1.80	1.53	1.67	0.14	0.00	1.97	0.08	0.00	0.18	0.00	0.01	2.45	1.37	1.46	1.55
Tb	0.29	0.22	0.26	0.30	0.32	0.00	0.00	0.32	0.00	0.00	0.00	0.00	0.00	0.31	0.29	0.30	0.27
Dy	1.94	1.99	1.88	2.17	1.87	0.10	0.01	2.09	0.02	0.00	0.01	0.01	0.03	2.43	1.98	1.86	1.96
Ho	0.37	0.40	0.37	0.43	0.43	0.00	0.01	0.47	0.01	0.00	0.00	0.01	0.00	0.40	0.32	0.46	0.38
Er	1.37	1.21	1.28	1.57	1.63	0.01	0.00	1.49	0.03	0.00	0.00	0.00	0.02	1.56	1.02	1.36	1.38
Tm	0.21	0.16	0.21	0.21	0.28	0.00	0.00	0.23	0.00	0.00	0.00	0.01	0.00	0.21	0.16	0.22	0.20
Yb	1.79	1.54	1.38	1.46	1.71	0.00	0.02	1.62	0.05	0.02	0.00	0.00	0.00	1.92	1.21	1.80	1.66
Lu	0.25	0.26	0.21	0.30	0.19	0.00	0.00	0.28	0.00	0.00	0.00	0.01	0.01	0.25	0.23	0.26	0.22

APPENDIX 1. continues

Locations	3. Location	3. Location	3. Location	3. Location	3. Location	3. Location	3. Location	3. Location	3. Location	3. Location	3. Location	3. Location	3. Location	3. Location	3. Location	3. Location	3. Location
Sample Name	TPC-12	TPC-13	TPC-13	TPC-13	TPC-14	TPC-14	TPC-14	BPC-14	BPC-14	BPC-14	BPC-15	BPC-15	BPC-15	BPC-16	BPC-16	BPC-17	BPC-17
SiO_2	78.38	76.66	76.25	77.47	77.92	76.00	77.16	77.54	78.30	77.94	78.15	78.40	77.77	78.99	78.15	80.16	81.43
Al_2O_3	11.85	12.01	12.00	11.47	11.01	12.18	11.01	11.99	11.63	11.90	11.40	11.51	11.51	11.34	11.62	10.57	10.54
Fe_2O_3 [T]	0.97	0.96	0.97	0.89	0.95	0.96	0.93	0.79	0.79	0.79	0.80	0.77	0.85	0.78	0.78	0.62	0.62
MgO	0.11	0.10	0.14	0.09	0.13	0.11	0.10	0.07	0.07	0.07	0.07	0.06	0.07	0.07	0.07	0.08	0.06
CaO	0.71	0.57	0.57	0.55	0.53	0.59	0.52	0.55	0.52	0.59	0.56	0.48	0.48	0.47	0.51	0.47	0.48
Na_2O	2.52	3.36	3.28	3.14	2.96	3.15	3.69	3.51	3.18	3.03	3.29	3.26	3.38	2.82	3.15	2.74	1.91
K2O	5.14	5.96	6.42	6.05	6.17	6.63	6.24	5.24	5.19	5.38	5.41	5.19	5.61	5.25	5.43	5.06	4.66
TiO_2	0.11	0.12	0.12	0.12	0.10	0.12	0.11	0.10	0.11	0.11	0.10	0.11	0.10	0.09	0.10	0.09	0.09
P_2O_5	0.01	0.03	0.02	0.02	0.03	0.03	0.04	0.01	0.02	0.02	0.02	0.02	0.02	0.01	0.01	0.01	0.02
MnO	0.06	0.06	0.06	0.06	0.06	0.07	0.06	0.06	0.06	0.06	0.06	0.06	0.06	0.06	0.06	0.06	0.05
SUM	99.84	99.85	99.84	99.86	99.86	99.84	99.86	99.86	99.86	99.87	99.85	99.86	99.86	99.87	99.87	99.87	99.88
Ba	381.84	423.05	417.29	413.07	397.35	438.55	406.02	408.54	392.61	389.99	386.51	369.67	395.55	385.08	385.22	372.03	348.29
Ni	0.04	2.19	2.21	2.12	4.93	2.21	2.39	0.00	0.00	3.13	0.69	2.63	1.29	0.00	0.00	3.41	0.10
Cr	12.59	18.26	20.91	18.66	7.82	14.81	6.30	2.98	9.44	9.64	12.27	10.26	7.90	6.08	8.53	14.11	14.51
Sc	3.37	3.09	3.16	2.89	3.11	3.23	2.38	2.91	2.72	2.82	2.88	2.53	3.02	2.47	2.56	2.61	1.68
Co	0.34	0.73	0.64	0.37	0.58	0.62	0.38	0.03	0.17	0.33	0.43	0.25	0.33	0.27	0.26	0.11	0.82
Ga	16.94	18.39	15.12	15.93	14.15	15.10	16.67	13.84	14.80	15.53	16.42	17.60	18.14	14.34	15.55	16.73	14.20
Nb	23.86	25.13	26.29	24.93	24.71	27.22	24.31	24.70	23.95	24.57	23.82	23.48	25.49	23.25	23.01	25.60	22.83
Rb	145.52	164.20	167.12	157.70	151.89	171.12	159.10	159.74	155.43	157.65	152.87	158.96	167.66	159.85	154.15	176.24	137.30
Sr	38.61	40.00	40.21	38.82	39.79	45.48	40.18	37.30	36.75	35.75	35.86	37.49	38.36	35.35	36.54	35.29	34.46
Th	14.30	15.77	15.63	14.79	14.12	15.70	13.99	15.32	14.48	14.04	13.36	13.27	14.56	12.88	14.38	40.97	10.57
U	5.88	7.02	6.86	6.76	6.30	7.02	6.60	6.65	6.09	6.82	6.02	6.41	7.30	6.32	6.57	6.23	5.43
V	3.18	3.57	7.81	2.27	3.03	2.90	4.11	2.41	2.20	2.14	2.20	2.29	2.67	1.99	2.18	2.12	2.40
Zr	49.72	52.76	52.52	50.16	47.42	50.53	48.07	48.29	48.44	44.68	119.41	43.77	43.81	42.49	45.36	42.54	39.19
Y	13.88	14.07	13.88	13.26	12.93	14.77	12.33	14.38	12.79	12.88	13.71	13.29	11.67	12.13	13.90	10.85	11.96
Pb	68.75	28.77	31.15	26.78	32.81	25.96	25.96	20.03	16.25	15.29	20.36	53.09	29.06	15.03	21.76	51.77	11.00
Zn	76.32	18.59	24.22	11.58	22.62	21.28	17.48	12.69	14.69	7.93	12.43	34.63	18.41	9.21	9.75	38.92	2.22
Cs	5.33	6.81	6.94	6.66	6.51	6.79	6.59	6.58	6.33	6.50	5.99	5.31	6.26	5.73	6.15	6.12	5.48
Hf	1.76	1.95	2.22	1.69	2.02	2.04	2.18	2.13	1.84	1.73	1.81	1.64	1.69	1.80	1.80	1.89	1.25
Ta	2.38	2.41	2.32	2.42	2.27	2.46	2.12	2.15	2.14	2.21	2.09	2.02	2.32	2.11	2.09	1.88	1.46
La	21.37	22.59	22.42	21.03	20.39	23.33	20.27	21.53	20.52	20.27	20.55	19.19	20.10	19.51	20.71	18.96	16.78
Ce	39.43	43.71	41.84	43.35	38.24	42.41	38.41	39.61	39.29	40.24	38.45	38.30	40.18	37.62	38.09	34.97	33.58
Pr	3.62	3.86	3.66	3.47	3.27	3.98	3.28	3.52	3.41	3.75	3.16	3.23	3.30	3.39	3.38	3.46	2.84
Nd	11.16	13.09	11.06	10.79	10.47	11.58	10.02	10.72	10.06	11.09	9.83	9.76	10.72	10.02	10.31	7.79	8.39
Sm	1.96	2.21	2.02	2.02	1.50	2.26	1.82	2.05	1.91	1.56	2.04	1.55	1.97	1.42	1.93	1.46	1.37
Eu	0.18	0.21	0.22	0.18	0.22	0.23	0.18	0.25	0.19	0.14	0.21	0.22	0.30	0.23	0.17	0.17	0.22
Gd	2.13	1.60	1.93	1.71	1.64	1.80	1.88	1.56	1.64	1.85	1.64	1.85	1.49	1.38	1.76	1.39	1.42
Tb	0.30	0.35	0.33	0.35	0.26	0.33	0.24	0.30	0.31	0.29	0.26	0.18	0.26	0.26	0.26	0.24	0.22
Dy	1.89	1.96	2.05	1.99	1.98	2.37	1.83	1.80	1.88	2.00	1.79	2.07	1.81	1.68	2.03	1.45	1.48
Ho	0.47	0.39	0.44	0.37	0.41	0.53	0.41	0.48	0.38	0.39	0.35	0.33	0.33	0.39	0.41	0.33	0.39
Er	1.44	1.56	1.41	1.40	1.26	1.61	1.19	1.52	1.44	1.39	1.42	1.16	1.31	1.42	1.48	1.41	1.00
Tm	0.19	0.20	0.20	0.19	0.21	0.23	0.22	0.23	0.22	0.18	0.17	0.18	0.20	0.24	0.22	0.26	0.10
Yb	1.47	1.75	1.67	1.70	1.65	1.64	1.67	1.83	1.25	1.55	1.80	1.31	1.73	1.38	1.88	1.20	1.09
Lu	0.30	0.26	0.24	0.23	0.27	0.24	0.28	0.24	0.27	0.28	0.22	0.28	0.24	0.23	0.22	0.18	0.19

APPENDIX 1. continues

Locations	3. Location	3. Location	3. Location	3. Location	3. Location	3. Location	3. Location	3. Location	3. Location	3. Location	4. Location	4. Location	4. Location	4. Location	4. Location	4. Location	4. Location
Sample Name	BPC-17	GLC	GLC	GLC	GLC	GLC	GLC	GLC	GLC	GLC	TPD-15	TPD-15	TPD-15	TPD-16	TPD-16	TPD-16	TPD-17
SiO_2	80.08	67.96	65.74	77.33	64.01	76.91	77.40	72.87	75.97	76.55	77.45	77.49	76.95	79.69	79.08	77.43	78.77
Al_2O_3	10.30	17.36	20.64	12.40	22.14	12.62	12.58	15.75	13.32	13.68	11.58	11.78	12.47	10.42	10.33	11.53	11.29
Fe_2O_3 [T]	0.61	0.30	0.13	0.74	0.14	0.87	0.60	2.40	1.10	1.31	0.86	0.98	0.90	0.69	0.96	0.75	0.75
MgO	0.07	0.02	0.00	0.14	0.00	0.20	0.08	0.84	0.28	0.47	0.09	0.11	0.08	0.06	0.20	0.08	0.07
CaO	0.46	2.59	3.43	0.61	4.06	0.50	0.55	0.40	0.59	0.65	0.56	0.52	0.63	0.46	0.51	0.69	0.59
Na_2O	2.94	9.05	9.01	3.68	8.84	3.17	3.67	2.09	3.31	2.05	4.11	3.21	3.15	3.90	3.99	3.67	2.62
K2O	5.24	2.53	0.90	4.76	0.69	5.37	4.83	5.02	5.02	4.75	5.01	5.55	5.46	4.49	4.55	5.51	5.59
TiO_2	0.10	0.05	0.01	0.13	0.00	0.14	0.10	0.33	0.17	0.20	0.11	0.12	0.11	0.10	0.17	0.11	0.11
P_2O_5	0.01	0.00	0.01	0.01	0.00	0.02	0.01	0.05	0.02	0.04	0.02	0.02	0.02	0.01	0.01	0.01	0.02
MnO	0.06	0.02	0.00	0.06	0.00	0.06	0.06	0.05	0.06	0.07	0.06	0.06	0.07	0.06	0.06	0.07	0.06
SUM	99.88	99.88	99.88	99.86	99.89	99.85	99.87	99.78	99.83	99.77	99.85	99.85	99.84	99.87	99.86	99.85	99.87
Ba	344.07	412.42	557.29	398.60	432.88	414.87	398.05	341.88	462.39	376.62	453.16	457.41	467.93	416.58	423.53	455.49	391.38
Ni	0.95	1.24	1.80	2.36	0.92	3.89	3.05	39.71	9.79	196.89	5.13	6.13	6.98	2.46	2.09	2.69	0.00
Cr	5.75	11.26	3.60	4.86	0.27	0.09	7.67	42.11	12.29	232.65	12.83	8.66	13.29	1.86	0.30	19.01	1.34
Sc	2.14	1.17	0.83	2.42	0.22	3.19	2.72	5.90	3.56	4.39	3.18	3.79	3.10	2.58	2.79	2.40	2.70
Co	0.18	0.00	0.06	0.44	0.00	1.17	0.41	3.58	1.58	4.02	0.41	0.65	0.60	0.29	0.63	0.16	0.27
Ga	14.92	17.44	18.69	14.22	22.07	15.67	14.42	22.07	18.11	17.22	15.18	19.05	13.94	10.30	12.52	14.30	14.84
Nb	20.92	9.61	0.03	23.29	0.01	24.61	23.20	28.64	25.15	25.07	24.11	26.05	26.84	22.28	22.68	24.81	25.45
Rb	156.22	56.51	1.19	150.95	0.89	155.59	153.73	174.40	152.09	154.12	146.74	160.16	154.81	132.85	133.60	160.74	153.72
Sr	32.52	307.23	453.71	41.45	476.00	40.34	37.77	40.30	46.97	42.28	42.22	43.52	47.03	35.37	37.08	44.44	37.34
Th	12.31	4.78	0.00	14.70	0.00	15.04	15.08	15.63	15.16	17.01	14.67	14.76	15.51	12.86	12.13	14.83	13.95
U	6.64	2.18	0.00	6.02	0.00	6.11	5.75	4.81	5.71	6.98	6.03	6.63	6.77	5.50	5.55	6.79	6.00
V	2.33	0.79	0.27	4.57	0.20	5.02	2.87	26.81	10.67	11.55	2.87	2.93	2.32	2.08	3.69	2.39	2.51
Zr	39.42	15.95	0.11	48.11	0.04	51.55	49.08	75.55	53.09	55.50	49.66	51.86	54.61	42.92	41.16	52.54	48.63
Y	11.35	4.89	0.15	13.40	0.11	15.69	14.05	14.63	18.26	16.39	13.87	13.43	14.59	11.51	11.05	13.67	13.18
Pb	15.76	9.40	8.53	17.52	9.21	18.34	14.65	23.35	19.00	28.44	15.64	29.86	34.86	13.43	13.34	45.94	15.76
Zn	7.77	1.35	1.47	9.57	1.53	10.57	7.90	20.72	16.26	13.41	10.79	27.95	16.17	10.07	13.30	41.87	10.29
Cs	5.81	2.40	0.01	6.30	0.03	6.45	5.67	7.96	6.43	6.15	5.59	6.84	6.60	5.11	5.19	6.11	5.73
Hf	1.38	0.64	0.00	1.65	0.02	2.00	1.65	2.50	2.10	2.03	2.21	1.60	2.06	1.63	1.60	1.79	1.76
Ta	1.77	0.72	0.00	2.22	0.02	2.19	1.86	2.33	2.05	2.40	2.29	2.48	2.42	2.09	2.10	2.21	2.31
La	17.42	12.67	6.56	21.33	8.94	23.88	21.48	24.99	25.24	26.36	21.97	22.67	23.09	18.65	18.28	21.15	20.42
Ce	36.21	20.52	8.28	39.20	9.44	43.56	39.57	50.12	44.21	53.37	40.98	40.69	45.16	37.30	37.37	40.71	39.27
Pr	3.10	1.46	0.53	3.55	0.60	3.94	3.42	5.12	4.28	4.88	3.65	3.64	3.85	3.17	2.98	3.34	3.19
Nd	9.12	4.83	1.05	11.13	1.37	12.56	10.52	14.63	13.68	15.99	10.89	11.05	10.93	9.45	9.29	10.11	10.56
Sm	1.48	0.86	0.01	1.52	0.01	2.28	1.65	2.26	2.28	2.47	1.37	1.73	2.07	1.78	1.72	1.26	1.88
Eu	0.16	0.48	0.76	0.19	0.86	0.26	0.19	0.35	0.33	0.37	0.16	0.25	0.22	0.19	0.18	0.20	0.22
Gd	1.14	0.71	0.00	1.53	0.09	1.99	1.81	2.41	2.21	2.76	1.55	1.91	1.85	1.56	1.51	1.45	1.56
Tb	0.28	0.12	0.00	0.30	0.01	0.40	0.30	0.38	0.39	0.47	0.34	0.30	0.29	0.26	0.24	0.30	0.28
Dy	1.51	0.67	0.08	2.00	0.07	2.33	2.01	2.13	2.54	3.11	1.81	2.14	2.07	1.76	1.66	2.15	1.64
Ho	0.34	0.15	0.00	0.41	0.00	0.49	0.43	0.38	0.47	0.50	0.37	0.43	0.37	0.33	0.33	0.38	0.37
Er	1.03	0.69	0.00	1.45	0.00	1.54	1.40	1.28	1.52	1.67	1.30	1.43	1.45	1.02	1.05	1.11	1.31
Tm	0.18	0.05	0.00	0.23	0.00	0.25	0.24	0.20	0.23	0.27	0.20	0.18	0.25	0.18	0.17	0.17	0.16
Yb	1.52	0.48	0.00	1.59	0.00	1.89	1.73	1.73	2.10	2.24	1.85	1.90	1.61	1.38	1.37	1.82	1.67
Lu	0.18	0.08	0.00	0.26	0.00	0.27	0.23	0.29	0.30	0.30	0.22	0.27	0.25	0.22	0.22	0.21	0.23

APPENDIX 1. continues

Locations	4. Location	4. Location	4. Location	4. Location	4. Location	4. Location	4. Location	4. Location	4. Location	4. Location	4. Location	4. Location	4. Location	4. Location	4. Location	4. Location	4. Location
Sample Name	TPD-17	BPD-18	BPD-18	BPD-18	BPD-19	BPD-19	BPD-19	BPD-20	BPD-20	BPD-20	BPD-21	BPD-21	BPD-21	GLD	GLD	GLD	GLD
SiO_2	79.58	79.03	79.45	78.81	78.16	80.59	79.83	79.49	78.31	79.07	79.29	78.45	78.55	78.17	62.22	78.93	78.01
Al_2O_3	10.33	10.62	11.25	11.35	11.63	9.56	10.59	11.05	11.92	11.37	11.31	11.72	11.55	11.98	23.30	11.64	12.45
Fe_2O_3 [T]	0.67	0.72	0.59	0.59	0.63	0.58	0.53	0.54	0.53	0.52	0.54	0.57	0.56	0.82	0.16	0.62	0.59
MgO	0.07	0.07	0.06	0.06	0.07	0.06	0.06	0.05	0.06	0.06	0.08	0.10	0.10	0.10	0.00	0.08	0.07
CaO	0.48	0.50	0.52	0.42	0.50	0.54	0.38	0.46	0.51	0.43	0.49	0.50	0.50	0.57	5.38	0.50	0.54
Na_2O	3.69	3.22	2.89	3.27	2.71	2.72	2.64	3.16	3.33	3.09	2.61	2.69	2.95	3.03	8.25	2.79	3.30
K2O	4.87	5.54	4.92	5.19	6.01	5.64	5.68	4.97	5.02	5.16	5.38	5.57	5.41	5.02	0.53	5.14	4.74
TiO_2	0.10	0.10	0.10	0.10	0.10	0.09	0.10	0.10	0.10	0.10	0.10	0.11	0.10	0.10	0.01	0.09	0.10
P_2O_5	0.01	0.01	0.02	0.01	0.01	0.02	0.02	0.01	0.01	0.01	0.01	0.02	0.02	0.02	0.00	0.01	0.01
MnO	0.06	0.06	0.06	0.06	0.07	0.06	0.06	0.06	0.06	0.06	0.06	0.12	0.13	0.06	0.00	0.06	0.06
SUM	99.87	99.86	99.87	99.87	99.87	99.87	99.88	99.88	99.86	99.87	99.87	99.86	99.85	99.85	99.85	99.85	99.86
Ba	354.49	391.89	406.59	403.68	399.49	388.86	370.25	400.33	425.30	402.01	386.35	440.72	423.09	507.76	571.21	439.85	420.96
Ni	0.00	0.34	1.25	1.39	0.00	0.00	0.00	0.00	0.58	0.58	1.31	5.83	23.10	11.55	0.00	8.36	0.00
Cr	1.24	10.14	11.60	2.86	10.78	6.58	8.26	9.56	10.32	11.22	5.68	18.22	21.47	6.64	5.62	2.41	3.26
Sc	2.79	2.68	1.99	2.11	2.36	1.98	2.27	2.68	2.78	2.40	2.38	2.40	2.91	3.12	0.41	2.58	2.19
Co	0.22	0.38	0.17	0.25	0.37	0.13	0.12	0.08	0.47	0.12	0.62	3.76	5.72	0.32	0.00	0.38	0.14
Ga	15.76	13.48	15.65	14.02	13.96	10.03	16.62	15.05	15.20	14.07	14.26	15.45	13.80	14.43	19.86	16.75	14.79
Nb	22.39	23.38	25.10	24.91	24.24	25.32	26.77	22.51	25.49	23.02	23.04	26.28	23.34	22.22	0.00	22.21	22.33
Rb	141.20	158.25	151.96	154.07	151.78	150.51	163.46	145.83	158.62	149.09	156.43	170.66	152.31	147.43	0.53	144.47	141.53
Sr	35.84	36.34	36.25	36.21	35.55	31.52	33.06	34.57	38.13	35.81	36.11	39.87	38.52	40.92	667.19	38.83	39.98
Th	12.43	12.57	12.79	12.72	13.40	11.02	11.46	12.62	14.34	12.75	12.42	13.68	12.95	14.37	0.00	15.19	14.75
U	5.97	6.61	6.49	6.41	6.77	6.44	6.02	6.48	7.51	6.32	6.18	6.59	6.11	5.91	0.00	5.65	5.77
V	2.53	2.41	2.09	1.96	2.45	2.48	2.31	2.28	2.47	2.30	2.62	3.82	3.53	4.24	0.04	2.04	2.17
Zr	43.76	44.42	44.49	46.37	43.91	35.59	40.28	40.50	45.94	43.53	44.76	46.60	43.65	47.07	0.05	46.95	47.97
Y	11.74	11.22	11.69	11.89	12.96	10.05	9.24	11.05	12.72	12.54	12.53	13.36	12.50	13.98	0.15	13.92	13.92
Pb	85.46	17.76	14.55	16.90	17.04	21.15	21.24	15.63	16.17	25.97	17.30	23.59	26.22	40.75	8.35	15.14	12.99
Zn	62.29	13.39	5.19	8.91	6.29	16.73	6.28	5.95	4.79	24.66	9.43	11.51	13.76	20.05	2.66	9.30	7.81
Cs	5.47	6.11	5.39	6.19	6.38	6.50	5.85	5.79	6.45	6.14	6.40	6.41	6.18	6.12	0.02	6.37	5.83
Hf	1.40	1.41	1.48	2.00	1.39	1.21	1.64	1.68	1.74	1.46	1.64	1.76	1.62	1.68	0.00	1.66	1.93
Ta	2.04	2.03	1.86	2.10	1.91	1.73	1.82	1.87	2.02	2.11	2.19	2.08	1.83	2.01	0.00	2.18	2.20
La	18.75	18.02	19.14	19.05	19.20	15.61	16.41	18.84	20.33	18.26	18.51	20.11	19.66	20.21	10.00	21.70	21.65
Ce	35.61	36.91	37.77	37.96	38.89	35.19	36.99	37.83	40.93	38.61	37.49	42.49	44.66	38.56	11.68	39.18	38.82
Pr	3.09	3.17	3.30	3.34	3.22	2.58	2.81	3.09	3.29	3.13	2.98	3.16	3.10	3.46	0.67	3.49	3.62
Nd	9.12	8.52	9.49	9.08	9.62	8.47	8.80	9.16	10.35	9.99	9.98	10.39	10.28	9.49	1.67	11.25	10.15
Sm	1.56	1.59	1.80	1.77	1.83	1.08	1.85	1.52	1.40	1.62	1.72	1.56	1.68	2.12	0.15	1.85	2.27
Eu	0.19	0.17	0.21	0.15	0.21	0.30	0.18	0.12	0.16	0.24	0.17	0.20	0.21	0.21	1.00	0.18	0.25
Gd	1.75	1.22	1.34	1.46	1.43	0.97	1.65	1.33	1.44	1.45	1.48	1.81	1.53	1.94	0.17	1.81	1.61
Tb	0.21	0.22	0.27	0.24	0.26	0.16	0.24	0.29	0.32	0.24	0.20	0.30	0.29	0.29	0.00	0.27	0.36
Dy	1.68	1.52	1.79	1.77	1.69	1.49	1.79	1.88	2.14	1.88	1.70	1.81	1.68	2.44	0.07	2.06	2.18
Ho	0.38	0.37	0.34	0.36	0.36	0.31	0.33	0.32	0.38	0.38	0.35	0.30	0.38	0.42	0.00	0.38	0.38
Er	1.27	1.29	0.94	1.17	1.18	0.71	0.97	1.34	1.32	1.21	1.13	1.53	1.41	1.39	0.00	1.12	1.36
Tm	0.18	0.19	0.16	0.16	0.22	0.17	0.16	0.18	0.22	0.17	0.18	0.22	0.21	0.20	0.01	0.23	0.20
Yb	1.51	1.49	1.49	1.77	1.65	1.69	1.40	1.79	1.42	1.41	1.52	1.53	1.36	1.75	0.01	1.43	1.54
Lu	0.20	0.23	0.22	0.25	0.18	0.15	0.25	0.22	0.23	0.18	0.18	0.20	0.19	0.23	0.00	0.23	0.26

APPENDIX 1. continues

Locations	4. Location	4. Location	4. Location	4. Location	4. Location	4. Location	4. Location	4. Location	5. Location	5. Location	5. Location	5. Location	5. Location	5. Location	5. Location	5. Location	5. Location
Sample Name	GLD	GLD	GLD	GLD	GLD	GLD	GLD	GLD	TPE-18	TPE-18	TPE-19	TPE-19	TPE-19	TPE-20	TPE-20	TPE-20	TPE-21
SiO_2	78.70	77.44	63.49	78.07	77.86	78.15	78.32	78.27	80.28	79.99	77.66	77.34	76.60	77.62	79.31	78.45	77.10
Al_2O_3	11.90	13.05	23.32	12.55	12.39	12.62	12.50	12.48	9.50	9.61	12.06	11.72	12.22	11.56	10.75	11.45	11.92
Fe_2O_3 [T]	0.59	0.79	0.16	0.54	0.79	0.54	0.51	0.58	0.64	0.67	0.78	0.80	0.74	0.75	0.66	0.70	0.83
MgO	0.07	0.13	0.00	0.06	0.18	0.07	0.06	0.09	0.09	0.09	0.08	0.12	0.14	0.06	0.06	0.06	0.17
CaO	0.50	0.50	5.33	0.53	0.54	0.52	0.52	0.51	0.46	0.44	0.67	0.65	0.65	0.52	0.49	0.52	0.61
Na_2O	3.40	3.19	6.99	3.51	3.32	3.41	3.30	3.34	3.84	3.92	3.49	3.66	3.54	3.60	3.77	3.18	3.70
K2O	4.55	4.58	0.51	4.44	4.57	4.41	4.50	4.41	4.91	4.98	4.93	5.32	5.32	5.56	4.65	5.32	5.30
TiO_2	0.10	0.11	0.01	0.10	0.14	0.10	0.10	0.10	0.10	0.10	0.12	0.15	0.12	0.11	0.11	0.11	0.15
P_2O_5	0.01	0.02	0.01	0.01	0.01	0.01	0.01	0.01	0.01	0.01	0.00	0.02	0.03	0.01	0.01	0.01	0.01
MnO	0.06	0.05	0.00	0.06	0.06	0.06	0.06	0.06	0.05	0.05	0.06	0.06	0.06	0.06	0.06	0.06	0.06
SUM	99.87	99.85	99.82	99.87	99.85	99.87	99.87	99.85	99.88	99.87	99.85	99.83	99.41	99.86	99.87	99.87	99.85
Ba	429.38	429.74	655.31	427.30	449.85	461.17	454.47	455.55	375.67	391.76	466.49	472.80	4080.35	452.18	413.01	427.48	445.80
Ni	2.53	9.93	7.45	0.00	9.15	0.42	2.83	5.91	4.06	3.66	3.87	8.73	1.33	0.66	0.44	0.91	0.44
Cr	5.05	1.27	2.26	9.98	1.25	6.29	2.36	15.96	0.08	4.49	5.03	17.90	4.26	2.65	3.88	0.53	0.98
Sc	2.35	2.85	0.37	2.17	2.76	2.31	2.27	2.39	2.38	2.29	2.97	3.00	2.74	2.88	2.67	2.47	3.20
Co	0.42	0.74	0.00	0.27	1.08	0.19	0.25	0.21	0.22	0.25	0.23	0.50	0.59	0.11	0.22	0.44	0.89
Ga	14.67	14.87	21.73	12.63	13.62	13.94	12.45	13.26	14.61	13.69	14.85	17.62	15.75	15.97	11.82	12.42	15.12
Nb	22.47	22.60	0.00	23.75	24.60	20.42	23.36	21.74	20.61	21.59	25.37	25.88	25.49	22.88	23.26	23.42	25.24
Rb	139.60	140.21	0.64	137.23	142.36	137.22	130.10	139.49	138.32	141.27	146.27	162.55	148.84	161.29	130.07	147.41	154.33
Sr	39.64	49.61	797.88	39.72	42.86	37.63	40.69	40.43	34.63	34.00	40.23	44.56	105.82	38.73	37.38	38.75	42.90
Th	13.76	14.72	0.00	14.93	14.48	15.16	14.89	13.79	11.34	11.62	14.02	15.13	13.78	14.31	13.24	13.76	14.71
U	5.75	5.89	0.00	6.17	6.20	6.07	5.77	5.55	5.78	5.85	5.92	6.19	6.34	6.32	5.39	5.79	6.28
V	2.35	5.88	0.00	2.12	5.54	2.04	1.95	5.42	1.71	2.12	2.32	2.21	1.96	2.34	1.59	1.55	4.47
Zr	47.25	49.93	0.00	52.52	50.07	50.00	49.95	45.28	39.38	39.41	47.49	49.51	45.53	46.41	43.70	46.07	51.13
Y	13.25	14.19	0.07	14.52	14.64	13.58	14.68	13.65	10.65	10.50	13.21	13.99	12.83	12.55	12.05	13.11	13.39
Pb	13.11	33.98	5.65	13.75	14.51	11.44	13.31	14.52	23.39	15.14	50.96	100.03	167.98	21.72	14.42	15.38	17.72
Zn	12.78	9.95	0.33	12.00	7.44	7.62	8.27	11.09	16.54	12.18	34.46	65.30	261.37	12.90	8.55	17.04	12.54
Cs	5.99	5.66	0.03	5.69	5.97	5.35	5.47	5.92	5.68	5.25	5.46	6.54	5.99	6.32	5.16	5.67	6.25
Hf	1.69	1.92	0.00	2.08	1.99	1.88	1.93	1.80	1.37	1.42	1.73	1.90	2.01	1.98	1.69	1.67	1.93
Ta	2.11	1.98	0.01	2.22	2.13	2.23	2.29	1.94	1.83	1.88	1.98	2.20	2.37	2.30	1.99	2.12	2.14
La	20.12	22.47	10.35	21.77	21.01	20.75	21.63	20.06	16.90	16.88	20.62	21.11	19.57	21.17	18.78	20.33	21.21
Ce	37.91	40.41	11.64	40.36	37.84	39.97	38.38	36.90	32.92	34.67	40.69	39.07	37.53	37.99	35.59	36.90	39.40
Pr	3.36	3.64	0.81	3.70	3.62	3.75	3.63	3.31	2.80	2.89	3.33	3.43	3.20	3.36	3.20	3.36	3.68
Nd	10.66	11.00	1.78	11.26	10.35	11.07	11.31	11.19	8.53	9.05	10.52	9.96	10.58	10.08	9.49	9.78	11.09
Sm	1.90	1.88	0.07	1.90	1.62	1.90	2.04	1.52	1.58	1.42	2.10	2.11	1.48	1.57	1.61	1.88	1.72
Eu	0.16	0.26	0.98	0.24	0.24	0.17	0.21	0.19	0.14	0.14	0.27	0.18	0.20	0.17	0.17	0.17	0.21
Gd	1.62	1.60	0.14	1.88	1.42	1.47	1.59	1.97	1.17	1.36	1.89	1.33	1.54	1.65	1.57	1.76	1.70
Tb	0.30	0.29	0.01	0.33	0.35	0.33	0.31	0.32	0.21	0.24	0.21	0.30	0.23	0.27	0.25	0.31	0.31
Dy	1.93	2.20	0.06	2.07	1.95	2.21	2.09	2.05	1.59	1.55	1.89	1.87	1.85	2.08	1.92	1.84	1.80
Ho	0.44	0.45	0.01	0.49	0.40	0.48	0.50	0.38	0.33	0.34	0.37	0.38	0.44	0.42	0.37	0.39	0.37
Er	1.41	1.47	0.00	1.41	1.47	1.52	1.25	1.27	1.07	0.98	1.11	1.57	1.45	1.26	1.11	1.12	1.23
Tm	0.21	0.27	0.00	0.24	0.22	0.20	0.26	0.21	0.19	0.16	0.21	0.17	0.23	0.20	0.20	0.18	0.24
Yb	1.44	1.85	0.00	1.78	1.86	1.90	1.65	1.74	1.25	1.38	1.80	1.54	1.87	1.82	1.52	1.62	1.93
Lu	0.27	0.24	0.00	0.26	0.28	0.24	0.27	0.24	0.20	0.19	0.27	0.24	0.29	0.21	0.24	0.22	0.25

APPENDIX 1. continues

Locations	5. Location	5. Location	5. Location	5. Location	5. Location	5. Location	5. Location	5. Location	5. Location	5. Location	5. Location	5. Location	5. Location	5. Location	5. Location	5. Location	5. Location
Sample Name	TPE-21	TPE-21	TPE-22	TPE-22	TPE-22	BPE-22	BPE-22	BPE-23	BPE-23	BPE-23	BPE-24	BPE-24	BPE-24	BPE-25	BPE-25	BPE-26	BPE-26
SiO_2	77.79	77.65	78.89	79.25	78.64	79.13	78.32	78.35	78.56	79.20	79.29	79.43	78.90	78.92	79.68	77.50	79.21
Al_2O_3	11.53	11.81	11.29	11.03	11.05	10.99	11.67	11.62	11.15	10.98	11.12	10.79	11.13	11.29	11.23	11.88	11.16
Fe_2O_3 [T]	0.76	0.66	0.65	0.60	0.59	0.48	0.54	0.50	0.59	0.51	0.52	0.60	0.51	0.55	0.55	1.02	0.56
MgO	0.12	0.08	0.08	0.06	0.06	0.07	0.08	0.06	0.08	0.06	0.07	0.09	0.07	0.08	0.07	0.19	0.07
CaO	0.51	0.57	0.55	0.53	0.55	0.52	0.50	0.65	0.63	0.57	0.52	0.55	0.57	0.54	0.52	0.74	0.51
Na_2O	3.91	3.27	2.76	2.84	3.87	2.92	3.20	3.54	3.75	3.35	2.81	3.11	3.45	2.82	2.77	3.19	3.27
K2O	5.05	5.65	5.46	5.37	4.92	5.60	5.39	4.97	4.93	5.02	5.36	5.11	5.07	5.49	4.89	5.14	4.92
TiO_2	0.13	0.11	0.11	0.11	0.11	0.10	0.10	0.10	0.10	0.10	0.10	0.10	0.11	0.11	0.10	0.10	0.10
P_2O_5	0.01	0.02	0.02	0.01	0.01	0.01	0.01	0.01	0.01	0.01	0.01	0.01	0.01	0.02	0.01	0.02	0.01
MnO	0.06	0.06	0.06	0.06	0.06	0.06	0.06	0.06	0.06	0.06	0.06	0.06	0.06	0.06	0.06	0.06	0.06
SUM	99.86	99.86	99.86	99.86	99.87	99.89	99.87	99.88	99.86	99.86	99.87	99.86	99.87	99.88	99.87	99.84	99.87
Ba	422.24	440.98	384.72	388.20	401.46	373.44	412.36	400.94	380.37	383.29	390.71	368.37	382.33	364.11	367.90	440.89	372.09
Ni	7.78	1.28	0.63	0.82	0.70	0.00	0.00	4.30	8.71	0.00	0.00	8.18	3.74	0.00	0.00	7.93	1.24
Cr	3.22	3.49	16.43	14.26	14.95	8.22	4.27	<1	12.55	<1	9.63	12.79	11.26	17.57	15.14	21.82	11.43
Sc	2.61	3.11	3.11	2.62	2.22	2.01	2.29	2.59	2.56	2.53	2.85	2.52	2.16	2.92	1.76	2.69	2.26
Co	0.44	0.34	0.43	0.31	0.11	0.42	0.39	0.16	0.76	0.11	0.87	0.98	0.19	0.52	0.09	0.69	0.16
Ga	13.93	13.96	15.06	14.49	13.23	18.18	16.22	13.92	13.18	15.07	13.50	16.09	14.86	13.76	13.66	14.96	13.26
Nb	23.56	25.25	23.61	24.30	24.67	24.85	25.56	25.58	24.25	25.02	23.69	24.60	24.18	22.50	22.86	22.21	25.19
Rb	153.93	153.77	148.90	141.50	141.84	165.67	156.19	157.45	147.37	147.20	146.28	146.46	149.00	146.65	151.02	146.09	143.84
Sr	41.22	41.68	37.15	34.75	36.69	32.82	37.73	35.64	34.09	35.96	35.13	37.15	37.34	34.93	34.90	56.95	36.50
Th	14.22	14.40	13.75	13.23	13.82	12.27	13.08	12.74	11.78	13.27	12.97	12.31	13.16	12.53	11.83	13.50	13.00
U	5.92	6.24	6.04	5.96	6.03	6.12	6.28	6.55	6.00	6.47	6.61	6.56	6.38	6.04	5.78	6.26	6.16
V	3.35	2.48	2.17	1.77	1.90	3.06	2.41	2.44	2.47	2.41	1.90	2.50	1.97	1.91	2.00	3.14	1.66
Zr	50.07	50.56	47.40	44.86	47.50	43.26	44.99	42.64	41.22	45.25	44.02	44.68	43.21	46.29	45.14	47.81	44.44
Y	12.86	13.98	12.82	12.23	12.08	12.68	12.14	11.58	11.24	11.78	13.31	11.64	11.85	11.29	12.28	13.11	12.35
Pb	15.57	20.05	45.63	50.72	29.66	15.51	15.44	16.98	58.04	51.32	17.43	41.53	16.56	19.23	14.49	22.08	36.32
Zn	12.00	12.97	36.13	59.31	22.12	3.28	19.39	9.35	33.92	42.53	10.14	30.35	8.80	12.79	9.11	47.33	41.93
Cs	6.17	7.21	5.84	5.86	5.63	5.86	6.69	6.15	5.56	5.91	6.51	6.42	6.03	5.61	5.23	5.87	5.15
Hf	1.72	1.86	1.72	1.45	1.62	1.91	1.45	1.64	1.55	1.38	1.89	1.36	1.58	1.46	1.74	1.98	1.44
Ta	2.19	2.24	1.94	2.01	2.23	1.96	2.05	2.06	2.15	1.78	2.04	2.03	2.05	2.06	1.84	1.83	2.04
La	20.62	22.05	20.37	18.83	20.15	18.09	19.38	19.15	17.21	18.00	18.99	18.38	18.89	19.58	18.76	20.38	18.92
Ce	37.92	39.88	37.48	37.37	37.95	36.46	38.38	38.67	36.73	38.25	38.22	38.85	39.15	37.77	36.23	38.67	37.25
Pr	3.45	3.63	3.49	3.32	3.24	3.00	3.28	3.15	3.13	2.99	3.19	2.85	3.26	3.27	3.19	3.58	3.21
Nd	10.03	10.78	10.44	8.83	9.39	8.66	9.45	9.17	9.37	8.64	9.50	8.65	9.56	9.93	9.30	9.87	9.56
Sm	1.59	1.63	1.72	1.42	1.55	0.91	1.90	1.73	1.78	1.41	1.53	1.57	1.87	1.71	1.43	1.53	1.53
Eu	0.21	0.22	0.19	0.18	0.15	0.14	0.12	0.19	0.41	0.21	0.21	0.24	0.18	0.32	0.18	0.17	0.11
Gd	1.51	2.00	1.70	1.32	1.68	1.45	1.36	1.24	1.65	1.47	1.44	1.93	1.41	1.67	1.40	1.87	1.46
Tb	0.31	0.32	0.29	0.24	0.29	0.20	0.25	0.27	0.20	0.23	0.24	0.29	0.27	0.20	0.28	0.31	0.26
Dy	1.93	2.02	1.91	1.78	1.91	1.48	2.00	1.65	1.85	1.87	1.77	1.79	1.56	1.51	1.50	1.96	1.56
Ho	0.42	0.38	0.39	0.34	0.40	0.45	0.40	0.33	0.36	0.30	0.37	0.34	0.38	0.31	0.36	0.38	0.38
Er	1.30	1.45	1.18	1.18	1.25	1.16	1.26	1.13	0.96	1.26	1.35	1.13	1.50	1.34	1.38	1.21	1.24
Tm	0.22	0.20	0.20	0.19	0.21	0.15	0.19	0.21	0.14	0.20	0.21	0.21	0.19	0.23	0.16	0.18	0.19
Yb	1.71	1.91	1.73	1.55	2.07	1.53	1.87	1.56	1.47	1.45	1.71	1.40	1.42	1.20	1.21	1.45	1.61
Lu	0.25	0.30	0.25	0.20	0.26	0.26	0.20	0.27	0.20	0.19	0.23	0.24	0.26	0.20	0.20	0.25	0.25

APPENDIX 1. continues

Locations	5. Location	5. Location	5. Location	5. Location	5. Location	5. Location	5. Location	5. Location	5. Location	5. Location	5. Location	5. Location	5. Location
Sample Name	BPE-26	GLE	GLE	GLE	GLE	GLE	GLE	GLE	GLE	GLE	GLE	GLE	GLE
SiO_2	78.86	65.52	78.23	78.67	78.54	78.37	78.43	77.94	78.41	77.36	78.53	78.59	76.94
Al_2O_3	11.51	20.74	12.08	12.14	12.20	12.24	12.25	12.27	12.05	12.38	11.75	11.86	12.21
Fe_2O_3 [T]	0.56	0.13	0.51	0.48	0.48	0.49	0.50	0.83	0.55	1.16	0.64	0.50	1.39
MgO	0.07	0.00	0.06	0.06	0.06	0.06	0.06	0.14	0.07	0.37	0.11	0.06	0.42
CaO	0.53	3.82	0.52	0.53	0.55	0.57	0.52	0.57	0.51	0.63	0.60	0.55	0.68
Na_2O	3.30	8.90	3.69	3.37	3.29	3.46	3.33	3.33	3.19	2.99	3.20	3.40	2.85
K2O	4.86	0.74	4.59	4.46	4.59	4.52	4.61	4.61	4.92	4.71	4.84	4.73	5.05
TiO_2	0.10	0.01	0.11	0.10	0.09	0.10	0.10	0.12	0.10	0.16	0.11	0.09	0.19
P_2O_5	0.01	0.00	0.01	0.01	0.01	0.01	0.01	0.01	0.01	0.01	0.01	0.01	0.02
MnO	0.06	0.00	0.06	0.06	0.06	0.06	0.06	0.06	0.06	0.06	0.06	0.06	0.08
SUM	99.87	99.86	99.86	99.87	99.86	99.87	99.86	99.86	99.87	99.83	99.86	99.86	99.82
Ba	386.55	612.88	445.28	415.24	438.42	453.32	416.73	418.98	417.47	412.08	417.51	443.84	419.43
Ni	5.28	0.00	0.00	0.00	0.00	0.00	1.87	5.25	0.00	22.60	5.60	1.55	24.35
Cr	14.94	6.25	7.17	4.56	3.79	0.27	4.58	1.50	4.89	4.86	7.97	7.86	20.68
Sc	2.31	0.41	2.63	2.36	2.37	2.27	2.11	2.73	2.52	3.66	2.62	2.30	4.42
Co	0.26	0.03	0.30	0.19	0.14	0.00	0.34	1.26	0.13	1.98	0.78	0.15	4.06
Ga	14.74	22.85	14.60	12.87	13.10	13.19	12.23	11.85	15.99	14.42	14.64	14.02	16.14
Nb	21.73	0.02	24.09	22.95	21.92	22.09	23.65	22.72	22.51	25.83	22.58	22.39	23.39
Rb	142.09	0.98	148.06	147.36	142.39	142.27	141.87	142.39	145.50	145.66	149.09	141.23	146.87
Sr	37.58	509.74	38.68	38.39	39.51	39.88	38.43	46.06	36.15	57.82	44.76	38.71	50.67
Th	12.78	0.00	13.47	14.40	14.65	14.50	14.41	14.42	13.45	26.67	13.64	13.48	14.57
U	5.90	0.00	5.77	5.82	6.12	6.19	6.02	5.96	5.75	10.64	5.73	5.77	5.81
V	1.78	0.00	2.38	2.12	1.97	2.05	1.88	3.73	2.55	10.74	3.46	2.17	13.48
Zr	44.56	0.00	46.13	48.99	51.82	49.71	50.02	51.34	52.01	76.17	48.50	49.55	60.95
Y	12.91	0.04	12.36	13.65	13.52	13.27	13.87	14.20	13.10	15.87	12.74	12.98	14.33
Pb	28.13	8.77	13.24	13.33	13.31	12.72	13.03	15.20	17.98	16.22	16.29	13.99	23.92
Zn	22.71	1.63	6.78	15.81	12.91	14.06	11.50	21.38	19.12	17.68	13.94	11.23	22.57
Cs	5.39	0.01	5.50	5.91	6.05	5.60	5.69	5.57	5.45	6.42	5.56	5.74	5.89
Hf	1.60	0.00	1.69	1.77	1.94	2.00	1.83	1.87	1.52	2.37	1.79	1.83	1.83
Ta	2.03	0.00	1.88	2.26	2.26	2.08	2.25	2.08	2.20	2.27	2.05	2.25	2.13
La	19.38	7.36	19.97	20.69	21.26	20.85	20.94	21.68	20.64	24.07	20.89	19.92	20.65
Ce	36.96	8.59	38.62	39.03	38.79	38.95	39.22	39.81	37.64	43.73	36.91	38.07	46.92
Pr	3.13	0.54	3.22	3.52	3.52	3.46	3.37	3.51	3.33	4.15	3.36	3.41	3.57
Nd	9.49	1.27	10.58	10.34	10.97	11.08	11.28	11.26	10.45	15.72	11.11	9.50	11.34
Sm	1.78	0.09	1.72	1.71	2.14	1.78	1.69	2.14	1.72	3.19	2.02	1.98	2.41
Eu	0.24	0.90	0.19	0.21	0.24	0.19	0.19	0.23	0.19	0.28	0.31	0.22	0.25
Gd	1.03	0.09	1.52	1.54	1.89	1.59	1.61	1.79	1.61	2.22	1.81	1.45	1.98
Tb	0.24	0.00	0.28	0.29	0.30	0.31	0.29	0.32	0.24	0.38	0.31	0.28	0.23
Dy	1.61	0.02	1.86	1.91	2.16	2.47	1.95	2.16	2.04	2.66	2.04	1.73	2.16
Ho	0.38	0.00	0.43	0.37	0.41	0.38	0.39	0.41	0.42	0.49	0.36	0.42	0.42
Er	1.13	0.00	1.15	1.40	1.37	1.47	1.41	1.51	1.16	1.71	1.46	1.35	1.43
Tm	0.20	0.00	0.22	0.20	0.23	0.22	0.19	0.27	0.20	0.24	0.20	0.22	0.25
Yb	1.59	0.00	2.07	1.69	1.50	1.66	1.76	1.66	2.02	1.70	1.60	1.65	1.91
Lu	0.31	0.00	0.18	0.25	0.31	0.24	0.24	0.28	0.29	0.29	0.23	0.27	0.22